Title
A More Extreme View of Molecular Gas in the Center of the Milky Way galaxy

Author
Mills, Elisabeth

Publication Date
2013

Peer reviewed|Thesis/dissertation

University of California
Los Angeles

A More Extreme View of Molecular Gas in the Center of the Milky Way galaxy

A dissertation submitted in partial satisfaction
of the requirements for the degree
Doctor of Philosophy in Astronomy

by

Elisabeth Anne Crossfield Mills

2013

Abstract of the Dissertation

A More Extreme View of Molecular Gas in the Center of the Milky Way galaxy

by

Elisabeth Anne Crossfield Mills

Doctor of Philosophy in Astronomy

University of California, Los Angeles, 2013

Professor Mark R. Morris, Chair

This thesis examines the molecular gas properties in the central 600 parsecs of the Galaxy (the CMZ). I first present a study of a group of HII regions in the central 10 parsecs embedded within the M-0.02-0.07 cloud, adjacent to the Sgr A East supernova remnant. To better depict the physical relationship between these sources, I use archival VLA observations and Paschen α images from the Hubble Space telescope to determine the extinction toward the HII regions (Mills et al. 2011). From the measured extinctions and source morphologies, I determine that three of the HII regions lie on the front side of the cloud and formed in the eastern part of the cloud which is unaffected by the supernova remnant's expansion. The higher extinction of the fourth HII region indicates it is embedded in the supernova-compressed ridge, and though younger than the other HII regions, is still older than the supernova. This work is an important determination of the their line-of-sight placement of these sources which helps to define their interaction and strengthens the case that the supernova did not trigger the formation of the HII regions.

I next present results from a project I led to survey a sample of CMZ clouds

for hot gas using the Green Bank Telescope (Mills & Morris 2013). I observe multiple highly-excited lines of NH_3 , and detect emission from the (9,9) line of NH_3 (excitation energy = 840 K) in 13 of 17 clouds, many of which have no associated star formation. For the three strongest sources, I derive rotation temperatures of 400-500 K, substantially higher than previous temperatures of 200-300 K measured for these clouds (Mauersberger et al. 1986). The widespread detections of gas hotter than 400 K indicates for the first time that his hot gas must be heated by global processes in the CMZ. These extremely high temperatures also suggest that cosmic rays are not responsible for the heating of this gas.

I also present a determination of the density of the Circumnuclear disk (CND) in the central two parsecs using multiple transitions of HCN and $HCO^+$with the APEX telescope, a 12m ALMA prototype dish. These molecules have critical densities $> 10^7$ $cm^{-3}$and directly constrain the existence of high-density gas. The excitation analysis of HCN and HCO^+yields significantly tighter limits on the typical densities in this gas ($n = 10^{5.0} - 10^{7.0}$ cm^{-3}), however I cannot rule out the possibility that a small number of individual gas clumps are tidally stable or in virial equilibrium (Mills et al., in prep.). The detection of the $v_2 = 1$ vibrationally-excited J=4-3 HCN line also indicates that infrared radiation may play a role in the excitation of HCN in this source, but it is not clear if radiative excitation in the CND is a localized or global phenomenon.

Finally, I present a summary of early results from a survey of four molecular cloud complexes in the CMZ (Mills et al. in prep.), which I led using the new capabilities of the VLA. The goal of this work is to determine the variation in temperature in these clouds on 0.1 pc scales to ultimately identify their heating sources. An unanticipated discovery of this study has been hundreds of weak, collisionally-excited CH_3OH masers which are detected in all of the clouds we

survey. The masers are distributed non-uniformly in the clouds, with concentrations indicating regions of shock activity which may be driving the evolution of physical conditions in these clouds. I also find that the $NH_3(3,3)$ line is weakly masing in several sources, which can be used to put constraints on the density of the gas clumps in these clouds (Walmsley & Ungerechts 1983).

The dissertation of Elisabeth Anne Crossfield Mills is approved.

Edward Young

Ben Zuckerman

Jean Turner

Mark R. Morris, Committee Chair

University of California, Los Angeles

2013

To my husband,

all of the graduate students who know what it takes to get here,

and Mr. Mongold: the best math teacher who ever was.

Table of Contents

List of Figures

List of Tables

Acknowledgments

There are so many people who have made the path to getting this degree a little shorter, a little easier, and a little more fun, and I would like to thank them all. But before I do so, there are also many people without whom I would not even still be on this path today. First and foremost, I would like to thank Liese Van Zee. Without her, I don't think I would have survived. For being kind to a precocious high school student in the first class she taught at Indiana University, and for always treating me like a colleague, and having the right words of support, I owe so much to her guidance. I would also like to thank the Indiana University Astronomy faculty, especially Dick Durisen, for teaching hands-down the best class I have ever experienced, reminding me how much I enjoy the challenge of studying astronomy. Thank you, James Aguirre, for giving me a chance as an REU student and getting me interested in in the Galactic center. Thank you, Andrea Stolte, for the enthusiasm which brought me to UCLA, and for always listening to me. Special thanks to Andrea Ghez, for helping me get a great start in Galactic center studies at UCLA, even though I decided that the central parsec just wasn't quite big enough for my interests.

I owe an enormous debt of gratitude to NRAO for their financial and professional support during my time as a graduate student, especially to Miller Goss, Deb Shepherd, Dale Frail, and everyone from the 2006 REU program. I can also never thank enough all of my collaborators in this work– Miguel Requena Torres, Rolf Güsten, Juergen Ott, Dave Meier, Lorant Sjouwerman, and most of all, Cornelia Lang, who has been the most tirelessly supportive, energetic, and all around wonderful collaborator and mentor I could ever hope for. I would also especially like to thank my fellow students– graduate students Natalie Butterfield,

Dominic Ludovici, Anika Schmeideke, and undergraduate Susie Schmidt. I know how hard you work, and you guys are amazing!

Thank you MPIA for giving me a desk in an amazingly vibrant institute, with so much exciting research going on all around me! Thanks to Katharine Johnston for being a great research buddy, and to Lisa Kaltenegger for being a wonderful adopted advisor.

Finally, I would like to thank my advisor Mark Morris, for alway being full of ideas, insight, and enthusiasm. His amazing career and relationships with collaborators all over the world are an inspiration to me.

Ultimately, I could not have accomplished any of this without my friends and family backing me all the way. Thanks to my mom for being my back to school buddy. You may have beaten me to a Masters degree by a year, but (thanks to you) now I will have a PhD! Thanks to my brother for always coming to visit me so I was able to have a few grad school vacations. Thanks also to my parents for encouraging me to do my undergrad studies at Indiana. I couldn't have hoped to aim higher than where I am today, and I am grateful not to have gotten in to debt in doing it! Last and most of all, thanks to my best friend Betsey who has been my partner in applications throughout our adventures with fellowships, graduate schools, and now postdoctoral jobs. We made it!

Chapter 2 of this thesis is based on a version of Mills et al. (2011). I would like to thank the anonymous referee of this paper for his detailed and insightful comments, which improved this paper. I would also like to thank R. Karlsson for sharing the results of his OH analysis with us before publication. Support for program HST-GO-11120 was provided by NASA through a grant from the Space Telescope Science Institute, which is operated by the Association of Universities for Research in Astronomy, Inc., under NASA contract NAS 5-26555. This ma-

terial is based upon work supported by the National Science Foundation under Grant No. 0907934

Chapter 3 is based on a version of a to-be-published article. I would like to thank Ryan Lau for sharing his maps of the CND dust opacity and temperature in advance of publication. This research has made use of the NASA/ IPAC Infrared Science Archive, which is operated by the Jet Propulsion Laboratory, California Institute of Technology, under contract with the National Aeronautics and Space Administration.

Chapter 4 is based on a version of Mills & Morris (2013). I would like to thank the Green Bank Telescope support staff, and especially to thank Ron Maddalena for extremely helpful discussions with regards to the calibration of the data. I also wish to thank T. Oka and D. Meier for their useful comments on the manuscript, and to thank the anonymous referee for the careful and insightful suggestions which improved the final version. This material is based upon work supported by a grant from the NRAO Student Observing Support program.

Chapter 5 is based on a version of a to-be-published article. We wish to thank the staff of the Karl G. Jansky Very Large Array, and especially to thank Dr. Claire Chandler for assisting us with setting up the observations.

Vita

1984	Born, Michigan, USA
2007	S.S. (Physics, Astronomy) Indiana University
2009	M.S. (Astronomy) University of California, Los Angeles.

Publications

Mills, E.A.C., Morris, M.R. *Detection of Widespread Hot Ammonia in the Galactic Center* Submitted to ApJ on April 12, 2013

Mills, E.A., Morris, M.R., Lang, C.C., Cotera, A., Dong, H., Wang, Q.D., Stolovy, S. *Properties of the Compact H II Regions G-0.02-0.07.* 2011, ApJ, 735:84-96

Mills, E.A., Morris, M.R., Lang, C.C., Cotera, A., Dong, H., Wang, Q.D., Stolovy, S. *Extinction toward the Compact HII Regions G-0.02-0.07* 2011, PASP, 439:125-127

Dong. H. , Wang, Q.D., Cotera, A., Stolovy, S., Morris, M.R., Mauerhan, J., **Mills, E.A.**, Schneider, G., Calzetti, D., Lang, C. *Hubble Space Telescope Paschen α survey of the Galactic Centre: data reduction and products.* 2011, MNRAS, 417:114-135

Stolte, A., Ghez, A.M., Morris, M.R., Do, T., Ballard, C., **Mills, E.A.**, Lu, J.R., Matthews, K. *L-band sources in the Arches cluster.* 2010, ApJ, 718:810-831

Bally, J., Aguirre, J., Battersby, C., Bradley, E.T., Cyganowski, C., Dowell, D., Drosback, M., Dunham, M.K., Evans, N.J. II, Ginsburg, A., Glenn, J., Harvey, P.,

Mills, E., Merello, M., Rosolowsky, E., Shirley, Y.L., Schlingman, W., Stringfellow,G., Walawender, J., Williams, J. *The Bolocam Galactic Plane Survey: Dust Continuum Emission in the Galactic Center Region.* 2010, ApJ, 721:137-163

Rafelski, M., Foley, M., Graves, G. J., Kretke, K. A., **Mills, E.**, Nassir, M., Patel, S. *Teaching Astronomy with an Inquiry Activity on Stellar Populations.* 2010, PASP, 436, 108-119

Sonnet, S., **Mills, B.**, Hamilton, J.C., Kaluna, H. *The 2009 Akamai Observatory Short Course Inquiry Activity: "Design and Build a Telescope"* 2010, PASP, 436, 131-137

Beers, T.C., Flynn, C., Rossi, S., Sommer-Larsen, J., Wilhelm, R., Marsteller, B., Lee, Y.S., De Lee, N., Krugler, J., Deliyannis, C.P., Simmons, A.T., **Mills, E.**, Zickgraf, F.J., Holmberg, J., nehag, A, Eriksson, A., Terndrup, D., Salim, S., Andersen, J., Nordström, B., Christlieb, N., Frebel, A., Rhee, J. *Broadband UBVRCIC Photometry of Horizontal-Branch and Metal-poor Candidates from the HK and Hamburg/ESO Surveys. I.* 2007, ApJS, 168:128-139

Mills, E.A.C., Güsten, R., Requena-Torres, M., Morris, M.R. *The Excitation of HCN and HCO^+, in the Galactic Center Circumnuclear Disk.* To be submitted June 2013

CHAPTER 1

Introduction

1.1 The Center of the Milky Way Galaxy

Together with the nearby Andromeda galaxy (distance $\sim$ 780 kpc Freedman & Madore 1990; Jensen et al. 2003, mass $\sim 1.6 \times 10^{12} M_{\odot}$, Klypin et al. 2002; Watkins et al. 2010), the Milky Way Galaxy in which we live is one of the two massive denizens of our small local group of galaxies, which consists of more than 99 galaxies, the majority of which are dwarf galaxies, and $\sim$ 27 of which are satellites of the Milky Way (Simon & Geha 2007; McConnachie 2012). Our Galaxy is a fairly typical example of a galaxy found in such a quiescent environment. It is a barred spiral (de Vaucouleurs 1964; Blitz & Spergel 1991) of approximate Hubble type SBbc (de Vaucouleurs 1970; Weaver 1970) with a total mass of $\sim 8 \times 10^{11} M_{\odot}$ (Bovy et al. 2012) and a luminosity of $\sim 2 \times 10^{10}$ $L_{\odot}$ (van den Bergh 1988; Pritchet & van den Bergh 1999). The merger history of our galaxy appears to have been quite quiescent within the past 8-10 Gyrs (Abadi et al. 2003; Font et al. 2006; Hammer et al. 2007), without substantial impacts on the structure of the Galactic disk (Bovy12a,Bovy12b, Bovy12c), though substructure in the halo bears witness to many events of small-scale consumption (e.g., Majewski et al. 2003). As a result of this quiet upbringing, our Galaxy has retained both its disk shape and its gas, and continues to form stars at at a relatively slow pace (its estimated present-day star formation rate (SFR) is

$\sim 2 M_\odot\,yr^{-1}$ Chomiuk & Povich 2011). Our Galaxy is less extreme than other star formation environments found in the local universe (e.g. M82, with a SFR of $\sim 10 M_\odot\,yr^{-1}$ O'Connell & Mangano 1978) or at high redshift, where populations of ultra-luminous infrared galaxies (ULIRGs) and submillimeter galaxies can have SFRs in excess of 500 $M_\odot\,yr^{-1}$ (Farrah et al. 2008; Magnelli et al. 2012; Hayward 2013). As such, although our galaxy is considered 'normal', the current conditions in its interior are actually not typical of the formation conditions for the majority of stars in our universe, which formed in the extreme starbursts which dominate the cosmic star formation rate during its peak between $z \sim 1-3$ (Le Floc'h et al. 2005; Pérez-González et al. 2005; Hopkins & Beacom 2006).

However, our Galaxy is still typical in many ways. Like the overwhelming majority (if not entirety) of galaxies of similar and greater mass (Kormendy & Gebhardt 2001; Kormendy et al. 2010, 2011), the center of the Milky Way is host to a central supermassive black hole (SMBH), its mass estimated to be $\sim 4.5 \times 10^6$ $M_\odot$ (Ghez et al. 2008; Gillessen et al. 2009b). In keeping with our Galaxy's quiet nature, the SMBH is currently quiescent, accreting at a sub-Eddington rate, compared to active galactic nuclei (AGN) found in local universe. Despite this low accretion rate, the black hole was first detected from the radio signature of this accretion as the compact source Sgr A* (Balick & Brown 1974). The central parsec of the Galaxy is also a strong infrared source, with the bulk of the emission emanating from a nuclear star cluster (Becklin & Neugebauer 1968, 1975; Becklin et al. 1978). At the center of this extended cluster is a compact cluster of young stars which have proved an extremely fortuitous means not only to accurately measure the mass of the SMBH (Eckart & Genzel 1996, 1997; Genzel et al. 1996, 1997; Ghez et al. 1998), but via the observed orbits, to restrict its maximal volume sufficiently that there is no astrophysically-likely alternative to its identification as a black hole (Kormendy 2004). Measurements of the stellar orbits and radial

velocities have also been used to determine the distance to the Galactic center, the current best estimate of which is 8.4±0.4 kpc (Ghez et al. 2008; Gillessen et al. 2009b).

The environment of the Galactic nucleus in the several hundred parsecs surrounding the central SMBH differs from the disk in several important ways. Slightly less than 5% of the total molecular gas reservoir of $\sim 8.4 \times 10^8$ $M_\odot$ in the Galaxy is concentrated in the center of the Galaxy, in a region with a diameter of $\sim$ 600 parsecs (Dahmen et al. 1998; Nakanishi & Sofue 2006). As a result, the surface density of molecular gas in this region is almost two orders of magnitude higher than that typical of the Milky Way as a whole, and is more comparable to gas surface densities observed for ULIRGS and starburst galaxies (see Figure 1.1 Tacconi et al. 2008), or the centers of more normal, nearby galaxies (Meier & Turner 2001; Meier & Turner 2004; Meier et al. 2008). The Galactic center molecular gas is also extremely turbulent, with line widths of 15-50 km s^{-1} (Bally et al. 1987), in comparison to widths of $\sim$ 1-10 km s^{-1} typically found in giant molecular clouds in the Galactic disk. Possibly related to its enhanced turbulence, the molecular gas is also significantly hotter than gas in the disk, with high average gas temperatures of (50−200 K, Morris et al. 1983; Güsten et al. 1985; Hüttemeister et al. 1993a). Gas in the Galactic center is also more processed than gas in the Disk, as seen in observations of an increasing radial abundance gradient in the Galaxy, measured both indirectly via electron temperatures in HII regions and directly via observations of oxygen and nitrogen in the HII regions (Churchwell & Walmsley 1975; Shaver et al. 1983; Quireza et al. 2006). Increased evidence of nuclear processing in the nucleus is also seen in the $^{12}C/^{13}C$ isotopic ratio, which is observed to decrease radially to a minimum value of 20-25 in the Galactic center (Wilson 1999; Riquelme et al. 2010). With its sizable concentration of turbulent, hot, and enriched molecular gas, the Galactic

center is one of the most extreme environments for star formation in our Galaxy. However, the effect of this environment on the star formation is not clear: although the average recent star formation rate per unit volume in this region is 2-3 orders of magnitude higher than the average in the Galactic disk (Figer et al. 2004; Crocker 2012b), there appears to be a dearth of ongoing star formation in comparison to what is expected from the sheer amount of molecular gas (Morris 1989; Beuther et al. 2012; Longmore et al. 2013).

The Milky Way's central concentration of molecular gas represents a unique laboratory for studying the mechanisms which control physical conditions in molecular gas, and which perhaps ultimately control the star formation process. Though globally, the molecular gas in our Galaxy represents a quiescent environment for star formation, the molecular gas in the central 600 parsecs is hot, dense, turbulent, and awash in a background of radiation from ultraviolet photons, X-rays, and cosmic rays. The proximity of our Galaxy's center allows us to probe these processes at spatial resolutions which are possible nowhere else. Ultimately, these studies will determine whether the physical processes which dominate in our Galactic nucleus can be scaled up to explain the properties of more extreme environments. In this environment it is possible to study the density distribution, kinematics, and heating of the gas, relating them to mechanisms of fueling and feedback, as gas is funneled into the nucleus and as previous generations of stars perhaps shape the formation of new stars. Here, one can study star formation in an environment closer to the extreme conditions in which most stars in the universe formed, and determine how important environment actually is to this process. For this thesis, I focus on one aspect of these studies: the current conditions in the molecular gas in the central 600 parsecs. By putting new constraints on both the extrema of temperature and density in this region, and the variations of temperature and density with spatial scale in the gas, this work contributes to

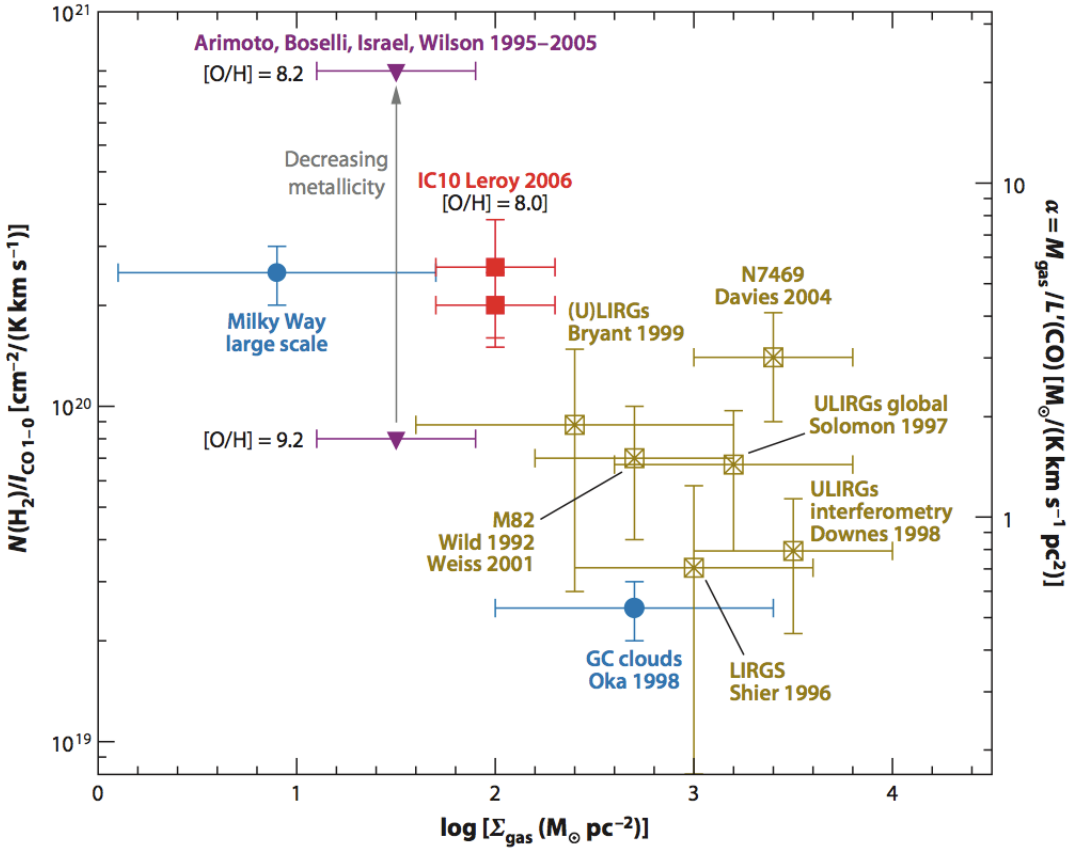

Figure 1.1: Values of X[CO], the conversion factor from the observed intensity of the J=1-0 CO line to H_2 column density. Notice that the surface density of H_2 (X-axis) in the center of the Galaxy is almost two orders of magnitude larger than the average for the Milky Way (blue points), and is more similar to typical surface densities in starburst and luminous infrared galaxies (LIRGs), or the centers of more normal, nearby galaxies (e.g., NGC 6946, IC342, and Mafffei 2, which also have X(CO) values 2-4 times lower than the Milky Way Meier & Turner 2001; Meier & Turner 2004; Meier et al. 2008). This figure is originally from Tacconi et al. (2008); the version here is from Kennicutt & Evans (2012).

our understanding of how the molecular gas in the Galactic center is affected by its environment, and as a result how star formation may ultimately proceed (or not) in these giant molecular clouds.

1.2 The Central Molecular Zone

The Central Molecular Zone, or CMZ, of our Galaxy is defined as the inner ∼600 parsecs (or 4 degrees) of the galaxy, where there is a concentration of primarily molecular gas (Figure 1.2). Historically, large-scale surveys of the molecular gas have been primarily carried out using ^{12}CO and its isotopologues (Bania 1977; Liszt et al. 1977; Liszt & Burton 1978; Bally et al. 1987, 1988; Oka et al. 1996, 1998a,b, 2001; Mizuno & Fukui 2004; Oka et al. 2012), in conjunction with studies of the neutral gas in HI (e.g., Burton & Liszt 1978; Lang et al. 2010; McClure-Griffiths et al. 2012). There have also been surveys of molecules which trace a denser gas component (e.g., HCN; Jackson et al. 1993, and CS; Tsuboi et al. 1999) as well as SiO, which traces the distribution of shocked gas (Martin-Pintado et al. 1997). More recently, with the advent of wideband radio and millimeter receivers, there have been simultaneous surveys of dozens of molecular species reflecting the full chemical complexity of this region (Walsh et al. 2011; Purcell et al. 2012; Jones et al. 2012, 2013). The total mass of molecular gas in the CMZ is believed to be $3^{+2}_{-1} \times 10^7$ M$_\odot$ (Dahmen et al. 1998), with 10% of this gas concentrated in one giant molecular cloud complex, Sgr B2 (Gordon et al. 1993), located ∼ 100 parsecs in projection to the east of the dynamical center of the Galaxy. Sgr B2 is an extremely active star forming region, consisting of a hot, photon-dominated envelope (Ceccarelli et al. 2002; Goicoechea et al. 2004) surrounding dozens of compact, ultracompact, and hypercompact HII regions (Gaume & Claussen 1990; Mehringer et al. 1993; Gaume et al. 1995; de Pree

et al. 1996, 1998; Zhao & Wright 2011), and two hot cores exhibiting both infall and outflow motions (Vogel et al. 1987; Lis et al. 1993; Kuan & Snyder 1996; Liu & Snyder 1999; Qin et al. 2008; Rolffs et al. 2010). The younger of the two cores, Sgr B2-N, is demonstrably the most chemically complex site in the Galaxy, in part due to its extremely high column density (Snyder et al. 1994; Miao et al. 1995; Belloche et al. 2008). Outside of the Sgr B2 complex, the rest of the gas in the CMZ is distributed in a population of several dozen giant molecular clouds that are 1-2 orders of magnitude less massive. For reference, those clouds which are the main subject of this thesis are identified in the bottom panel of Figure 1.2. Below, I review the current picture of the molecular gas, describing the dynamics of gas clouds in the CMZ, their physical properties, the environment this gas is subject to, and finally the impact this environment has upon the heating of this gas and the formation of stars in this region.

1.2.1 Gas Dynamics

1.2.1.1 Molecular Gas Orbits

Individual giant molecular clouds in the CMZ are found primarily on orbits which are controlled by the strong gravitational potential of the nuclear bar (Liszt & Burton 1980; Binney et al. 1991). The influence of the bar potential on gas motions can be seen as a parallelogram in a position-velocity diagram of the gas in the central 4 degree (Figure 1.3). The first molecular gas is found on the last non-intersecting X_1 orbit, which has its major axis aligned with the bar. This orbit crosses the outermost of a separate family of orbits, the X_2 orbits, which have their major axes perpendicular to the bar. The resulting large-scale shocks at this orbit intersection along the bar at radii of 200 pc, similar to those observed in other galaxies (Meier & Turner 2005; Jogee et al. 2005), are believed to convert

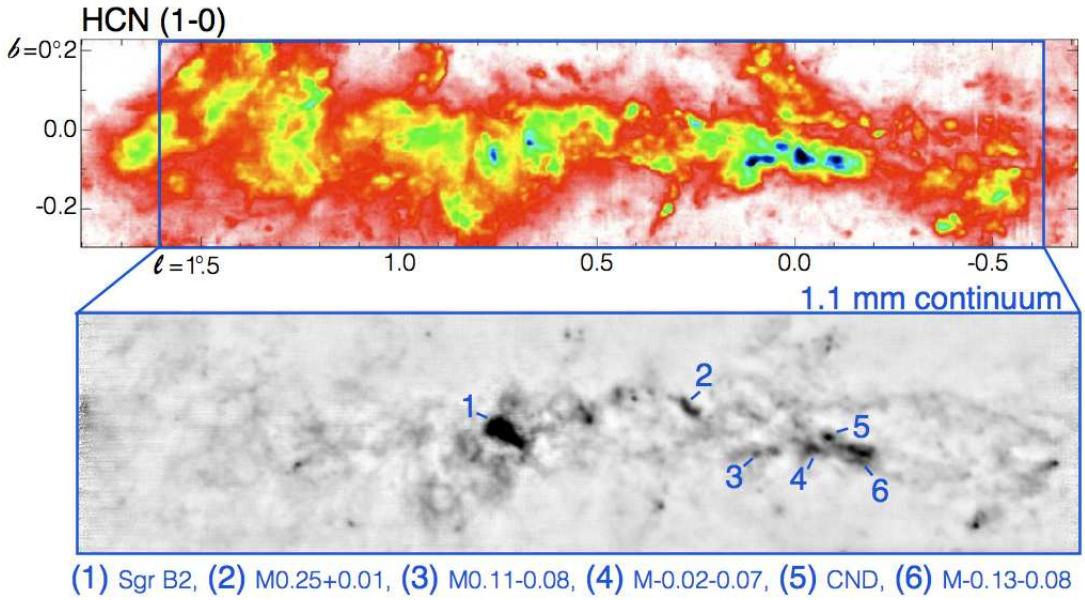

Figure 1.2: Top: Integrated intensity of the HCN (1-0) line, showing the distribution of dense gas in the Central Molecular Zone of the Galaxy. Figure taken from Jones et al. (2013). Bottom: A map of the 1.1 mm continuum emission in the Galactic center (Bally et al. 2010), tracing the dense cool dust in the centers of the highest column-density molecular clouds. Individual clouds studied in this thesis are labeled.

the gas from primarily neutral to primarily molecular (Binney et al. 1991), and drive gas inward onto the X_2 orbits. The majority of molecular clouds in the central 600 parsecs have kinematics consistent with X_2 orbits, and it is suggested that these clouds trace a twisted ring with an orbital period of a few 10^6 years, which is visible in cool dust emission (Molinari et al. 2011).

Not all of the molecular gas motions in the CMZ are consistent with these orbits. In particular, a highly UV-irradiated gas complex spanning more than 50 parsecs in projection, has negative velocities which are forbidden in the sense of Galactic rotation. The ionized faces of clouds in this complex form the Arched Filaments, a series of ionized structures stretch over 900 square parsecs and arranged in concentric shells around the Arches star cluster (Yusef-Zadeh et al. 1984; Yusef-Zadeh & Morris 1987a; Lang et al. 1997). This extremely massive ($M > 10^4 M_\odot$, with ∼150 O and Wolf-Rayet type stars) and compact young cluster (age $\sim 2-3$ Myrs, Figer et al. 2002; Clarkson et al. 2012) is believed to be entirely responsible for their ionization (Cotera et al. 1996; Lang et al. 2001). Gas in this complex is also associated with an extended group of more than a dozen compact HII regions (representing the largest star forming complex interior to the Sgr B2 cloud), which have velocities similar to the gas in the Arched Filaments, and span an additional 30 parsecs (Zhao et al. 1993). Due to the unusual kinematics of this gas complex, it is thought that this gas is located on the far side of the CMZ, and is kinematically perturbed by the bar potential.

1.2.1.2 Outflows

Not only does gas likely flow into the inner nuclear regions of the Galaxy via shocks along the bar, it may also flow out: there are fossil indications of energetic events that may represent episodes of gas expulsion from the Galactic center.

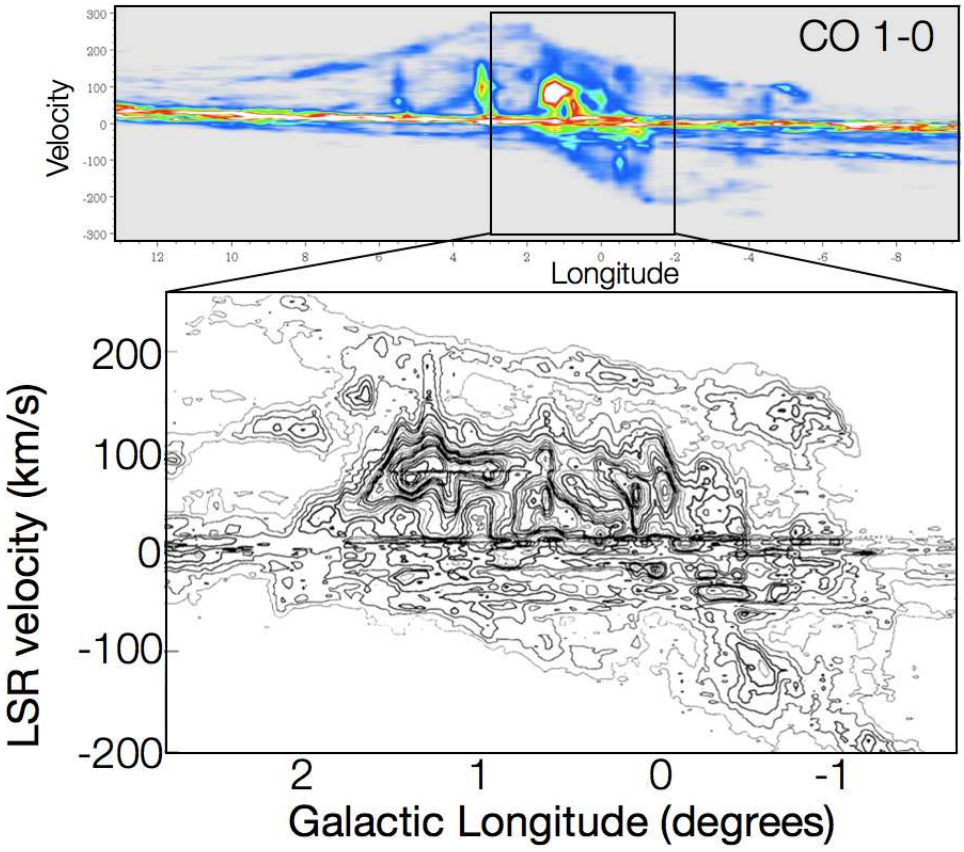

Figure 1.3: A position-velocity diagram of molecular gas (traced by ^{12}CO 1-0) in the central 600 parsecs of the galaxy. The tilted 'parallelogram' feature is the 'Expanding Molecular Ring', which is often interpreted as the influence of the bar potential on gas motions and orbits. Figure adapted from Morris & Serabyn (1996).

On small scales, there is debate as to whether there is any evidence for a jet from the central supermassive black hole (Falcke & Markoff 2000; Markoff et al. 2007; Yusef-Zadeh et al. 2012). On large angular scales, a 1° tilted lobe-like structure is observed in the central 100 parsecs of the galaxy, to the north of the Galactic plane. This structure, the northern extent of which was first seen in radio continuum (Sofue & Handa 1984) and which appears to have a bipolar counterpart in 8 μm dust emission (Bland-Hawthorn & Cohen 2003), is suggested to be an outflow from the central parsecs, consistent with being fueled by a starburst (Law 2008, 2010). On far larger scales, recent gamma-ray observations from the Fermi telescope uncovered enormous, symmetric lobes extending 50° above and below the Galactic plane, which are believed to originate in the Galactic center (Su et al. 2010) . Competing theories for their origin involve either jets (or collimated outflows) from an active galactic nucleus (AGN) (Zubovas & Nayakshin 2012; Guo & Mathews 2012; Su & Finkbeiner 2012; Yang et al. 2012), or the outflow from either a nuclear starburst or a prolonged high rate of star formation in the Galactic center (Crocker 2012a; Carretti et al. 2013). A new population of compact, high velocity HI clouds in the central $8° \times 8°$ of the Galaxy may also be related to one or both of these large-scale outflows. More than 80 candidate clouds with velocities up to 200 km s^{-1} are suggested to have kinematics consistent with entrainment in a starburst-driven outflow (McClure-Griffiths et al. 2013).

1.2.1.3 Asymmetries

One unusual large-scale feature of molecular gas in the CMZ is its asymmetric distribution. As can be seen both in Figures 1.2 and 1.3, the highest gas surface densities are found to the east of the dynamical center of the Galaxy, at positive

latitudes and velocities. Launhardt et al. (2002a) estimate that there is three times more mass at positive latitudes as at negative. The gas in the CMZ is also lies in a plane which is tilted with respect to the plane of the Galaxy. One explanation for these asymmetries is that the gravitational potential experienced by gas in the CMZ is asymmetric, leading to an m=1 or 'one-armed spiral' mode: a density wave which orbits around the Galaxy's dynamical center. This is in addition to the m=2 mode which is due to the bar potential. Intriguingly, whatever the dynamical origin of the gas asymmetry, it is also currently reflected in the distribution of massive star clusters– both of the young massive young star clusters in the CMZ– the Arches (Nagata et al. 1995; Cotera et al. 1996) and the Quintuplet (Nagata et al. 1990), as well as the similarly massive but nascent Sgr B2 star forming region, are found to the east of the dynamical center. This combination of massive clusters and gas at positive latitudes also leads to an asymmetry in the free-free radio emission observed in the Galactic center, highlighting that the eastern side of the CMZ is far more active than the west.

1.2.2 Physical Conditions in the dense gas

1.2.2.1 Density

The highest density gas in the CMZ is found in a population of several dozen giant molecular clouds. In keeping with the overall asymmetry of the CMZ, 6 of the 8 clouds with the greatest concentration of mass are found at positive latitudes (Longmore et al. 2013). Global measurements of the average molecular gas densities in the CMZ have been made using several methods. This simplest is to assume the gas density to be in excess of the critical density of the tracer molecule. In this way, average densities ranging from $\sim 10^4$ cm^{-3} (inferred from observations of CO, Bally et al. 1988), $\gtrsim 10^4$ cm^{-3} (from CS 1-0 observations

of Tsuboi et al. 1999), and $\gtrsim 10^5$ cm^{-3} (from HCN 1-0 observations by Jackson et al. 1993) have been found for the molecular gas in the CMZ. A second method is to conduct radiative transfer modeling of non-LTE gas conditions to match observed line intensities to the temperatures, volume densities, and column densities responsible for their excitation. Using lines of CO 3-2 and 1-0, (Nagai et al. 2007) are able to fit the observed intensities to models with gas densities of $10^{3.5-4.0}$ cm^{-3}, though they note they are unable to find solutions to some regions that are affected by self absorption. An excitation analysis using ratios of 3 mm and 7 mm molecular lines, including ^{13}CS and HC_3N finds typical densities of a few 10^4 cm^{-3} (Jones et al. 2012, 2013). For comparison, Martin et al. (2004) performed excitation analyses of CO 7-6 and 4-3, which have higher excitation energies than the lines probed by Nagai et al. or Jones et al. and find densities in cloud interiors up to $10^{4.5}$ cm^{-3}, which is the upper limit to which their analysis code is sensitive. Densities in excess of 10^4 cm^{-3} are also supported by excitation analyses of H_2CO emission (Zylka et al. 1992). However, the accuracy of all of these excitation analyses can be limited by several factors, including high optical depths and self absorption, as well as the excitation energies of the observed molecules.

Locally higher densities have also been inferred from studies of individual clouds. Observations of multiple transitions of CS in several clouds (M-0.02-0.07, and the Sickle cloud which adjoins the Quintuplet star cluster) indicate that gas densities in these clouds can range from a few 10^5 from up to a few 10^6 cm^{-3} (Serabyn & Güsten 1991; Serabyn et al. 1992). In M0.25+0.01, a quiescent molecular cloud which is suggested to be sufficiently massive to form a super-star cluster, densities are estimated to be lower, lying between $\sim 8 \times 10^4$(Longmore et al. 2012) to a few times 10^5 cm^{-3} (Kauffmann et al. 2013). The highest densities in the CMZ are suggested to exist in the Circumnuclear disk (CND),

a ring of gas and dust surrounding the central SMBH at a projected radius of ∼1.5 pc. A summary of density measurements in this cloud is given in Table 1.1. In the CND, densities up to have been inferred from interferometric observations of individual clumps in HCN and HCO^+, assuming the clumps to be in virial equilibrium (Christopher et al. 2005; Montero-Castaño et al. 2009). However, single-dish observations with tracers such as dust emission and CO (for which an excitation analysis was conducted), the inferred densities are substantially lower, only a few 10^4 to 10^5 cm^{-3} (Etxaluze et al. 2011; Requena-Torres et al. 2012). These disagreements over the mass and density of the CND have a substantial impact on our understanding of the nature of the CND, and the future evolution of the central parsecs. If the gas density in individual clumps is greater than $\sim 10^7$ cm^{-3}, the Roche limit for gas at this projected radius from the SMBH, then the gas is capable of gravitational collapse to form stars. If the gas is less dense, then it will continue to orbit until it either more gas accretes on to the CND and its density increases, or it undergoes viscous evolution, transporting angular momentum outwards, and it accretes onto the central parsecs.

Table 1.1: Mass and Density estimates of the CND

Tracers	Local CND Densities (cm^{-3})	Total CND Mass ($M_\odot$)	Assumed T_{gas} (K)	Reference
CO (1–0) (2–1) (7–6) (16–15) (20–19)	3×10^4	10^4	300	Harris et al. (1985)
CO (1–0) (2–1) (7–6) (14–13) (16–15) (20–19) (21–20)	5×10^4		370	Lugten et al. (1987)
CO (1–0) (3–2) (7–6)	$2 \times 10^4 - 2 \times 10^5$	5.6×10^6	100 - 200	Sutton et al. (1990)
CO (7–6) [1]	$(5 - 7) \times 10^4$	2000	200 - 300	Bradford et al. (2005)
CO (2–1) (3–2) (4–3) (6–5) (7–6) (10–9) (11–10) (13–12) (16–15)	$6 \times 10^3 - 8 \times 10^5$	1.2×10^4	150-600	Requena-Torres et al. (2012)
CS (2–1) (3–2) (5–6)	$5 \times 10^4 - 10^6$		100	Serabyn et al. (1989)
CS (7–6) [2] [3]	$2 \times 10^7 - 3 \times 10^8$	$> 3.6 \times 10^5$		Montero-Castaño et al. (2009)
HCN, $H^{13}CN$ (1–0) [4]	2×10^5		250	Marr et al. (1993)

Table 1.1 – Continued

Tracers	Local CND Densities (cm^{-3})	Total CND Mass ($M_\odot$)	Assumed T_{gas} (K)	Reference
HCN (1–0) [3]	(3-4) $\times 10^7$	10^6		Christopher et al. (2005)
HCN (3–2)	$10^6 - 10^8$		50 - 200	Jackson et al. (1993)
HCN (3–2) (4–3)	$10^5 - 10^7$		> 50	Marshall et al. (1995)
HCN (4–3) [2] [3]	$3 \times 10^7 - 4 \times 10^8$	$> 1.3 \times 10^6$		Montero-Castaño et al. (2009)
HCO^+(1–0) [3]	10^7	3×10^5		Shukla et al. (2004)
Submm/mm continuum	10^5	10^4		Mezger et al. (1989)
Far-IR continuum		2.5×10^4		Davidson et al. (1992)
Far-IR/submm continuum [4]	$(1.2 - 2.4) \times 10^4$	4.71×10^4		Etxaluze et al. (2011)
[OI],[CII] [5]	10^5	2×10^4	350	Genzel et al. (1985)
[OI] [5]	3×10^5		170 ± 70	Jackson et al. (1993)

[1]Total mass is only for the warm gas component of the CND
[2]Total mass is a lower limit derived from their published clump masses
[3]Densities and total masses determined by assuming virial equilibrium in the gas clumps
[4]The mass determined is for the inner 0.8 pc of the CND, which falls within an 85″ ISO-LWS beam centered on Sgr A*
[5]Masses and density are for gas in the PDR only

1.2.2.2 Temperature

Just as there is a range of densities measured for the CMZ gas, there is also a wide range of temperatures measured for molecular clouds in the CMZ, from tens to hundreds of K (Table 1.2). Hot gas is found throughout the CMZ, from the intersection of the aforementioned X_1 and X_2 orbits to high-latitude structures suggested to be interacting with the surrounding halo gas (Riquelme et al. 2013).

The first indication that gas in the CMZ is hotter than gas in the disk of the Galaxy was from NH_3 studies toward individual CMZ clouds (Güsten et al. 1981; Morris et al. 1983), indicating average temperatures of ∼50 K. Followup studies of larger samples of CMZ clouds using NH_3 transitions with energies up to 300 K above the ground state confirmed average gas temperatures of 60-120 K (Güsten et al. 1985), and suggested that the temperature distribution could be well approximated by two temperature components, 25 K and 200 K (Hüttemeister et al. 1993a). Note that this cool component is not insubstantial, it is estimated to contain ∼75% of the total column density of NH_3. Observations of yet more highly excited NH_3 indicated that the hottest gas was at least 250-330 K (Mauersberger et al. 1986). Toward Sgr B2, even hotter gas is inferred from more highly-excited lines of NH_3, though it is only seen in absorption against the hot core (extent is unclear). Temperatures of 600-700 K are inferred from transitions with energies up to 2000 K above the ground state (Wilson et al. 1982; Hüttemeister et al. 1995; Flower et al. 1995; Ceccarelli et al. 2002; Wilson et al. 2006).

Globally-distributed hot gas is also seen in other molecules. Güsten et al. (1985) also verified temperatures of 50-100 K with millimeter observations of the symmetric tops CH_3CN and CH_3CCH. High temperatures are further confirmed by observations of H_2CO (Ao et al. 2013), indicating temperatures of 70

K, and up to 100 K (though these observations are not sensitive to the presence of temperatures above 100 K). Observations of CO are also consistent with temperatures of 70 K. In contrast, an excitation analysis of lower-excitation CO lines indicates temperatures between 20 and 30 K (Nagai et al. 2007). This range of kinetic temperatures is consistent with the observed antenna temperatures of the presumably optically thick and thermalized CO (1-0) line (Martin et al. 2004), and is also consistent with the $\sim$ 25 K gas component measured by Hüttemeister et al. (1993a) using the NH_3 (1,1) and (2,2) lines. Direct observations of the pure-rotational transitions H_2 indicate a much warmer temperature, 150 K, as well as the existence of an even hotter component (600K), which is also dense (Rodríguez-Fernández et al. 2001). The 150 K warm gas is estimated to make up 30 % of the total H2 column, while the hot component contributes less than 1% to the total column density of gas in CMZ clouds.

Although a multitude of observational data are in support of molecular gas in the CMZ being far hotter than typical gas temperatures in the Galactic disk, the exact temperature structure of molecular clouds in the CMZ is still unclear. Just how do all of these observations fit together to make a self-consistent picture of the molecular gas in the CMZ? For example, in Sgr B2, NH_3 observations indicate temperatures ranging from 150 K to 600 K and possibly $>$ 1300 K (Ceccarelli et al. 2002; Wilson et al. 2006). While it is likely that the majority of CMZ clouds consist of a a continuum of temperatures, determining how much gas is at each temperature, and how it is distributed throughout the clouds is critical for constraining theories of cloud heating. Does the temperature vary with density or throughout the cloud (e.g., a core-halo structure)? Is the bulk of dense gas in CMZ clouds cool, as suggested by observations of the lowest-excitation NH_3 and CO lines (Hüttemeister et al. 1993a; Nagai et al. 2007), or is it warm, as suggested by observations of the dense-gas tracer H_2CO (Ao et al. 2013)? Just

how hot can the dense gas get?

Table 1.2: Molecular Gas temperatures in the CMZ clouds

Lines used to derive T	T_{Cool} (K)	T_{Warm} (K)	T_{Hot} (K)	Clouds surveyed	References
H_2 (2–0) (3–1)		150		16 pointings from $-1 < l < 3$	Rodríguez-Fernández et al. (2001)
H_2 (6–4) (7–5)			600	6 pointings from $-0.3 < l < 0.8$	Rodríguez-Fernández et al. (2001)
CO (1–0) (3–2) (7–6)		100-200		CND	Sutton et al. (1990)
CO (1–0) (2–1) (7–6) (16–15) (20–19)		150-450		CND	Harris et al. (1985)
CO (1–0) (2–1) (7–6) (14–13) (16–15) (20–19) (21–20)		100-500	300-700	Sgr A/CND	Lugten et al. (1987)
CO (4–3) (7–6)		50-70		maps from $-1.3 < l < 2$	Martin et al. (2004)
NH_3(1,1) (2,2) (3,3)	30-60			maps from $-2 < l < 2$	Morris et al. (1983)
NH_3(2,2) (5,5)		60 ± 10		12 pointings from $-0.5 < l < 1.5$	Güsten et al. (1985)
NH_3(4,4) (5,5)		100±20		7 pointings in Sgr A	Güsten et al. (1985)
NH_3(1,1) (2,2)	30-40			5 pointings from $-0.1 < l < 1.6$	Mauersberger et al. (1986)
NH_3(5,5) (7,7)		200-300		6 pointings from $-0.1 < l < 1.6$	Mauersberger et al. (1986)

Table 1.2 – Continued

Lines used to derive T	T_{Cool} (K)	T_{Warm} (K)	T_{Hot} (K)	Clouds surveyed	References
NH_3(1,1) (2,2) (3,3) (6,6)	25	200		36 pointings from $-1 < l < 3$	Hüttemeister et al. (1993b)
NH_3(1,1) (2,2)	50	< 100		maps from $-0.2 < l < 0.8$	Ott et al. (2006)
NH_3(1,1) (2,2)	16-36			CND	Coil & Ho (1999)
NH_3(1,1) (2,2)	25-60			CND	McGary et al. (2001)
NH_3 (1,1) (2,2) (3,3) (8,8) (9,9)		~ 200		Sgr B2 (M),(N)	Wilson et al. (1982)
NH_3(1,1) to (11,10)		150-300		Sgr B2 (M),(N)	Hüttemeister et al. (1993b)
NH_3 (8,8) to (14,14)			> 600	Sgr B2	Hüttemeister et al. (1995)
NH_3(1,1) to (14,14)			400-600	Sgr B2 (M),(N)	Flower et al. (1995)
NH_3(3, 0)a(2, 0)s to (9, 8)s(8, 8)a			700 ± 100	Sgr B2 (M),(N)	Ceccarelli et al. (2002)
NH_3(1,1) to(8,8)		160		Sgr B2 (M),(N)	Wilson et al. (2006)
NH_3(9,9) to(15,15)			630	Sgr B2 (M),(N)	Wilson et al. (2006)
NH_3(15,15) to(18,18)			> 1300	Sgr B2 (M),(N)	Wilson et al. (2006)

Table 1.2 – Continued

Lines used to derive T	T_{Cool} (K)	T_{Warm} (K)	T_{Hot} (K)	Clouds surveyed	References
H_2CO				maps from $-0.3 < l < 0.3$	Ao et al. (2013)
CH_3CN (6–5) (5–4)		60-100		3 pointings in Sgr A	Güsten et al. (1985)
CH_3CCH (6–5) (5–4)		50-70		2 pointings in Sgr A	Güsten et al. (1985)

Global molecular gas temperatures may be as high as $\sim$ 100 K, but dust temperatures in the CMZ are much cooler. Apart from a few localized enhancements, such as within the central parsec, dust temperatures in CMZ clouds are between $\sim$15-30 K (Mezger et al. 1986; Lis et al. 1994; Rodríguez-Fernández et al. 2004; Molinari et al. 2011; Etxaluze et al. 2011). The wide separation between the gas and dust temperature in many clouds, for example M0.25+0.01, for which dust temperatures are 19 K (Longmore et al. 2012) and gas temperatures are 40-80 K (Ao et al. 2013; Hüttemeister et al. 1993a, although the latter also measure an 18 K cold component), are hard to explain. For cloud densities $> 10^5$ cm^{-3}, one would expect under normal interstellar conditions for the dust and gas to be thermalized (Goldsmith 2001). Why is this not observed to be the case for the CMZ? First, it may be, as suggested by the cold gas component of 20-30 K observed by Hüttemeister et al. (1993a) and Nagai et al. (2007), that molecular gas in the CMZ is characterized by multiple temperature components, and the densest gas has temperatures comparable to the dust. However, H_2CO measurements indicate that even the densest gas can have temperatures up to 70 K, and so the problem of thermalization remains. Another explanation could be that, as these measurements of gas temperature have all been conducted with single-dish (and thus, low-resolution observations), the derived temperatures could be biased by the presence of a warm, diffuse cloud envelope. Alternatively, it is possible that the observed gas and dust are truly not in thermal equilibrium. This could either be because the densities of the cloud interiors are overestimated, and the hot gas is sufficiently low density that is is not coupled to the dust, or because there is a heating process which acts non-uniformly on gas and dust. The latter is the most popular explanation, and two frequently cited candidates for heating gas temperatures in excess of dust temperatures are a high cosmic ray ionization rate or the dissipation of turbulent energy, both of which are discussed more in

Section 1.2.4.

1.2.3 Physical conditions in the diffuse gas

The CMZ has also been found to contain a low-density molecular gas component, first traced by H_3^+ (Oka et al. 2005) in sightlines through the CMZ, and followed by observations of numerous new species with Herschel. These species are observed in absorption toward multiple lines of sight against strong infrared and submillimeter continuum sources, especially toward Sgr B2 and Sgr A. Observations of H_3^+ were the first to characterize this gas component as warm (T$\sim$ 250-350 K), diffuse (n$\sim 10 - 100$ cm^{-3}) and pervasive– the inferred sizes of the absorbing clouds are several tens of parsecs, and presumably constitute a substantial fraction of the volume filling factor in the CMZ (Oka et al. 2005; Goto et al. 2008, 2011). Significantly, these observations of high abundances of H_3^+ (which is formed from a fast ion-molecule reaction between H_2 and H_2^+ ions formed via cosmic ray ionization, and is quickly destroyed via either dissociative recombination, or in denser environments, proton transfer with neutral species such as CO or O, Dalgarno 2006) also indicated that the cosmic ray ionization rate in the CMZ is several orders of magnitude higher than the typical interstellar value. A variety of other species have also been observed to show similar absorption spectra toward the CMZ, including CO (Geballe & Oka 2010), H_2O^+ (Schilke et al. 2010), H_2Cl^+ (Lis et al. 2010a), H_2O (Lis et al. 2010b; Sonnentrucker et al. 2013), SH^+ and CH^+ (Menten et al. 2011), HF (Monje et al. 2011; Sonnentrucker et al. 2013), and H_3O^+ (Lis et al. 2012). All of these detections are generally consistent with the molecules existing in a diffuse, PDR environment. While some species, such as HF, have CMZ abundances consistent with those observed toward other lines of sight in the Galactic disk, molecules such as H_3O^+ and H_2O are found to

be enhanced in CMZ sightlines toward both Sgr A and Sgr B2, likely due to the unique chemistry induced by the Galactic center environment.

1.2.4 Environment and Heating

As was seen in the previous sections, the diffuse CMZ gas and a substantial fraction of the dense molecular gas in the CMZ (25-30%) has temperatures in excess of 100 K, with a smaller, and perhaps more localized fraction of the gas showing evidence for temperatures as high as 600 K. The question is, what mechanisms are responsible for heating gas in the CMZ to these observed values? Below, I discuss several potential heating mechanisms which may operate more strongly in the Galactic center than in the Galactic disk.

1.2.4.1 Far-Ultraviolet Background

The Galactic center is home to a large population of massive stars, including three massive, young star clusters (Nagata et al. 1990, 1995; Cotera et al. 1996; Figer et al. 1999; Figer et al. 2002) which are ionizing the surrounding ISM on scales of tens of parsecs (Ekers et al. 1983; Yusef-Zadeh & Morris 1987b; Lang et al. 1997; Lang et al. 2001; Simpson et al. 2007), as well as an equal number of massive stars found in the field (Cotera et al. 1999b; Mauerhan et al. 2007, 2010c,b,a). The effective temperature of the ionizing radiation in the CMZ is estimated to be ∼37,000 K (Rodríguez-Fernández et al. 2004; Rodríguez-Fernández & Martin-Pintado 2005). Molecular gas in the CMZ will be heated through its interface with this radiation field, forming photodissociated or photon-dominated regions (PDRs). PDR heating is one way to explain the observed gas and dust temperature discrepancy: in external regions of a PDR, gas temperatures will be on the order of several hundred K, with dust temperatures < 50 K (Hollenbach

et al. 1991). Comparing PDR models of Tielens & Hollenbach (1985) to observations of ionic, neutral and molecular species in the CMZ, Rodríguez-Fernández et al. find that photoelectric heating through PDRs is consistent with being responsible for 10-30% of the observed warm (T$\sim$ 150 K) H_2 column density (Rodríguez-Fernández et al. 2001; Rodríguez-Fernández et al. 2004). However, as noted by Ao et al. (2013), PDR heating is not likely important for the densest gas (for example, the 70 K component they trace with H_2CO) because heating does not penetrate to the dense cloud interiors where molecules like H_2CO are found. Thus, while PDR heating may be important for heating the diffuse gas traced by H_3^+ or H_2, it is not likely to be responsible for heating the dense gas at temperatures of 50 -200 K traced with NH_3 (Rodríguez-Fernández et al. 2004 estimate that if NH_3 is found in PDRs it would be destroyed on timescale of 7 years), H_2CO, and CH_3CN (Güsten et al. 1985; Hüttemeister et al. 1993a; Ao et al. 2013). Another mechanism must then be responsible for heating the dense gas, and contributing to the observed discrepancy between the temperature of the dense gas and the dust temperatures in CMZ clouds.

1.2.4.2 X-ray Background

X-rays, or heating through X-ray dominated regions (XDRs), are another possible heating source for the CMZ gas, as X-rays penetrate more deeply into cloud interiors than ultraviolet radiation. The Galactic center is an extended source of X-ray emission (Koyama et al. 1989), which is believed to originate in a variety of sources, including a population of discrete point sources (Wang et al. 2002; Muno et al. 2003, 2009), Fe K-α emission from the surfaces of molecular clouds which is interpreted as an X-ray reflection nebula (Koyama et al. 1996; Murakami et al. 2000), as well as some potential contribution from a diffuse, hot plasma

(Koyama et al. 1996). Although Rodríguez-Fernández et al. (2004) acknowledge that an XDR could penetrate as much as 10× deeper into CMZ gas than a PDR, potentially sufficient to heat the entire column of observed warm gas in the CMZ, both they and Ao et al. (2013) find that the total X-ray luminosity in the CMZ is three orders of magnitude too low to account for gas temperatures >100 K. At present then, X-rays are not a dominant factor in the environment of the Galactic center, which, as might be expected, also does not exhibit strong mid-infrared ionic emission indicative of XDRs or active galactic nucleus (AGN) activity (An et al. 2013). However, it is worth noting that, if the Fe K-α emission is an X-ray reflection nebula, it requires a recent (within the last few hundred years) event with an energy generation rate of 10^{41-42} erg s^{-1} (Koyama et al. 1996). If, as is often suggested (Koyama et al. 1996; Murakami et al. 2000; Inui et al. 2009; Ponti et al. 2010), the source of this event was an accretion event on the central SMBH, the required luminosity would be six orders of magnitude greater than its quiescent value (Baganoff et al. 2001). Depending on the frequency of these and larger events (note that an analysis by Bower et al. 2012 predicts that the infalling object G2, if it is a gas cloud, would only increase the flux of the accretion disk by an order of magnitude) this could make X-ray heating from intermittent AGN-like activity more viable.

1.2.4.3 Cosmic Ray Background

An even more penetrating heating source for CMZ gas is cosmic rays (highly energetic protons and nuclei). A high Galactic center cosmic ray ionization rate of $\zeta \sim 2 \times 10^{-15}$ s^{-1} was first suggested by (Güsten et al. 1981) to explain the observed discrepancy between dust and gas temperatures in the CMZ. (For comparison, the typical interstellar cosmic ray ionization rate ζ_0 is estimated

to be 3×10^{-17} s^{-1}, although recent observations by Indriolo & McCall 2012 suggest that it may be an order of magnitude higher). More recently, independent observations of absorption from H_3^+ toward multiple sightlines are also found to require $\zeta \sim 10^{-15} - 10^{-14}$ s^{-1} (Oka et al. 2005; Goto et al. 2008; Goto et al. 2013). It is suggested that a similarly high ζ is also required by observations of TeV emission in the central 600 parsecs (Yusef-Zadeh et al. 2013b), with values as high as 10^{-13} s^{-1} inferred for one particularly highly-irradiated cloud (Yusef-Zadeh et al. 2013). However, such high values of ζ may not be a uniform property of the CMZ. van der Tak et al. (2006) observe H_3O^+ in the envelope of Sgr B2 and find that its abundance is best fit with models having $\zeta = 1-4\times10^{-16}$, much lower than values inferred toward other clouds in the CMZ. Their observations also indicate that ζ is a factor of three lower in dense gas compared to diffuse clouds, which they attribute to cosmic ray scattering (Padoan & Scalo 2005).

Cosmic ray ionization rates several orders of magnitudes above typical interstellar values have implications for both the heating and chemistry of gas in the CMZ. First, as previously mentioned, cosmic rays penetrate to high column densities, leading to uniformly high temperatures in cloud interiors. Secondly, as cosmic rays preferentially heat molecular gas through a combination of mechanisms including elastic scattering, rotational and vibrational excitation of H_2, dissociation of H_2, and chemical heating (ionization) of H_2 (Glassgold et al. 2012), heating by cosmic rays can lead to the observed discrepancy between dust and gas temperatures in CMZ clouds (Ao et al. 2013). Assuming $\zeta = 3\times10^{-14}$ s^{-1}, a model of cosmic ray heating for a typical CMZ cloud indicates that cosmic rays can effectively raise gas temperatures in excess of dust temperatures, even at the high densities of $10^4 - 10^5$ cm^{-3} typical of CMZ clouds (Clark et al. 2013). At cloud densities of 10^5 cm^{-3}, their model predicts dust temperatures of 17-30 K and gas temperatures of 50-80 K. With this ζ, Clark et al. (2013) find that gas

and dust do not become thermally coupled until densities exceed a few 10^6 cm^{-3}. A high ζ also has implications for the chemistry of the CMZ. First, a high cosmic ray ionization rate will lead to a high fractional ionization of the molecular gas (Papadopoulos 2010; Ao et al. 2013; Yusef-Zadeh et al. 2013b). Yusef-Zadeh et al. (2013b) estimate that for their inferred values of ζ, the ionization fraction n_e/n_{H2} in gas with densities 10^4 cm^{-3} should be a few 10^{-6}, 1-2 orders of magnitude higher than the typical ISM values, and the highest value observed anywhere in the Galaxy (Caselli et al. 1998; Papadopoulos 2010). Güsten et al. (1981) also note that a high ζ should lead to a high fraction of neutral hydrogen in CMZ clouds. Another implication of high ζ is that it can lead to strong and variable emission from the FeI Kα line (Capelli et al. 2012; Yusef-Zadeh et al. 2013b; Yusef-Zadeh et al. 2013). While enhanced and variable iron K-α emission is observed from CMZ clouds, an accepted explanation for this emission (an X-ray reflection nebula, see previous Section) already exists, and explains the apparent propagation of the emission at the speed of light. Finally, Papadopoulos (2010) predict that in cosmic-ray-dominated regions, the minimum gas temperature should be 80-100 K, while in the Galactic center, many clouds appear to have a temperature component < 50 K (Hüttemeister et al. 1993a; Nagai et al. 2007). Thus, while low-energy cosmic rays are a viable heating source, it is not yet certain that an extremely high cosmic ray ionization rate is the globally dominant source of heating in the CMZ.

1.2.4.4 Turbulence

Another heating source for CMZ gas, which can also explain the observed discrepancy between gas and dust in the CMZ is the dissipation of supersonic turbulence in CMZ clouds (Goldreich & Kwan 1974; Pan & Padoan 2009). Typical

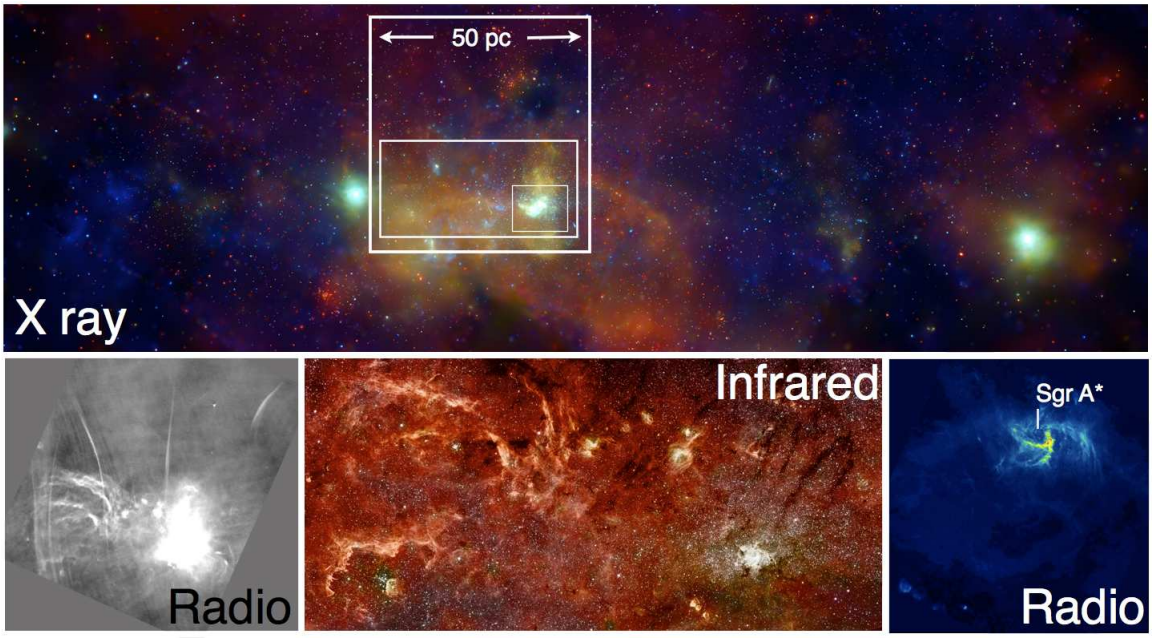

Figure 1.4: Composite of images (increase in zoom level counterclockwise from top), from the Chandra Space Telescope (Top, showing the X-ray emission in the central 600 parsecs; Muno et al. 2009; Johnson et al. 2009), the Hubble and Spitzer Space Telescopes (Bottom center, showing the dense concentrations of stars, hot dust, and ionized gas in this region; Wang et al. 2010; Stolovy et al. 2006), and the Very Large array (Bottom Left, showing the perpendicular nonthermal filaments, thought to trace a strong, poloidal magnetic field, and Right, showing the ionized gas surrounding the black hole, and adjacent supernova remnant Sgr A East; Yusef-Zadeh et al. 1984).

line full-width half maxima (FWHM) for CMZ clouds range from 20 to 50 km s^{-1} (Bally et al. 1987; Lis & Menten 1998). Given an isothermal sound speed of 0.3-0.6 km s^{-1} for gas temperatures of 30-100 K, this implies Mach numbers of 10-60, or highly supersonic turbulence. The dissipation of this supersonic turbulence in shocks within CMZ clouds provides a means of preferentially heating the molecular gas (Wilson et al. 1982; Martin-Pintado et al. 1997; Ao et al. 2013). As shown by Ao et al. (2013), turbulent dissipation is sufficient to heat gas with densities between $10^4 - 10^5$ cm^{-3} to observed temperatures of 50-60 K. The ubiquity of turbulent shocks in the CMZ also appears clear: all clouds in the CMZ exhibit strong emission from shock-tracing molecules such as SiO, the abundance of which is enhanced when it is knocked off of grains in strong shocks (Martin-Pintado et al. 1997, although see also Yusef-Zadeh et al. 2013, who suggest that a high SiO abundance could be a consequence of a high cosmic ray ionization rate). There are also recent observations of widespread CH_3OH emission in the CMZ (these are likely collisionally-excited masers, though the velocity resolution of the data is insufficient to show this unambiguously; Yusef-Zadeh et al. 2013a). Although the initial interpretation of this emission is that the CH_3OH abundance is enhanced by a high cosmic ray flux, it can also be argued that if these are collisionally-excited masers, they are tracing widespread shocks (See Chapter 5 for further discussion). Of course, if the dissipation of turbulence is the dominant source of CMZ heating, there must be an energy injection mechanism which maintains the observed turbulence in a steady state. One suggested mechanism is tidal shearing due to differential Galactic rotation (Fleck 1980; Wilson et al. 1982; Güsten 1989).

1.2.5 Star Formation

It is clear that the raw material for star formation in the Galactic center is fundamentally different than that found in the Galactic disk. On scales of tens of parsecs, CMZ clouds are characterized by high nonthermal linewidths, with observed FWHM on the order of 20-50 kms^{-1} (Bally et al. 1987; Lis & Menten 1998), believed to be due to turbulence in the cloud interiors. On these same scales, CMZ clouds have gas temperatures far in excess of the 10-20 K gas temperatures typical in disk clouds, (T=$50-300$ K: Morris et al. 1983; Güsten et al. 1985; Hüttemeister et al. 1993a; Mauersberger et al. 1986), and they have relatively high densities (n $> 10^4$ cm^{-3}), which are necessary if the clouds are to maintain their integrity in the face of the strong tidal shear near the Galactic center (Güsten 1989). These conditions may partly explain why CMZ clouds appear largely quiescent and devoid of star formation at these densities (Longmore et al. 2013), which is remarkable, as disk molecular clouds, when they reach densities of $\sim 10^4$ cm^{-3}, are already observed to be actively forming massive stars.

But, is the resulting star formation process in the CMZ different than that in the disk? The answer is inconclusive, at least when considering the CMZ as a whole. Based on the oddities of the CMZ environment, including high temperatures, strong turbulence, tidal shearing, and a likely strong magnetic field, Morris (1993) predicts that the resulting initial mass function of stars which form in this environment should either favor massive stars, or have an unusually high cutoff mass, below which low mass stars are unable to form. Examining the products of recent star formation in the CMZ, several groups have found that although the two massive star clusters in this region may have unusual present-day mass functions, this is just as likely to be a function of the evolution of these clusters in the strong potential of the Galactic nucleus as it is to be the

result of an initial mass function (IMF) which deviates from a Salpeter form (Espinoza et al. 2009; Clarkson et al. 2012; Hußmann et al. 2012; Habibi et al. 2012). The only region where a strong case can currently be made for an unusual IMF is the Nuclear cluster, a large cluster of stars in central parsec. Here, the evidence (including spectroscopic identification of stellar populations and a lack of young, X-ray bright low-mass stars), more clearly supports a flat or 'top-heavy' initial mass function (Nayakshin & Sunyaev 2005; Paumard et al. 2006; Maness et al. 2007; Lu et al. 2013). However, the formation environment for these stars– in the central parsecs where tidal shear from the central SMBH is extremely strong– is not likely typical of stars in the CMZ as a whole. One recent approach, which may help constrain initial mass function in the CMZ as a whole, is to study the so-called 'clump mass function' (CMF), the distribution of masses in the substructure of molecular clouds before star formation occurs. Studies have suggested that the shape of CMF is related to the shape of the IMF, modulo an approximately constant efficiency factor (e.g., Alves et al. 2007; Lada et al. 2008; Enoch et al. 2008). The first study of the CMF in a CMZ cloud suggests that there may be a flatter clump mass function in regions of the cloud which are being compressed by a nearby supernova remnant, compared to the undisturbed core of the cloud, but the number of clumps studied is still too small for this to be a statistically significant result (Tsuboi & Miyazaki 2012).

Finally, one apparently global oddity of the CMZ is the quantity of dense molecular gas which does not apparently have associated star formation activity, as traced by radiatively-excited CH_3OH masers, H_2O masers, and young stellar objects (Beuther et al. 2012; Longmore et al. 2013; Kruijssen et al. 2013, Figure 1.5). A case in point is the M0.25+0.01 cloud, which has a mass of several 10^5 $M_\odot$, but no indications of associated star formation apart from a single H_2O maser (Lis et al. 1994; Lis & Menten 1998; Lis et al. 2001; Longmore et al.

2012; Kauffmann et al. 2013). This cloud and similar clouds in the CMZ appear to deviate from the observed relationship between gas surface density and star formation (the Kennicutt-Schmidt relation) observed in other galaxies, either suggesting that this relation is not universal (at least not on sub-galactic scales), or that observational biases are affecting our understanding of Galactic center star formation. While this may be true to a limited extent– for example, surveys are only just beginning to identify protostellar sources in the CMZ (Yusef-Zadeh et al. 2009; An et al. 2011) and there are even new suggestions of ongoing star formation in M0.25+0.01 (Rodríguez & Zapata 2013), it is not clear that this can fully make up for the observed discrepancy. There are also observations of deviations from the Kennicutt-Schmidt relation in regions of other Galaxies, for example in M51, where the reduced surface pressure from large-scale streaming motions along the bar is suggested to be inhibiting star formation in large regions of the galaxy (Meidt et al. 2013). Kruijssen et al. (2013) argue that the lack of current star formation in the CMZ is real, and a result of high turbulent pressure in the gas, which raises the density threshold for star formation to 10^8 cm^{-3} several orders of magnitude above that typical for the disk ($\sim 10^4$ cm^{-3}) and which they suggest dominates over other retarding effects such as the magnetic field, radiation pressure, and tidal stripping of clouds. They further put forward a model in which the star formation in the CMZ is is cyclical, governed by the time it takes for infalling gas into the CMZ to build up sufficient densities to overcome the turbulent pressure. This theory has many testable aspects, as it predicts that the strong turbulence in Galactic center clouds extends to small scales within the clouds, and predicts that star formation should only occur in clouds in which the densities are $> 10^8$ cm^{-3}.

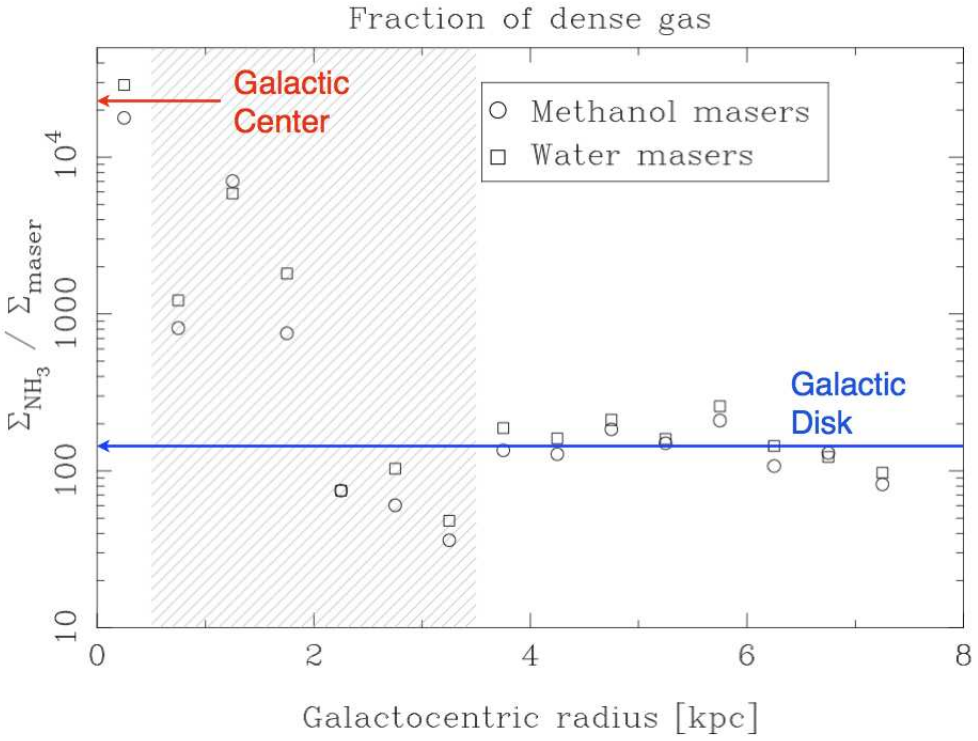

Figure 1.5: A comparison of the amount of dense molecular gas (traced by NH_3) associated with each 'unit' of star formation (traced by H_2O and CH_3OH masers) as a function of Galactic radius. The shaded area between 0.5 and 3.5 kpc corresponds to measurements for which where the rotation curve, and thus the derived Galactocentric radii, are not reliable. The Galactic center is observed to have several orders of magnitude more dense gas per associated unit of star formation, compared to typical values in the Galactic disk.

1.3 New Frontiers for Galactic Center Research

Much work remains to be done to fully understand the physical conditions in the CMZ which lead to its unusual observed properties. For example, although the average densities of CMZ molecular clouds are known to be more dense than disk clouds, the highest local densities a typical cloud in the CMZ is able to reach before it begins widespread star formation have not been observationally quantified, and the densest gas in CMZ clouds has not been well studied. Existing molecular line observations of molecular clouds in the Galactic center have been sensitive to densities up to $\sim 10^5 - 10^6$ cm^{-3} (Bally et al. 1987; Serabyn & Güsten 1991; Serabyn et al. 1992; Lis et al. 2001). However, more recent studies of the Circumnuclear Disk (CND), a ring of molecular gas lying just a few parsecs from the SMBH, indicate that molecular gas densities several orders of magnitude greater may exist in the Galactic center. Densities of molecular clumps in the CND, indirectly determined from the linewidths of several species by using an assumption of virial equilibrium, have been measured to range from 10^7-10^8 cm^{-3} (Christopher et al. 2005; Montero-Castaño et al. 2009). However, such high densities have not yet been confirmed in the CND by other methods (Etxaluze et al. 2011; Requena-Torres et al. 2012; Liu et al. 2013, Table 1.1), nor observed in other CMZ clouds, and so there remains some uncertainty as to the highest densities which may be present in these clouds.

Similarly, although CMZ clouds are known to be hotter than disk clouds, the temperature and distribution of the hottest molecular gas in these clouds are not well constrained, and the primary sources of cloud heating are uncertain. Molecular line studies indicate temperatures ranging from 25 K to 600 K may exist in CMZ clouds (Morris et al. 1983; Güsten et al. 1985; Mauersberger et al. 1986; Hüttemeister et al. 1993a; Rodríguez-Fernández et al. 2001). An even higher

temperature gas component has also been detected toward Sgr B2 (Hüttemeister et al. 1993b; Ceccarelli et al. 2002) with a temperature of at least 700 K, and possibly as high as 1300 K (Wilson et al. 2006). No other CMZ clouds have been similarly surveyed for such hot gas, and so its distribution in the CMZ, which could help determine if the hottest gas in this cloud is heated by local or global phenomena, is not known.

More importantly for understanding how star formation proceeds in the CMZ environment, the temperatures, densities and turbulence of CMZ clouds need to be constrained on the spatial scales most relevant to star formation, those of individual clumps and cores within the molecular clouds. The majority of gas temperature measurements in CMZ clouds have been made with pointed spectra, and so there are few detailed gas temperature maps of CMZ clouds (the exceptions being a few maps of global temperature on parsec scales, which are sensitive to kinetic temperatures < 70K (Ott et al. 2006; Martin et al. 2004) and interferometric maps of local temperature in the CND (Coil & Ho 1999; McGary et al. 2001). Although some moderately high-resolution maps of dust temperature have been made (Molinari et al. 2011), the gas and dust temperatures in CMZ clouds appear not to be coupled, so the distribution of dust temperatures may not reflect the distribution of gas temperatures. In addition to quantifying the thermal pressure in pre-star forming clumps and cores, high resolution maps of the gas temperature structure in individual clouds could also be used to discern signatures of local versus global heating in CMZ clouds.

Due to the combined effects of the distance of the Galactic center (8.5 kpc, Ghez et al. 2008; Reid et al. 2009) and the time-intensive nature of resolving fine detail in necessarily small fields of view over the large area of the CMZ, especially at radio wavelengths, the detailed properties of CMZ clouds have not previously

been uniformly probed on small scales. As a result, it is not known how local temperatures, densities, and turbulent velocities compare to the average values determined over the whole cloud, nor is it known whether or not the conditions of the star forming cores are as radically different from that in the disk as the molecular cloud envelopes appear to be. Limited temperature and density studies have been made with interferometric observations of the CND and central 10 pc. (Herrnstein & Ho 2005; Christopher et al. 2005; Montero-Castaño et al. 2009), however, outside of this region, much less is known about how the density and temperature of clouds vary on different size scales.

Many facilities both new and old provide new tools to address these questions. This thesis uses data from Hubble, the 100m Green Bank Telescope, both the Very Large Array (VLA) and upgraded Jansky VLA, and the ALMA pathfinder (APEX) telescope in order to provide new constraints on the physical conditions which exist in the CMZ gas and motivate future studies with SOFIA, ALMA, and the full capabilities of the new VLA.

1.4 The Structure of this Thesis

The research presented in this thesis comprises a multiwavelength probe of the Galactic center environment and consists of four related studies which place new limits on the gas properties in a sample of clouds throughout the CMZ. Together, the studies I have led indicate the widespread presence of hot gas in CMZ clouds, determine the density of gas close to the black hole, and yield the first measurements of physical conditions in individual clumps interior to CMZ clouds.

Chapter 2 of this thesis comprises a study of a group of compact HII regions

associated with the M-0.02-0.07 cloud in the Sgr A complex including an analysis of their ionization sources, the extinction in the direction of the HII regions, and their interaction with surrounding molecular clouds (Mills et al. 2011). The M-0.02-0.07 molecular cloud is a unique example of the variety of hostile environmental factors CMZ molecular gas is subject to. This cloud lies just 6 parsecs from the central supermassive black hole, is being compressed by the nearby Sgr A East supernova remnant (Serabyn et al. 1992), and has experienced recent star formation evidenced by a group of compact HII regions. To better depict the physical relationship between these sources, I use archival VLA observations and Paschen α images from the Hubble Space telescope to determine the extinction toward the HII regions. From the measured extinctions and source morphologies, I determine that three of the HII regions lie on the front side of the cloud and formed in the eastern part of the cloud which is unaffected by the supernova remnant's expansion. The higher extinction of the fourth HII region indicates it is embedded in the supernova-compressed ridge, and though younger than the other HII regions, is still older than the supernova.

Chapter 3 of this thesis entails a survey for hot molecular gas in molecular clouds across the CMZ using the Green Bank Telescope (Mills & Morris 2013). An extremely hot gas component has previously been detected toward the Sgr B2 cloud, using absorption lines of highly excited NH_3 ($\sim$ 700 K, Ceccarelli et al. 2002; Wilson et al. 2006). However, there have been no analogous studies for other clouds to indicate whether this hot gas is unique to Sgr B2 or ubiquitous in the CMZ. Finding that several clouds in the CMZ exhibited emission in the (9,9) line of NH_3, with an excitation energy $\sim$ 840 K above the ground state, I surveyed 17 positions across the CMZ with multiple highly-excited lines of NH_3 from (8,8) through (15,15). Emission is detected toward 14 of these positions, many of which have no associated star formation. For the three strongest sources,

I further derive rotation temperatures of 350-450 K, substantially higher than previous temperatures of 200-300 K measured for these clouds (Mauersberger et al. 1986). My widespread detections of gas hotter than 400 K indicate for the first time that his hot gas must be heated by global processes in the CMZ.

Chapter 4 of this thesis presents a study of gas densities in the Circumnuclear disk (CND), a ring of gas and dust at a radius of 1.5 pc from the central black hole (Mills et al., in prep.). Recent studies of gas densities in the CND are contradictory, indicating either densities that exceed $10^7 - 10^8$ cm^{-3} (e.g., Christopher et al. 2005; Montero-Castaño et al. 2009) or densities $< 10^5 - 10^6$ cm^{-3} (e.g., Etxaluze et al. 2011; Requena-Torres et al. 2012). In the former case, densities are determined by assuming virial equilibrium, which may not apply to gas which is strongly sheared due to its proximity to the black hole. In the latter case, densities are inferred from dust properties (which are subject to systematic uncertainties as to grain size and temperature) and excitation analyses of CO, which may not faithfully trace the highest density gas that is present. Resolving this density discrepancy is necessary to understand the evolution of this structure, as for the gas to be tidally stable and form stars, it must have densities greater than 10^7 cm^{-3}. To resolve this disagreement in densities, I conduct an excitation analysis using submillimeter transitions of HCN and HCO$^+$observed with the APEX telescope, a 12m ALMA prototype dish. Unlike CO, the observed transitions of these molecules have critical densities $> 10^7$ cm^{-3} and directly constrain the existence of high-density gas. Excitation analyses of these molecules and their optically-thin ^{13}C isotopologues with both the escape-probability radiative transfer code RADEX and the Monte Carlo radiative transfer code RATRAN yield significantly tighter limits on the density (n= $10^{5.7} - 10^{7.6}$ cm^{-3}), and indicate that the majority of the CMZ gas is not virialized.

Chapter 5 of this thesis revisits the sources studied in the first three chapters of this thesis. This project comprises a Jansky Very Large Array (VLA) study of 5 CMZ clouds to determine the physical conditions in the interiors of these clouds on 0.1 pc scales (Mills et al., in prep.). As part of this work, I have observed the CND in multiple lines of NH_3, yielding new limits on the gas temperature which can be used to refine the densities I previously derived from my excitation analyses of HCN and HCO^+(Chaper 3). I also detect weak emission in all of these clouds from the highly-excited NH_3 (9,9) line that I previously observed with the GBT (Chapter 4). This chapter also presents several unanticipated results from this study. The first is hundreds of weak, collisionally-excited CH_3OH masers which are detected in all of the clouds surveyed. The masers are distributed non-uniformly in the clouds, with concentrations indicating regions of shock activity which may be driving the evolution of physical conditions in these clouds. I also find that the NH_3 (3,3) line is weakly masing throughout the clouds studied here, constraining the gas densities to be $< 10^6$ cm^{-3} (Walmsley & Ungerechts 1983). Finally, in one cloud in this survey which is almost completely devoid of star formation, weak and spatially extended radio continuum emission is detected, indicating a mix of ionized gas (likely due to external ionization of the cloud) mixed with dust emission.

CHAPTER 2

Properties of the Compact HII Region Complex G-0.02-0.07

Star formation in the Galactic center is a mysterious process. As conditions in this region are so unique – the gas is extremely dense, turbulence in the clouds is strong, and the presence of a supermassive black hole and massive stellar population contribute to intense irradiation in the far-ultraviolet, and potentially in X-rays (Inui et al. 2009; Capelli et al. 2012; Gando Ryu et al. 2012) and in cosmic rays (Oka et al. 2005; Goto et al. 2008; Yusef-Zadeh et al. 2013a,b)– it is uncertain whether the gas here obeys the same laws as elsewhere in the Galaxy, or the universe. By some estimations the star formation rate in this region is high: there is large population of stars several millions of years old both in massive clusters (Nagata et al. 1990, 1995; Cotera et al. 1996; Figer et al. 1999; Figer et al. 2002, 2004) and outside of these clusters (Cotera et al. 1999b; Mauerhan et al. 2007, 2010c,b,a; Dong et al. 2012). However, there is an apparent deficit of ongoing star formation in the central 300-500 parsecs, as traced by masers and young stellar objects (Beuther12, Longmore13) compared to elsewhere in the Galaxy. Individual giant molecular clouds in the Galactic center also exhibit a wide variation in their current star formation rate. As an example, if one uses embedded HII regions as an indicator of a cloud's recent star formation activity, the difference between the numbers of these objects in clouds can be

up to two orders of magnitude. There are over 100 compact, ultracompact, and hypercompact HII regions in the massive Sgr B2 cloud, compared to just five in the (admittedly less massive) Sgr A complex of clouds in the central ten parsecs (one in M-0.13-0.08, and four in M-0.02-0.07; Ho et al. 1985; Ekers et al. 1983; Goss et al. 1985). M0.25+0.01 in particular, one of the next most massive clouds in the Galactic center after Sgr B2, shows almost no evidence for ongoing massive star formation (Lis et al. 1994; Lis & Menten 1998; Lis et al. 2001; Longmore 2012; Kauffmann et al. 2013, but see also Rodríguez & Zapata 2013). To understand why some clouds form stars and some do not, and what sets the current rate of star formation to be so globally low in this area, one can start by studying the properties of recent massive star formation episodes in individual clouds, and their current impact on the molecular gas of the surrounding cloud. By investigating the total mass of these stars, and kinematics and line-of-sight position of their surrounding HII regions compared to their natal cloud, one can compare the nature of star formation in each cloud, and look for evidence of triggering events, which could be indicative of rules which govern the observed diversity of star formation environments in the Galactic center

In this Chapter, I present new extinction maps and high-resolution Paschen-alpha images of G-0.02-0.07, a complex of compact HII regions located adjacent to the M-0.02-0.07 giant molecular cloud, 6 parsecs in projection from the center of the Galaxy. These HII regions, which lie in projection just outside the boundary of the Sgr A East supernova remnant, represent one of the most recent episodes of star formation in the central parsecs of the Galaxy. The 1.87 μm extinctions of regions A, B and C are almost identical, approximately 3.7 magnitudes. Region D, in contrast, has a peak extinction of $A_{1.87} = 5.9$ magnitudes. Adopting an extinction law specific to the Galactic center, we find these extinctions correspond to visual extinctions of $A_V = 45$ and $A_V = 71$. The similar and

uniform extinctions of regions A, B and C are consistent with that expected for foreground extinction in the direction of the Galactic center, suggesting that they lie at the front side of the M-0.02-0.07 molecular cloud. Region D is more compact, has a higher extinction and is thus suspected to be younger and embedded in a dense core in a compressed ridge on the western edge of this cloud.

2.1 Introduction

G-0.02-0.07 is a group of 4 HII regions (three compact and one ultracompact) in the Galactic center (hereafter GC) which lie $\sim$ 6 parsecs in projection from the central supermassive black hole. Individually, the regions are also identified as Sgr A-A through Sgr A-D, as they were first identified in radio images of the Sgr A complex of ionized gas surrounding Sgr A*, the radio counterpart of the central black hole (Ekers et al. 1983). All four HII regions are projected to lie along the edge of the Sgr A East supernova remnant (see Figure 2.1) which lies between these regions and Sgr A*.

Several studies have been made of the G-0.02-0.07 complex, both in radio continuum and recombination lines (Ekers et al. 1983; Goss et al. 1985), as well as in mid infrared fine structure lines (Serabyn et al. 1992, hereafter S92), including the recent work of Yusef-Zadeh et al. (2010). These observations have shown that the regions are consistent with each being ionized by a single late O-type star. The radial velocities of all four HII regions have also been measured to be very similar, ranging from 43 to 49 km s^{-1}, indicating that these regions are kinematically associated both with each other, and with M-0.02-0.07, the nearby 50 km s^{-1} cloud. The HII regions appear to lie along a spatially coincident dense ridge of the M-0.02-0.07 cloud, denoted the "molecular ridge"by Coil & Ho (2000), which shows evidence of interaction with the Sgr A East supernova remnant (Serabyn

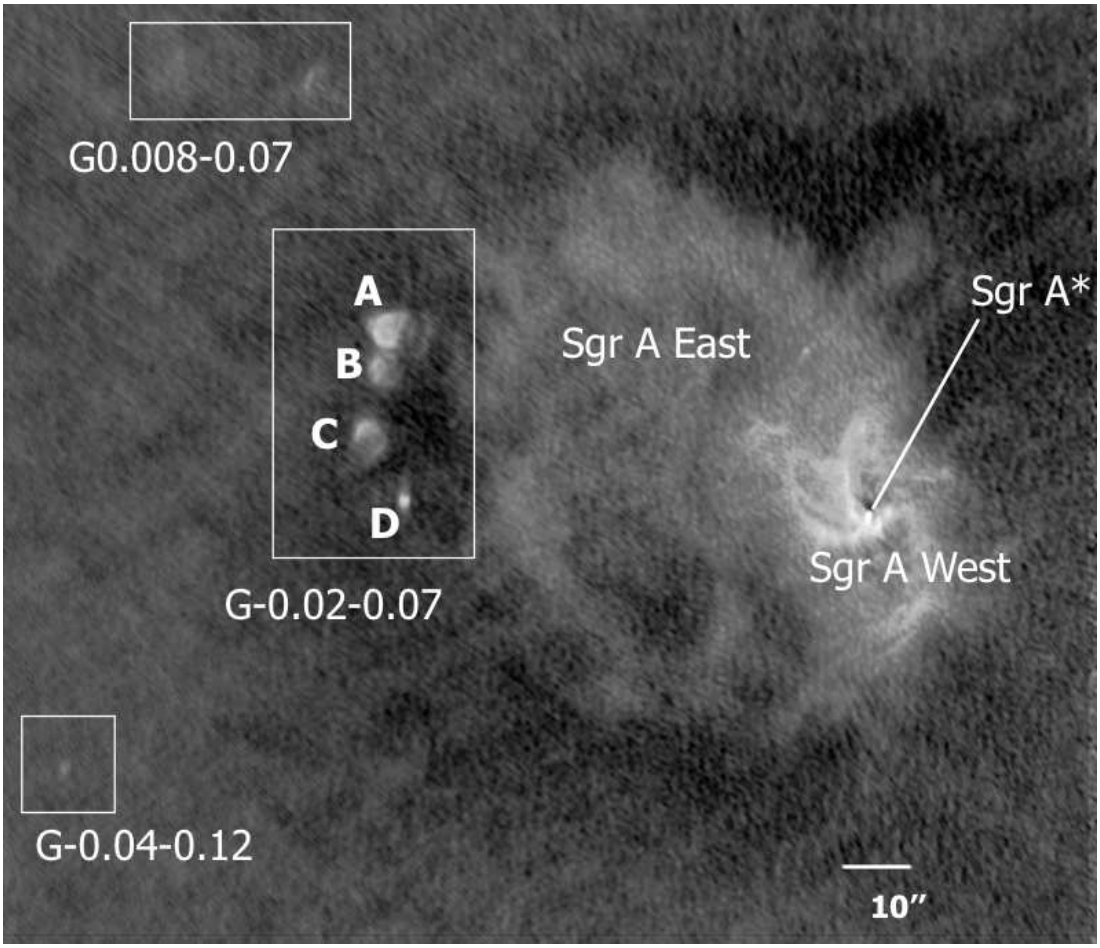

Figure 2.1: 8.4 GHz image showing the G-0.02-0.07 HII regions (A,B,C and D), the Sgr A East supernova remnant, and the Sgr A West complex of ionized gas surrounding the bright point source Sgr A*, the Galaxy's central supermassive black hole. Also shown are two previously unknown radio sources, G0.008-0.07 and G-0.04-0.12. In this image, North is up, and East is to the Left.

et al. 1992; Yusef-Zadeh et al. 1996; Sjouwerman & Pihlström 2008). Despite the suggestive arrangement of the HII regions along the periphery of Sgr A East, estimates of its age ($10^3 - 10^4$ years: Fryer et al. 2006; Mezger et al. 1989) suggest that the star formation event that produced the G-0.02-0.07 complex predates the explosion, as the lifetimes of ultracompact HII regions, precursors to compact HII regions, are believed to span 10^5 years (Wood & Churchwell 1989). In particular, region D, likely the youngest of the four, has a minimum age of at least a few times 10^4 years, estimated from the mass loss rate of the central star, and the expansion rate of the nebula (Yusef-Zadeh et al. 2010).

Although these regions are thus unlikely to be an example of supernova-triggered star formation, they are valuable to study not only as the closest episode of recent (within $0.1 - 1$ Myrs) massive star formation to the center of the Galaxy, but also as one of very few examples of recent massive star formation in the central hundred parsecs. The central hundred parsecs of the galaxy are estimated to have a star formation rate of at least 0.05 $M_{\odot}yr^{-1}$ (Güsten 1989), and likely higher (Yusef-Zadeh et al. 2009; Schuller et al. 2005), are host to three young star clusters with initial masses in excess of 10^4 $M_{\odot}$ (Figer et al. 1999; Figer et al. 2002; Schödel et al. 2009), and at least 4×10^6 solar masses of molecular material (Launhardt et al. 2002b). However the G-0.02-0.07 complex of HII regions is one of the few regions (along with a single compact HII region in the nearby cloud M-0.13-0.08 and a complex of HII regions in the -30 km/s cloud; Ho et al. 1985; Zhao et al. 1993), of apparent massive star formation associated with the massive but largely quiescent giant molecular clouds interior ($R < 120$ pc) to the active star formation regions Sgr B2 and Sgr C.

We have used a combination of new infrared data and archival radio data to study these HII regions in greater detail, and to better determine their location

and relationship with the M-0.02-0.07 cloud and Sgr A East remnant. In this paper we present high resolution ($0''.2$) images of this complex obtained with HST-NICMOS in the 1.87 μm Paschen α (hereafter Pα) line, showing the fine filamentary structures and unusual morphologies of these regions in new detail. We also present the first maps of the extinction structure within the G-0.02-0.07 HII regions, made from a comparison of the Pα and 8.4 GHz radio data, at arcsecond resolution. Finally, we compare our extinction measurements and morphological study of these regions with recent measurements of their gas dynamics, and discuss unusual features of two of the HII regions, regions A and D, in more detail.

2.2 Observations and Data Reduction

Two main data sets were analyzed for this paper: an emission line map of the near-infrared Pα (n = 4–3) recombination transition of hydrogen, and 8.4 GHz data obtained from the archives of the Very Large Array radio interferometer in New Mexico.

2.2.1 NICMOS Paschen α Observations

The Pα emission line map of the G-0.02-0.07 region (Figure 2.2) is part of a larger survey of the inner $39'$ by $15'$ of the Galaxy in this line (Wang et al. 2010) using data from 144 orbits of the Hubble Space Telescope between February and June 2008. Observations were made with the NIC3 camera in both the F187N and F190N narrowband (1% bandpass) filters, one of which is centered on the Pα line at 1.87 μm, and the other centered on the nearby continuum at 1.90 μm. The native pixel size of NIC3 at these wavelengths is $\sim 0''.2$ on a side, which

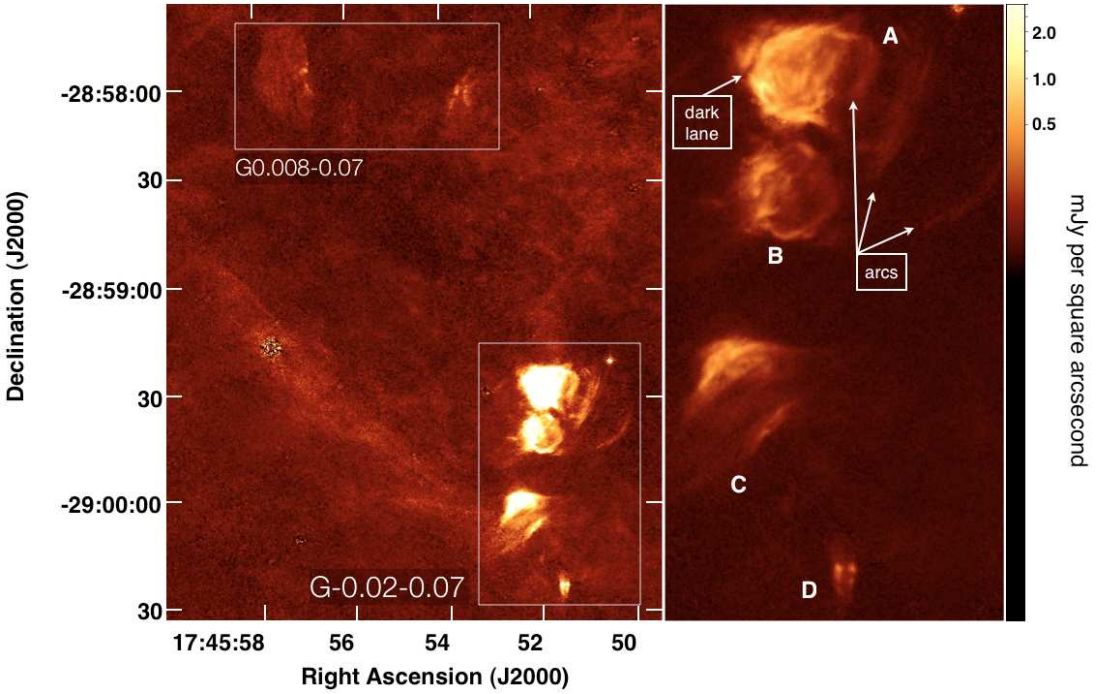

Figure 2.2: Left: Pα image showing a view of the G-0.02-0.07 HII regions (from top to bottom: A,B,C and D) and their surroundings, including a bright emission line star located to the northwest of region A. A ridge of emission can be seen, which appears to emanate from region C, and extend up to the northeast. Visible in the box to the upper left is the newly discovered HII region G0.008-0.07. Right: An enlarged view of the G-0.02-0.07 HII regions, the focus of this paper, with a stretch chosen to enhance the various filamentary features visible in the Pα image. Regions A through D are individually labeled, as are several features of interest, including a dark lane separating region A from a slight extension to the northeast, and a series of filaments extending outward from the West side of region A.

leads to an undersampled PSF. The images were dithered to achieve a sub-pixel resolution of 0″.2 (0″.1 pixels). The resulting sensitivity of these images is 0.13 mJy arcsec^{-2}. The data reduction and the mosaicking process used to make the map of the survey region is described in more detail in a separate paper (Dong et al. 2011).

2.2.1.1 Continuum Subtraction

To produce a map of pure Pα line emission, it is necessary to remove the primarily stellar continuum emission also observed in the filter. In principle, this is accomplished with duplicate observations in a neighboring narrowband filter sampling only the continuum (in this case, separated by 3000 km/s, which is sufficient to ensure there is no Doppler shifting of line emission into the continuum filter), and differencing the two images. However, the ratio of continuum emission in the two filters depends on both the spectral type of the star, and to a greater extent, the local extinction, which is highly variable toward the GC. In comparison to the reddening from the high extinction toward the GC, the former effect is negligible here. To take the effects of extinction into account, an adaptive F187N/F190N ratio is calculated over the map: the colors of the nearest 101 stars are averaged in 0″.4 by 0″.4 boxes. The majority of these stars are assumed to lie at the distance of the GC. However, where the stars are too few, due to attenuation by dense molecular clouds, and cannot be generally assumed to be located at the distance of the GC, the extinction map of Schultheis et al. (2009) is used to determine the ratio. Additional details of this process are discussed in Dong et al., (2011).

2.2.1.2 Flux Calibration

After we flat-field the data and remove the instrumental background, we transform them to an absolute flux scale by applying a standard conversion factor from ADU s^{-1} to Jy, obtained via observations of two principle calibration stars, which is assumed valid for all NIC3 data. Since the Pα images are pure line emission, their natural unit is line flux per pixel, or erg cm^{-2} s^{-1} $pixel^{-1}$. To convert the Pα images to units of line flux per pixel, we then multiply the flux density per pixel in Jy by the width of the F190N filter, as in Scoville et al. (2003).

2.2.2 Archival VLA Data

We obtained radio continuum data of the G-0.02-0.07 HII regions from the archive of the Very Large Array (VLA) Radio Telescope of the National Radio Astronomy Observatory [1]. The observations were made during 1991-1992 in three array configurations (D, C and A/B (antenna move time)) and the integration time on source was $\sim$1 hour in each array configuration. The field of view of these observations is centered on RA, DEC (J2000): (17^h 45^m 51.7^s, -28 59′ 23.7″), which is $\sim$6″ to the NE of region A. These data were taken in standard continuum mode (four IFs, 50 MHz per IF).

2.2.2.1 Calibration and Imaging

The data from the D,C and A/B configurations were calibrated using the standard AIPS software packages of the NRAO. The data were combined and imaged using IMAGR, and self-calibrated using Sgr A* as a reference source. The resulting final image has an RMS noise of 0.2 mJy/beam, and a dynamic range of 1300.

[1] The National Radio Astronomy Observatory is a facility of the National Science Foundation operated under cooperative agreement by Associated Universities, Inc.

The angular resolution of this image was 1.5″x 0″.8, PA = -4.78 degrees. The overall noise was ∼10 times the theoretical expectation for a point source, which is reasonable, given the complicated source structure, and the presence of the bright (∼20 Jy), extended structure of Sgr A East and West at the edge of the beam. The final image does, however, display a low-level pattern of linear artifacts, or striping, running from southwest to northeast, the origin of which could not be identified in the UV data. This structure is faint enough not to affect our analysis.

The D-array data contribute many short spacings to the (u,v) coverage; the shortest spacing in the (u,v) data used to make the final images is 0.75 kilolambda. At 8.4 GHz, this should lead to sensitivity to structures with sizes less than 5′.6. The largest (north-south) extent of G-0.02-0.07 is only 1′, and thus we are satisfied that there should be no flux missing from our measurements of these regions beyond the smooth synchrotron background of the GC.

2.3 HII Region Properties from Radio and Pα

The Pα images offer an unprecedented look at the detailed morphologies of this group of compact HII regions. At an assumed distance of approximately that of Sgr A*, (8.4 kpc; Reid et al. 2009; Ghez et al. 2008), the angular resolution of 0″.2 corresponds to a spatial resolution of 0.008 pc (∼1600 AU), higher resolution than any existing radio studies of these HII regions. The resolution of the Pα images allows us to identify new structures including knots, filaments, diffuse ridges, and the detailed shape of the boundaries of these HII regions. An image of the entire complex is shown in Figure 2.2, with a logarithmic stretch in order to emphasize the diffuse structure of these regions.

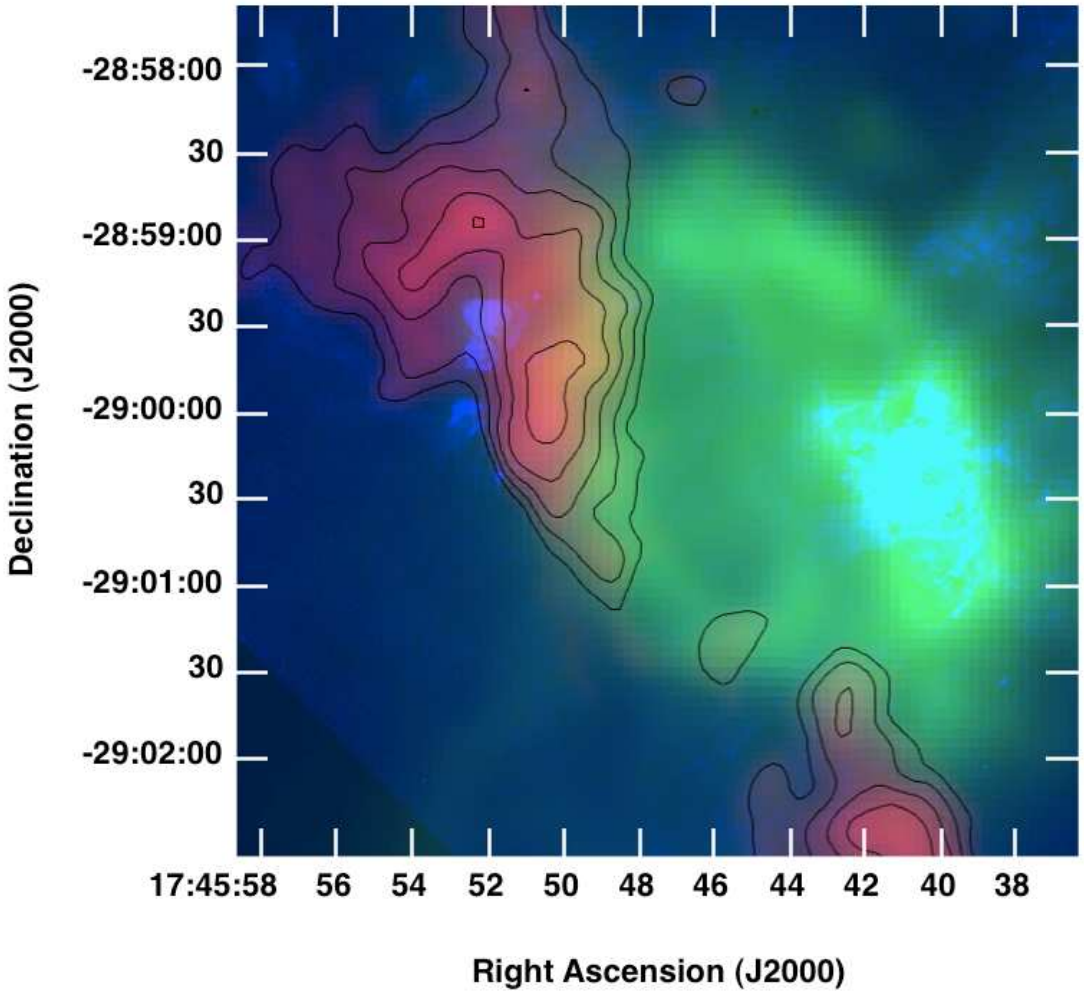

Figure 2.3: Composite image of Pα in blue, VLA 1.4 GHz data in green (Lang et al. 2010), and SCUBA 450 microns (Pierce-Price et al. 2000) in red. The main structures traced by Pα emission (blue) are the G-0.02-0.07 HII regions at middle left, and Sgr A West at lower right. The 1.4 GHz image (green) also traces these structures, but most prominent at 1.4 GHz is Sgr A East, the large shell of nonthermal emission that borders G-0.02-0.07 and appears to enclose Sgr A West. The 450 micron image (red with black contours) traces an entirely different component, the dense cool dust that corresponds to some of the densest parts of M-0.02-0.07, the 50 km/s molecular cloud, in which the HII regions appear embedded. At the bottom of the image, part of M-0.13-0.08, the 20 km/s cloud, can also be seen.

2.3.1 Regions A,B, and C

Regions Sgr A-A, Sgr A-B, and Sgr A-C (hereafter A, B, and C) have similar sizes ($\sim$ 10 arcsec or 0.4 pc in diameter), and exhibit shell-like morphologies in various stages of disruption. Region A is the brightest, as well as the most extended. It has a semicircular shell shape which appears open on the western edge, where there is an unusual series of roughly parallel linear features which decrease in brightness toward the west of the HII regions. The nature of these features is discussed in more detail in Section 2.5.3. On the northeast edge of this region, at approximately the ten o'clock position (see Figure 2.2, right) there also appears to be a dark lane separating the main shell from a slight extension. We discuss the nature of this feature further in Section 2.5.2.

Region B is the faintest of the three, and has a complete, albeit faint, shell morphology which can be seen in Figure 2.2. Its circular shape suggests that it is still embedded on all sides in the natal cloud, or is being viewed from a different angle than A and C. Like regions A and C, the eastern side of this shell appears brightest, thickest, and has the best defined edge.

Region C has a larger opening angle than region A, and the shell appears discontinuous on the northern and southern edges. The nature of the western edge of region C is unclear; possibly it is part of the original boundary of the region, or alternatively it may be that the star responsible for ionizing region C is also ionizing another, nearby cloud front. In addition to these prominent features, there is a faint larger-scale ridge of diffuse Pα emission that can be traced in Figure 2.2 from the southeast edge of region C, where its shell appears to end discontinuously, several parsecs toward the northeast. This faint emission appears to trace the surface of the M-0.02-0.07 cloud as seen in 450 micron continuum images from Pierce-Price et al. (2000) (Figure 2.3).

2.3.2 Region D

Sgr A-D (hereafter D) is the most compact region. With a size of 0.06 pc (RA) × 0.2 pc (dec), this region is at the upper end of the distribution of ultra-compact HII (UCHII) region sizes, which typically have sizes less than 0.1 pc (Churchwell 2002).

The 8.4 GHz flux density we measure for D is significantly different than that recently measured for this HII region using the same data set (Yusef-Zadeh et al. 2010). They find the total flux density for both peaks of this region combined to be 60 ± 4 mJy, whereas we find a flux of 105 ±15 mJy. This difference is not due solely to a different integration over the source, as the peak flux densities we find are higher than those measured by Yusef-Zadeh et al. (2010).[1] We are satisfied that our measurements of region D do not resolve out any of its flux, and further note that our total flux density for region D is more consistent with the expected flat spectrum of an HII region at radio frequencies, given the published 14 GHz and 5 GHz flux densities for this HII region (see Table 2.1).

The Pα morphology of region D is irregular.There are two bright peaks which are slightly north-south asymmetric, each peak appearing to have a tail of emission extending toward the south. The peaks appear composed of several clumps, although these clumps are near the limits of the spatial resolution of the Pα observations. The two peaks are separated by an apparent void of Pα emission, similar to that seen on the northeast edge of region A. The nature of this void is

[1]We measure peak fluxes of 20 mJy and 24 mJy for the eastern (D1) and western (D2) peaks, respectively, whereas the peak intensities reported in Yusef-Zadeh et al. (2010) for these sources are 8.6 mJy and 10.0 mJy. Our beam area is larger by a factor of 1.7. If the source were emitting uniformly over the beam area, our larger beam would collect more flux, but not enough to resolve the discrepancy. However, we find that the source is largely unresolved in our beam, and so the peak flux value we measure should be somewhat diluted, and less than the peak value measured by Yusef-Zadeh et al. (2010) for a beam size smaller than the source size. Thus, the different geometry of our beams is insufficient to explain the discrepancy.

discussed further in Section 2.5.2.

2.3.3 New Radio Sources

In producing the radio images, we discovered two new radio sources in the field of view (see Figure 2.1). One source, G0.008-0.07, is extended in the 8.4 GHz images, and has a morphologically similar counterpart in the Pα data. In the Pα image (Figure 2.2), the radio source appears to consist of two regions of diffuse emission surrounding several brighter compact knots. The other radio source, G-0.04-0.12, is a faint, compact region of emission which lies just outside the boundary of the area surveyed in the Pα line. However, it appears to have a faint counterpart in 24 μm images of the Galactic plane (Yusef-Zadeh et al. 2009), suggesting the radio emission to be thermal in nature.

2.3.4 HII Region Properties

As the radio data are not affected by extinction, we use them to determine the physical properties of the HII regions. Traditionally, HII region parameters are determined by assuming the geometry of a uniform-density sphere (e.g., Mezger & Henderson 1967). This geometry predicts a peak in emission at the center of the HII region, and is a good approximation for unresolved HII regions, or partially-resolved HII regions such as region D.

However, the larger HII regions A, B, and C are resolved and exhibit an edge-brightened morphology inconsistent with this density distribution. We therefore determined parameters of the HII regions A, B, and C by modeling them as shells of uniform density, adjusting the outer radius and thickness of the shell to fit the observed HII region profiles. Such a model is physically motivated by observations and simulations of wind-swept shell HII regions, which indicate that

Table 2.1: HII Region Parameters

Region	A	B	C	D
8.4 GHz Flux Density (mJy)	550 ± 75	175 ± 44	180 ± 50	105 ± 15
Radius (pc)	0.22	0.22	0.20	0.03
Electron Density (cm^{-3})	5100	3600	4100	21000
Emission Measure (pc cm^{-6})	$6.8e6$	$3.4e6$	$4.0e6$	$3.1e7$
Mass in HII ($M_\odot$)	2.2	0.8	0.4	0.1
Lyman Continuum Flux (s^{-1})	$4.8e48$	$1.3e48$	$1.6e48$	$8.1e47$
Ionizing Spectrum[1]	O7	O8.5	O8.5	O9
Temperature[2] (K)	5800	6600	5300	7400
14.7 GHz Flux Density[2] (mJy)	570 ± 20	173 ± 20	245 ± 20	95 ± 15
5 GHz Flux Density[3] (mJy)	812 ± 100	166 ± 40	196 ± 40	130 ± 15
1.5 GHz Flux Density[3] (mJy)	380 ± 80	103 ± 17	108 ± 20	45 ± 7

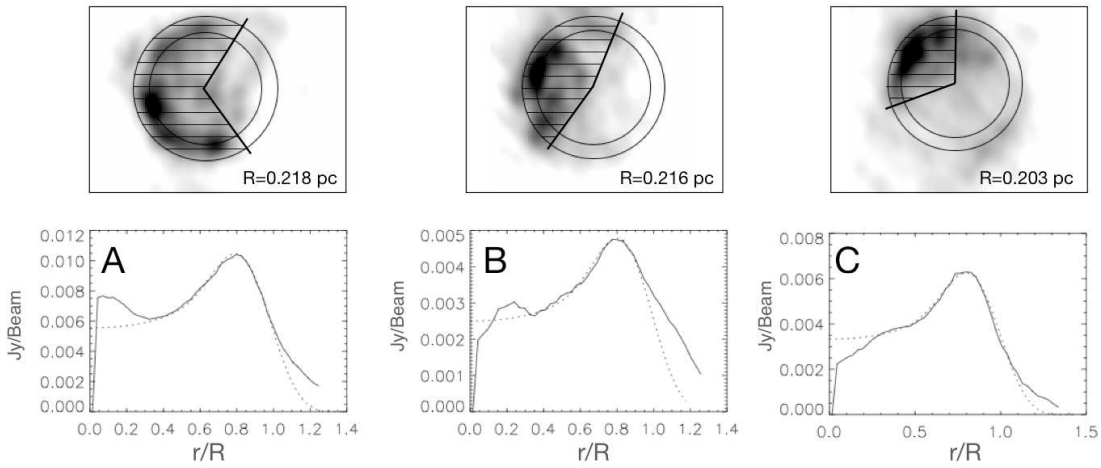

Figure 2.4: Top: Projected shells (with outer radius size indicated for each shell) are superposed on the 8.44 GHz images used to fit shell parameters. Bottom: Azimuthally-averaged radial profiles for each HII region are shown (solid lines). A shell model of the emission measure (dotted lines) is fit to each HII region, from which the electron density can be derived.

the regions interior to these shells are largely evacuated, with the ionized gas flowing along the surface of the shell (Arthur & Hoare 2006; Zhu et al. 2005). This method of fitting a shell model is still a rough approximation of the HII region parameters, as the shells are clearly clumpy, and deviate from spherical symmetry.

To determine a representative radial profile for each shell, we azimuthally average the intensity of each shell (Jy/beam) over the angles where the shell is most continuous, which are indicated by the shaded regions in Figure 2.4. This simple model (given by Equation 2.1a) can then be fit to the averaged profile in order to solve for the parameters of each HII region, which are reported in Table 2.1. The intensity of emission from the shell as a function of position is given by:

$$\mathrm{I}_\nu = 1680 \, \langle \, g_{ff} \rangle \, \mathrm{T_e}^{-0.5} \, \Omega_{\mathrm{beam}} \, \mathrm{L(p)} \, n_\mathrm{e}^2 \tag{2.1a}$$

$$\mathrm{L(p)} = 2 \begin{cases} \left(R^2 - p^2\right)^{\frac{1}{2}} - \left((R - tR)^2 - p^2\right)^{\frac{1}{2}}, & p \leq R - tR \\ \left(R^2 - p^2\right)^{\frac{1}{2}}, & p > R - tR \end{cases} \tag{2.1b}$$

Here L(p) is the path length through the HII region at projected offset p (measured in arcseconds) from the center, R is the outer radius of the shell (also measured in arcseconds), and t is the thickness of the shell as a fraction of R.

The emission measure is given by $\mathrm{L(p)}n_\mathrm{e}^2$, and the mass of ionized gas in the the HII region can be calculated by multiplying $\langle n_e^2 m_p \rangle$ for the shell by the volume of the shell section used to compute the radial profile (the shaded area in Figure 2.4). The calculated masses only account for the mass of this shaded portion of the HII region; there is also some residual radio emission outside of the modeled area which is not accounted for, and if corrected for would lead to an increase in the total $\mathrm{M_{HII}}$. We can estimate the magnitude of this correction from the

percentage of the total HII region flux outside of the modeled area, which is 17 % of the flux for region A, 4 % for region B, and 30 % for region C.

The Lyman continuum flux required to ionize each nebula, which yields the spectral type of the star primarily responsible for the ionization, is largely independent of the geometry assumed, depending only upon the distance to the HII regions and the flux and temperature for each (Rubin 1968). We adopt the temperatures derived from the recombination line measurements of Goss et al. (1985), given in Table 2.1. The stellar types we derive for the dominant ionizing source in each nebula (O7-O9) are consistent with those previously determined by Goss et al. (1985) and S92, who both concluded that the HII regions were each consistent with being ionized by a single O star. However, the ionizing source of each nebula remains unidentified. Neither A,B, nor C have a detectable emission line stellar counterpart in the Pα map. It is also not possible to uniquely identify a central star or stars responsible for ionizing any of these nebulae against the stellar background in the 1.90 μm continuum images. Each of these HII regions has several dozen stars inside of its boundary, and if the HII regions are indeed stellar wind bowshocks, as suggested in a recent interpretation of their kinematic structure (Yusef-Zadeh et al. 2010), then the primary ionizing source may be offset from the geometric center of the nebula. Near-infrared integral field spectroscopy of these regions (Cotera et al. 1999b) indicates there are three stars which may be potential ionizing sources for regions A,B and C. They have spectra devoid of strong emission or absorption features, and thus could be main sequence O stars, however no follow-up work has been done to verify their nature. The only emission line star we see in this area in our Pα images is a previously identified Wolf-Rayet star to the northwest of region A (see Figure 2.2; Cotera et al. 1999b). This star appears not to be related to these HII regions, as we see no evidence of the expected ionization front were it neighboring the M-0.02-0.07

cloud.

2.4 Extinction from the Paschen α and Radio Continuum Data

2.4.1 Calculating the Extinction

Together, the 8.4 GHz radio continuum maps and Pα images can be used to determine the extinction toward each HII region. Although the emission mechanisms are different, the Pα and the radio emission trace the same ionized gas component, and the intensity of both is proportional to the square of the electron density. The free-free radio emission suffers little or no extinction, whereas the Pα emission will be significantly reduced by extinction. By comparing the observed flux density ratio between the radio and the Pα to the theoretical expectation, we can then determine by what factor the Pα emission has been reduced, and thus find the dust extinction at 1.87 μm toward these regions along the line of sight.

Following the calculations of Scoville et al. (2003), hereafter S03, who similarly derive the extinction from NICMOS Pα observations and 5 GHz continuum observations, we estimate the expected flux per pixel for both Pα and the 8.4 GHz continuum, using Table 4 from Osterbrock (1989).

Assuming case B recombination, and in the event of zero attenuation, the intrinsic flux in the Pα line, per pixel, is given by:

$$F_{P\alpha} = 6.4 \left(\frac{T_e(K)}{6000} \right)^{-.87} \frac{n_e n_p l a}{4\pi d^2} \text{ mJy Hz} \tag{2.2}$$

Here, n_e and n_p are the electron and proton densities, l is the path length in

the ionized gas, a is the projected area of a pixel on the sky, d is the distance, and T_e is the electron temperature, values of which have been previously calculated for G-0.02-0.07 using H92α recombination line measurements and assuming LTE (Goss et al. 1985, see Table 2.1).

The flux density per pixel of the radio continuum emission can be similarly expressed:

$$S_{ff} = 4.2 \times 10^{-13} \left(\frac{T_e(K)}{6000}\right)^{-.35} \left(\frac{\nu}{5\text{GHz}}\right)^{-.1} \frac{n_e n_p l a}{4\pi d^2} \text{ mJy} \tag{2.3}$$

All of the input variables here are assumed to have the same values as for the Pα emission, although the temperature dependence is different. As a result, the intrinsic ratio of the Pα line flux to the radio free-free flux density can be expressed as:

$$\frac{F_{P\alpha}}{S_{ff}} = 1.5 \times 10^{13} \left(\frac{T_e(K)}{6000}\right)^{-.52} \left(\frac{\nu}{5\text{GHz}}\right)^{-.1} \text{ Hz} \tag{2.4}$$

The factor by which the observed ratio of Pα to 8.4 GHz emission is reduced compared the theoretical expectation yields the 1.87 μm extinction.

2.4.2 The Choice of Extinction Law

To calculate the extinction in more standard visual magnitudes or A_V, an extinction law must be assumed. We adopt the near-infrared extinction law of Nishiyama et al. (2008), which has been widely used for recent GC studies. This law is specific to the particular properties of dust and molecular clouds toward the GC and has a $\sim \lambda^{-1.99}$ power law form. Applying this law yields A_H/A_V = 0.108 and A_{Ks}/A_V= 0.062. The Pα line (1.87 μm) lies between the H (1.6 μm) and K (2.2 μm) bands, and we fit a power law equation $A_\lambda/A_V = 0.29\lambda^{-1.99}$ to

these values to determine $A_{P\alpha}/A_V$ The resulting equation to determine A_V from our 8.4 GHz flux density (S_{ff}) and Pα flux measurements is as follows:

$$A_V = 30.4 \times \log\left(\frac{(F_{P\alpha}/S_{ff})_{intrinsic}}{(F_{P\alpha}/S_{ff})_{observed}}\right) \tag{2.5}$$

This law gives significantly different results than the law of Rieke & Lebofsky (1985) which was previously the standard for GC work, and was used by, e.g., Scoville et al. (2003) in their Pα study of Sgr A West. Adopting the Rieke & Lebofsky (1985) law would change the constant in Equation (2.5) from 30.4 to 18.1, and thus would make our measured extinctions substantially lower. We discuss the comparison of our results with previous extinctions measured using the Rieke & Lebofsky (1985) law further in section 2.5.1.

2.4.3 Constructing the Extinction Map

The steps to make an extinction map include aligning the 8.4 GHz radio and Pα maps, matching the pixelization (0″.15 pixels) and smoothing the Pα map to the resolution of the radio CLEAN beam (1″.85 × 0.6″) with AIPS tasks HGEOM and CONVL. In the process we found that the Pα and 8.4 GHz images were offset by 1”.2 in right ascension, and so after smoothing the Pα image we performed a normalized cross-correlation of the diffuse emission in the two images in IDL with the procedure CORREL_OPTIMIZE to find the translation that resulted in optimal alignment. Even though the Pα may be affected by non-uniform local extinction, we still expect that the radio and Pα images will trace the same structure in these HII regions, and so this should yield the proper alignment of the two maps. There are no point sources other than Sgr A* in the radio image to compare, however the positions of stars in the Pα survey images with known

SiO masers have been compared to the catalog of Reid et al. (2007), and the astrometric uncertainty for all the Pα images is measured to be $\sim 0.05''$(Dong et al. 2011). This suggests that the majority of the offset originates in the radio reference frame. The radio frame was then corrected to match the Pα data, the Pα image was divided by the radio image, and Equation (2.5) was applied so that the pixel values represent the local value of A_V.

Before constructing the final map, the radio map was also clipped to the 3 σ level to eliminate any extraneous peaks in the background noise. Other apparent extinction peaks may still occur where there are over-subtracted stars in the Pα images.

The extinction has a slight dependence on temperature (Equation 2.4), and as temperatures for each HII region were measured by Goss et al. (1985), this was taken into account for the extinction values we calculate for each individual HII region. However, this effect is small: for example, lowering the temperature of region D by 2000 K results in only a 4% change in the median extinction measured for that source.

2.4.4 Measured Extinctions

The extinction maps which we derive, shown in Figure 2.5, are the first measurements of the extinction structure across these regions. Due to the substantial difference in the visual extinctions calculated using different extinction laws, we report in Table 2.2 the 1.87 micron extinction, which is not affected by the choice of extinction law, in addition to the A_V we calculate using the Nishiyama et al. (2008) law. To measure the extinction toward each HII region, we calculate the median of all pixels in our map from each HII region. We report the median extinction toward each individual HII region in Table 2.2.

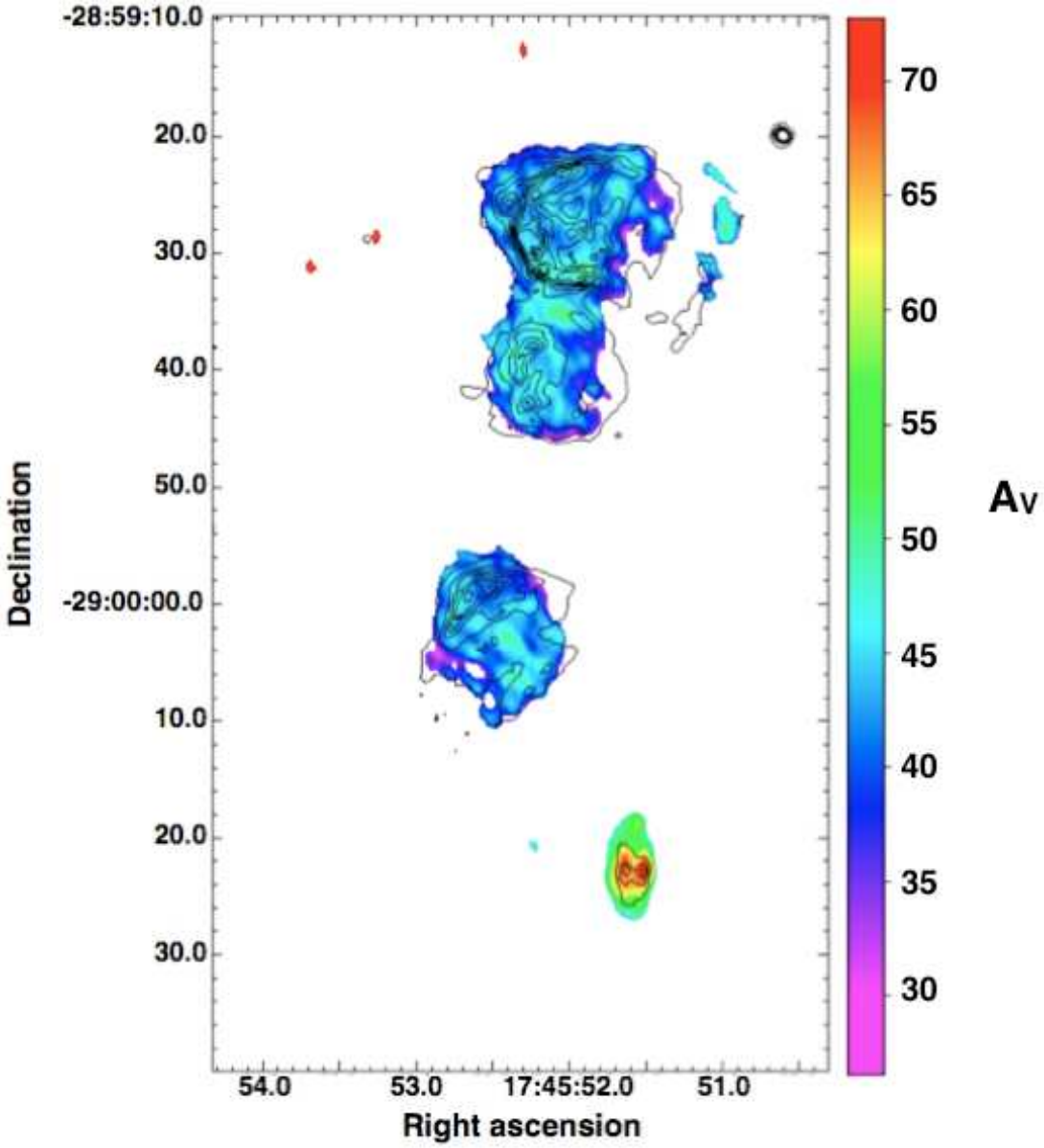

Figure 2.5: Map of the extinction toward the HII regions G-0.02-0.07 derived from a comparison between Pα and 8.4 GHz continuum data. The resolution of the map is the same as the 8.4 GHz data, or 1.5 x 0.8 arcseconds. The contours represent the flux density of the smoothed Pα emission. The lowest contour has a values of 0.5 mJy per arcsec^{-2}, and the contours are spaced by 0.8 mJy per arcsec^{-2}.

Table 2.2: HII Region Extinctions

Region	**A**	**B**	**C**	**D1**	**D2**
Median $\mathbf{A_{1.87\mu m}}$	3.7	3.7	3.7	–	–
Maximum $\mathbf{A}_{1.87\mu m}$	4.3	4.3	4.3	5.8	5.9
Standard Deviation	0.28	0.33	0.28	–	–
Area (Square″)	185	107	120	–	–
[1]Median $\mathbf{A_V}$	45	45	45	–	–
[1]Maximum $\mathbf{A}_V$	52	52	52	69	71
Standard Deviation	3.2	3.9	3.4	–	–
[2]Median $\mathbf{A}_{8\mu m}$	1.1	1.1	1.1	1.82[3]	1.85[3]
[4]Serabyn et al. $\mathbf{A}_{12.8\mu m}$	1.0	1.1	1.3	3.3	3.3

2.4.4.1 Regions A, B, and C

We measure the median extinction values for regions A, B, and C to be the same within our uncertainties: A_V=45. We also measure the same maximum extinction value, $A_V = 52$, for each of these HII regions. Some parts of these regions, such as the westernmost ionized ridge of region A, and the diffuse interior of region C, are too faint to appear above the noise level in the 8.4 GHz map, and so there is no extinction information for these areas. The extinction measured across each HII region is relatively uniform, varying locally by 3-4 magnitudes. We also observe that the maxima in extinction for regions A and B are located near their apparent mutual boundary, on the southern edge of region A, and on the northern edge of region B.

The center of the 8.4 GHz image of region C is somewhat affected by the previously mentioned background striping artifacts of the radio data, leading to enhanced emission in its center which appears as a slight peak in the extinction map in this region. As a result, the extinction values at the center of region C should not be considered reliable.

2.4.4.2 Region D

As region D is mostly unresolved at the resolution of our extinction map, we report only the maximum values of the extinction toward D1 (the eastern peak of the HII region) and D2 (the western peak). These values are $A_V = 69$ and $A_V = 71$, respectively, which is almost 20 magnitudes more than the maximum extinction measured for regions A, B and C. Comparing the extinction map of region D to the radio and Pα maps (Figure 2.6), we see that the eastern peak in the extinction map is slightly offset from the peak of D1 in the Pα emission. We measure the area between D1 and D2 to have a minimum extinction of $A_V = 66$.

However, as the two peaks of region D are not fully resolved in the radio image or the resulting extinction map, this extinction value is likely not representative of what appears to be a void in the ionized gas emission in both the radio and Pα images, and instead most likely results from the overlapping PSFs of the two compact peaks D1 and D2. On the northern edge of region D is a diffuse extension that appears only in the 8.4 GHz images, likely because it is too faint or extinguished to appear in Paschen alpha. We determine the lower limit to the extinction toward this structure to be $A_V = 61$ magnitudes.

2.5 Discussion

2.5.1 Comparison with existing extinction results

Average extinctions have been previously measured for the individual HII regions in the Sgr A East complex at 12.8 microns (S92), and using Brackett-γ (Cotera et al. 2000, hereafter C00). S92 derived approximate extinction values for each of the HII regions at 12.8 μm from fractional ionic abundances of Ne, S, and Ar measured from mid-infared fine-structure lines. Our results are consistent with their findings that region D suffers substantially higher extinction than the other three regions. They conclude that regions A-C are located at the front edge of the cloud, with D more embedded. Although our results are qualitatively the same, it is difficult to more quantitatively compare our values. The recently determined GC extinction law of Nishiyama et al. (2009) covers infrared wavelengths up to 8.0 μm, and although it shows the mid-IR extinction law to be quite flat, the extinction curve immediately beyond 8 μm is known to rise sharply due to the wide 10 μm silicon bump. Using the Nishiyama law, we find the median A_V values measured toward A,B, and C (all $\sim$ 45 magnitudes) correspond to

8 μm extinctions that are comparable to the 12.8 μm extinctions estimated by S92 (see Table 2.2). However, the peak extinction we measure toward region D corresponds to an 8 μm extinction substantially less than that reported by S92 at 12.8 μm.

Our Pα-derived extinctions are, on average, about a magnitude higher than extinctions calculated in a similar manner by C00 using Br γ imaging along with 6 cm data from Yusef-Zadeh & Morris (1987a). Using J, H, and K' colors, C00 also determined a median stellar extinction (hereafter MSE) along the line-of-sight toward the HII regions with $1'$ resolution. Here, it can be assumed that the majority of the stars in a narrow, pencil-beam line of sight toward the GC lie at the distance of the GC, and furthermore, if that line of sight intersects an opaque molecular cloud, one expects the MSE to be slightly less than the extinction of a source just in front of or embedded in the cloud. C00 found that the MSE was consistently higher than the HII region extinctions, leaving open the possibility that these regions lie in the foreground of the GC. However, the extinctions we measure for regions A, B and C with Pα are comparable with the MSE of C00, with the extinction we measure for region D being much larger than the MSE. This is consistent with regions A, B, and C being located at the distance of the GC, and region D likely being embedded in the M-0.02-0.07 molecular cloud.

We also compare the extinctions we derive with the extinction map of Schultheis et al. (2009), which is the most recent large-scale map ($2^\circ \times 1.4^\circ$) of the MSE toward the GC, constructed using Spitzer-IRAC mid-infrared colors of long-period variables. This map, however, has very low resolution, with pixel sizes of $2'$ on a side. In the four pixels of the map which overlap the HII regions, Schultheis et al. (2009) measure extinctions of A_V = 26, 32, 46, and 48. As these pixels are very large compared to the size of the HII regions and even compared to

the M-0.02-0.07 cloud, we interpret these values as global averages, biased by the filling fraction of cloud in each pixel. Even in the two pixels which have the highest extinction and overlap the largest portions of the molecular cloud, the measured extinction values likely significantly underestimate the extinctions present in the small-scale substructure or densest cores of the cloud. We thus interpret our extinction values as consistent with a scenario in which regions A-C lie at a similar distance as the M-0.02-0.07 cloud, though likely in front of it due to the uniformity of extinction across the three regions. The higher extinction we observe toward region D suggests it is not in front of the cloud with the other three regions, but rather is embedded in an especially dense core of the M-0.02-0.07 cloud.

The median extinction values we found for regions A-C ($A_V = 45$) correspond to extinctions of $A_V = 26$, if we use the extinction law of Rieke & Lebofsky (1985). This is similar, though slightly lower than the extinction values measured by Scoville et al. (2003) for Sgr A West using the same law, which vary from $A_V =$ 20 to 50, with a median value of $A_V \sim 31$. As Sgr A West is not significantly occulted by either the M-0.02-0.07 or M-0.13-0.08 molecular clouds, its extinction should be due as well to the foreground screen from intervening spiral arms. The higher median extinction observed in that direction, relative to that observed toward the G-0.02-0.07 HII regions, may be partly due to the fact that Sgr A West suffers somewhat higher extinction on its periphery due to the surrounding circumnuclear disk of molecular gas (Scoville et al. 2003), which likely biases the median value upward.

In summary, our results agree with those of S92, confirming that the extinction toward A-C is consistent with a location at the GC, but is sufficiently low and uniform toward these regions that it is not consistent with significant local

attenuation from M-0.02-0.07. The higher and non-uniform extinction of D, in contrast, suggests it is embedded in a dense core of the M-0.02-0.07 cloud.

2.5.2 The Nature of Region D

Yusef-Zadeh et al. (2010) recently examined the kinematic structure of region D using mid-infrared spectroscopy of the Ne II line. They found that the centroids of the two peaks of region D have velocities differing by 10 km s^{-1}, with the eastern peak appearing redshifted, and the western peak appearing blueshifted. Each peak exhibits a range of velocities, ranging from the ambient cloud velocity to offsets as much as 30 km s^{-1}. The authors argue that the velocity offsets of the two peaks, as well as the observed width of the Ne II line emission, are best described by a collimated outflow or jet from the central star which is impacting a surrounding, evacuated cavity. Based on the observed velocity shifts, the western edge of the disk is tipped toward us, with an estimated disk position angle of 70°.

Our observations largely support this model, though we disagree on a few points. We interpret the continuum source seen in the 1.87 and 1.90 μm images (Figure 2.7) as more likely to be from the central young stellar object than light scattered off of the western radio peak of region D, as suggested by Yusef-Zadeh et al. (2010). If the compact and luminous infrared source arises from light scattered off of a nearby clump of gas and dust, one would expect that the same part of that clump would be a density peak in the ionized gas, and thus be brightest point in the radio. However the radio peak is offset to the northwest of the infrared peak, as can be seen in Figure 2.6. The ionizing source for region D is then much more offset from the centroid of the HII region than implied by the model of Yusef-Zadeh et al. (2010) in their Figure 9.

Cotera et al. (1999b) also suggest that this star is a B[e] type star based on the

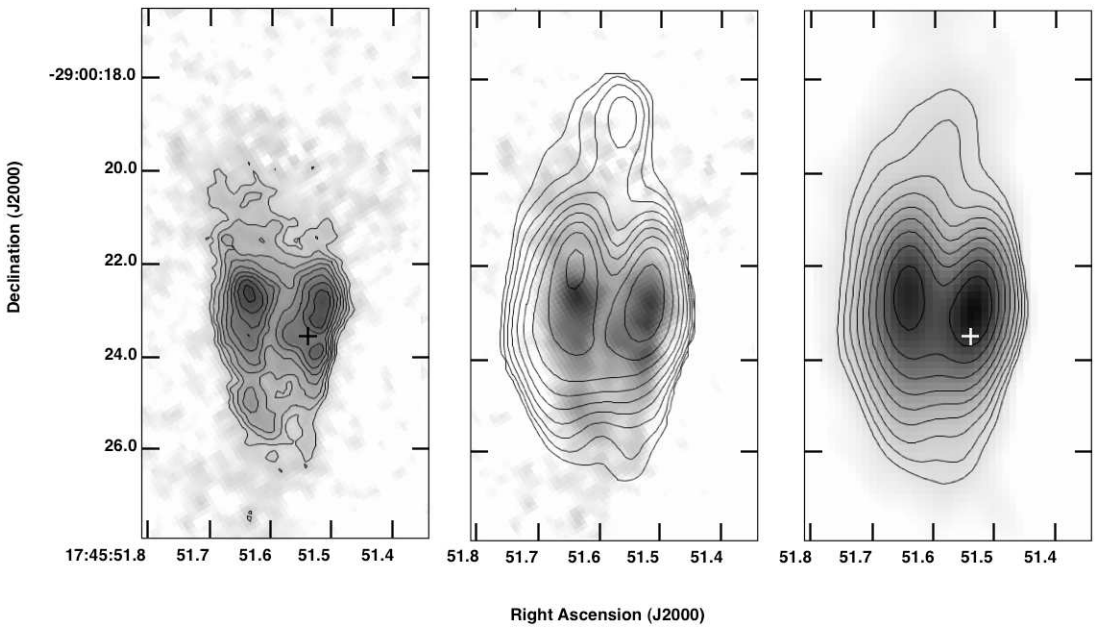

Figure 2.6: Detail maps of the structure of region D in pure Paschen alpha line emission, with contours of flux density (Left) and extinction (Center) overlaid. For comparison, the 8.4 GHz image of region D is also shown (Right). On the Left, the flux density contours have a logarithmic spacing, with the lowest contour having a value of 0.5 mJy per arcsec^{-2}, and the highest having a value of 3 mJy per arcsec^{-2}. The cross marks the position of the star seen in Figure 2.7. In the Center, the lowest and highest extinction contours correspond to values of $A_V = 50$ and 70, respectively, with a contour spacing of 2.5 magnitudes. On the Right, the contours on the radio image are logarithmically space, with the lowest contour corresponding to a flux density of 0.5 mJy and the highest corresponding to 20 mJy.

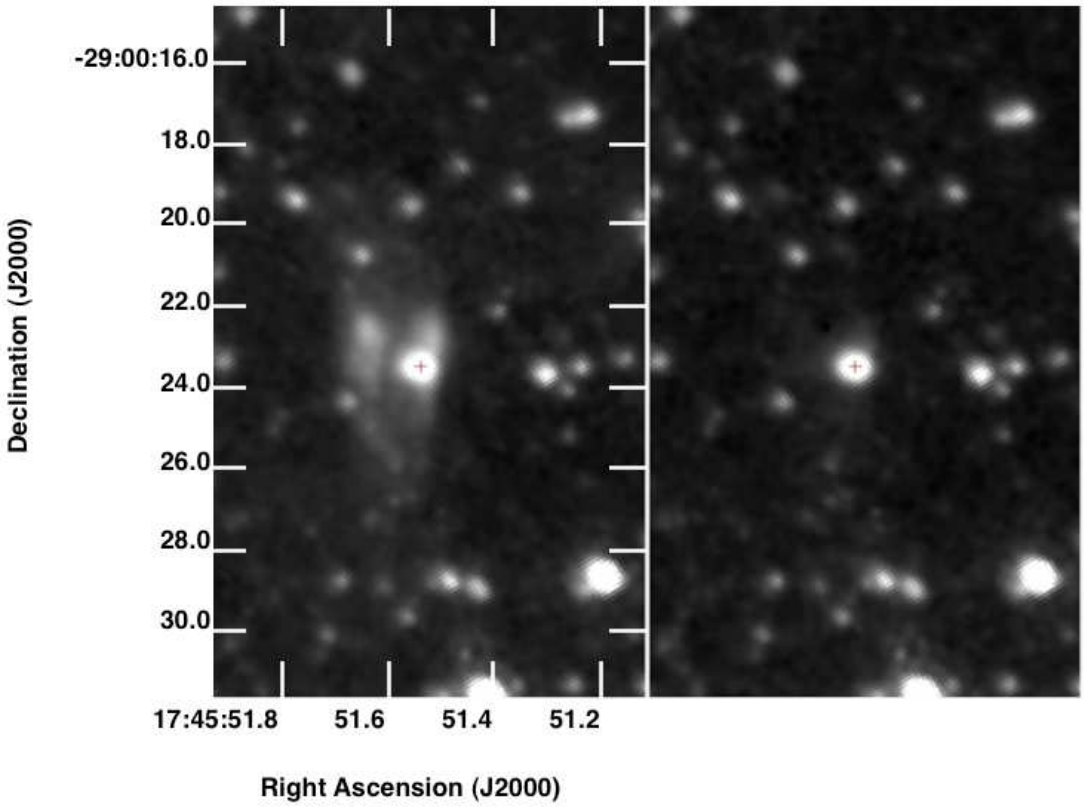

Figure 2.7: A comparison of the emission toward region D from the F187N and F190N filters. Slightly offset from the center of region D is a point source (indicated in both images with a cross) which has a F187N/F190N ratio consistent with being purely stellar continuum, with no excess emission from the Pα line. This point source was identified by Cotera et al. (1999b) as having a stellar spectrum, and classified as a B[e] star (although this is not confirmed by our lack of detection of a Pα excess).

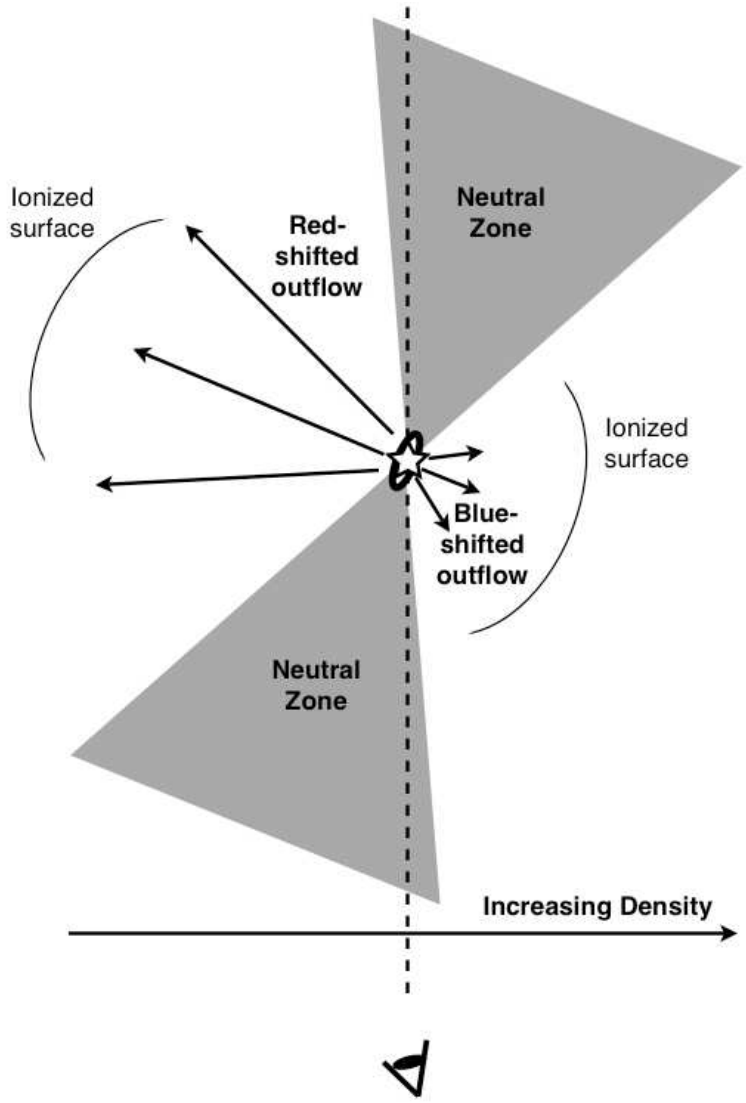

Figure 2.8: A model of the disk structure of region D. In this model, the disk at the center is small, and does not occult ionized emission along the line of sight, consistent with the lack of a high extinction value measured toward the location of the disk. We explain the dark lane visible in radio and Pα images which divides the two peaks of region D as due to disk absorption of ionizing radiation from the star. The dark lane represents a region of largely neutral gas which has been shielded from the ionizing radiation of the central star by the disk. The dominant source of the radio and Pα emission is the ionized surface of cavities evacuated by an outflow from the central disk. The edge of the western cavity appears to be located closer to the ionizing star, suggesting this cavity is smaller. This can be explained if region D is embedded in a density gradient which is increasing to the west.

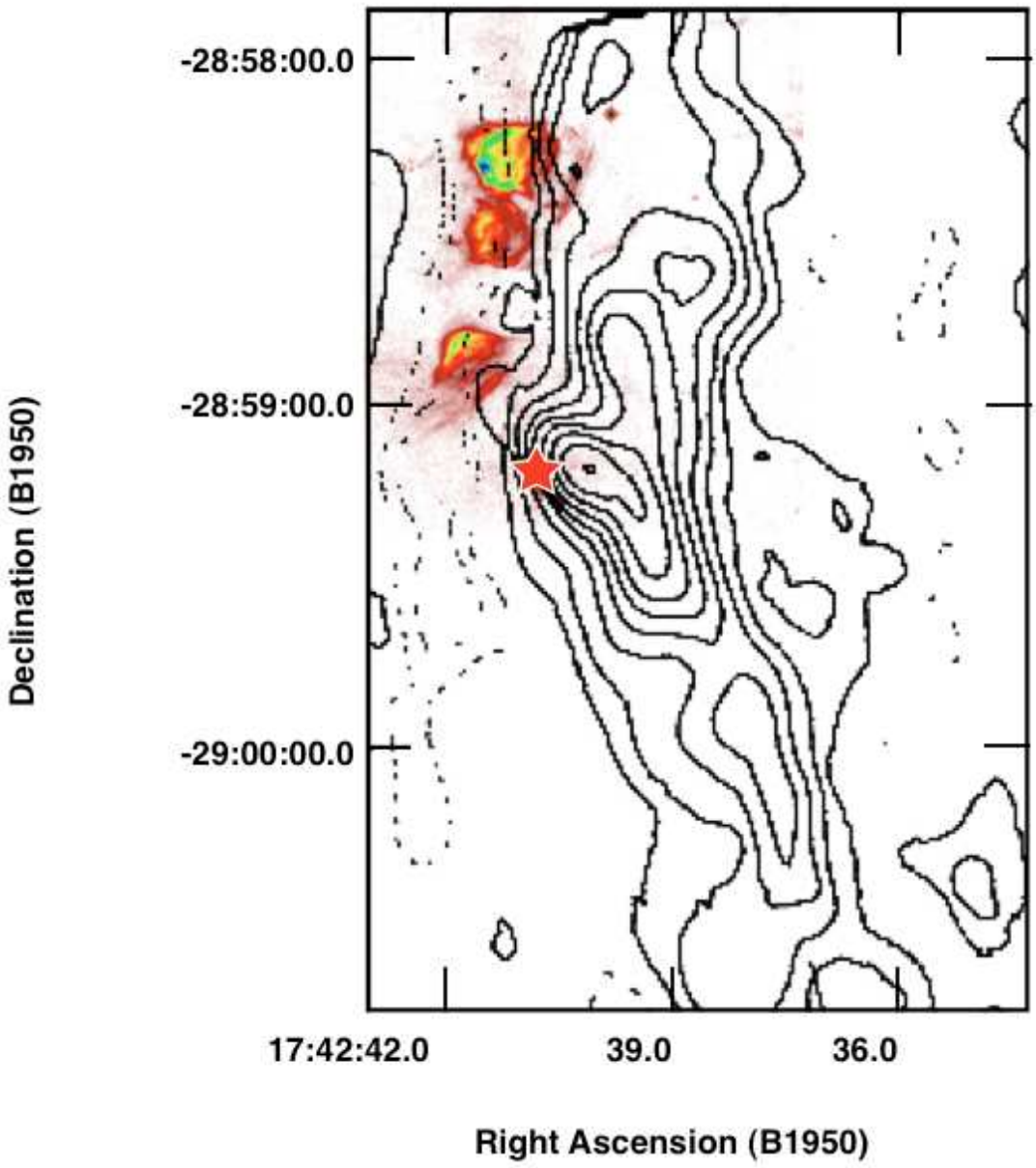

Figure 2.9: Superposition of Ammonia (1,1) contours (Coil & Ho 2000, magnification of their Figure 6, Left) and Pα emission, showing the apparent association of region D (indicated with a star) with a dense core in the western ridge of M-0.02-0.07. Region D appears to be immediately adjacent to a steep gradient in the ammonia emission from the core.

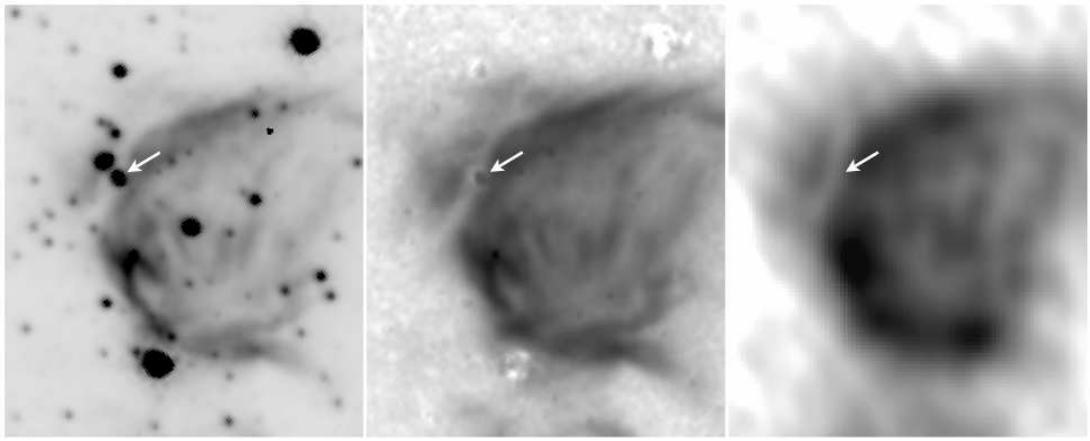

Figure 2.10: A comparison of the emission toward the northeast extension of region A from the F187N filter, the pure Pα line image, and the 8.4 GHz radio image, from left to right. An emission-free lane is seen separating the main shell of region A from a slight extension at the 10 o'clock position. Like region D, there is a star apparently located slightly offset from the center of this lane (its location indicated in all images with an arrow). The apparent Pα excess at the position of this star is at has the same intensity as the emission from the surrounding nebula, and is likely an artifact due to the difficulty of subtracting stellar emission in the presence of a diffuse background. No counterpart to the apparent Pα excess at the position of this star is seen in the radio image. In images of Cotera et al. (2000), this star appears highly reddened, but its H-K' color is not given.

detection of weak He I and Br γ line emission. With the higher spatial resolution of the Pα data, we do not resolve significant line emission coming from the stellar point source (see Figure 2.6, Left). It is likely that the spectrum of Cotera et al. (1999b) resulted from a superposition of nebular emission lines from the UCHII region and the stellar continuum from this star.

The strongest evidence for a disk in region D from our data is the apparent void of radio and Pα emission between the the two peaks of region D , a dark lane running north-south through its center in both radio and Pα images. We suggest that this dark lane represents a region of largely neutral gas which has been shielded from the ionizing radiation of the central star by a compact disk (see Figure 2.8). Absent a disk, one might expect to see a more continuous spherical shell of ionization around the star. Although our extinction map does not clearly identify a peak of extinction at or around the ionizing star corresponding to this disk, this is not inconsistent with the presence of a dense disk. We can explain the lack of significant extinction detected toward this disk if the disk is small, and thus unresolved by our observations, or if the disk does not occult significant ionized emission along the line of sight, in which case we would have no information on the extinction toward the neutral gas, including the disk, along the line of sight of the disk. An example sightline for which this would be the case is shown in Figure 2.8.

We concur with Yusef-Zadeh et al. (2010) that the asymmetry of the emission from region D, with the blueshifted emission arising much closer to the central star than the redshifted emission, is almost certainly due to the HII region being embedded in a density gradient (see Figure 2.8). The extinction measured toward the eastern peak of D is slightly lower than that measured toward the western peak, and the Pα emission falls off much more steeply on the western edge of

D, suggesting a more steeply increasing column density in that direction. This increase in column density corresponds to the location of the dense western ridge of the M-0.02-0.07 cloud, located between the HII regions and Sgr A East (see Figure 2.3). Indeed, a comparison of the position of region D to higher resolution observations of dense gas traced by ammonia (1,1) emission in the western ridge (Coil & Ho 2000) shows that region D appears to lie on the eastern edge of a dense core (see Figure 2.9). Based on its extinction, region D is likely embedded in or behind this core.

A structure reminiscent of region D is also seen on the northeast edge of region A (Figure 2.10). A protrusion of emission is separated from the main shell of region A by another apparently dark lane, exhibiting a lack of emission in both Pα and 8.4 GHz images. This protrusion of emission is also resolved in the Ne II spectra of Yusef-Zadeh et al. (2010), but appears not to have the same kinematic structure as region D: emission on each side of the dark lane appears to have the same radial velocity. It is still possible that this structure, like region D, is a young massive disk, with the dark lane corresponding to the shadow of the disk, but either it has no collimated outflows, or we are observing this system closer to edge-on. Like region D, a star is visible slightly offset from the center of the dark lane. The star is visible in near-infrared images of Cotera et al. (2000) and appears similar in color to the star in region D, though no value for its H-K' color is reported.

To verify the presence of a disk in regions A and D, one could observe these regions at high spatial-resolution in the millimeter and radio regimes to search for warm dust or molecular gas in the disk, or even free-free emission from the surface of the disk. Higher resolution spectra of the stars in regions A and D could also help determine whether their properties are consistent with extremely

young, massive stars.

2.5.3 The Ionized Ridges of Region A

To the southwest of region A lie three roughly linear ionized ridges with increasing separation from the opening of the HII region (Figures 2.2, 2.11). While it is possible that these ridges could be pre-existing structures that are ionized as the central star of region A passes by, their unusual alignment with each other and with the opening of region A suggests a closer relationship. We interpret them as most likely to be the interaction between an ionized flow from inside region A and the diffuse surrounding ISM. These limb-brightened shells would propagate outward at the sound speed in the HII region. If, as suggested by Yusef-Zadeh et al. (2010), region A is moving both to the east and toward us, then we should be able to see a difference in velocity between the radial velocities of region A and the expanding shells. However, the magnitude of such a velocity difference would be on the order of the sound speed ($\sim$ 10 km s^{-1}) projected along the line of sight, and for motion 20 to 30 degrees out of the plane of the sky would correspond to a velocity difference of only 3 to 5 km s^{-1}. In Figure 8 (Left) of Yusef-Zadeh et al. (2010), two of the ridges are seen to have radial velocities around $\sim$ 50 km s^{-1}, similar to the mean radial velocity of the HII region, and of the ambient medium of the M-0.02-0.07 cloud. The data show no evidence for a velocity difference between region A and the ridges of greater than 5 km s^{-1}, and detection of a smaller velocity shift would be limited by the large width of the lines. It is possible that future observations with high S/N could sufficiently resolve the lines with sufficient accuracy to search for shifts on the order of several km s^{-1} in their centroids.

Alternatively, it is possible these structures could be due to an instability

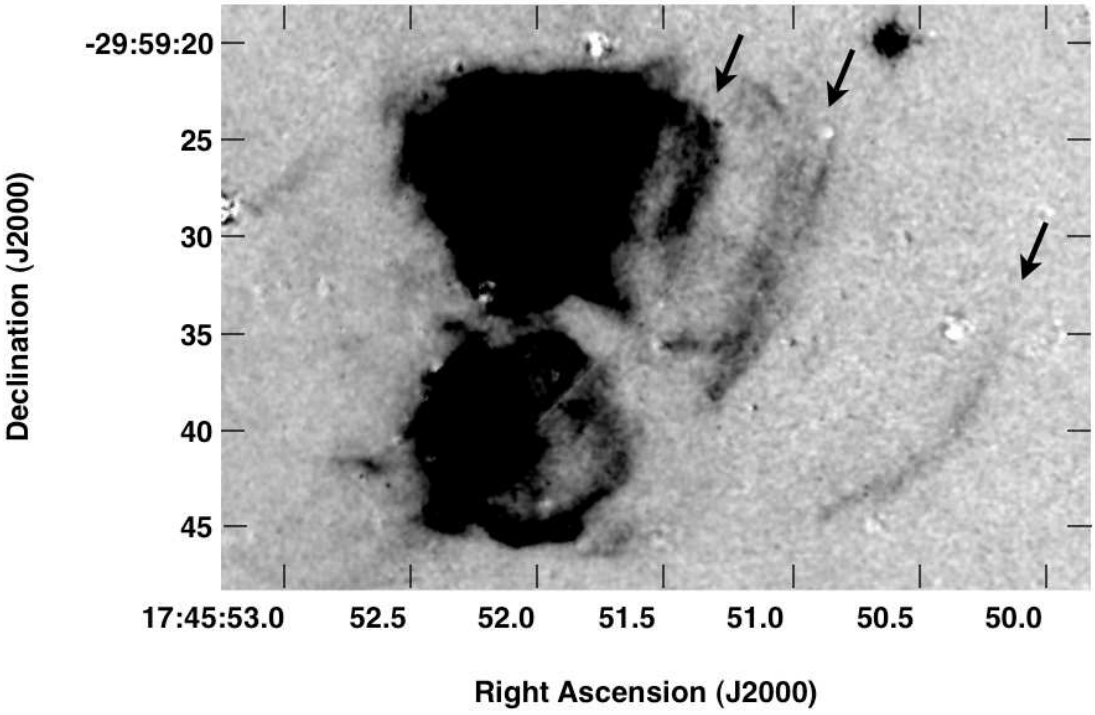

Figure 2.11: A magnification of the ionized ridges lying to the southwest of region A. The faint line that intersects region B at a 45 degree angle is an artifact from the edge of one of the mosaicked subimages used to construct this map.

first proposed for the case of old planetary nebulae passing through a magnetized ISM, essentially a magnetic Rayleigh-Taylor instability (Dgani & Soker 1998; Soker & Dgani 1997). As post-shock material cools isothermally, it is subject to a magnetic Rayleigh-Taylor instability, stabilized in the direction perpendicular to the magnetic field, leading to a density pattern of ridges in the ISM behind the HII region, parallel to the ambient magnetic field. Although the inferred velocity of the central star of region A (30 km s^{-1}, Yusef-Zadeh et al. 2010) is slower than the minimum estimated by Soker & Dgani (1997) for significant instabilities to develop (40 km s^{-1}), the warm, dense ISM of the GC combined with the likely presence of a strong pervasive magnetic field (50 - 100 μGauss, Crocker et al. 2010), are both factors that should be conducive to the development of such instabilities. However, it is unclear why similar instabilities would not also be seen to be associated with regions B and C, which are believed to be have the same stellar wind bowshock kinematics (Yusef-Zadeh et al. 2010).

More sensitive observations of the faint ionized gas in these ridgelike features are necessary to determine whether the ridges of region A have kinematics consistent with shells propagating outward at the sound speed. In addition, if the ionizing sources for these HII regions were identified, measuring the radial velocities of the stars could test the possibility that the ridges are due to a magnetohydrodynamic instability.

2.5.4 Locating the HII Regions

Measurements of consistent radial velocities for the G-0.02-0.07 HII region complex and the M-0.02-0.07 cloud (S92) have established that the two structures are associated. However, it is less clear where in the cloud the HII regions lie. From their CS maps of dense gas in the cloud, S92 divide it into two main struc-

tures: an eastern quiescent lobe, lying predominantly to the north of G-0.02-0.07 (the eastern region of 450 μm emission in Figure 2.3), and a western dense ridge (Figures 2.3 and 2.9) of gas showing evidence for strong large scale shocks traced by vibrationally excited H_2 (Yusef-Zadeh et al. 2001) and 1720 MHz OH masers (Yusef-Zadeh et al. 1996) resulting from an apparent interaction with the supernova remnant Sgr A East (Figure 2.3, in green). The HII regions appear to lie between the two cloud structures, but their arrangement follows the western ridge, and the eastern periphery of Sgr A East.

The Pα images and extinction maps presented in this paper provide some additional insight into the location of the individual HII regions in G-0.02-0.07 with respect to Sgr A East and the two components of M-0.02-0.07. Previous extinction measurements for region A indicated that it was in front of M-0.02-0.07; however, as seen in Figures 2.3 and 2.9, the main body of this HII region and the dense gas in this cloud do not significantly overlap, which suggests the extinction for the bulk of this region would be low even if behind the western ridge. Our extinction map, which provides extinction values for the first time for the faint ionized ridges to the west of region A, shows the extinctions of those ionized ridges to be consistent with that for the rest of the region A, and does not show any evidence for an extinction gradient across the region, as might be expected if the ionized ridges were behind the western ridge of M-0.02-0.07. Assuming these ridges are associated with region A, as their morphology suggests, this places region A in front of the western ridge of M-0.02-0.07. As observations of OH absorption indicate that the western ridge of M-0.02-0.07 lies in from of Sgr A East (Karlsson et al. 2003), region A must also then lie in front of Sgr A East.

Given the high extinction toward region D, and radio properties and compact

morphology which are all consistent with a young UCHII region still embedded in its natal cloud, we believe that region D is located in the western ridge of M-0.02-0.07. This is consistent with the previously noted apparent close association between region D and a peak in ammonia (1,1) emission in the ridge. If region D is embedded in the western ridge, we would expect to see OH absorption from the cloud against the continuum emission from this region, as is seen where M-0.02-0.07 lies in front of Sgr A East (Karlsson et al. 2003). Although Karlsson et al. (2003) report no absorption for any of the G-0.02-0.07 regions, a new analysis of the data presented in Karlsson et al. (2003) combined with additional, lower-resolution data, which are more sensitive to the extended structure of the HII regions, does show absorption toward region D (R. Karlsson, Private communication). The absorption is strongest in velocities of 32.2 km s^{-1} and 41.0 km s^{-1}, which correspond to the western peak (D2), and weaker but present at velocities of 49.8 km s^{-1} and 58.6 km s^{-1}, corresponding to the eastern peak (D1). The detection of OH absorption toward region D is then consistent with our measurement of slightly lower extinction toward D1, and consistent with our finding that region D is embedded in or behind M-0.02-0.07.

2.6 Summary

We have presented new high-resolution maps of the G-0.02-0.07 HII regions in the Pα line and have produced extinction maps of these regions using a combination of the Pα maps and archival radio data. The morphologies of these regions and the extinction we measure toward them confirm that they are located in front of, but near to, the M-0.02-0.07 cloud, with region D likely embedded in the dense western ridge of this cloud. In addition, we find that the uniform extinction across region A requires it to be entirely in front of the dense western ridge of

the M-0.02-0.07 cloud.

We interpret the series of ionized ridges located to the west of region A as most likely to be a succession of limb-brightened shells resulting from shocks produced as a thermal wind from the HII region interacts with diffuse, ambient gas .

Region D is interpreted as containing a small, opaque disk which shields the neutral gas from ionization by the central star, forming a dark lane which appears to bisect the HII region in both radio and Pα images. We explain the lack of a measured extinction maximum in this dark lane as being most likely due to the absence of ionized gas along the line of sight of this dark lane.

Although the current star formation of the G-0.02-0.07 HII regions was not triggered by the energetic Sgr A East supernova event, the star formation in this cloud is some of the most recent which has been identified in the central 10 parsecs. The search for recent star formation even closer to the black hole continues because star formation in this environment (though it is extreme) should be occurring, based on the population of young ($\sim$ a few Myr) stars in the central 0.5 pc (Lu et al. 2013). The innermost of these stars, the 'S' stars, lie in the central 0.1 pc, approaching the black hole as closely as a few hundred AU (e.g., Genzel et al. 2010). Currently, the best way to explain stars this young this close to the black hole appears to be for these stars to form in situ, in a dense gas disk a few tenths of parsecs from the black hole (Nayakshin & Sunyaev 2005; Nayakshin et al. 2007; Perets et al. 2009). As I discuss in the next Chapter, although there is currently no gas disk at these radii, however there is a disk of molecular gas in the central 2 parsecs, which may have sufficient densities to be tidally bound against disruption from the black hole. Could there be ongoing star formation closer to the black hole? What would this star formation look like under such extreme conditions?

CHAPTER 3

The Excitation of HCN and HCO^+ in the Galactic Center Circumnuclear Disk

Understanding the density distribution of gas in the Central Molecular zone of the Galaxy is critical to understand the evolution of these largely quiescent gas clouds, to determine whether they are strongly disrupted by tidal shear, or whether there is gas with sufficient density that it should be actively forming stars. Nowhere is the gas density more critical to its fate than in the central parsecs of the Galaxy. Here, molecular gas approaches the zone of influence of the central supermassive black hole. If it is sufficiently dense, it may be able to form stars in this extremely hostile environment, adding to generations of previous star formation in the Nuclear cluster. However, if the gas is less dense, it will be sheared, possibly losing enough velocity to plunge closer to the black hole. Will the gas fuel the black hole, form stars, or be ejected entirely? The fraction of gas succumbing to each fate is a fundamental question of galaxy evolution which the central regions of our own Galaxy offer the opportunity to investigate by probing the initial conditions of this gas in detail.

In this chapter, I present new observations of HCN and HCO^+ in the circumnuclear disk (CND) of the Galaxy, obtained with the APEX telescope. Emission from this cloud is mapped in rotational lines of HCN $J = 3$–2, 4–3, and 8–7, as well as HCO^+ $J = 3$–2, 4–3, and 9–8. Spectra of $H^{13}CN$ $J = 3$–2 and 4–3,

and $H^{13}CO^+$ J = 3–2 and 4–3 are also presented toward four positions in the CND. Using the intensities of all of these lines, an excitation analysis for each molecule is conducted toward these four positions using the non-LTE radiative transfer code RADEX. The HCN line intensities in the Northern part of the CND yield log densities (cm^{-3}) of $5.6^{+0.6}_{-0.6}$, consistent with those measured with HCO^+ as well as densities recently reported for the Northern part of the CND from an excitation analysis of highly-excited lines of CO. These densities are too low for the gas to be tidally stable. The HCN line intensities in the southern emission peak of the CND yield log densities of $6.5^{+0.5}_{-0.7}$, higher than densities determined for this part of the CND with CO (although the densities measured with HCO^+, log n = $5.6^{+0.2}_{-0.2}$, are more consistent with the CO-derived densities). I also investigate whether the higher densities inferred from HCN are affected by the mid-infrared radiative excitation of this molecule through its 14 μm rovibrational transitions. I find that radiative excitation is important for at least one clump in the CND, where the J = 4–3, v_2 = 1 vibrationally-excited transition of HCN is additionally detected, requiring dust temperatures of $\gtrsim$ 150 K. If this hot dust is present throughout the CND, its effect would be to lower the inferred densities by a factor of up to 5, which would bring the HCN-derived densities for the southern emission peak of the CND into agreement with those measured using HCO^+ and CO. However, as the presence of a hot dust component in the CND has not been observationally constrained, the possibility that the mid-infrared excitation is only important in the localized environment of this clump, and that HCN preferentially traces higher-density CND gas, cannot be ruled out. Additional sensitive, high-resolution submillimeter observations, as well as possibly mid-infrared observations are necessary to assess the importance of the radiative excitation of HCN in this environment.

The Circumnuclear Disk (CND) is a ring of gas and dust around the central

supermassive black hole (SMBH), with an inner radius of $\sim$ 1.5 pc and an inclination of 70 degrees from the Galactic plane (Güsten et al. 1987; Jackson et al. 1993). The CND has been studied for decades in a range of molecular transitions; Amo-Baladrón et al. (2011) provide a comprehensive list of molecular lines studied in the CND to date. The molecular gas temperatures determined from observations of CO range from 50 - 400 K (Harris et al. 1985; Lugten et al. 1987; Bradford et al. 2005; Oka et al. 2011). Atomic gas temperatures measured at the inner edge of the CND are comparable, ranging from 200 to 350 K (Genzel et al. 1985; Jackson et al. 1993). Measured dust temperatures are much lower, ranging from 20 to 90K (Becklin et al. 1982; Mezger et al. 1989; Etxaluze et al. 2011; Molinari et al. 2011, Lau et al. 2013). Kinematic studies of the CND (Jackson et al. 1993; Martín et al. 2012) show that the motion of the bulk of its gas is consistent with orbiting filaments in several planes.

The CND is the closest large molecular structure to the SMBH (mass $\sim$ 4.5×10^6 $M_\odot$; Ghez et al. 2008; Gillessen et al. 2009a; Genzel et al. 2010), and thus should be subject to strong tidal shearing forces. If the CND is to be stable against tidal shearing, it must have an extremely high density: the fluid Roche approximation for gas at a radius of 2 pc from the SMBH states that gas clumps will be unstable for densities less than a few 10^7 cm^{-3}. Observations of molecular clumps in the CND with lines of HCN and HCO^+ have led to virial density estimates for individual clumps that range from 10^7 to 10^8 cm^{-3} (Shukla et al. 2004; Christopher et al. 2005; Montero-Castaño et al. 2009). However, the high densities derived in this way are in disagreement with lower densities recently inferred from the dust emission characteristics (Etxaluze et al. 2011) and from an excitation analysis using the CO molecule (Requena-Torres et al. 2012, hereafter RT12).

Both Christopher et al. and Montero-Castaño et al. also estimate a total mass for the CND ($\sim 10^6$ $M_\odot$), by assuming virialization, which greatly exceeds previous mass estimates of a few $\times 10^4$ $M_\odot$, based on CO excitation and dust emission (Harris et al. 1985; Genzel et al. 1985; Lugten et al. 1987; Mezger et al. 1989). More recent estimates of the mass from the FIR and submillimeter dust emission also favor a lower mass: Etxaluze et al. (2011) estimate a mass of 5×10^4 $M_\odot$, and RT12 estimate a mass of 10^3 - 10^4 $M_\odot$. Lau et al. (2013) measure an even lower mass, $\sim$ 600 $M_\odot$, just for the hottest inner material of the CND. Currently then, it is not clear whether the discrepancy in derived CND mass and density is due to the assumption of virialization, or due to the different tracers used in each analysis (HCN and HCO^+, versus CO and dust). Verifying the source of the discrepancy is important for constraining the size of the molecular gas reservoir in the central two parsecs of the galaxy, and determining whether the gas densities are consistent with recent suggestions of star formation in the CND (Yusef-Zadeh et al. 2008), given the strong tidal forces which are present in this region.

To investigate the effect of the choice of molecular tracer on the derived properties of the CND, we have conducted an excitation analysis using the J = 3–2, 4–3 and 8–7 transitions of HCN and the J = 3–2, 4–3, and 9–8 transitions of HCO^+ from single-dish observations with the Atacama Pathfinder Experiment telescope (APEX[1]). These lines should be particularly sensitive to the presence of dense gas, having critical densities of $10^6 - 10^9$ cm^{-3}, and spanning a range of energies from 25 K to 190 K above the ground state. Single-dish observations also have the advantage that they are not subject to the filtering out of spatially-

[1]This publication is based on data acquired with the Atacama Pathfinder EXperiment. APEX is a collaboration between the Max-Planck-Institut für Radioastronomie, the European Southern Observatory, and the Onsala Space Observatory.

extended flux, which may have affected previous interferometric studies. This is the first excitation analysis of the CND using these dense gas tracers, and the first detection of the highly excited HCN $J = 8$–7 and HCO^+ $J = 9$–8 lines in the CND. In Section 3.1, we describe the APEX observations. In Section 3.2, we present velocity-integrated maps and spectra of all of the observed transitions. In Sections 3.3 and 3.4 we discuss the excitation analysis and our derived constraints on the temperature and density of the CND. Finally we conclude in Section 3.6 with a discussion of the excitation mechanisms for HCN in the CND, and an assessment of the validity of the assumption that all CND gas clumps are virialized. We also comment on whether the chemistry in the CND is likely to be affected by X-rays or cosmic rays.

3.1 Observations and Calibration

All of the data used for the analysis in this paper were obtained with the APEX telescope (Güsten et al. 2006), a single 12 meter modified ALMA prototype antenna located at an elevation of 5106 m on the Chajnantor plain in Chile. Data were obtained over a multiple day run in July 2010. Conditions for the run were excellent, with a precipitable water vapor overburden of less than 0.5 mm. Additional observations of $H^{13}CN$ $J = 4$–3 and $H^{13}CO^+$ $J = 4$–3 were obtained in November 2010 toward the northern emission peak of the CND. Observations of $H^{13}CN$ $J = 3$–2, $HC^{15}N$ $J = 3$–2, $H^{13}CN$ $J = 4$–3 and $HC^{15}N$ $J = 4$–3 were obtained in April 2012 toward the southern emission peak of the CND and an additional pointing toward the Southwest component of this peak. Properties of all of the observed transitions are listed in Table 3.1.

Table 3.1: Properties of the Observed Transitions

Molecule	**Transition**	**Frequency**	**Upper State Energy**	**Critical Density**[1]	**APEX beam**
	J–J-1, v_2	[GHz]	[K]	[cm^{-3}]	FWHM
HCN	3–2	265.88618	25.5	5.2×10^{7}	23.6″
	4–3	354.50548	42.5	1.1×10^{8}	17.7″
	4–3, 1f	356.25561	1067.1	[2]3.1×10^{11}	17.6″
	8–7	708.87721	153.1	8.7×10^{8}	8.9″
$HC^{13}N$	3–2	259.01182	24.9	4.8×10^{7}	24.3″
	4–3	345.33976	41.4	1.1×10^{8}	18.2″
HCO^+	3–2	267.55753	25.7	3.5×10^{6}	23.5″
	4–3	356.73413	42.8	8.2×10^{6}	17.6″
	9–8	802.45822	192.6	1.0×10^{8}	7.8″
$H^{13}CO^+$	3–2	260.25534	25.0	3.1×10^{6}	24.2″
	4–3	346.99834	41.6	7.3×10^{6}	18.1″

3.1.1 260 GHz observations

Using the APEX1 facility receivers, we simultaneously observed the J = 3–2 transition of HCN and the J = 3–2 transition of HCO^+ over a rectangular field covering the CND. Our maps were centered on the position of Sgr A*, at RA=17h 45m 39.92s, Dec=-29°00′28.1″ (J2000). In addition, we made pointed observations toward three positions in the CND in the J = 3–2 transitions of the isotopologues $H^{13}CN$ and $H^{13}CO^+$. The GILDAS[2] software CLASS90 was used to reduce the calibrated data. We fit and removed a first-order baseline from all of the spectra, and boxcar-smoothed the spectra to a resolution of 5.2 km s^{-1}. A correction for a main-beam efficiency of 0.71 for the 2010 data and 0.75 for the 2012 data was also applied. The data were then gridded onto rectangular maps of $\sim 5.8 \times 2.3'$ extent (13 × 7 parsecs at the assumed 8.4 kpc distance of the Galactic center; Ghez et al. 2008; Gillessen et al. 2009a), with a pixel size of 11.8″. The spatial resolution of the maps varies slightly for each line, but at these frequencies is ∼24 ″. The estimated calibration uncertainty of these data is 10%.

3.1.2 350 GHz observations

Using the FLASH receiver (Heyminck et al. 2006), we also simultaneously mapped the J = 4–3 lines of HCN and HCO^+ over a field centered on Sgr A*. We additionally made pointed observations toward three positions in the CND in the J = 4–3 transitions of the isotopologues $H^{13}CN$ and $H^{13}CO^+$. All of these data were processed in the same manner as the 260 GHz observations, with the main-beam efficiency at the frequency of this line being 0.67 for the 2010 data and 0.73 for the 2012 data. The data were then gridded onto rectangular maps

[2]http://www.iram.fr/IRAMFR/GILDAS

of $\sim 4.2' \times 2.3'$, with a pixel size of $8.9''$. The angular resolution of the maps at these frequencies is $\sim 18''$. The estimated calibration uncertainty of these data is 10%.

3.1.3 700-800 GHz observations with CHAMP$^+$

Using the CHAMP$^+$ heterodyne array receiver (Güsten et al. 2008; Kasemann et al. 2006), we simultaneously observed the HCN $J = 8$–7 transition and the HCO$^+$ $J = 9$–8 (The HCO$^+$ $J = 8$–7 transition at 713 GHz is not observable from the ground, due to low atmospheric transmission at that frequency). Emission from both of these lines was mapped around two positions in the CND, toward the northern and southern emission peaks. These data were processed in the same manner as the 260 and 350 GHz observations. The HCN 8–7 data were then gridded onto rectangular maps of $\sim 1.5' \times 1.5'$ covering the southern emission peak of the CND and $1.3' \times 0.7'$ covering the northern emission peak, with pixel sizes of $5''$. The angular resolution for HCN 8–7 is $9''$. The HCO$^+$ 9–8 data were also gridded onto rectangular maps of $\sim 1.2' \times 1.2'$ (for the southern emission peak) and $1.0' \times 0.5'$ (for the northern emission peak), with pixel sizes of $5''$. A correction for a main-beam efficiency of 0.40 was applied, with the estimated calibration uncertainty for both lines being 20%.

3.2 Results

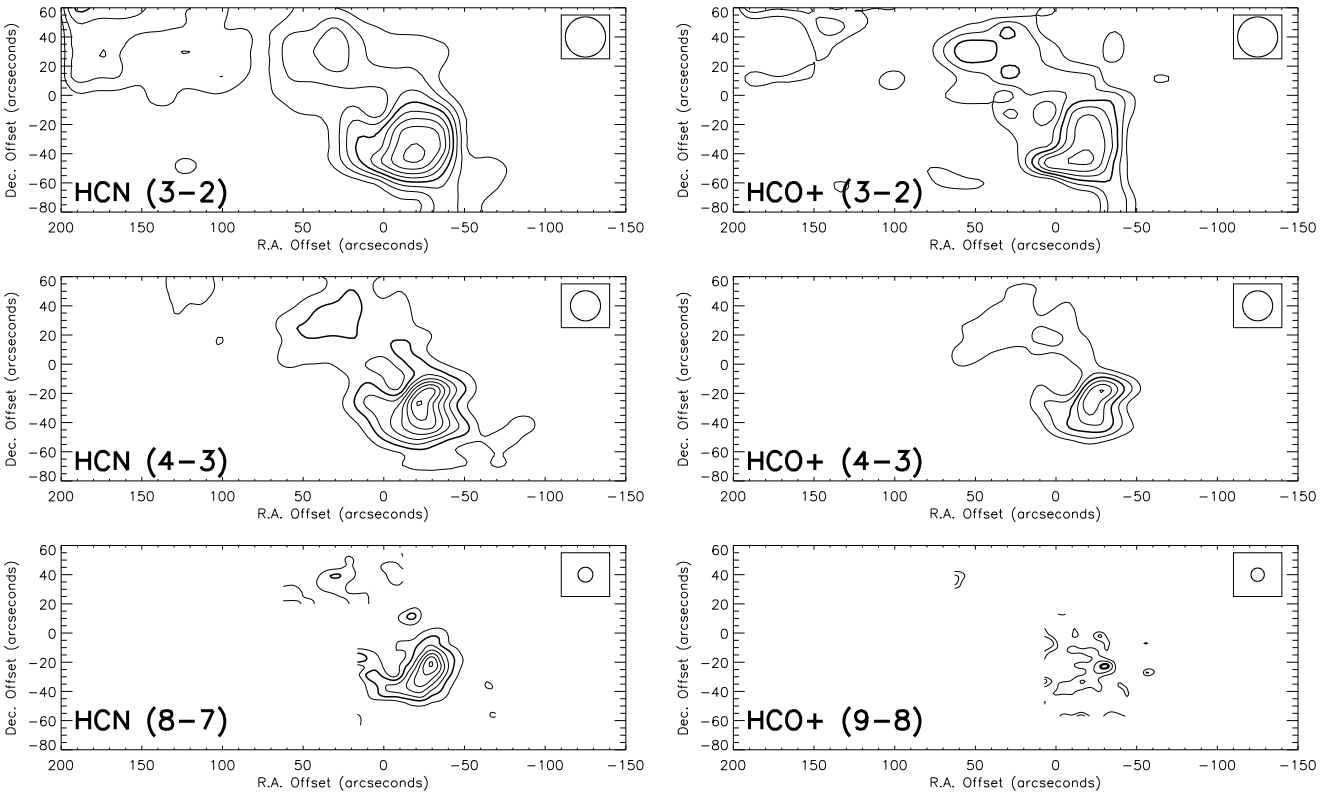

Figure 3.1: Contour maps of spatially unconvolved main beam brightness temperature integrated from -200 to 200 km s^{-1} for the observed lines of HCN and HCO^+. Contours are linearly spaced. Top Left: HCN 3–2, contours from 750 to 2650 K km s^{-1}. Top Right: HCO^+ 3–2, contours from 575 to 1400 K km s^{-1}. Middle Right: HCN 4–3, contours from 600 to 2620 K km s^{-1}. Middle Left: HCO^+ 4–3, contours from 575 to 1400 K km s^{-1}. Bottom Left: HCN 8–7, contours from 150 to 810 K km s^{-1}. Bottom Right: HCO^+ 9–8, contours from 110 to 250 K km s^{-1}. The beam sizes are given in Table 3.1

Contour maps of HCN and HCO^+ integrated intensity are shown in Figure 3.1. For all the mapped lines, the strongest emission is seen toward the southern emission peak of the CND, consistent with the HCN 4–3 and CS 7–6 maps of Montero-Castaño et al. (2009). Emission from M-0.02-0.07, the 50 km s^{-1} cloud, can be seen in the northeast corner of the HCN and HCO^+ 3–2 and 4–3 maps. The HCN and HCO^+ maps exhibit largely the same morphology, though the HCO^+ intensity in a given transition is weaker than HCN in the same transition by a factor of $\sim$ 1.5-2.

3.2.1 Pointed isotopologue observations

Pointed observations of the ^{13}C isotopologues of HCN were made toward four positions: the southern emission peak (RA, Dec offset[3] = -20″, -30″), the southwest portion of the southern emission peak (-30″, -20″), the northern emission peak (+25″, +40″), and the western edge of the CND (-20″, +0″) . Observations of $H^{13}CO^+$ were made toward three of these positions (North, South, and West). The locations of all four pointings are shown in figure 3.2.

[3]All offset positions are given in arcseconds with respect to the position of Sgr A*, which we adopt as (17h 45m 39.92s, -29°00'28.1")

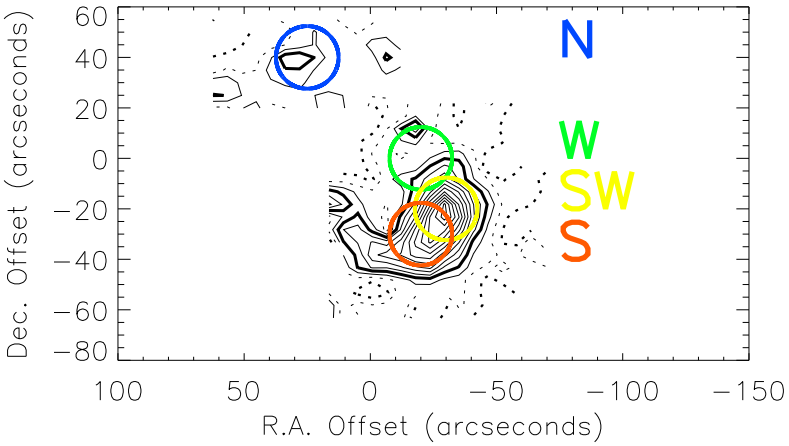

Figure 3.2: Contour map of unconvolved HCN 8–7 emission in the CND integrated over a velocity range from -200 km s^{-1} to 200 km s^{-1}. Contours are linearly spaced, from 0 to 810 K km s^{-1}. The circles are the size of the $H^{13}CN$ 3–2 beam and show positions where spectra of the ^{13}C isotopologues were obtained.

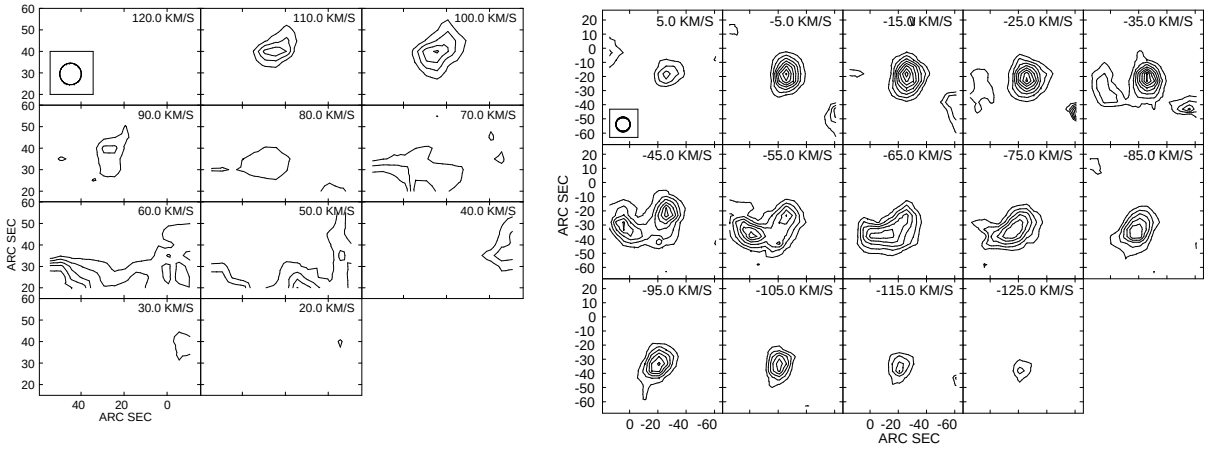

Figure 3.3: Channel maps of unconvolved HCN 8–7 emission toward the northern (Left) and southern (Right) emission peaks of the CND. Contours are linearly spaced by 0.21 K, from 0.43 to 2.13 K. Data are binned into 5 km s^{-1} channels, with every other channel pictured here

These pointings cover four (or possibly five) distinct features in position and velocity space (listed in Table 3.2), the properties of which will be the focus of this paper. We identify these features in our HCN 8–7 cubes, as they have the highest spatial resolution. Channel maps of these cubes toward the northern and southern emission peaks of the CND are shown in Figure 3.3. The locations of the HCN 8–7 peak emission deviate slightly from the positions of the pointed isotopologue observations, but all features fall in the beam of the corresponding isotopologue pointings. Compared to $H^{13}CN$, the $H^{13}CO^+$ intensities for the same J-transition are typically a factor of 2.5-5 times weaker. The relative intensities of HCN and HCO^+ are discussed further in Section 3.6.4.

Feature SW (v = -5 to -25 km s^{-1}, offset = -30″, -20″) is the source of the strongest HCN 8–7 emission. It also is the location of the strongest $H^{13}CN$ 4–3 emission. Emission at the velocities of this feature is seen in both the Southwest and South pointings; we refer to emission at these velocities detected in the South pointing as feature S2 (v = -5 to -25 km s^{-1}, offset = -20″, -30″), though it is possible that S2 and SW are parts of the same, extended source. The S1 feature (v= -90 to -120 km s^{-1}, offset = -20″, -30″) is slightly fainter than SW or S2 in HCN 8–7, but is the location of the peak HCN 4–3 emission. Feature N (v = 90 to 115 km s^{-1}, offset = +25″, +40″) is the faintest of these four (or five) features. Feature W (v = 35 to 55 km s^{-1}, offset = -20″, +0″) is the location of very strong HCN 3–2 emission. The velocity range for each of the features is shown shaded in grey in Figures 3.4 and 3.5.

Although we observed both the $HC^{15}N$ 3–2 and 4–3 lines toward the Southern pointing (corresponding to features S1 and S2), we do not detect either line. In both cases, the observations are somewhat confused by overlap with a nearby strong line. However, we report upper limits for the peak brightness temperatures

of these lines of 0.05 K for $HC^{15}N$ 3–2 and 0.03 K for $HC^{15}N$ 4–3.

Table 3.2: Clumps

Name	**Offset (RA, Dec)**	**Velocity**	**Alternate ID #1**[1]	**Alternate ID #2**[2]
N	(+25″,+40″)	90 to 110 km s^{-1}	D	A
S1	(–20″, –30″)	-115 to -95 km s^{-1}	O	Q
S2	(–20″, –30″)	-25 to -5 km s^{-1}	–	–
SW	(–30″, –20″)	-25 to -5 km s^{-1}	P	N
W	(–20″, +0″)	35 to 55 km s^{-1}	T	K

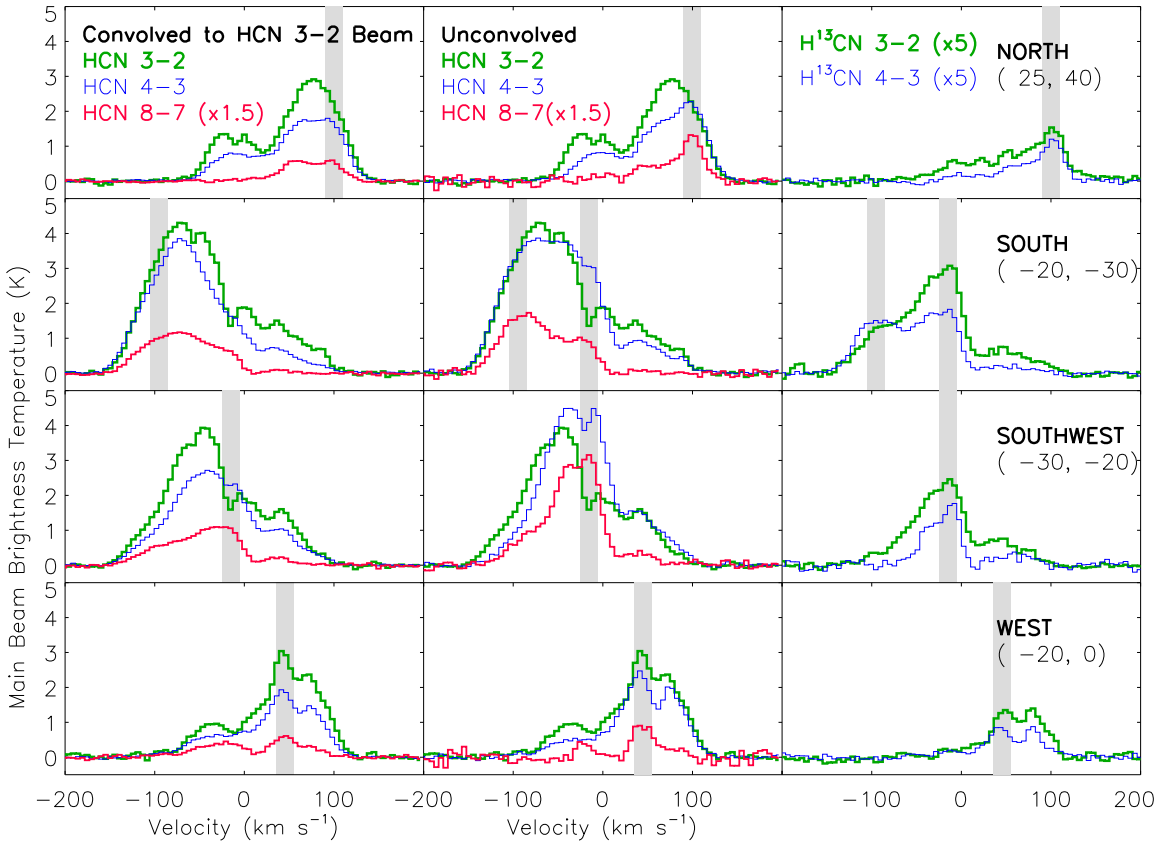

Figure 3.4: Line profiles of HCN (Left) and $H^{13}CN$ (Right) toward four positions in CND, from the top: North, South, Southwest, and West. Spectra have been extracted from maps convolved to the beam size of the 3–2 observations (23.6"). The grey-shaded regions represent the narrow velocity ranges corresponding to the individual features listed in Table 3.2.

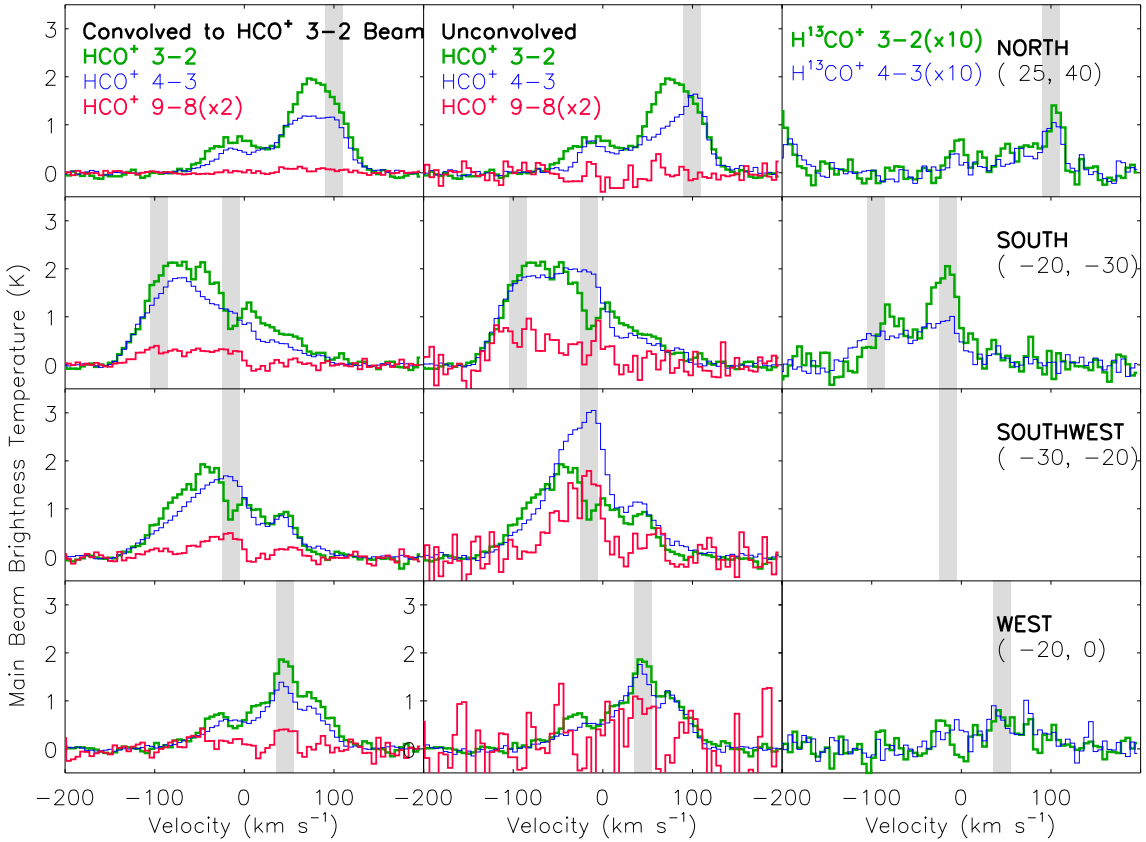

Figure 3.5: Line profiles of HCO^+ (Left) and $H^{13}CO^+$ (Right) toward four positions in CND, from the top: North, South, Southwest, and West. Spectra have been extracted from maps convolved to the beam size of the 3–2 observations.

3.2.2 Comparison to other studies

Interferometric maps of the CND with resolutions of a few arcseconds in lines of HCN 1–0 and 4–3, (Christopher et al. 2005 and Montero-Castaño et al. 2009, respectively), resolve the CND into numerous clumps. Our spectra (Figures 3.4 and 3.5) allow us to associate the features which we can resolve in velocity space using our single-dish data with spatially-resolved, interferometrically-detected counterparts. The isotopologue spectra are most useful for this purpose, as they trace the highest column-density gas. This gas generally corresponds well to that detected by the interferometric data, which are less sensitive to faint and extended structure.

Our feature N corresponds to clump A from Montero-Castaño et al. (see their Figure 4). Gas from this clump peaks at a central velocity of +100 km s^{-1}. Our feature S corresponds to their clump Q, which peaks at a central velocity of -110 km s^{-1} and is one of the brightest sources of HCN 4–3 emission detected by Montero-Castaño et al. The observed profiles of HCN 8–7 and the isotopologues (Figure 3.4) toward our feature W are most similar to the spectrum of clump K from Montero-Castaño et al. Clump H of Montero-Castaño et al. also lies on the edge of the West pointing and can be seen in the HCN 8–7 maps (Figures 3.1 and 3.2), however the line profile of clump H in Montero-Castaño et al. (which is very narrow and peaks at 60 km s^{-1}), does not match our observed isotopologue profiles. This is likely because clump H lies at the very edge of the beam of the West isotopologue pointing, and emission from this source is not well sampled.

Our feature SW corresponds to clump N from Montero-Castaño et al. Their line profile for clump N is double-peaked, with a dip at a velocity of -20 km s^{-1} that Montero-Castaño et al. ascribe to missing short baselines. We see the same dip in our HCN and HCO^+ 3–2 and 4–3 line profiles (Figures 3.4 and 3.5,

third row), and significantly, the line profiles of $H^{13}CN$ and $H^{13}CO^+$ peak at the central velocity of the dip, indicating the main lines suffer from self-absorption. As the line profile of HCN 8–7 peaks at the same velocity, this self-absorption is likely related to the dense CND gas, and not to foreground gas along the line of sight. Absorption at this velocity can also be seen in the CS 7–6 spectrum of Montero-Castaño et al. for this clump, as well as in spectra of CO 6–5 and 7–6 from RT12. Absorption at the same velocity is also seen in our spectra of HCN and HCO^+ in the South pointing, toward what we call feature S2. The position of clump N from Montero-Castaño et al. puts it $\sim 14''$ from the center of the South pointing, placing this clump at the very edge of the beam of our South pointing, consistent with feature S2 and feature SW being the same source, with their emission sampled at slightly different positions.

3.2.3 Line intensities

Before measuring the line intensities, we correct the maps for the varying beam sizes by spatially convolving all maps to the resolution of the HCN J = 3–2 observations and interpolating so that the pixelization of the maps is identical. All of the data are also convolved in velocity to a common resolution of 5 km s^{-1}. We report line intensities which are integrated over the majority of the line profile, avoiding emission from other contaminating features such as the nearby '50 km s^{-1}' cloud (M-0.02-0.07) and the southern streamer, an extension of the '20 km s^{-1}' cloud (M-0.13-0.08) identified by Coil & Ho (1999) that may interact with the CND. The chosen velocity ranges for each line profile and the resulting integrated intensities are also given in Table 3.3.

Table 3.3: Integrated Brightness Temperatures

$\int \mathbf{T}_{MB}\ \mathbf{d}v$ **(K km s^{-1})**

	HCN			**H^{13}CN**		**HCO$^+$**			**H^{13}CO$^+$**	
	3–2	4–3	8–7	3–2	4–3	3–2	4–3	9–8	3–2	4–3
Integrated over the majority of the line profile										
North *v = 20 to 120 km s^{-1}*										
	198.2±19.8	136.5±13.7	27.3± 5.5	17.9±1.8	10.8±1.1	127.1±12.7	93.2± 9.3	2.8± 0.6	5.6±0.6	4.1±0.4
South *v = -120 to -20 km s^{-1}*										
	340.3±34.0	284.9±28.5	61.9±12.4	33.3±3.3	28.1±2.8	173.5±17.4	140.4±14.0	14.2± 2.9	7.4±0.7	6.1±0.6
South *v = -50 to 5 km s^{-1}*										
	152.0±15.2	117.2±11.7	25.3± 5.1	29.1±2.9	17.1±1.7	81.7± 8.2	67.8± 6.8	7.7± 1.6	7.5±0.8	4.4±0.4
Southwest *v = -50 to 5 km s^{-1}*										
	159.3±15.9	137.1±13.7	36.0± 7.2	22.5±2.3	13.2±1.3	82.10± 8.2	86.0± 8.6	10.1± 2.0	7.5±0.8	4.4±0.4
West, *v = 0 to 100 km s^{-1}*										
	193.6±19.4	124.3±12.4	20.4± 4.1	17.1±1.7	9.8±1.0	111.0±11.1	83.7± 8.4	5.8± 1.2	3.2±0.3	4.4±0.4
Integrated over the velocity ranges of individual features (reported in Table 3.2)										
N	49.0±4.9	35.0±3.5	7.5±1.5	5.6±0.6	4.3±0.4	33.8±3.4	23.5±2.4	0.7±0.1	1.7±0.2	1.7±0.2
S1	57.2±5.7	49.9±5.0	11.9±2.4	4.4±0.4	5.8±0.6	29.5±3.0	24.3±2.4	3.4±0.7	0.6±0.1	1.2±0.1
S2	38.0±3.8	35.8±3.6	8.7±1.7	12.2±1.2	7.1±0.7	21.6±2.2	23.4±2.3	3.0±0.6	3.8±0.4	1.9±0.2
SW	62.6±6.3	68.8±6.9	18.3±3.7	13.1±1.3	8.2±0.8					
W	57.9±5.8	37.0±3.7	7.6±1.5	5.2±0.5	3.1±0.3	35.9±3.6	26.1±2.6	4.0±0.9	1.3±0.1	1.3±0.1

For each of the four pointings, the line intensities are also integrated over velocity ranges (width ~ 20 km s^{-1}) corresponding to interferometrically-detected clumps from Christopher et al. (2005) and Montero-Castaño et al. (2009), given in Table 3.2. The velocity range of each feature is chosen to correspond to velocities where the clump is isolated and there is minimal confusion from nearby clumps at similar velocities. The resulting integrated intensities toward all of the features we identify are also reported in Table 3.3.

Figures 3.4 and 3.5 show the spectra extracted from the spatially-convolved maps (lefthand column) and unconvolved maps (central column) at each position in the CND. The velocity range corresponding to individual features is shaded in grey. The noise in each spectrum is much higher for the West position than for other positions in the HCN 8–7 and HCO^+ 9–8 lines, as this pointing lies near the edge of the map. All of the HCO^+ 9–8 spectra are also suffer from increased noise.

3.2.4 The detection of the $v_2 = 1f$ vibrationally-excited transition of HCN J= 4–3

In addition to the transitions already mentioned, we also detect the J = 4–3, v_2=1f line of HCN (ν= 356.256 GHz) toward the southern emission peak of the CND (in our Southwest pointing). This is the first detection of vibrationally-excited HCN in the CND. The v_2=1 transition corresponds to the bending mode of HCN, and is the lowest-energy of the vibrational modes of this molecule. This line is a doublet, however the $v_2 = 1e$ line at 354.460 GHz is strongly blended with emission from the main HCN 4–3 line and is not detected. The upper-level energy of the $v_2 = 1f$ J = 4–3 transition of HCN is 1067.1 K. The line spectrum is shown in Figure 3.6. The peak intensity of the line is $\sim$40 mK, and it has an

integrated brightness temperature of 2.28±0.23 km s^{-1}. The peak of this line lies at a velocity of -20 km s^{-1}, associating it with the S2/SW clump.

3.2.4.1 Properties of the vibrationally-excited emission

By comparing the upper-level column densities of the HCN J=4–3 v_2=0 and v_2=1 lines, we can derive the vibrational excitation temperature for feature S2/SW (technically, just for the SW component of this clump, as we do not have a good observation of the vibrationally-excited line from the South pointing).

We assume that the HCN J=4–3 v_2=1 line is optically thin. As the HCN J=4–3 v_2=0 line is not optically thin, we determine the integrated intensity of this line by scaling the H^{13}CN 4–3 line intensity (assumed to be optically thin) by the ^{12}C/^{13}C ratio of 25. The column densities are then determined using:

$$N_{\rm HCN} = \frac{8\pi k\nu^2}{A_{ul}hc^3} \int {\rm T_{MB}} dv, \tag{3.1}$$

where $A_{4-3} = 2.054 \times 10^{-3}$ s^{-1} is the Einstein A-coefficient for the $v_2 = 0$ transition (Dumouchel et al. 2010), taken from the Leiden Atomic and Molecular Database (LAMDA, Schöier et al. 2005), $A_{4-3} = 1.876 \times 10^{-3}$ s^{-1} for the $v_2 = 1$ transition (Harris et al. 2006), ν_0 is the frequency at line center, and $\int {\rm T_{MB}} dv$ is the velocity-integrated main beam brightness temperature.

Solving for the vibrational excitation temperature, we find $T_{\rm ex} = T_{vib} = 205\pm$ 10 K for feature S2/SW. If, however, the H^{13}CN 4–3 line is not optically thin, the value we derive would be an overestimate of the true T_{vib}.

3.2.4.2 Collisional vs. Radiative excitation of the $v_2 = 1$ line

We consider two possibilities for the excitation of this line: either collisional excitation, due to extremely high volume densities, or radiative excitation though the rovibrational transitions of HCN at 14 μm. For collisional excitation to excite this transition requires the density to be at least comparable to the critical density of the v_2=1 transition, which is $\sim 5 \times 10^{11}$ cm^{-3} (Ziurys & Turner 1986). As we will show in Section 3.4, such a density is more than four orders of magnitude above the highest densities that we constrain in the CND, making purely collisional excitation an unlikely source of excitation. More likely is that HCN is radiatively excited, either externally (via a sufficiently strong 14 μm background radiation field), or internally, via sufficiently hot dust mixed with the gas.

Radiative excitation of HCN will not just populate the $v_2 = 1$ states, but will also affect the populations of the rotationally-excited levels in the ground vibrational state. In the presence of a strong 14 μm radiation field, molecules in a given rotational state have a statistical likelihood to be vibrationally excited, and subsequently decay into a higher rotational level of the ground vibrational state (Morris 1975; Carroll & Goldsmith 1981). This pumping shifts the populations of the rotationally excited levels to the higher J levels, mimicking the effect of a higher gas density. This phenomenon was first observed for HCN in the ISM by Ziurys & Turner (1986), and more recently was suggested to be an important source of excitation for HCN in NGC 4418 (Sakamoto et al. 2010). It has also been observed for other molecules, e.g, CS (Hauschildt et al. 1995). Given the inferred vibrational temperature, we can determine which levels of the ground vibrational state would be affected by this radiative pumping. The criterion for effective radiative pumping is given by Equation (2) of Sakamoto et al. (2010),

reproduced here:

$$e^{-T_0/T_{\rm vib}} \mathrm{A}_{\rm vib} \geq \mathrm{A}_{{\rm rot}J}, \tag{3.2}$$

where T_0 is the level energy of the J=4, $v_2 = 1$ state, $\mathrm{T}_{\rm vib}$ is our computed vibrational excitation temperature, $\mathrm{A}_{\rm vib}$ is the Einstein A for the rovibrational transition which links the J=4 $v_2 = 0$ and $v_2 = 1$ states, equal to $\sim$2.3 s^{-1} (Harris et al. 2006), and $\mathrm{A}_{{\rm rot}J}$ is the Einstein-A coefficient for J= 4–3, v_2=0.

Given our observed T_{vib}, Equation 3.2 shows that pumping of the rotational transitions of HCN via the rovibrational transitions should be efficient up to J $\sim$12 for feature S2/SW, indicating the level populations of all observed lines in this feature are likely affected by radiative pumping.

3.3 Excitation Analysis

For the remainder of this paper, we focus on excitation analyses of the lines of HCN and HCO^+ in the CND, both for the majority of the line profile as well as for selected velocity intervals corresponding to previously identified clumps in the CND, listed in Table 3.2. Again, we separately report both emission from feature S2 observed at $(-20'', -30'')$ and feature SW observed at $(-30'', -20'')$, although these are likely part of the same structure. The resulting velocity-integrated main beam brightness temperatures for five transitions of both HCN and HCO^+ for each feature (Table 3.3) are sufficient to constrain a fit to single gas component characterized by four parameters: the temperature, H_2 density, molecular column density, and beam filling factor, with a fifth parameter, $[^{12}C]/[^{13}C]$, set to a fixed value of 25 (Wilson & Rood 1994; Wilson 1999; Riquelme et al. 2010).

To fully model the line radiative transfer of HCN and HCO^+, we also consider

contributions to the radiation field due to the local and global radiation background. In addition to the cosmic microwave background, emission from warm dust in the CND gives rise to a continuum background at the frequencies of the rotational lines of HCN and HCO^+. Both HCN and HCO^+ also have rovibrational transitions in the near and mid-infrared (the lowest energy modes for both are the bending modes, occurring at 14 and 12 μm, respectively). Our initial analysis reveals that radiative excitation through these rovibrational transitions is the most likely source of excitation of the detected $v_2 = 1f$ J= 4-3 line of HCN (see Section 3.2.4), making it important to include an accurate description of the radiation field in the CND.

We first use the statistical equilibrium radiative transfer code RADEX (van der Tak et al. 2007), a one-dimensional non-LTE code, which employs the escape probability formalism to model the observed line intensities as a function of the physical conditions in the source. The escape probability method simplifies the radiative transfer calculation by assuming that photons either completely escape the source (the likelihood of this is dependent on the local opacity, which is itself determined by the source geometry), or are immediately absorbed at the same location where they were emitted. A further simplification employed in the above method is the assumption of uniform physical conditions throughout the source.

In addition, in Section 3.5 we also compare the RADEX results for HCN to those from a more sophisticated radiative transfer code (Ratran, Hogerheijde & Tak 2000) which takes into account the internal radiation field due to embedded dust.

3.3.1 RADEX

3.3.1.1 Input Parameters

The radiative and collisional coefficients were obtained from LAMDA for the rotational lines of both HCN and HCO^+ (Dumouchel et al. 2010; Flower 1999). We also used the radiative excitation rates of the vibrationally-excited lines of HCN from Harris et al. (2006) to model the observed v_2=1 line. As the collisional coefficients of the vibrationally-excited transitions are unknown, we do not take into account any collisional excitation of the vibrationally-excited states, consistent with our previous conclusion that collisions do not contribute to the excitation of this line. We assume in our analysis of the collisional excitation of the rotationally-excited levels that H_2 is the main collisional partner for HCN and HCO^+.

For fits to the intensities of individual features, we assume velocity full-width half maxima (FWHM) of 20 km s^{-1} for the determination of the escape probability, consistent with values of $15 - 50$ km s^{-1} measured by interferometric studies for the corresponding clumps (Christopher et al. 2005; Montero-Castaño et al. 2009). For fits to the majority of the profile, we use a larger FWHM of 50-100 km s^{-1}.

For the radiation field at the wavelength of the rovibrational transitions of HCN and HCO^+, we adopt the mid-infrared spectrum as measured by ISO. Only the observations centered on the nucleus, Sgr A*, have been published (Lutz et al. 1996), however an additional spectrum of the southern emission peak of the CND is available from the NASA-IRAC Infrared Science Archive[1] (IRSA) toward an offset of (-1.3″,-37.6″) from the position of Sgr A*, which we use for this analysis.

[1]http://irsa.ipac.caltech.edu/

The calibrated spectrum is not corrected for the variable extinction in the region, and additionally represents the total flux of radiation from a fairly large aperture (14″ by 20″). The local intensity of the ambient radiation field might then differ by a factor of 2 or more from the measured value.

3.3.1.2 Grids

We use RADEX to construct grids of predicted line intensities over the given range of input temperature, density, and column density. For each set of temperature, density, and column density values, RADEX calculates main line intensities and opacities, from which the isotopologue intensities can also be derived using our assumed $[^{12}C]/[^{13}C]$ ratio. We fit separately for each molecule (HCN and HCO^+). The line intensities generated by RADEX for all five lines of each species can then be compared to the measured line intensities by introducing an additional parameter: a beam filling factor for the emitting region. Given the measured uncertainties on the line intensities, one can then determine the (reduced) chi-squared parameter for the fit of the measured to the modeled line intensities for the entire range of temperature, density, and column density considered.

3.3.1.3 Fitting Constraints

We impose several constraints on our model to eliminate unphysical solutions. First, as ammonia temperature measurements indicate that gas temperatures in the CND are at least as hot as 50 K (McGary et al. 2001), we exclude lower temperatures from our input parameter grid. We also find that where column densities are in excess of 10^{16} cm^{-2}, and densities are between 10^5 and 10^6 cm^{-3} the HCN 1–0 line undergoes strong maser action. HCN 1–0 masering is not

observed (Christopher et al. 2005) and so this region of parameter space is also excluded.

3.3.1.4 Models

We fit the observed line intensities of the majority of the line profile at each position (North, South, Southwest, and West) with a single temperature and density model. We consider temperatures in the range 50 to 600 K, densities in the range of 10^4 to 10^8 cm^{-3}, and column densities in the range of $10^{14.5}$ to $10^{16.5}$ cm^{-2} for HCN and 10^{13} to 10^{15} cm^{-2} for HCO$^+$. In addition, we perform fits over the same range of physical parameters to line intensities from each of the identified features (N, S2, S2/SW, and W) integrated over the velocity ranges given in Table 3.3.

3.4 Results of the RADEX Excitation Analyses

3.4.1 Fits to the majority of the line profile

For the observed CND positions, we find acceptable fits ($\chi^2 < 5$, where the χ^2 values presented here are equivalent to the reduced chi-squared values, as our fits have a single degree of freedom) to line intensities integrated over the majority of the line profiles for all positions except HCO$^+$ intensities toward the South-2, Southwest and West positions. We show plots of the χ^2 distribution for the fits to HCN and HCO$^+$ emission over the majority of the line profile at all positions in Figures 3.7, 3.8, 3.9 and 3.10. The resulting best-fit density, temperature, column density, and filling factor for each position as well as 1-σ errors are reported in Table 3.4. The volume density for typical dense gas in the CND is relatively well constrained by these fits to be between n $\sim 10^5 - 10^7$ cm^{-3}. In contrast, the

temperature is more poorly constrained, and varies from 60 K to 600 K, which is the upper limit of the range of temperatures probed by our models. For several cases, including HCN fits to the North and West pointings, and HCO^+ fits to the South-1 pointing, the upper bound on the temperature is unconstrained by these fits.

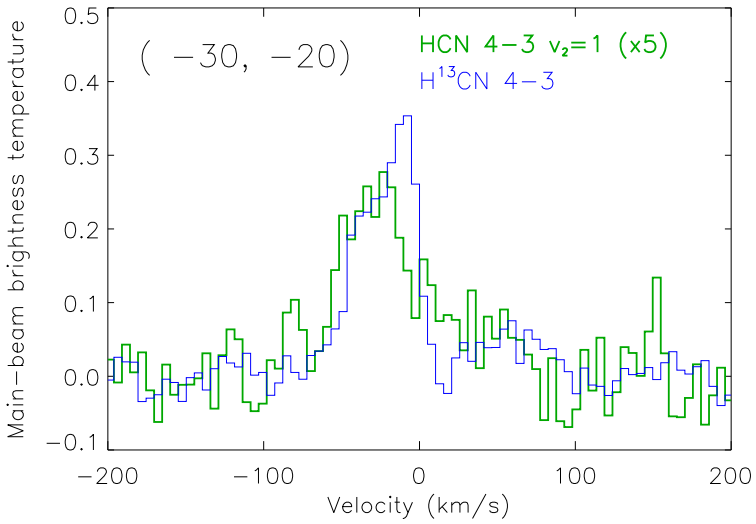

Figure 3.6: The $J = 4$–3, $v_2 = 1$ line of HCN detected toward the Southwest emission peak of the CND. The spectrum of the $H^{13}CN$ $J = 4$–3, $v_2 = 0$ line toward the same position is superposed for comparison.

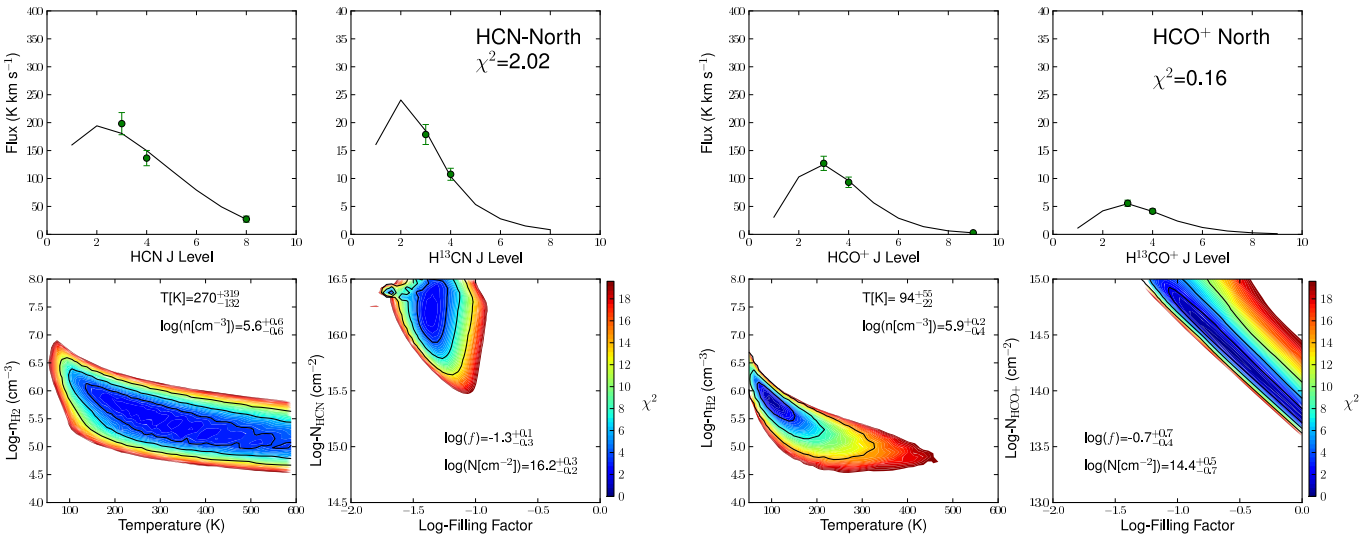

Figure 3.7: Chi-squared fits to a 1-component model of HCN and HCO$^+$ excitation for line intensities toward the North position in the CND (integrated over the majority of the line profile). Top Row: Boltzmann plots for HCN (left) and H^{13}CN (right), showing the best fit solution. Bottom row: two dimensional likelihood distributions, with contours of the 1-,2-, and 3-σ deviations from the most likely value over the full grid of temperatures and densities considered as well as filling factor and column density.

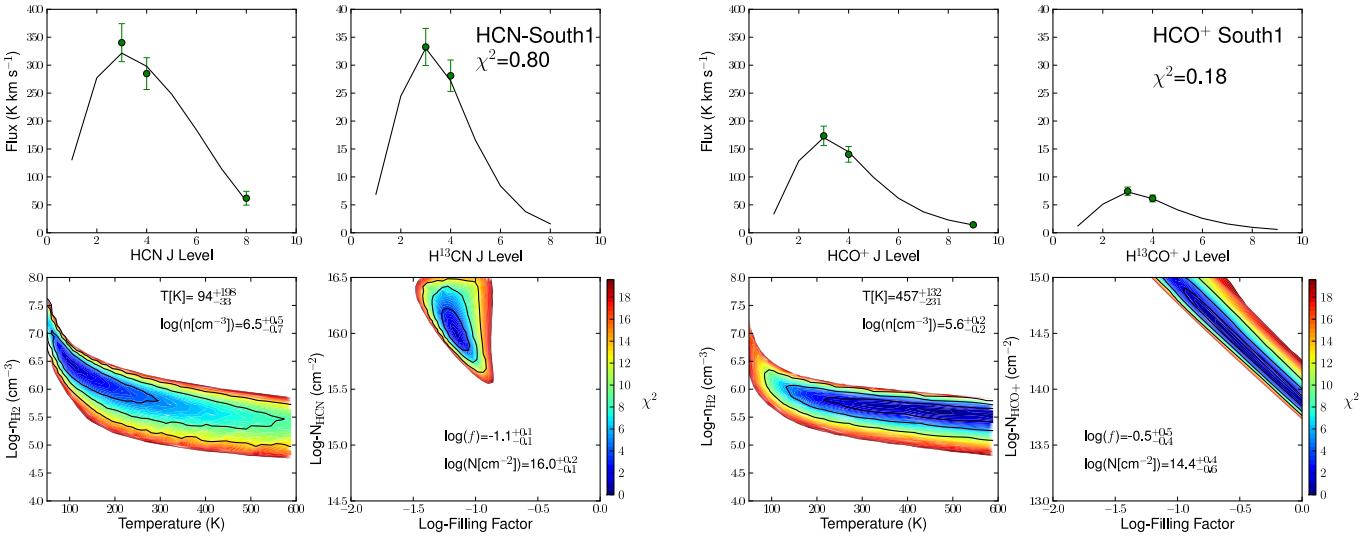

Figure 3.8: Chi-squared fits to a 1-component model of HCN and HCO$^+$ excitation for line intensities toward the South-1 position in the CND (integrated over the majority of the line profile). Rows are the same as for Figure 3.7.

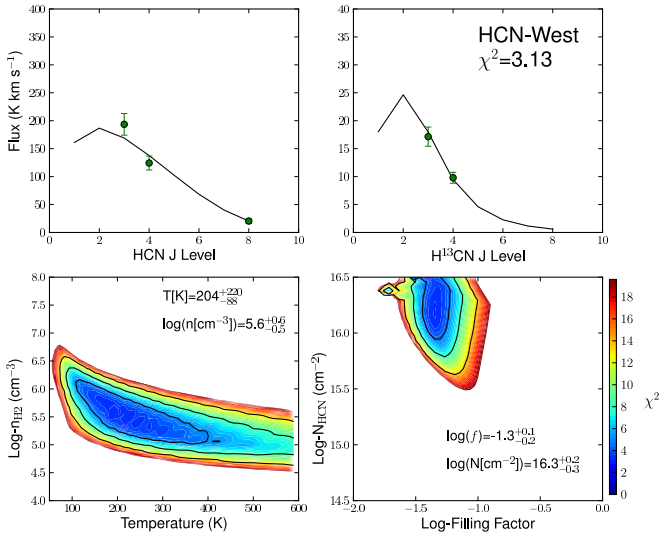

Figure 3.9: Chi-squared fits to a 1-component model of HCN excitation for line intensities toward the West position in the CND (integrated over the majority of the line profile). Rows are the same as for Figure 3.7.

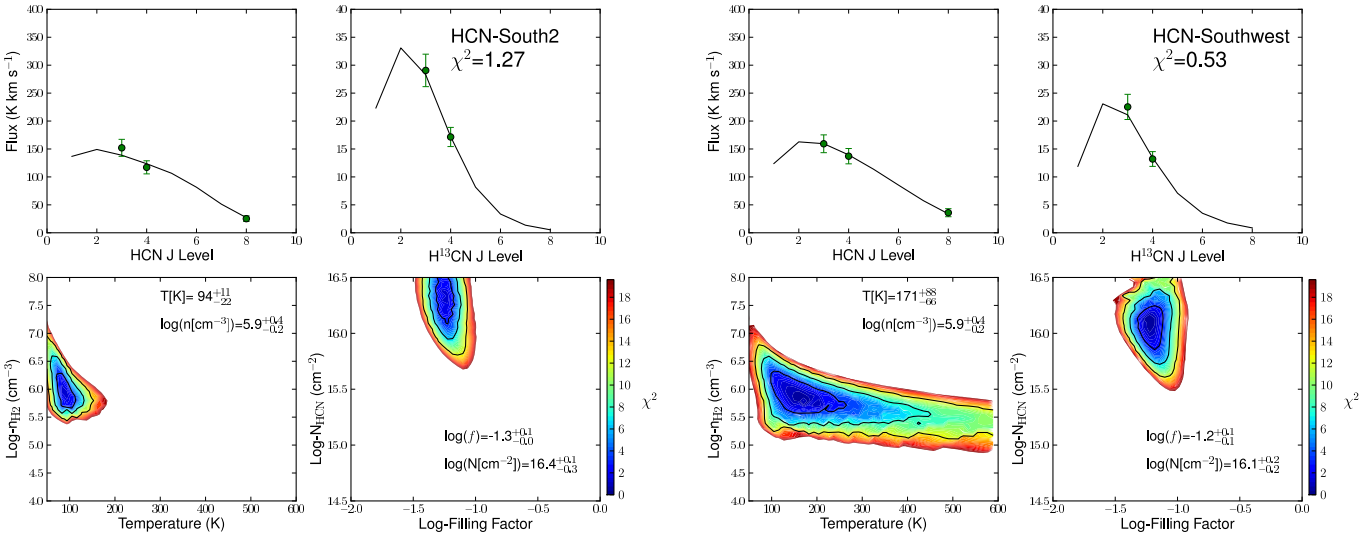

Figure 3.10: Chi-squared fits to a 1-component model of HCN excitation for line intensities toward the South-2 and Southwest positions in the CND (integrated over the majority of the line profile). Rows are the same as for Figure 3.7.

Table 3.4: Results of RADEX Excitation Analysis

	min. χ^2	$\mathbf{T_{kin}}$ [K]	$\mathbf{log(n_{H_2})}$ [cm^{-3}]	$\mathbf{log(N_{Mol})}$ [cm^{-2}]	f	**Radius** [pc]	**Mass** [$M_\odot$]	τ_{3-2}	τ_{4-3}
	HCN fits (majority of the line profile)								
North (v=20,120)	2.0	270^{+319}_{-132}	$5.6^{+0.6}_{-0.6}$	$16.2^{+0.3}_{-0.2}$	$0.04^{+0.01}_{-0.02}$			$5.0^{+5.7}_{-2.3}$	$7.1^{+7.4}_{-3.2}$
South-1 (v=-120,-20)	0.8	94^{+198}_{-33}	$6.5^{+0.5}_{-0.7}$	$16.0^{+0.2}_{-0.1}$	$0.07^{+0.01}_{-0.02}$			$2.1^{+1.9}_{-0.4}$	$3.1^{+2.8}_{-0.6}$
South-2 (v=-50,5)	1.3	94^{+11}_{-22}	$5.9^{+0.4}_{-0.2}$	$16.4^{+0.1}_{-0.3}$	$0.05^{+0.01}_{-0.01}$			$10.3^{+5.2}_{-5.0}$	$15.0^{+6.3}_{-7.3}$
Southwest (v=-50,5)	0.5	171^{+88}_{-66}	$5.9^{+0.4}_{-0.2}$	$16.1^{+0.2}_{-0.2}$	$0.06^{+0.01}_{-0.01}$			$4.6^{+4.0}_{-1.7}$	$7.0^{+5.7}_{-2.4}$
West (v=0,100)	3.1	204^{+220}_{-88}	$5.6^{+0.6}_{-0.5}$	$16.3^{+0.2}_{-0.3}$	$0.04^{+0.01}_{-0.01}$			$9.8^{+1.7}_{-7.2}$	$13.8^{+1.5}_{-10.0}$
	HCN fits (narrow features)								
N (v=90,110)	3.0	94^{+77}_{-22}	$6.3^{+0.4}_{-0.8}$	$15.5^{+0.9}_{-0.2}$	$0.04^{+0.01}_{-0.02}$	$0.10^{+0.01}_{-0.03}$	480^{+1100}_{-450}	$3.8^{+47.4}_{-1.4}$	$5.6^{+17.3}_{-2.0}$
S1 (v=-115,-95)	1.7	61^{+77}_{-11}	$7.2^{+0.4}_{-0.7}$	$15.1^{+0.1}_{-0.1}$	$0.09^{+0.02}_{-0.02}$	$0.15^{+0.01}_{-0.02}$	13000^{+34000}_{-11000}	$1.5^{+0.4}_{-0.3}$	$2.1^{+0.7}_{-0.2}$
S2 (v=-25,5)	0.8	72^{+11}_{-11}	$5.7^{+0.6}_{-0.2}$	$16.4^{+0.1}_{-0.4}$	$0.04^{+0.01}_{-0.01}$	$0.10^{+0.01}_{-0.02}$	120^{+420}_{-80}	$26.4^{+11.1}_{-17.2}$	$37.1^{+14.2}_{-23.8}$
SW (v=-25,-5)	3.1	116^{+11}_{-33}	$6.0^{+0.4}_{-0.5}$	$15.9^{+0.5}_{-0.2}$	$0.04^{+0.01}_{-0.01}$	$0.10^{+0.01}_{-0.02}$	240^{+560}_{-200}	$6.8^{+25.4}_{-2.6}$	$10.4^{+21.2}_{-4.0}$
W (v=35,55)	3.7	237^{+286}_{-110}	$5.6^{+0.5}_{-0.6}$	$15.5^{+0.3}_{-0.2}$	$0.06^{+0.02}_{-0.02}$	$0.12^{+0.02}_{-0.02}$	170^{+660}_{-150}	$4.8^{+5.9}_{-2.0}$	$6.9^{+10.9}_{-2.7}$
	HCO^+ fits (majority of the line profile)								
North (v=20,120)	0.2	94^{+55}_{-22}	$5.9^{+0.2}_{-0.4}$	$14.4^{+0.5}_{-0.7}$	$0.22^{+0.78}_{-0.14}$			$0.3^{+0.7}_{-0.2}$	$0.4^{+0.7}_{-0.3}$
South-1 (v=-120,-20)	0.2	$^{1}457^{+132}_{-231}$	$5.6^{+0.2}_{-0.2}$	$14.4^{+0.4}_{-0.6}$	$0.29^{+0.71}_{-0.18}$			$0.2^{+0.4}_{-0.2}$	$0.3^{+0.4}_{-0.2}$
South-2 (v=-50,5)	9.7								
Southwest (v=-50,5)	7.3								
West (v=0,100)	7.4								
	HCO^+ fits (narrow features)								
N (v=90,110)	4.5	61^{+22}_{-11}	$6.2^{+0.2}_{-0.3}$	$14.5^{+0.2}_{-0.3}$	$0.07^{+0.06}_{-0.02}$	$0.13^{+0.06}_{-0.02}$	840^{+3300}_{-590}	$0.9^{+0.3}_{-0.2}$	$1.3^{+0.3}_{-0.3}$
S1 (v=-115,-95)	3.5	$^{1}336^{+253}_{-165}$	$5.9^{+0.2}_{-0.2}$	$13.1^{+0.7}_{-0.0}$	$1.00^{+0.00}_{-0.80}$			$0.0^{+0.0}_{-0.0}$	$0.1^{+0.0}_{-0.0}$
S2 (v=-25,5)	19.8								
SW (v=-25,-5)	23.5								
W (v=35,55)	4.0	589^{+0}_{-352}	$5.6^{+0.2}_{-0.1}$	$13.3^{+0.9}_{-0.2}$	$0.69^{+0.31}_{-0.59}$			$0.1^{+0.3}_{-0.0}$	$0.1^{+0.4}_{-0.0}$

The volume densities derived from our HCO^+ and HCN observations are comparable for the North position, but the densities derived for the South position are not consistent within the uncertainties; the best-fit density derived for this position from HCN is an order of magnitude higher than that derived using HCO^+. In contrast, the derived temperatures are consistent for the South position, but the temperature derived from HCO^+ is significantly cooler for the North position than that derived using HCN.

The derived filling factors for both positions also differ significantly: the best-fit filling factors for HCN emission toward all positions are less than 0.08, while they are substantially greater for HCO^+(Table 3.4). This suggests either that the HCN emission in the CND is significantly more clumpy than HCO^+ emission, or (as interferometric maps show the two species exhibit similar small-scale structure; Christopher et al. 2005) that more of the HCO^+ emission detected in single-dish observations originates in an extended gas component. If the extended component has different excitation conditions than the gas which is predominantly traced by HCN, this could also explain the fact that we are unable to fit the HCO^+ intensities well with a single excitation component for three positions in the CND (South-2, Southwest, and West).

The best-fit HCN column densities are somewhat higher than mean HCN column densities of $\sim 10^{15}$ cm^{-2} derived by Christopher et al. (2005) from observations of HCN 1-0 in individual clumps in the CND. This could either be the result of missing flux in the interferometric observations of Christopher et al., or could indicate that column densities derived from the HCN 1–0 line are underestimated, if for example the line is more optically thick than assumed. However, our best-fit models predict that the HCN 1–0 line should be optically thin and/or weakly inverted ($\tau < 1$) in all cases except possibly toward feature S2 (for which

our best fit model predicts $\tau \sim 4$), making the former scenario more likely.

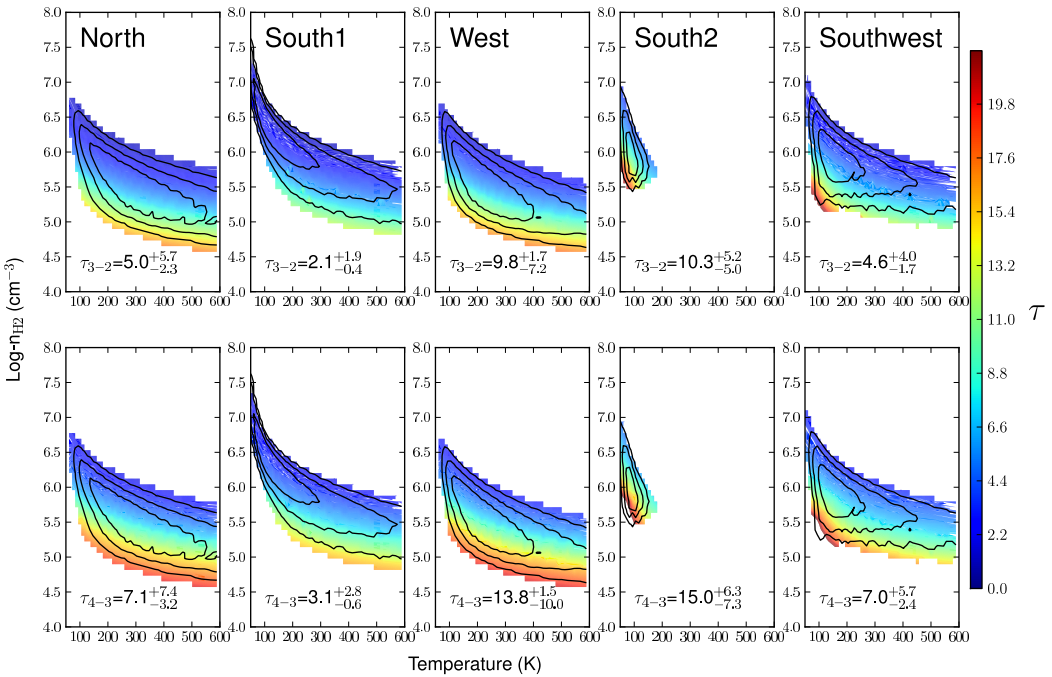

Figure 3.11: HCN line opacities for the 3-2 (Top) and 4-3 (Bottom) transitions, derived from fits to line intensities integrated over the majority of the line profile. Contours show the 1-,2-, and 3-σ deviations from the most likely temperature and density over the full grid of physical conditions that were considered.

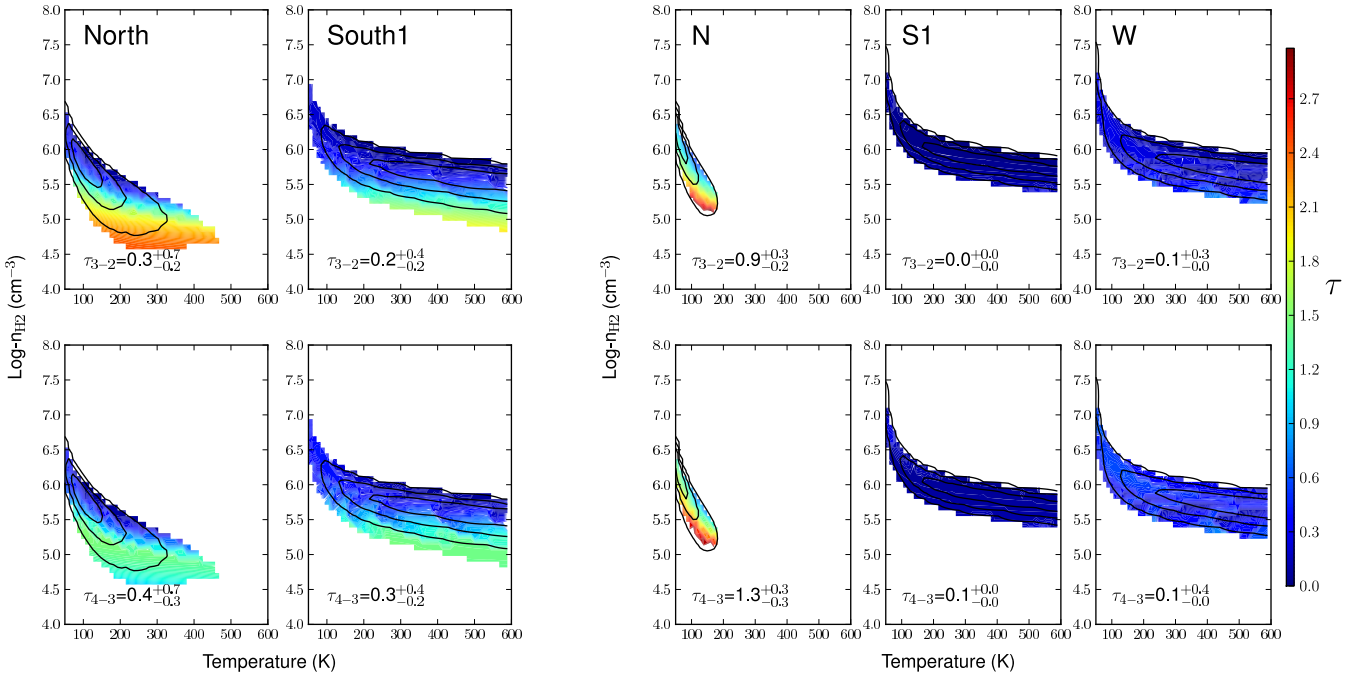

Figure 3.12: HCO^+ line opacities for the 3-2 (Top) and 4-3 (Bottom) transitions, derived from fits to line intensities integrated over the majority of the line profile (Left) and fits to individual features (Right). Contours show the 1-,2-, and 3-σ deviations from the most likely temperature and density over the full grid of physical conditions that were considered.

The HCO^+ 3–2 and 4–3 emission toward the North and South pointings is also found to be optically thin ($\tau < 1$), while the HCN 3–2 and 4–3 emission is everywhere quite optically thick ($\tau > 2$), with HCN 8–7 predicted to be optically thick as well ($\tau > 1$), although we do not observe this transition in $H^{13}CN$. The distribution of opacities are shown in Figures 3.11 and 3.12. Opacities are not determined for HCO^+ toward the South-2, Southwest, and West pointings, as acceptable model fits were not found for the line intensities toward those positions. The HCO^+ emission is however likely optically thick toward the South-2 and Southwest positions, as the ratios of $H^{12}CO^+$ lines to their ^{13}C isotopologues are between 10 and 20, significantly less than the assumed $[^{12}C]/[^{13}C]$ isotope ratio of 25. It is not possible however to accurately determine the opacity just from the ratio of these line intensities and the intrinsic $[^{12}C]/[^{13}C]$ isotope ratio, as this also requires knowledge of the excitation temperature for each level. The excitation temperatures for the ^{12}C and ^{13}C isotopologues cannot be assumed to be the same; models show that the excitation temperature for the ^{13}C isotopologue for typical CND conditions can be up to a factor of 2 lower than for the main line.

3.4.2 Fits to individual features

In addition to fitting for the brightness temperatures integrated over the entire line profile, we also fit to the brightness temperatures integrated over limited ($\Delta v = 20$ km s^{-1}) velocity ranges corresponding to individual clumps identified in interferometric studies of the CND. For the five features we analyze, we find reasonable fits to observations of all features except for the HCO^+ observations of the S2/SW clump. Plots of the χ^2 distribution for all features are shown in Figures 3.13, 3.14, 3.15, and 3.16, and the fit parameters are reported in Table 3.4. Within our uncertainties, the volume densities of individual features range

from $n = 10^{5.0}$ to $10^{7.6}$ cm^{-3}(for feature S1). The densities and temperatures derived from fits to HCN and HCO^+ are consistent except in the case of feature S1, where the HCN-derived density is higher by an order of magnitude. In this case, the HCN fits favor a cooler temperature ($\sim$ 100 K) than fits to HCO^+ which favor a temperature $>$ 170 K. For HCO^+ fits to S1, and fits for both molecules to feature W, the constraints from the observed lines are insufficient to constrain the temperatures, and acceptable fits are found for temperatures up to 600 K, the largest value considered in our grids of parameter values. In general however, fits to the limited velocity ranges of individual features yield lower temperatures and higher densities than fits to the entire profile.

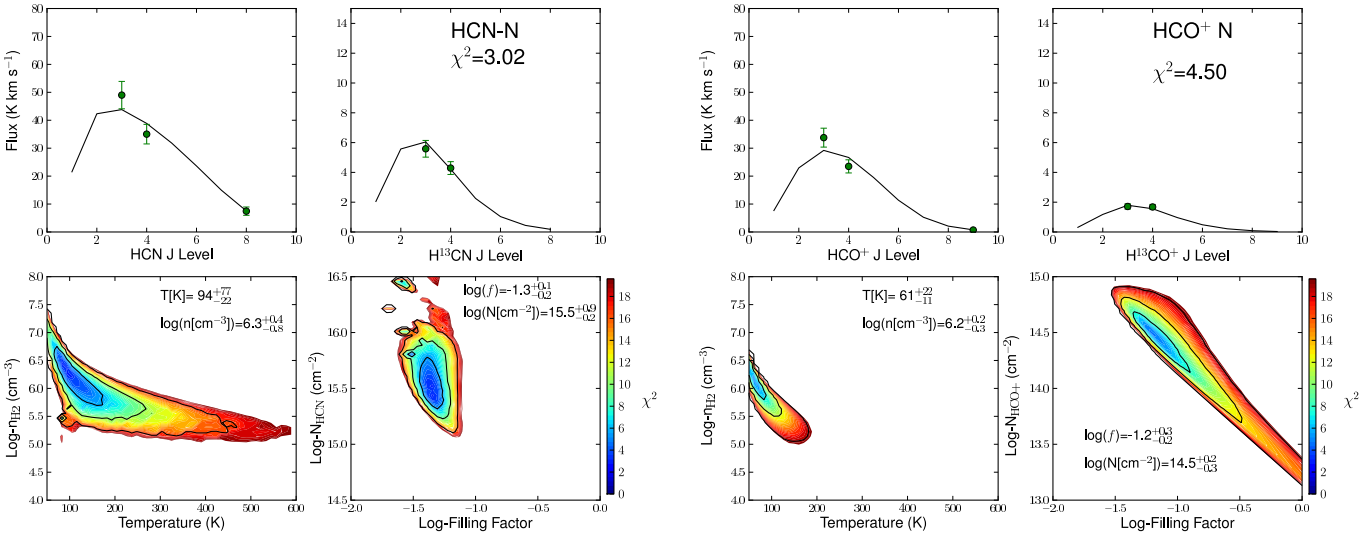

Figure 3.13: Chi-squared fits to a 1-component model of HCN and HCO$^+$ excitation for feature N in the CND. Rows are the same as for Figure 3.7.

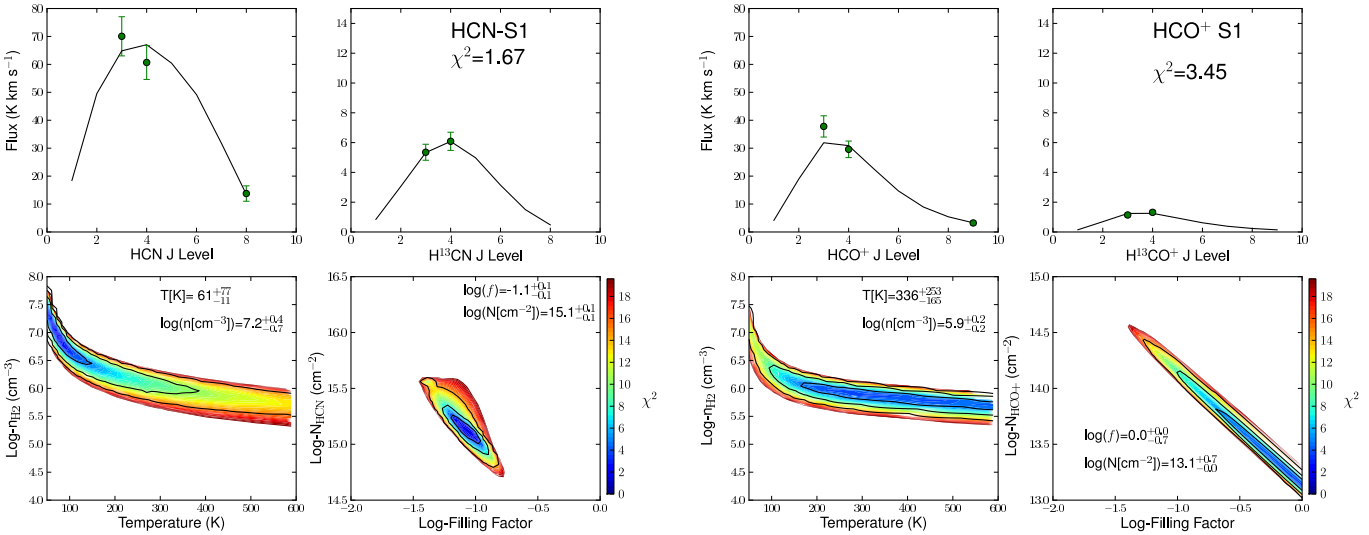

Figure 3.14: Chi-squared fits to a 1-component model of HCN and HCO$^+$ excitation toward feature S1 in the CND. Rows are the same as for Figure 3.7.

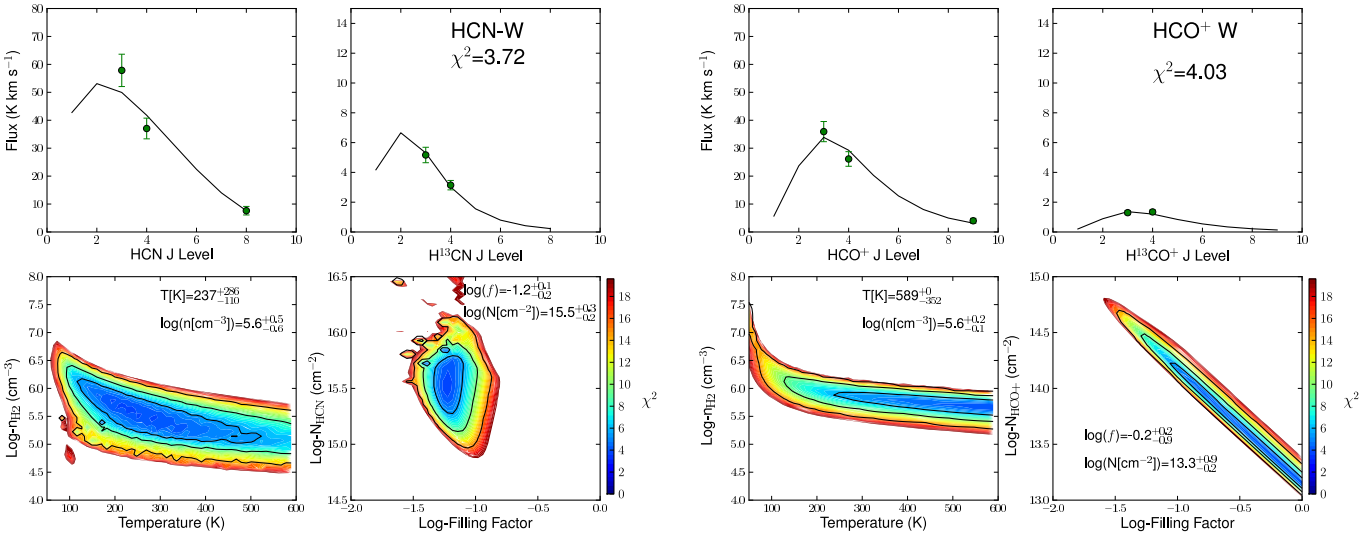

Figure 3.15: Chi-squared fits to a 1-component model of HCN and HCO$^+$ excitation toward feature W in the CND. Rows are the same as for Figure 3.7.

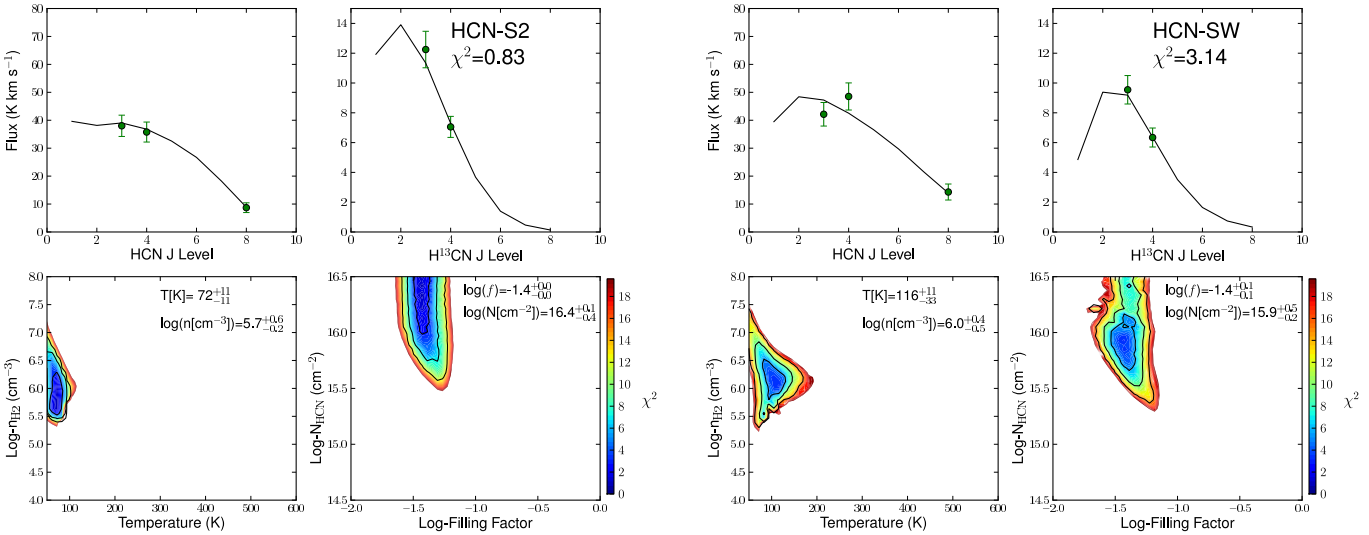

Figure 3.16: Chi-squared fits to a 1-component model of HCN excitation toward feature S2/SW in the CND. Rows are the same as for Figure 3.7.

One other difference between the HCN and HCO^+ fits to these individual features are the inferred filling factors. The filling factors for HCO^+ (which range from 0.07 to > 0.1 or 0.2) are uniformly larger than the filling factors derived for HCN, which are all less than 0.1. This implies that the HCO^+ emission, even that potentially associated with individual features, is significantly more extended than the HCN emission. Possibly related to this, but more likely a factor of the lower relative HCO^+ abundance in the CND, the emission from HCO^+ features is generally optically thin, with only emission from feature N being optically thick. In contrast HCN emission is extremely optically thick, with opacities ranging from 1.5 to potentially higher than 30 (for feature S2, if $T < 100$ K and $n < 10^6$ cm^{-3}). The distribution of opacities derived from our fits to individual features are shown in Figures 3.17 and 3.12. For features N, S1, and W, the HCN optical depths are lower than those derived from fits to the majority of the line profile.

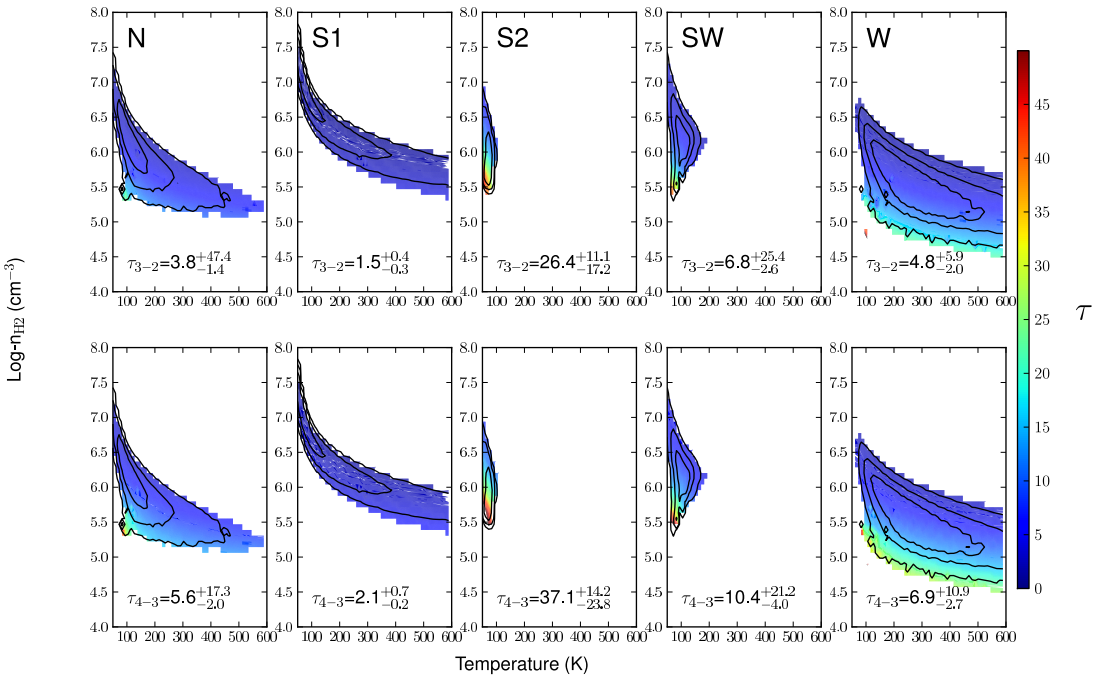

Figure 3.17: HCN line opacities for the 3-2 (Top) and 4-3 (Bottom) transitions, derived from fits to individual features. Contours show the 1-,2-, and 3-σ deviations from the most likely temperature and density over the full grid of physical conditions that were considered.

3.4.2.1 Feature properties

If the source being observed is smaller than the telescope beam, its brightness temperature will be diluted. Assuming the features we observe are circularly symmetric Gaussian clumps at the center of the circular beam, the filling factor which describes this dilution is given by the expression:

$$f = \frac{\theta_{clump}}{\theta_{MB} + \theta_{clump}}, \tag{3.3}$$

where θ_{MB} is the FWHM of the telescope beam and θ_{clump} is the FWHM of the clump. Taking the clump to be a sphere with a radius equal to half of the FWHM, we use the best fit filling factors to determine equivalent radii for the observed features. These radii range from 0.1 to 0.15 pc, and are reported in Table 3.4. In all cases, the radii we derive are slightly smaller than those derived from interferometric observations of the individual clumps (Montero-Castaño et al. 2009).

Using the clump radii we derive, we can also estimate masses for individual clumps, assuming a uniform clump density equal to the best-fit value. The resulting masses are reported in Table 3.4 The typical clump mass is a few hundred solar masses, except for clump S1, for which we estimate a mass of a few 10^4 $M_\odot$ from our HCN observations. All of the masses derived using HCN are at least an order of magnitude lower than the virial masses determined for these clumps by Montero-Castaño et al. (2009) using HCN 4–3. For HCO^+ the situation is somewhat different, as we only have model fits for three features, and two of these features have large filling factors inconsistent with emission from a clump. For the remaining feature (N), the mass we derive using HCO^+ (~ 840 $M_\odot$) is larger than that derived for this clump using HCN, and is roughly a factor of 5 lower

than the mass derived for this feature by Montero-Castaño et al. (2009).

Finally, given the clump radii we derive, we can also compare the observed line brightness temperatures from our convolved data to that in the unconvolved HCN 8–7 data, which has a higher resolution (8.9″). We find that, for the derived clump radii, the difference in beam dilution should lead the unconvolved HCN 8–7 brightness temperatures to be a factor of 3-4 times brighter than the HCN 8–7 brightness temperatures from data convolved to the resolution of the HCN 3–2 beam (23.6″). However, we find that it is only typically a factor of 2-3 times brighter for these features. This suggests that the sources are actually slightly more extended than our analysis suggests, and/or that other estimates made when deriving radii from the filling factors (that the sources are circular, Gaussian, and lie in the center of the beam) may not hold.

Altogether, our results indicate that conditions in individual clumps in the CND deviate from the average physical conditions in the bulk of the CND gas. However, the results presented here for individual features are based upon line intensities which still likely suffer from the superposition of line profiles from multiple clumps in the large beam of these observations. Higher spatial-resolution observations are necessary in order to fully isolate the contribution to the CND emission from these individual clumps, and to properly model their line profiles.

3.4.3 Radiative excitation of HCN due to the 14μm background field

Thus far in these analyses, we have been assuming that HCN (and HCO^+) are purely collisionally excited. However, our detection of the J = 4-3 $v_2 = 1$ line of HCN suggests that the excitation of HCN in the CND is not entirely collisional, and that radiative excitation also plays a role. There are two possibilities for this radiative excitation, either the gas traced by HCN is irradiated externally

by a mid-infrared background field, or it is irradiated internally, through embedded hot dust mixed with the gas. We use the mid-infrared background spectra measured by Lutz et al. (1996) to run multiple RADEX models incorporating a mid-infrared background radiation field. We find that the results from these runs are indistinguishable from the case in which no mid-infrared background radiation is included, for the full range of temperatures and densities we consider. We thus conclude that background 14 μm radiation fields up to several times the highest value measured toward the central parsec (250 Jy nSr^{-1}, for an apertures centered on Sgr A*) are a negligible contribution to the excitation of HCN. This favors embedded hot dust as the most likely excitation mechanism for the observed $J = 4$-3 $v_2 = 1$ HCN line, which we explore further with excitation analyses using Ratran.

3.5 Ratran

3.5.1 Input Parameters

We model the radiative excitation of HCN in the CND with Ratran, using the same collisional and radiative excitation data as for the RADEX analysis. Like RADEX, Ratran is a one-dimensional non-LTE code. However, Ratran differs from RADEX in that it uses Monte Carlo techniques to more carefully sample the radiation field, combined with an accelerated lambda convergence method which allows the code to operate efficiently even for extremely high opacities. Unlike RADEX, Ratran is not limited to the assumption of uniform source conditions, but can model gradients in the physical parameters, allowing for a more realistic modeling of the shape of the emergent line profiles, as opposed to the simple RADEX model of a rectangular line profile (having constant intensity and

opacity).

Ratran modeling requires several more constraints on the gas properties. We assume the same turbulent line FWHM (20 km s^{-1}) as used in RADEX fitting. However, when modeling the majority of the line profile, instead of increasing this width, we assume the broader profile is due to CND rotation, and additionally consider a velocity gradient dv/dr of 150 km s^{-1} pc^{-1}, consistent with observations of the kinematics of CND gas (Christopher et al. 2005; Martín et al. 2012). We constrain the source radii (assuming spherical clumps), which we take from the interferometric observations to be $\sim$ 0.19 pc, consistent with our best-fit filling factors from the RADEX analysis. We also have to input the abundance of HCN compared to that of its primary collision partner (H_2).We assume the radiative excitation of HCN is predominantly due to the emission from hot dust which is mixed with the gas, and fix the intensity of the internal mid-infrared radiation field by assuming a dust temperature (we model a range of dust temperatures from 100 to 150 K) and applying a dust emissivity model (grains with no ice mantle and $\sim 10^5$ years of coagulation, Ossenkopf & Henning 1994). As there are now more free or uncertain parameters to our fit, including the dust temperature and the HCN abundance, we do not try, as with RADEX, to produce grids of conditions to constrain the most likely solution. Instead, we look for the existence of well-fitting solutions, which may not be unique.

3.5.2 Overlap of the 14 μm rovibrational lines

In addition to taking into account radiative excitation due to embedded hot dust, we also consider the effects of line overlap in the Q-branch transitions at 14 μm, which connect the $v_2 = 0$ and $v_2 = 1$ states.

If the opacity at the wavelength of the v_2 = 1–0 rovibrational transitions

($\lambda = 12.5 - 16.0$ μm) is sufficiently high, then the mid-infrared photons at this wavelength are less likely to escape the vicinity of a given gas molecule, and can instead be re-absorbed by the molecule. This trapping phenomenon reduces both the critical density for collisional excitation and the infrared background necessary for radiative excitation of the $v_2 = 1$ line.

Although both Ratran (and RADEX) take into account the trapping of radiation for high opacities, neither code treats the effects of overlapping line emission on the excitation. The 14μ m rovibrational transitions of HCN occur in three bands: the R-branch ($\Delta J = +1$), Q-branch ($\Delta J = 0$), and P-branch (ΔJ = -1). The Q-branch transitions in particularly are sufficiently closely spaced that for CND line widths (20 to 100 km s^{-1}) transitions up to $J \sim 4$ will overlap. We calculate the expected overlap as a function of line width and make a correction for this overlap (as seen in Figure 3.18, lines overlap by a factor of 1.5 to 2.75 for J up to 5) by dividing the Einstein-A values of the Q-branch transitions by the overlap factor, which will increase the populations in the $v_2 = 1$ states. Here, the overlap factor for each line is defined as the contributions from Gaussian profiles of all the lines (where the peak intensity of the gaussian is normalized to 1) summed at the frequency of each line.

We find that including the effects of Q-branch overlap for line widths as large as 100 km s^{-1} has a substantial effect on the predicted intensity of the v_2=1 J = 4-3 line, while the effect of overlap on the predicted intensities of the v_2=0 rotational lines is much smaller. Accounting for this overlap alters the $v_2 = 1$ J=4–3 line intensity by a factor of 2-4 for line widths of 50-100 km s^{-1}, however the $v_2 = 0$ line intensities vary by $< 10\%$. The smaller variation observed in the $v_2 = 0$ lines is likely because the Q-branch transitions are $\Delta J = 0$ transitions, and so do not directly contribute to altering the level populations of the $v_2 = 0$

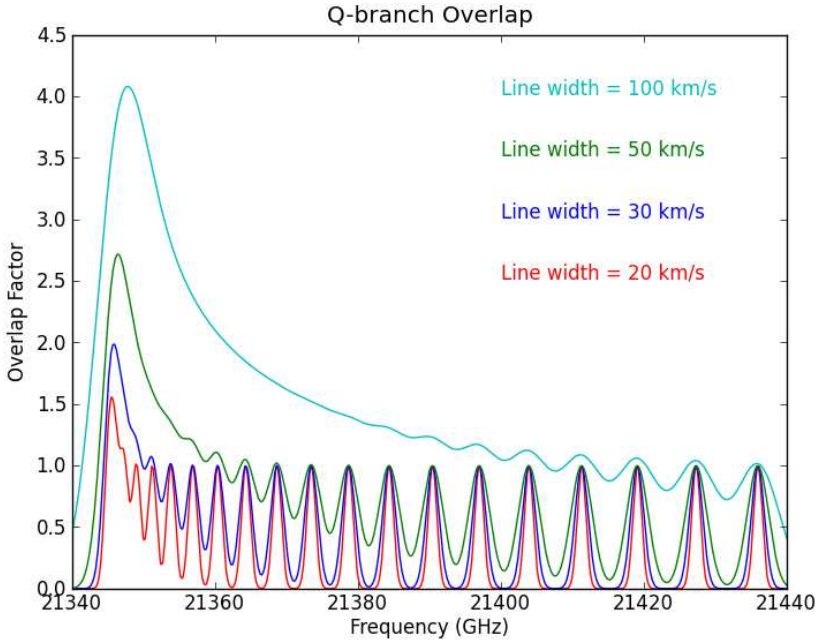

Figure 3.18: The degree of overlap in the Q-branch rovibrational lines of HCN for a range of line widths. An overlap factor of 1 signifies no overlap.

rotational lines. For the following analysis, we include the effects of overlap for the HCN 4–3 line widths from interferometric observations of individual clumps: 50 km s^{-1} for the South pointing, and 100 km s^{-1} for the Southwest pointing (Montero-Castaño et al. 2009).

3.5.3 Radiative excitation of HCN by embedded dust

The $J = 4$–3 $v_2 = 1$ line is predominantly detected at velocities around -20 km s^{-1}, corresponding to the Southwest pointing (or the S2/SW clump). For this source, we adopt the interferometrically-determined properties from Montero-Castaño et al. (2009), namely a radius of 0.25 pc and a velocity FWHM of ∼100 km s^{-1}. We then run a coarse grid of Ratran models covering the range of conditions indicated by our RADEX fitting to the observed line intensities toward Southwest

(T=100 K, n = $10^{5.5} - 10^{6.4}$ cm^{-3}, [HCN/H$_2$] = $5 \times 10^{-9} - 1 \times 10^{-8}$), varying the dust temperatures between 100 and 175 K. We find that dust temperatures of $\sim 125 - 150$ K are required to generate the observed $J = 4$–3 $v_2 = 1$ line strength ($\int$ T$_{MB}$ dv = 2.28 K km s^{-1}). The Q-branch excitation temperatures for these models are ∼150 K, smaller than our derived T$_{vib}$ of $\sim$ 200 K (although, the T$_{vib}$ we determine could be an overestimate, if the H^{13}CN 4–3 line used to calculate this value is actually optically thick).

These dust temperatures are also sufficient to cause the derived density for South-1 to be up to a factor of 5 lower than predicted by RADEX. Thus, as we discuss further in Section 3.6.2, if this hot dust is widespread throughout the CND and not just localized in feature S2/SW, this could bring the densities derived using HCN for the southern emission peak into agreement with those derived by RT12 using CO. If our density estimates for other clumps are indeed overestimated due to the radiative excitation of HCN, v_2 =1 emission should be seen in these clumps as well.

3.6 Discussion

3.6.1 Hot dust in the CND

The detection of the J = 4-3 v_2 = 1 HCN line toward the southwest emission peak of the CND and subsequent Ratran modeling of its intensity indicate that HCN emission from this region is radiatively excited, and that a 125-150 K dust component is necessary to explain the observed strength of this line.

However, existing observations have not detected this hot dust component in the CND. Etxaluze et al. (2011) fit the far-infrared and submillimeter emission spectrum of this region with photometric data from 21.3 to 180 μm, indicating

the presence of at least three temperature components in the dust: 23, 44.5, and 90 K. More recently, Lau et al. (2013) used the FORCAST instrument on the Stratospheric Observatory For Infrared Astronomy (SOFIA) to map emission from the CND and central parsec at 19.7, 31.5, and 37.1 μm and to construct a map of the dust color temperature, showing clearly that the hottest dust, with temperatures up to 150 K, originates in the central cavity, while in the CND, the dust color temperature ranges from 60-90 K, consistent with lower-resolution observations at similar wavelengths by Telesco et al. (1996).

There are several possible reasons why such a hot dust component in the CND could have been missed by previous observations. First, the wavelengths observed by Etxaluze et al. (2011) and Lau et al. (2013) are slightly longer than the wavelengths of the HCN rovibrational transitions, so they do not constrain the existence of hotter dust components which could dominate the dust emission at the wavelengths of the rovibrational lines of HCN. For example, a 12.5-20.3 μm color temperature map of the 'minispiral' region interior to the CND indicates dust color temperatures ranging from 200 to 270 K (Cotera et al. 1999a), significantly higher than the $\sim$ 150 K dust temperatures derived by Lau et al. and others for the minispiral. Also, short wavelength emission from the hottest dust should originate from the inner edge of the CND, and given the orientation of the CND, this emission from clump S2/SW should lie on the far side of the bulk of the gas in the southern emission peak of the CND (see, e.g., Lau et al.). Emission from hot dust in this source could then be significantly extincted. If there is hot dust all along the inner edge of the CND, we predict that this hot dust component could be indirectly detected via the radiative excitation of HCN: the 14 μm rovibrational lines should be seen in absorption against the background dust continuum (where they are not extincted by the dense CND torus), and emission from the $v_2 = 1$ rotational lines of HCN should also be present in other

CND clumps lying along its inner edge.

We also note that it is not clear whether radiative excitation may also contribute to the excitation of HCO^+. We do not detect the $v_2 = 1$ lines of HCO^+, however this may not rule out radiative excitation, as HCO^+ has a lower abundance than HCN in the CND, as we discuss in Section 3.6.4, making these lines to faint to be detected in our data. However, the rovibrational transitions of HCO^+ also occur at 12 μm, at which wavelength archival ISO spectra show the mid-infrared emission from the CND to be a factor of 2-3 less intense than at 14 μm, so it is possible that radiative excitation is not energetically important for HCO^+.

3.6.2 CND Densities

Comparing our HCO^+ and HCN-derived densities to those derived by RT12 using CO, we find that in general, the best-fit densities from our fits to the majority of the line profile are consistent within the uncertainties with densities from RT12 toward the northern and southern emission peaks of the CND, although they tend to be slightly higher. However, the best-fit density for the South-1 pointing determined from our HCN observations, ($\log$ [n cm^{-3}] = $6.5^{+0.5}_{-0.7}$), is higher than the CO-derived densities found by RT12 for the southern emission peak ($\log$ [n cm^{-3}] = $5.2^{+0.4}_{-0.2}$), and does not agree within the uncertainties of both measurements. There is also some tension in the best-fit temperatures; the temperature determined from HCN line intensities toward South -1 (as well as the temperature determined from HCO^+ toward the North pointing) is lower than allowed by the RT12 CO fits to the high-density component of gas. There are two main scenarios which can explain this discrepancy: either there truly is higher density (and cooler) gas in the southern emission peak of the CND, or the

HCN lines are affected by the pumping of the rotational levels due to radiative excitation, the resulting alteration in the level populations mimicking a higher density than is actually present.

It is possible that HCN (and HCO^+) trace gas which is preferentially excited in higher-density clumps of the CND, as the critical densities of the highest lines we measure (HCN 8–7 and HCO^+ 9–8) are $\sim 10^9$ cm^{-3}, and $\sim 10^8$ cm^{-3}, respectively, whereas the critical density of the highest line measured by RT12, CO 16–15, has a critical density of just a few times 10^6 cm^{-3}, three orders of magnitude lower. Our fits to limited velocity ranges corresponding to individual interferometrically-detected clumps also tend to indicate higher densities than fits to the entire line profile, which suggests that there may be denser clumps embedded in the CND, even though these higher densities may not be typical of conditions in the bulk of the CND gas, as traced by CO. However, if radiative excitation is important outside of clump S2/SW (where we detect the $v_2 = 1$ J=4-3 line of HCN), this could also lower the gas density we derive for the southern emission peak, potentially bringing it into agreement with the lower density measured by RT12. Our current observations are not sufficient to distinguish between these scenarios; sensitive observations of the $v_2 = 1$ lines of HCN toward more positions in the CND should be conducted in order to determine whether the radiation from hot dust plays a role in the observed excitation of HCN throughout the CND.

3.6.2.1 Is CND gas virialized?

Previous interferometric observations of the CND with HCN and HCO^+ have suggested that, if virialized, the CND gas should have extremely high densities, on the order of n$\sim 10^7 - 10^8$ cm^{-3}(Christopher et al. 2005; Montero-Castaño

et al. 2009). However, even the highest density we find (feature S1) is substantially lower than the large virial densities calculated by Montero-Castaño et al., which are on the order of a few times 10^8 cm^{-3}. In general, we find densities less than a few 10^6 cm^{-3}, suggesting that the clump densities determined by Montero-Castaño et al., Shukla et al. (2004) and Christopher et al. (2005) are overestimated, and CND clumps are not in virial equilibrium. We also compare our derived densities to the Roche limit for stability of 0.1 pc scale clumps in CND at a radius of 2 pc from the black hole, which is $\sim 10^7$ cm^{-3}. The densities we derive for all positions in the CND except one are lower than this value, meaning that the majority of the gas in the CND is not tidally stable. The densities allowed by our single-component HCN fit to feature S1 are log (n cm^{-3}) $7.2^{+0.4}_{-0.7}$, and so for this clump, we cannot rule out the possibility that this clump could be marginally stable against tidal disruption. Intriguingly, this is also the only CND clump which has a strong submillimeter counterpart (Liu et al. 2013). However, overall our analysis indicates that, consistent with the findings of RT12, the bulk, if not the entirety, of the CND gas is not tidally stable, and the observed clumps must be transient features.

3.6.3 Feature SW/S2

The most unusual properties from this analysis are associated with feature SW/S2, at a velocity of -20 km s^{-1}. This is the feature from which we detect the $J =$ 4–3 $v_2 = 1$ line of HCN, as well as the only feature from which we see significant self-absorption in the J= 3–2 and 4–3 spectra of both HCN and HCO$^+$ (Figures 3.4, 3.5).

RADEX fits to this feature indicate that it has the highest column density of all features we survey (the best fit HCN columns are $10^{16.4}$ cm^{-2} and $10^{15.9}$ cm^{-2}

toward SW and S2 respectively), and that extremely high opacities ($\tau \sim 10 - 50$) are needed to account for the observed self-absorption in the line profiles. However, this self-absorption could also be explained by either a line-of-sight temperature gradient (The S2/SW feature could lie on the near side of the CND, with its rear face heated by the inner cavity), or a separate, cooler gas clump in front of a warmer, dense clump at the same velocity in the CND. In these scenarios, the column densities could be lower than those found by our RADEX fits. One way to test this is by looking for emission from rarer isotopologues of HCN and other species. Although the opacities from our RADX fits are sufficiently high that the $HC^{15}N$ lines should be detectable (with intrinsic line intensities of a few hundred mK, assuming a Galactic center $^{15}N/^{14}N$ ratio of 600 Wilson & Rood 1994), the large beam sizes of our observations dilute the expected signal so that it is still lower than our observed upper limits for the $HC^{15}N$ lines. Higher-resolution observations of this region, with for example ALMA, should be able to either detect the $HC^{15}N$ line or put stronger upper limits on its presence. Ultimately, interferometric follow-up is necessary to distinguish between the scenarios presented above. Such observations are also critical to disentangling and successfully fitting the potentially multiple gas components in feature SW/S2, and to more precisely modeling the radiative excitation occurring in this region.

3.6.4 CND Chemistry

Recent measurements suggest that the central 300 parsecs of the Galaxy are subject to an elevated cosmic ray ionization rate, ranging from $\zeta \sim 10^{-15} - 10^{-14}$ s^{-1} (Oka et al. 2005; Goto et al. 2008, 2011; Goto et al. 2013) up to 10^{-13} s^{-1} (Yusef-Zadeh et al. 2007; Yusef-Zadeh et al. 2013b; Yusef-Zadeh et al. 2013). For comparison, the typical interstellar cosmic ray ionization rate ζ_0 is estimated to

be 3×10^{-17} s^{-1}, although recent observations by Indriolo & McCall 2012 suggest that it may be an order of magnitude higher. A high flux of cosmic rays is suggested to be responsible for heating the molecular gas in the Galactic center, particularly for elevating the observed gas temperatures (50-200 K, e.g.; Güsten et al. 1985; Hüttemeister et al. 1993a) above the observed dust temperatures (15-30 K, e.g.; Mezger et al. 1986; Molinari et al. 2011) in this region (Güsten et al. 1981; Ao et al. 2013; Clark et al. 2013). A predicted result of such a high ionization rate is a high fractional ionization of the molecular gas (Papadopoulos 2010; Ao et al. 2013; Yusef-Zadeh et al. 2013b): molecular ions such as HCO^+ should be more abundant, and this should be reflected in a lowered [HCN]/[HCO^+] relative abundance (Meijerink et al. 2006). A high flux of X-rays could also alter the gas chemistry in this region. As the CND gas is in close proximity to the central supermassive black hole which may have recently (within the past few hundred years) undergone an outburst several orders of magnitude stronger than its typical flares (Koyama et al. 1996; Murakami et al. 2000; Inui et al. 2009; Ponti et al. 2010), it is also possible that molecular abundances in this environment have been affected by an enhanced X-ray flux.

The ratio of observed HCN and HCO^+ line intensities has been suggested to be a useful diagnostic for identifying gas in both X-ray dominated (XDR) and cosmic-ray dominated (CRDR) environments (Meijerink et al. 2006, 2007). We investigate the possibility that gas in the CND is subject to either a XDR or CRDR environment by comparing the observed ratio of the HCN and HCO^+ J = 4-3 transitions in the CND to those derived in the XDR and CRDR models of Meijerink et al. (2006, 2007). The observed ratios of HCN 4-3 and HCO^+ 4-3 in the CND are between 1.5 and 2.0 (and the ratios of the $H^{13}CN$ and $H^{13}CO^+$ isotopologues of the same transition, which are free of opacity effects, are even higher, ranging from 2.5 to 5). The predicted HCN 4-3 to HCO^+ 4-3 ratio for

a CRDR with a cosmic ray ionization rate of 5×10^{-15} s^{-1} and a density of 10^5 cm^{-3} is 0.85 (Meijerink et al. 2006). Predicted ratios for HCN 4-3 to HCO$^+$ 4-3 in an XDR with densities higher than 10^5 cm^{-3}are less than 0.4. As HCN 4-3 is significantly stronger than HCO$^+$ 4-3 in the CND, the environment of this gas is not consistent with predictions for molecular gas in a CRDR (at least for densities $\sim$ a few 10^5 cm^{-3}; it is possible that for higher densities than those probed by this model, the observed HCN/HCO$^+$ ratio could be consistent with a moderate cosmic ray flux like that inferred from H_3^+ measurements of Oka et al. 2005), or an XDR of any density. At a minimum, these observation constraints indicate that there may be variations in the cosmic ray ionization rate throughout the CMZ, which is consistent with observations of H_3O^+ in Sgr B2, indicating $\zeta = 1 - 4 \times 10^{-16}$ (van der Tak et al. 2006), much lower than values inferred for some individual clouds (Yusef-Zadeh et al. 2013). These observations also suggest that neither X-rays nor cosmic rays are responsible for heating the CND gas, consistent with recent findings by Goicoechea et al. (2013) for hot gas interior to the CND. Other possible heating mechanisms for the gas are photodissociation regions (PDRs): we find that the measured HCN / HCO$^+$ ratios are consistent with the model predictions of Meijerink et al. (2007) for a relatively high-density PDR ($10^5 - 10^6$ cm^{-3}, similar to densities derived by our excitation analysis), or shocks, both of which have been suggested to heat gas temperatures in Galactic center clouds above dust temperatures (Rodríguez-Fernández et al. 2004).

3.7 Summary

In this paper, we present observations of multiple lines of HCN and HCO$^+$, including the ^{13}C isotopologues, toward four positions in the circumnuclear disk (CND) of molecular gas and dust in the central parsecs of the Galaxy. We use

the measured main beam brightness temperature of each line over the majority of the line profiles (excluding velocity ranges where there is contamination from other nearby clouds) to constrain the H_2 volume densities, kinetic temperatures, molecular column densities, and areal filling factors of dense gas in the CND. We also model the physical conditions over limited velocity ranges corresponding to single clumps identified in interferometric studies, in order to determine whether the conditions in individual clumps deviate from the average physical conditions in the CND gas. Our main findings are summarized below:

1. Using the RADEX radiative transfer code to fit to the majority of the line profiles from HCN and HCO^+, and assuming purely collisional excitation, we find typical densities of $\log(n[\ cm^{-3}]) \sim 5.3 - 6.5$, and typical temperatures of $T \sim 100 - 400$ K for the dense gas in the CND, although in some cases the highest temperatures present are unconstrained by these fits. Fitting to limited velocity ranges in the profile corresponding to individual clumps, we derive slightly lower temperatures and slightly higher densities. This suggests conditions in individual clumps may deviate from the average physical conditions in the CND gas. However, from our RADEX models, we find only one feature (S1) which could have a density sufficiently high to be tidally stable; the bulk of the gas in the CND is not stable against tidal shearing.

2. The average HCN and HCO^+ densities for the CND gas indicated by the RADEX fits are consistent within the uncertainties with results from other tracers including CO and dust, although the best-fit HCN densities tend to be slightly higher than inferred by these other excitation analyses.

3. We also detect vibrationally-excited HCN for the first time in the CND. We observe the J=4-3 $v_2 = 1$ line toward the southern emission peak of

the CND, at a velocity of -20 km s^{-1}, consistent with the SW/S2 clump. We model the excitation of this line by including radiative excitation of HCN due to hot dust in the CND, and find that the observed brightness temperature of this line requires dust temperatures in this region to be $> 125 - 150$ K. If such hot dust is present in other clumps along the inner edge of the CND, this would have the effect of lowering the densities we find with HCN. Dust temperatures of T$\sim$150 K are sufficient to bring the densities we derive for the southern emission peak into agreement with those found using other tracers, such as CO and dust, and would then make it unlikely that *any* of the gas in the CND is tidally stable.

CHAPTER 4

Detection of Widespread Hot Ammonia in the Galactic Center

Typical gas temperatures throughout the Central Molecular Zone are so hot that the chemistry of this entire 600 pc region of this galaxy resembles that found in typical 'hot cores'– the precursors to massive protostars. However, the heating source for this gas is debated– is it due to the dissipation of turbulent energy (in which case, the source of turbulent energy must also be identified), due to the far-ultraviolet flux impinging upon photodissociation regions (PDRs), due to a high cosmic ray flux, or the result of episodes of past X-ray irradiation? It is likely that many of these factors combine to generate the observed high temperatures in CMZ clouds, but the degree to which each contributes is not clear. Separating the effects of local and global heating sources throughout the CMZ will require studies of hot gas in clouds tracing the full range of environments in the central 600 parsecs, including clouds which are strong PDRs, have high cosmic ray fluxes, are interacting with supernova regions, and clouds which appear entirely isolated from these potential heating sources.

In this chapter, I present the detection of metastable inversion lines of ammonia (NH_3) from energy levels high above the ground state. These lines are detected in both emission and absorption toward fifteen of seventeen positions in the central 300 parsecs of the Galaxy. In total, seven metastable transitions

of $NH_3$are observed: (8,8), (9,9), (10,10), (11,11), (12,12), (13,13) and (15,15), with energies (in Kelvins) ranging from 680 to 2200 K. Emission from NH_3(8,8) and (9,9) is also mapped in two clouds in the Sgr A complex (M-0.02-0.07 and M-0.13-0.08), showing that the line emission is concentrated toward the the dense centers of these molecular clouds. The rotational temperatures derived from the metastable lines toward M-0.02-0.07 and M-0.13-0.08 and an additional cloud (M0.25+0.01) range from 350 to 450 K, too hot for cosmic rays to be the source of heating for this gas. Similarly highly-excited lines of NH_3 have previously been observed toward Sgr B2, where gas with kinetic temperatures of $\sim$ 600 K had been inferred. These observations show that the existence of a hot molecular gas component is not unique to Sgr B2, but rather appears common to many Galactic center molecular clouds.

4.1 Introduction

The physical conditions in the molecular gas of the central 300 parsecs of the Galaxy (the Central Molecular Zone or CMZ) differ significantly from conditions in the molecular gas in the rest of the Galactic disk. Molecular gas in the CMZ exists primarily in giant molecular clouds of sizes 15 to 50 pc, and masses $10^4 - 10^6$ $M_\odot$. The average densities in these clouds ($10^4 - 10^5$ cm^{-3}) are a few orders of magnitude above those typically found in Galactic disk clouds. Gas in CMZ giant molecular clouds also more turbulent, as indicated by typical linewidths of $20-30$ km s^{-1} (Bally et al. 1988; Morris & Serabyn 1996). The gas in these clouds, most of which are not actively forming stars, is further measured to be warmer (T $\sim$ 25 - 200 K, Güsten et al. 1981; Hüttemeister et al. 1993a; Ao et al. 2013) than gas in quiescent molecular clouds in the disk, which is generally measured to have T $\sim$ 5 - 10 K.

The observed temperature structure of CMZ clouds is complex. Hüttemeister et al. (1993a) used ammonia to measure two temperature components, 25 K and 200 K, with the 25 K component attributed to gas with densities of $n \sim 10^5$ cm^{-3} and the 200 K component attributed to less dense gas of n $\sim 10^4$ cm^{-3}. Ao et al. (2013) confirm via observations of formaldehyde that the dense gas has temperatures up to at least 100 K. Rodríguez-Fernández et al. (2001) also observe a hot (T$\sim 400-600$ K) and dense ($n \lesssim 10^6 cm^{-3}$) molecular gas envelope in CMZ clouds in rotational transitions of H_2. In Sgr B2, the densest and most massive molecular cloud in the CMZ, which is actively forming massive stars, an extremely hot (T$\sim$ 700 K) component of gas is observed in absorption lines of NH_3 (Mauersberger et al. 1986; Hüttemeister et al. 1993b; Hüttemeister et al. 1995; Ceccarelli et al. 2002; Wilson et al. 2006). Not only is hot gas associated with molecular clouds in the CMZ, there is also evidence for a diffuse ($n \sim 50 - 200$ cm^{-3}), warm (T = 250-400 K) molecular gas component throughout the CMZ, inferred from absorption line measurements of H_3^+ toward numerous lines of sight in the CMZ (Oka et al. 2005; Goto et al. 2008, 2011) and measurements of H_3O^+ and para-H_2O toward Sgr B2 and Sgr A (Lis et al. 2010b, 2012; Sonnentrucker et al. 2013).

The ammonia molecule (NH_3) is a very useful thermometer for dense molecular gas. Its relatively low dipole moment ($\mu = 1.47$ D) means that its metastable levels can relatively quickly come to thermal equilibrium with the surrounding gas via collisions with H_2 for densities of n $\geq 10^4$ cm^{-3}. NH_3 also has a symmetric top structure which gives rise to inversion doublets as the nitrogen atom tunnels back and forth through the potential barrier presented by the plane of the hydrogen atoms. The non-metastable ($J \neq K$) levels decay downward quickly (A $\sim 10^{-2}$ sec^{-1}), populating the metastable $J = K$ levels. These latter levels cannot radiatively decay by allowed transitions (Oka et al. 1971, except for a slow

octopole transition;). The $\Delta K = \pm 3$ collisional transitions are similarly very slow ($A \sim 10^{-9}$ sec^{-1}, Cheung et al. 1969), so that the rotational temperature derived from the ratio of column densities of metastable levels is close to but less than the kinetic temperature, T_K(Morris et al. 1973; Danby et al. 1988). Because the decay time of the non-metastable levels is so much shorter, the rotational temperatures derived from the column densities of non-metastable levels with $\Delta K = 0$ are not sensitive to the kinetic temperature, but are instead sensitive to the local excitation conditions, reflecting the gas density and/or the intensity of the far-infrared radiation field.

Using measurements of highly excited metastable inversion lines of NH_3, we find evidence for a $T \gtrsim 400$ K gas component, similar to that observed toward Sgr B2 (Wilson et al. 2006), but which appears common to dense molecular clouds in the CMZ. We present spectra of NH_3 (8,8) and (9,9) lines toward a sample of 15 molecular clouds in the CMZ, as well as spectra of higher-excitation NH_3 lines toward three of these clouds. Additionally, we map the distribution of NH_3 (8,8) and (9,9) emission in the molecular clouds near Sgr A: M-0.02-0.07 and M-0.13-0.08, and we detect non-metastable ammonia emission in these clouds for the first time. Based on these observations, we discuss our constraints upon the density and column density of this gas, and its relation to previously-observed hot molecular gas components in the CMZ.

4.2 Observations and Data Reduction

The observations presented in this paper were primarily made with the 100 m Green Bank telescope (GBT) of the National Radio Astronomy Observatory[1]

[1]The National Radio Astronomy Observatory is a facility of the National Science Foundation operated under cooperative agreement by Associated Universities, Inc.

during the periods of May 12- 29, 2009, November 12, 2010; January 3 and 23, April 15, and Dec 24, 2011. Single pointing measurements of the (8,8) and (9,9) metastable NH_3 inversion lines were made toward a sample of 17 positions in 15 clouds (Table 4.1; Figure 4.1). For three of these positions (M-0.02-0.07, M-0.13-0.08, M0.25+0.01) we additionally observed the (10,10), (11,11), (12,12), (13,13) and (15,15) lines. We also observed the (2,1), (3,2) and (4,3) non-metastable inversion lines in M-0.02-0.07 and M-0.13-0.08. Frequencies of all the observed transitions are given in Table 4.2. The spectral resolution of the observations was 390.625 KHz, or 3.1 to 4.4 km s^{-1}over the observed range of frequencies, sufficient to resolve lines with intrinsic widths of 15 to 30 km s^{-1}.

Table 4.1: Observed Sources

Source	**RA (J2000)**	**Dec (J2000)**	Galactic **Longtitude**	Galactic **Latitude**
G1.6-0.025	$17^h49^m19.9^s$	-27° 34′ 11.0″	1°.376	-0°.122
M0.83-0.10	$17^h47^m57.9^s$	-28° 17′ 00.0″	0°.383	-0°.368
Sgr B2 (N)	$17^h47^m20.1^s$	-28° 22′ 21.0″	0°.321	-0°.244
Sgr B2 (M)	$17^h47^m20.3^s$	-28° 23′ 06.0″	0° .321	-0°.245
Dust ridge	$17^h46^m11.5^s$	-28° 37′ 10.0″	0°.207	-0°.020
M0.25+0.01	$17^h46^m10.3^s$	-28° 43′ 37.0″	0° .205	-0°.016
G0.18-0.04	$17^h46^m14.0^s$	-28° 46′ 49.0″	0°.211	-0°.028
M0.16-0.10	$17^h46^m26.8^s$	-28° 51′ 05.0″	0°.233	-0°.070
M0.11-0.08	$17^h46^m13.3^s$	-28° 53′ 29.0″	0°.210	-0°.026
Polar Arc	$17^h45^m06.6^s$	-28° 46′ 27.0″	0°.099	+0°.191
G0.07+0.04	$17^h45^m37.5^s$	-28° 52′ 40.0″	0°.151	+0°.091
M-0.02-0.07	$17^h45^m52.4^s$	-28° 59′ 02.0″	0°.175	+0°.042
S. Streamer/CND	$17^h45^m39.5^s$	-29° 01′ 07.0″	359°.300	-0°.437
M-0.13-0.08-b	$17^h45^m37.9^s$	-29° 03′ 52.0″	359°.298	-0°.432
M-0.13-0.08	$17^h45^m37.4^s$	-29° 05′ 37.0″	359°.297	-0°.431
M-0.32-0.19	$17^h45^m37.7^s$	-29° 18′ 28.0″	359°.297	-0°.431
Sgr C	$17^h44^m40.7^s$	-29° 27′ 59.0″	359°.203	-0°.247

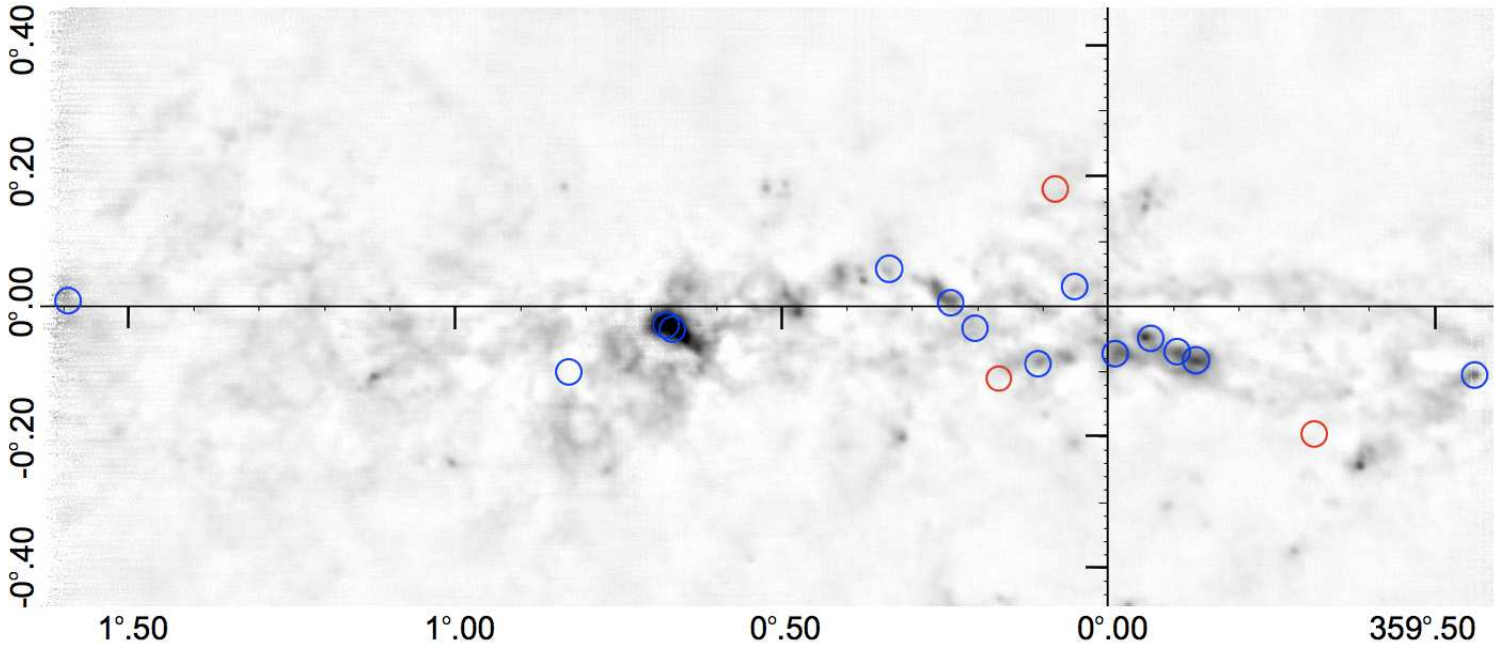

Figure 4.1: Positions of observed NH_3 spectra overlaid on a Bolocam 1.1 mm image of the CMZ (Bally et al. 2010). Blue circles represent positions where NH_3 (9,9) is detected (in either emission or absorption); red circles represent non-detections of NH_3 (9,9).

The metastable NH_3 inversion transitions were made using one beam from the dual-beam Ka-band receiver, and the non-metastable observations were made using the K-band receiver (decommissioned in 2011). We employed a position-switching technique, with an offset position of RA = 17h46m00s -28°13′57″, for clouds east of ($l = 0.1°$), and an offset position of RA = 17h45m59.9s, Dec. = -29°16′47″ for more westerly clouds.

4.2.1 GBT Mapping

In addition to spectra from the pointed observations described above, we also mapped emission from the NH_3 (8,8) and (9,9) lines simultaneously over two $5' \times 5'$ fields toward M-0.02-0.07 and M-0.13-0.08. Toward M-0.02-0.07, we additionally mapped emission from the (1,1), (2,2), (3,3), (4,4) and (6,6) line over the same field. The maps were made using an on-the-fly mapping technique, alternately scanning along both Right Ascension and Declination. After every two scans, an emission-free off position was observed. The data were gridded in AIPS using the routine SDGRD.

4.2.2 VLA Mapping

Observations of the NH_3 (9,9) line in the M-0.02-0.07 cloud were also made with the VLA in the DnC configuration in January 2012. The phase calibrator for these observations was J1744-3116, and the flux calibrator was 3C286. The total integration time on this target was 31 minutes. We mapped emission from this line in two overlapping fields centered on R.A., decl. (J2000): ($17^h45^m53^s.266$, $-28°59'12''.61$) and ($17^h45^m51^s.245$, $-28°59'52''.65$), with a primary beam size of $1.8'$. The spectral resolution of these observations was similar to that of the GBT, 250 kHz or 2.7 km s^{-1}. The data were cleaned using the multi-scale CLEAN

Table 4.2: Observed Transitions of NH_3

Transition	Frequency	Upper State Energy[1]	GBT beam
(J, K)	**(MHz)**	**(K)**	**FWHM**
(4,3)	22688.3120	237.8	33.3″
(3,2)	22834.1851	150.2	33.0″
(2,1)	23098.8190	80.4	32.7″
(1,1)	23694.4955	23.3	31.8″
(2,2)	23722.6333	64.4	31.8″
(3,3)	23870.1292	123.5	31.6″
(4,4)	24139.4163	200.5	31.3″
(6,6)	25056.0250	408.1	30.1″
(8,8)	26518.9810	686.8	28.4″
(9,9)	27477.9430	852.8	27.5″
(10,10)	28604.7370	1036.4	26.4″
(11,11)	29914.4860	1237.6	25.2″
(12,12)	31424.9430	1456.4	24.0″
(13,13)	33156.8490	1692.7	22.8″
(15,15)	37385.1280	2217.2	20.2″

algorithm in the CASA reduction package[1], resulting in a synthesized clean beam FWHM of $2''.3 \times 2''.4$. The noise in the final image is 0.25 Jy beam^{-1}.

4.2.3 GBT Calibration

Using the GBTIDL[2] reduction and analysis software, we corrected the antenna temperature of the observed targets for the frequency-dependent opacity at the observed elevation. Given the latitude of the GBT, the elevation at which the Galactic center targets were observed was uniformly low, ranging from 10° to 23°. The atmospheric opacity estimate was taken from a GBT archive of frequency-dependent opacities calculated from the weather conditions at the time of the observations. We then fit for and removed the local baseline fluctuations around each line.

We next used observations of the flux calibrator 3C286 to more accurately determine the relative amplitude calibration of the data, which is otherwise limited to $10 - 15\%$ accuracy by temporal fluctuations in the noise diode. The amplitude of the noise diode will also vary with frequency, so this relative calibration is important for an accurate comparison of line intensities across a range of frequencies. The expected flux density (S_ν) of 3C286 at the line frequency is determined by interpolating the data of Ott et al. (1994). The theoretical aperture efficiency as a function of frequency for the GBT (Ron Maddalena, personal communication) is given by:

$$\eta_{\rm eff,theor} = 2.0 \exp\left(-\left[0.00922\,\nu\,({\rm GHz})\right]^2\right) \tag{4.1}$$

The measured aperture efficiency for 3C286 can be calculated as:

[1]http://casa.nrao.edu/
[2]http://gbtidl.nrao.edu/

$$\eta_{\rm eff,meas} = {\rm T}_A \exp\left(\tau_{atm}/\sin\theta\right)/{\rm S}_\nu, \tag{4.2}$$

where θ is the elevation at which the flux calibrator was observed, and τ_{atm} is the atmospheric opacity estimate calculated from the archived weather conditions at the time of the observations. 3C286 is observed at a higher elevation than the Galactic center, however, as with the Galactic center sources, the resulting differences in the atmospheric path are accounted for by correcting the antenna temperature in the above equation for the frequency-dependent opacity at the observed elevation.

We then apply an amplitude correction to the data, that is the ratio of the theoretical to measured aperture efficiency. Our measured amplitude corrections vary both with frequency and between observing runs, and range from 0.7 to 1.3, a slightly larger correction than the stated 10-15% variation attributable to the noise diodes. Finally, assuming that the observed emission is extended over an area larger than the telescope beam (see Section 4.4.2.2), we also apply a correction for the main-beam efficiency, to convert the measured antenna temperatures to main-beam brightness temperatures. For the GBT, this correction is 1.32 at all frequencies.

We estimate the uncertainty of our relative amplitude calibration to be $< 5\%$, based on the RMS fluctuations in the observed spectrum of the phase calibrator.

4.3 Results and Analysis

4.3.1 Detection of the metastable NH_3 (9,9) through (15,15) lines

From our survey of 17 positions toward 15 giant molecular clouds we detect the NH_3 (9,9) metastable inversion line toward thirteen positions, all but two of which we also simultaneously detect in the NH_3 (8,8) line. The locations of the 13 positions for which we detect the (9,9) line are shown in blue in Figure 4.1. We detect NH_3 (9,9) in emission toward ten of these positions, and in absorption toward three of them (Figure 4.2). We also marginally ($\sigma \lesssim 3$) detect emission from the (8,8) and (9,9) lines toward two additional positions.

The strongest emission from these highly-excited lines of NH_3 is toward M-0.02-0.07. For this cloud and two other of the strongest detections, M-0.13-0.08 and M0.25+0.01, we performed follow-up observations of the NH_3 (10,10), (11,11), (12,12), (13,13) and (15,15) lines. We detect all of these lines except for the (15,15) line in M0.25+0.01, for which we have only an upper limit (Figure 4.3). The parameters of all of the observed lines of NH_3 are reported in Table 4.3. We derive temperatures for these three clouds in Section 4.3.4.

NH_3 (1,1), (2,2), (3,3), (4,4) and (6,6) spectra from maps of M-0.02-0.07 at the same positions as the higher-excitation lines are also shown in Figures 4.4 and 4.5. Parameters for all lines except the (1,1) and (2,2) lines (which have hyperfine structure, and are reported separately in Table 4.4) are also reported in Table 4.3.

Table 4.3: NH_3 Line Parameters

Source	Transition	T_{mb} (K)	v_{center} (km s^{-1})	Δv (km s^{-1})	Velocity-integrated T_{mb} (K km s^{-1})	Column Density (cm^{-1})
G1.6-0.025	(8, 8)	< 0.08				
	(9, 9)	0.211±0.068	158.6±0.8	25.3±1.8	5.91± 0.41	3.7±0.26 $\times 10^{13}$
M0.83-0.10	(8, 8)	0.081±0.018	32.8±2.2	50.3±5.2	4.15±0.22	2.7±0.15 $\times 10^{13}$
	(9, 9)	0.084±0.032				
Sgr-B2-M	(8, 8)	-4.797±0.153	61.9±0.2	19.9±0.5	-104.68± 5.26	[1] 2.5±0.07 $\times 10^{13}$
	(9, 9)	-5.580±0.228	62.8±0.2	17.5±0.4	-103.83± 5.26	[1] 2.7±0.06 $\times 10^{13}$
Sgr-B2-N	(8, 8)	-3.034±0.612	71.1±0.9	27.7±2.2	-82.21± 4.84	[1] 2.9±0.23 $\times 10^{13}$
	(9, 9)	-4.391±0.753	71.1±1.1	29.1±2.6	-129.62± 7.09	[1] 4.1±0.37 $\times 10^{13}$
M0.34+0.06	(8, 8)	< 0.07				
	(9, 9)	0.144±0.051	0.8±1.6	20.2±3.8	3.42± 0.26	2.1±0.16 $\times 10^{13}$
M0.25+0.01	(8, 8)	0.370±0.016	34.2±0.2	19.0±0.6	7.37± 0.37	4.8±0.25 $\times 10^{13}$
	(9, 9)	0.431±0.034	34.6±0.4	21.2±1.0	9.79± 0.50	6.1±0.32 $\times 10^{13}$
	(10,10)	0.143±0.028	37.9±0.4	16.3±1.0	2.45± 0.17	1.5±0.10 $\times 10^{13}$
	(11,11)	0.100±0.023	37.9±0.4	15.2±1.0	1.60± 0.12	9.0±0.67 $\times 10^{12}$

Source	Transition	T_{mb} (K)	v_{center} (km s^{-1})	Δv (km s^{-1})	Velocity-integrated T_{mb} (K km s^{-1})	Column Density (cm^{-1})
	(12,12)	0.126±0.022	35.5±0.4	19.7±0.9	2.69± 0.16	1.4±0.08 $\times 10^{13}$
	(13,13)	0.048±0.013	35.8±0.6	13.2±1.3	0.70± 0.06	3.5±0.28 $\times 10^{12}$
	(15,15)	< 0.04				
G0.18-0.04	(8, 8)	0.023±0.008				
	(9, 9)	0.056±0.008	23.6±0.5	14.0±1.2	0.82± 0.05	5.1±0.32 $\times 10^{12}$
M0.16-0.10	(8, 8)	< 0.08				
	(9, 9)	< 0.10				
M0.11-0.08	(8, 8)	0.480±0.048	50.9±0.4	20.8±0.9	10.82± 0.58	7.1±0.38 $\times 10^{13}$
	(9, 9)	0.733±0.053	51.4±0.3	20.5±0.8	16.50± 0.85	1.0±0.05 $\times 10^{14}$
Polar-Arc	(8, 8)	< 0.04				
	(9, 9)	< 0.05				
G0.07+0.04	(8, 8)	0.053±0.010	-32.9±0.7	19.8±1.7	1.12± 0.07	7.4±0.45 $\times 10^{12}$
	(9, 9)	0.051±0.010	-30.3±0.6	22.6±1.3	1.23± 0.07	7.7±0.47 $\times 10^{12}$
M-0.02-0.07	(2, 1)	0.120±0.011	46.0±0.6	28.4±1.4	3.85± 0.20	1.6±0.08 $\times 10^{14}$
	(3, 2)	< 0.05				
	(3, 3)	19.412±0.049	45.6±0.4	22.7±1.0	533.14±63.98	4.6±0.55 $\times 10^{15}$

Source	Transition	T_{mb} (K)	v_{center} (km s^{-1})	Δv (km s^{-1})	Velocity-integrated T_{mb} (K km s^{-1})	Column Density (cm^{-1})
	(4, 4)	3.312±0.072	45.9±0.3	22.7±1.1	93.19±11.18	7.5±0.90 $\times 10^{14}$
	(6, 6)	2.987±0.125	46.2±0.3	22.7±1.1	73.57± 8.83	5.3±0.64 $\times 10^{14}$
	(8, 8)	0.663±0.021	46.3±0.2	25.4±0.4	18.59± 0.93	1.2±0.06 $\times 10^{14}$
	(9, 9)	0.843±0.029	46.6±0.2	24.8±0.4	22.66± 1.14	1.4±0.07 $\times 10^{14}$
	(10,10)	0.314±0.033	46.8±0.3	21.2±0.6	6.85± 0.37	4.1±0.22 $\times 10^{13}$
	(11,11)	0.242±0.021	47.5±0.2	21.3±0.5	5.54± 0.29	3.1±0.16 $\times 10^{13}$
	(12,12)	0.286±0.015	45.5±0.2	26.2±0.5	8.12± 0.41	4.3±0.22 $\times 10^{13}$
	(13,13)	0.116±0.013	46.9±0.3	21.2±0.8	2.53± 0.13	1.3±0.07 $\times 10^{13}$
	(15,15)	0.098±0.017	44.2±0.5	21.7±1.3	2.21± 0.12	9.8±0.54 $\times 10^{12}$
Streamer	(8, 8)	-0.136±0.029	34.2±0.5	19.6±1.2	-3.09± 0.20	[1] 2.8±0.17 $\times 10^{12}$
	(9, 9)	-0.159±0.016	35.0±0.3	15.0±0.6	-2.52± 0.14	[1] 3.6±0.15 $\times 10^{12}$
CND	(8, 8)	0.049±0.02				
	(9, 9)	0.068±0.026	-62.0±6.3	52±14.8	3.78± 0.21	2.4±0.13 $\times 10^{13}$
M-0.13-0.08-b	(8, 8)	0.290±0.016	8.7±0.3	20.2±0.6	6.44± 0.33	4.2±0.22 $\times 10^{13}$
	(9, 9)	0.343±0.017	8.0±0.3	23.0±0.7	8.74± 0.44	5.5±0.28 $\times 10^{13}$
M-0.13-0.08	(2, 1)	0.250±0.013	19.6±0.3	20.9±0.6	5.64± 0.29	2.3±0.12 $\times 10^{14}$

Source	Transition	T_{mb} (K)	v_{center} (km s^{-1})	Δv (km s^{-1})	Velocity-integrated T_{mb} (K km s^{-1})	Column Density (cm^{-1})
	(3, 2)	0.099±0.019	20.1±0.6	18.7±1.4	1.92± 0.13	3.9±0.27 $\times 10^{13}$
	(4, 3)	0.047±0.012	19.8±0.6	14.2±1.5	0.64± 0.07	9.7±1.01 $\times 10^{12}$
	(10,10)	0.211±0.025	19.8±0.3	15.1±0.7	3.32± 0.19	2.0±0.11 $\times 10^{13}$
	(11,11)	0.126±0.009	18.7±0.3	18.4±0.8	2.43± 0.12	1.4±0.07 $\times 10^{13}$
	(12,12)	0.197±0.014	19.4±0.2	18.4±0.5	3.91± 0.20	2.1±0.11 $\times 10^{13}$
	(13,13)	0.050±0.016	20.1±0.9	15.8±2.1	0.91± 0.07	4.6±0.35 $\times 10^{12}$
	(15,15)	0.055±0.013	20.9±0.5	15.3±1.1	0.90± 0.06	4.0±0.27 $\times 10^{12}$
M-0.32-0.19	(8, 8)	< 0.07				
	(9, 9)	< 0.09				
Sgr-C	(8, 8)	0.064±0.019	-53.0±0.8	12.5±1.9	0.77± 0.09	5.1±0.56 $\times 10^{12}$
	(9, 9)	0.089±0.017	-52.9±0.4	12.4±0.9	1.18± 0.09	7.4±0.56 $\times 10^{12}$

[1]Reported quantity is N/T_{ex}, in units of cm^{-2} / K.

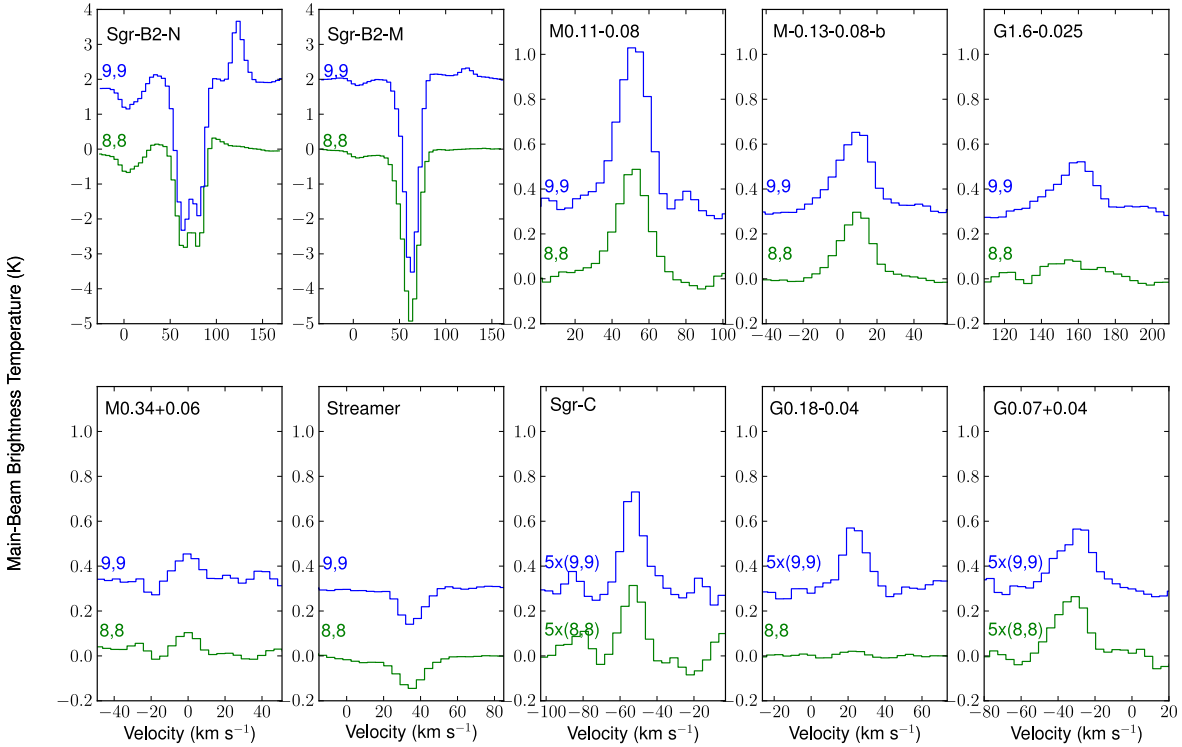

Figure 4.2: Spectra of NH_3 (8,8) and (9,9) toward the 9 positions where at least NH_3 (9,9) is detected. In the spectra of NH_3 (9,9) toward Sgr B2, the emission line to the right of the NH_3 absorption feature is the J_K= 13_2-13_1 line of CH_3OH, with a rest frequency of 27.47253 GHz.

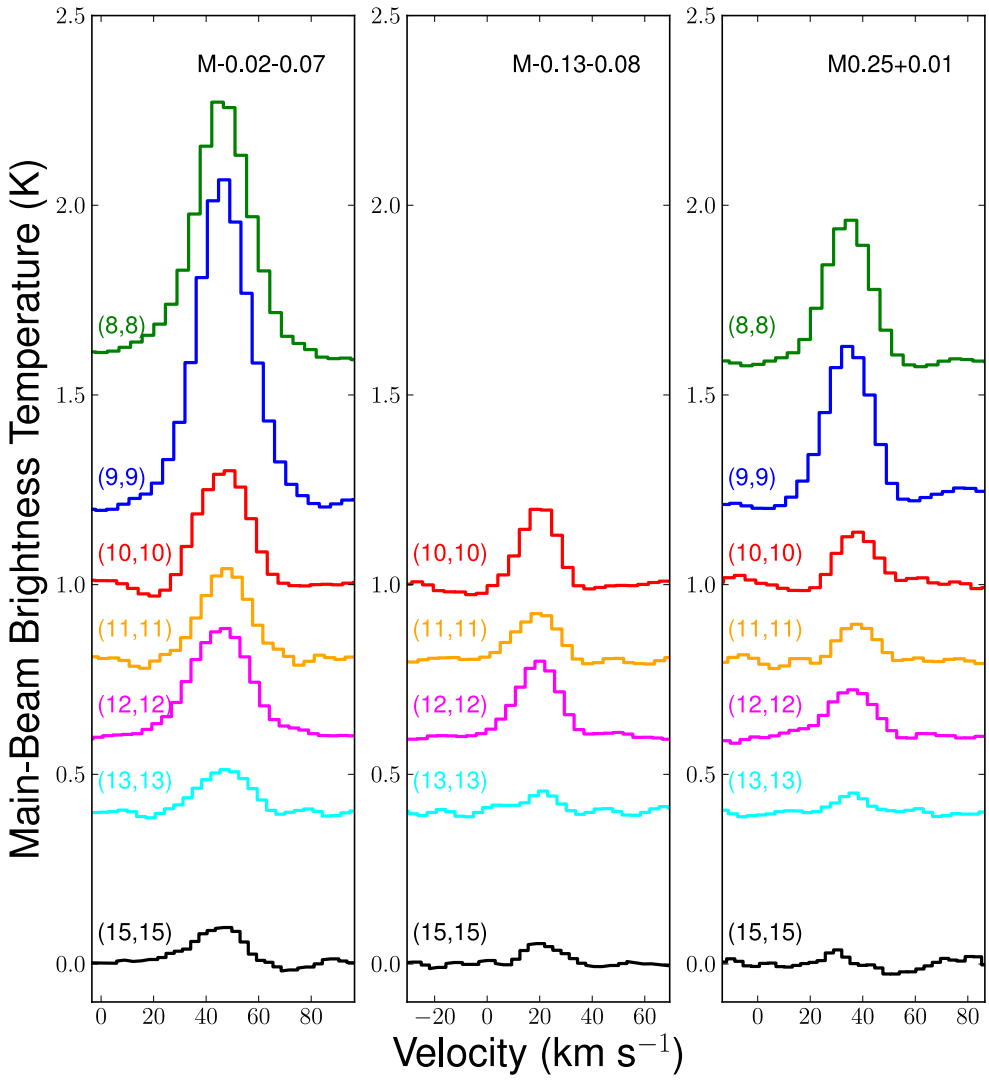

Figure 4.3: Spectra of NH_3 (8,8) through (15,15) toward the three clouds for which we measure the rotational temperature.

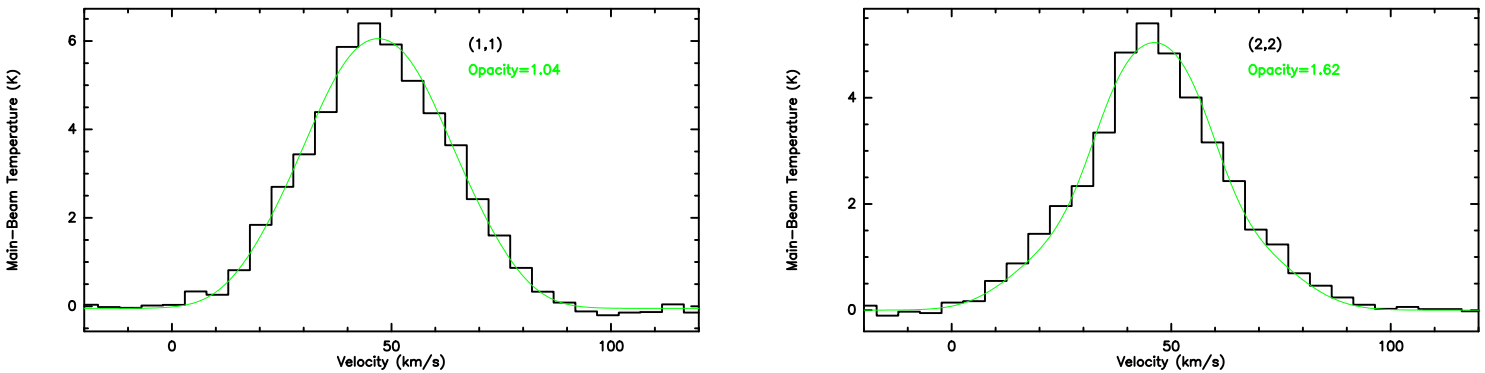

Figure 4.4: Fits to the hyperfine structure of the two lowest metastable NH_3 lines toward M-0.02-0.07. Although the individual hyperfine line components are not resolved, by assuming an intrinsic width we are able fit to the strength of the satellite lines and thus constrain the line opacities. Here, we have assumed the line width is 22.7 km s^{-1}, equal to that of the (3,3), (4,4) and (6,6) lines, for which the hyperfine components are too faint to affect the line profile.

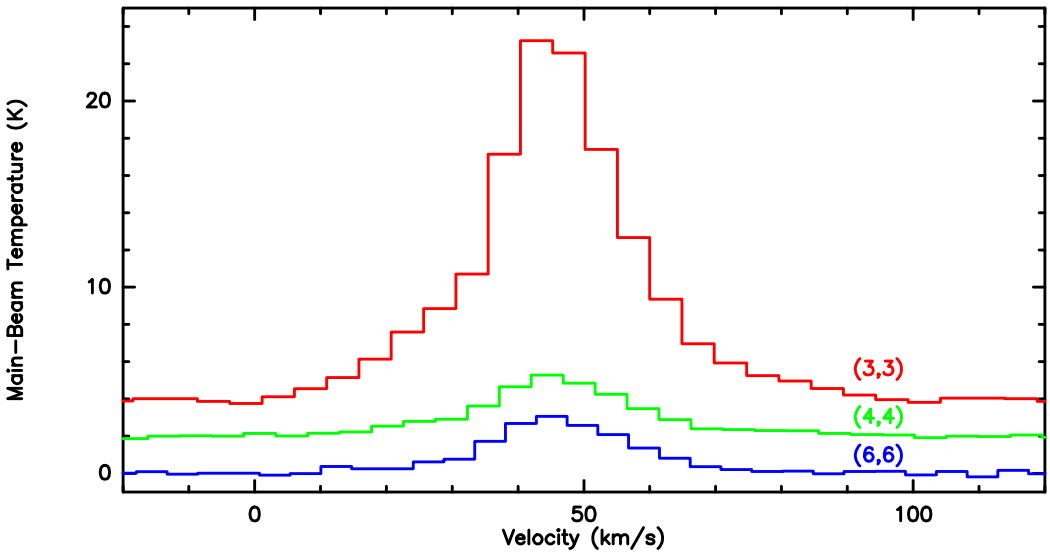

Figure 4.5: Metastable NH_3 (3,3) through (6,6) line profiles extracted from a map of M-0.02-0.07 at the position of the pointed, higher-excitation line observations shown in Figure 4.3.

Table 4.4: NH_3 Fits to Hyperfine Line Structure for M-0.02-0.07

Transition	Peak $T_{ex} \times \tau$ (K)	v_{center} (km s^{-1})	Δv (km s^{-1})	Velocity-integrated $T_{ex} \times \tau$ (K km s^{-1})	[1]Column Density (cm^{-1})	Opacity (τ)
(1, 1)	$8.0^{+1.3}_{-4.0}$	47.0 ± 0.1	[2]$22.7^{+9.3}_{-1.7}$	430^{+70}_{-220}	$5.7^{+0.9}_{-2.9} \times 10^{15}$	$1.04^{+0.26}_{-0.94}$
(2, 2)	$10.0^{+8.5}_{-5.2}$	46.2 ± 0.1	[2]$22.7^{+9.3}_{-5.7}$	510^{+430}_{-260}	$5.1^{+4.3}_{-2.6} \times 10^{15}$	$1.62^{+1.96}_{-1.52}$

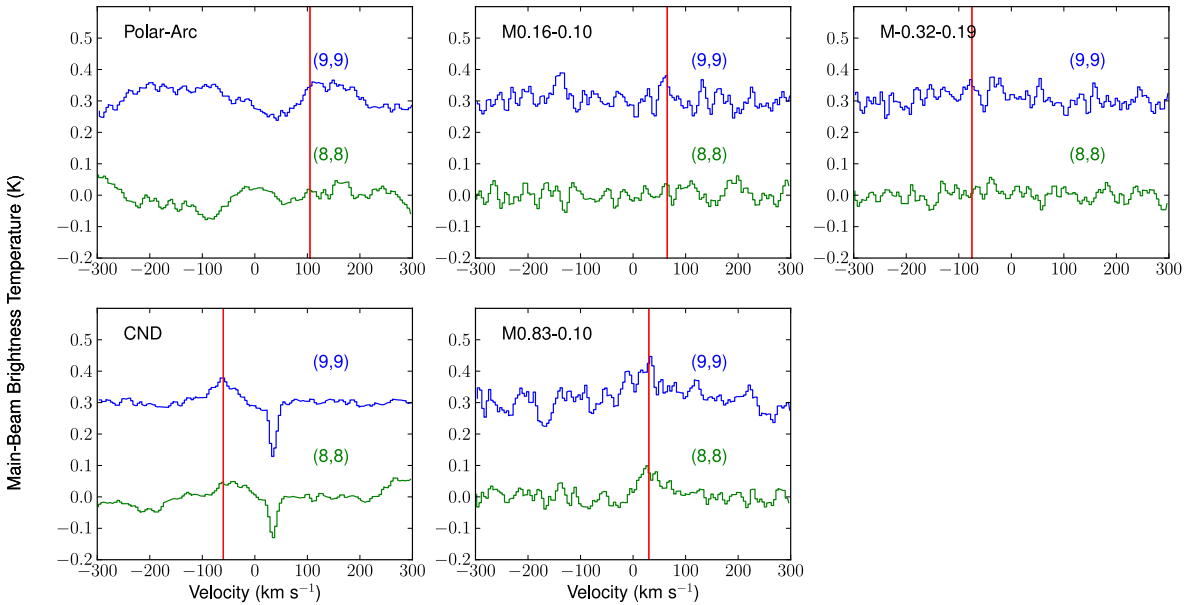

Figure 4.6: **Top row:** Observations of NH_3 (8,8) and (9,9) toward the 3 positions where neither line is detected. The central source velocity is shown as a red line in each plot. **Bottom row:** Observations of NH_3 (8,8) and (9,9) toward two positions where these lines are marginally detected. The CND and Polar Arc were observed during more optimal weather conditions on a different date than the other sources, resulting in lower system temperatures and a lower noise level. The absorption line at 20 km s^{-1}in the spectrum of the CND is the same as that shown in Figure 4.2, and is from the Southern Streamer feature

4.3.2 Nondetections

Toward three positions, we do not detect either the NH_3 (8,8) or (9,9) lines: the polar arc, M0.16-0.10, and M-0.32-0.19 (Figure 4.6). Upper limits on the line intensities for these clouds are reported in Table 4.3. The polar arc is a higher-latitude filament extending at a 40° angle from (l,b = 0°, 0.05°) to (l,b = 0.2°, 0.25°) which is seen in CO and CS surveys of the Galactic center (Bally et al. 1988). There is a strong velocity gradient along the arc, from 70 to 140 km s^{-1}, but it is not clear from its kinematics where this feature lies along the line of sight. The other two positions correspond to Galactic center clouds for which temperatures in excess of 500 K have been inferred by Rodríguez-Fernández et al. (2001) using mid-infrared observations of pure rotational lines of H_2. We discuss these non-detections and their significance further in Section 4.4.3.

4.3.3 Detection of Non-metastable Ammonia

We also detected several low-excitation non-metastable NH_3 lines toward the two strongest sources of metastable NH_3: M-0.02-0.07 and M-0.13-0.08. Non-metastable NH_3 lines have previously been detected in the Galactic center cloud Sgr B2 (Zuckerman et al. 1971; Hüttemeister et al. 1993b), but only upper limits existed for M-0.02-0.07 and M-0.13-0.08 (Armstrong & Barrett 1985). The (2,1) and (3,2) lines were detected toward both clouds, and the (4,3) line was additionally detected toward M-0.13-0.08. The line parameters are listed in Table 4.3. Whereas M-0.02-0.07 has stronger metastable line emission, M-0.13-0.08 exhibits stronger non-metastable line emission. As we discuss in Section 4.4.4, non-metastable line emission requires either a strong far-infrared radiation field or very high densities to populate these transitions, so it is possible that the non-metastable line emission originates in a gas component distinct from the

metastable emission, since the same constraints do not apply to the metastable lines.

4.3.4 Ammonia Temperatures

4.3.4.1 Column Densities

To determine the rotational temperatures using Boltzmann statistics, we must first determine the level populations from each rotational transition. We can only measure temperatures for those clouds for which we detect at least two lines of either para ($K \neq 3n$, where n is an integer) or ortho ($K = 3n$) NH_3, as ortho- and para-NH_3 have different spin-alignment states, so transitions between para- and ortho-NH_3 are forbidden, and the two behave as separate species.

For lines observed in emission, assuming the emission to be optically thin, the beam-averaged column density can be calculated as:

$$N(J,K) = \frac{1.55 \times 10^{14}\,\mathrm{cm}^{-2}}{\nu} \frac{J(J+1)}{K^2} \int T_{\mathrm{m}b}\,\mathrm{dv}\,, \tag{4.3}$$

as in Mauersberger et al. (2003). Here, the transition frequency ν is in GHz, and $\int T_{\mathrm{m}b}\,\mathrm{dv}$ is the integrated intensity of the line, in units of K km s^{-1}.

For lines observed in absorption against the background continuum, to determine the column density requires knowledge of the excitation temperature across the inversion doublet. As this quantity is indeterminate without radiative transfer modeling, which we do not undertake here, we thus report the quantity N/T_{ex}, as follows:

$$\frac{N}{\mathrm{T}_{ex}} = \frac{1.61 \times 10^{14}}{\nu} \frac{J(J+1)}{K^2} \tau \Delta v_{1/2}\,\mathrm{cm}^{-2}/K\,, \tag{4.4}$$

as in Hüttemeister et al. (1995). Here, $\Delta v_{1/2}$ is the FWHM of the line in km s^{-1}, and τ is the line optical depth, which can be measured directly from the brightness temperature of the line relative to the continuum:

$$\tau = -ln\left(1 - \frac{|T_L|}{T_C}\right). \tag{4.5}$$

We also observed the (1,1) and (2,2) lines in M-0.02-0.07. These lower-excitation lines have prominent hyperfine structure made up of multiple satellite lines spaced a few tens of km s^{-1} from the main line. As the relative LTE line strengths of the satellite lines are a small fraction[1] of the total line intensity, the hyperfine satellites are generally optically thin, and so the ratio of the satellite line strengths to the main line provides a good measure of the line opacity. However, for the wide linewidths typical of Galactic center clouds, these satellite lines are strongly blended with the main line, and the intrinsic line widths are uncertain. First, we fit to the hyperfine structure and estimate the opacities using the FIT routine in the CLASS software package[2] by assuming that the (1,1) and (2,2) line widths are the same as that measured for the (3,3), (4,4) and (6,6) lines: 22.7 km s^{-1}(Table 4.4). The fits to these lines are shown in Figure 4.4.

However, if the line width is not fixed, there is a wide range of equally good fits for widths from 17 to 30 km s^{-1}. We also report in Table 4.4 the range of parameter space for which the fit is at least as good as the fixed-width fit. Comparably-good fits are found for opacities ranging from 0.1 to 1.3 for the (1,1) line and from 0.1 to 3.6 for the (2,2) line. For comparison, Hüttemeister et al. (1993a) find (1,1) and (2,2) opacities of $\sim 5 - 5.7$ for M-0.13-0.08, which has

[1]The ratio of the intensities of the hyperfine satellites to the main line are 0.28 and 0.22 for the inner and outer pairs of satellite lines to the (1,1) line, and 0.06 for the both pairs of satellites to the (2,2) line

[2]http://www.iram.fr/IRAMFR/GILDAS

comparable (and in fact slightly lower) hot NH_3 column densities. This difference in opacity is likely because the linewidths in this cloud are much narrower (Hüttemeister et al. measure the widths of the (1,1) and (2,2) lines to be ∼10 km s^{-1}, or half of that which we measure for M-0.02-0.07).

We calculate the column density of the optically thick (1,1) and (2,2) lines in M-0.02-0.07 according to Equation 1 from Appendix B of Hüttemeister et al. (1993a):

$$N(J,K) = 6.8 \times 10^{12}\,\mathrm{cm}^{-2}\frac{J(J+1)}{K^2}\int T_{ex}\,\tau \mathrm{dv}. \tag{4.6}$$

For these two lines, the calculated column densities are the actual, rather than beam-averaged column densities. We convert these column densities to beam-averaged column densities by assuming that the emission from these low-excitation lines fills the beam, and the beam filling factor is equal to one. If the actual beam filling factor is smaller than one, then the column densities we report are upper limits on the true beam-averaged column densities. The calculated column densities for all of the detected lines are given in the last column of Tables 4.3 and 4.4a.

4.3.4.2 Rotational Temperatures

The rotational temperature of NH_3 can be determined by plotting the logarithm of the normalized column density: $log_{10}[N(J,K)/(g_{op}(2J+1))]$, where the statistical weight factor, g_{op}, is 2 for ortho-NH_3 (K = 9, 12, 15), and 1 for para-NH_3 ($K = 8, 10, 11, ...$), against the upper level energy of each rotational state (Figure 4.7). From the Boltzmann equation, the rotational temperature is then related to the slope m as T_{rot}= -log_{10}(e)/m. As described previously, the rotational tem-

perature is close to but less than the kinetic temperature, T_K(Morris et al. 1973; Danby et al. 1988). The amount by which the rotational temperature underestimates the true kinetic temperature is lessened when the upper level energy of the highest transition used to measure the temperature is equal to or greater than the kinetic temperature of the gas being measured. However, rotational temperatures determined using transitions between lower (J, K) levels will significantly underestimate the true kinetic temperature of a hot gas component. When the logarithm of the level populations implied by observations is plotted against the upper level energy (a Boltzmann diagram, e.g., Figure 4.7), one can see this effect manifested as a slightly upward-concave curve instead of a straight line expected for a constant T_K. This is especially apparent for the lowest-excitation metastable lines of NH_3 , (c.f., Hüttemeister et al. 1993a).

As we have both ortho- and para- species of NH_3, we perform a simultaneous fit for both the slope of the line and the ortho/para ratio, or the multiplicative factor between the two species required for the best fit lines to have the same intercept. Since, as previously discussed, the measured rotational temperature is a lower limit to the actual kinetic temperature, and the more highly-excited lines yield a better limit for a high kinetic temperature than lower lines, we also determine the rotational temperatures between the two highest para-lines $(K = 11, 13)$, and between the two highest ortho-lines $(K = 12, 15)$.

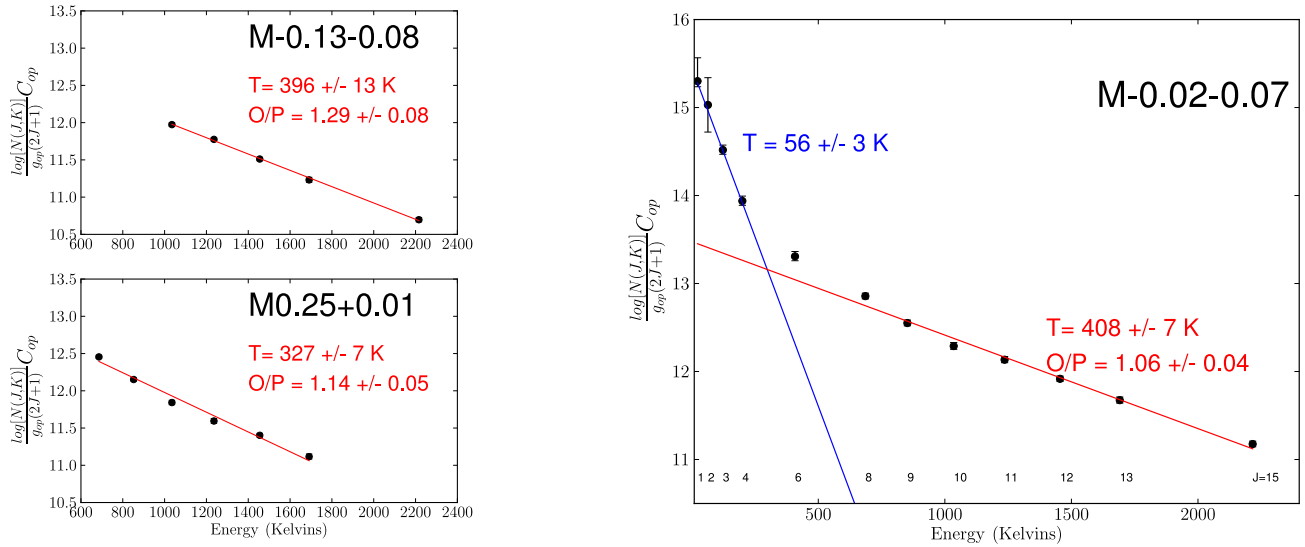

Figure 4.7: Rotational NH_3 temperatures determined for three clouds. The temperatures are fit to the slope of the normalized NH_3 column density (corrected for the level degeneracy) plotted against the energy of each transition in units of Kelvins. The plotted column densities are multiplied by an additional factor, C_{op}, which is equal to one for lines of ortho-NH_3, and for lines of para-$NH_3$is equal to the ortho-to-para ratio (O/P) calculated using the J$\geq$ 8 lines. For the J $\leq$ 6 lines in M-0.02-0.07, we multiply by the C_{op} determined for the higher-J lines.

Table 4.5: NH_3 Rotational Temperatures

Source	$T_{Fit-All}$ (K)	Ortho / Para Ratio	T_{Ortho} (K)	T_{Para} (K)	$T_{13,13-11,11}$ (K)	$T_{15,15-12,12}$ (K)
M0.25+0.01	330 ± 7	1.1 ± 0.1	350 ± 16	320 ± 9	410 ± 75	
M-0.02-0.07	410 ± 7	1.1 ± 0.1	430 ± 10	380 ± 10	430 ± 61	450 ± 31
M-0.13-0.08	400 ± 13	1.3 ± 0.1	410 ± 18	380 ± 21	360 ± 47	410 ± 33

Temperatures for the three clouds for which we observe NH_3 lines up to (J, K) = (15,15) are reported in Table 4.5. We find best-fit rotational temperatures using all measured lines that range from 340 K for M0.25+0.01, up to 410 K for M-0.02-0.07. The rotational temperatures calculated between the most highly-excited transitions, $T_{(15,15)-(12,12)}$ and $T_{(13,13)-(11,11)}$, are systematically higher, ranging from 410 K to 450 K.

For M-0.02-0.07 we also mapped the (1,1) through (4,4) and (6,6) lines. Using the spectra extracted from these maps at the same position as we observed the (8,8) through (15,15) lines in this cloud we can also derive rotational temperatures from the lower-excitation lines of NH_3. We derive rotational temperatures of $\sim$ 50 K for the para-NH_3 lines, and $\sim$ 100 K for the ortho-NH_3 lines (Figure 4.7). Using the results from the radiative transfer models of Ott et al. (2011), these rotational temperatures correspond to kinetic temperatures of $\sim$ 70 K (from the (2,2)-(4,4) rotational temperature), and $\sim$ 150 K (from the (3,3)-(6,6) temperature). However, as previously noted, the column densities of the (1,1) and (2,2) lines are quite uncertain, due to difficulty in fitting the hyperfine structure. If the column densities of these two lines are underestimated, then there may also be a cooler gas component present, more consistent with the $\sim$ 25 K component detected by Hüttemeister et al. (1993a) toward a large sample of CMZ clouds.

4.3.4.3 Ortho/Para ratio

As part of our temperature fits using the highly-excited NH_3 transitions observed toward M0.25+0.01, M-0.02-0.07, and M-0.13-0.08, we also derive the ortho/para ratio for each cloud. Because radiative and gas-phase collisional transitions are not allowed between ortho and para states, the ortho/para ratio is representative of the conditions (either the gas temperature, or if the NH_3 is formed via

grain surface reactions, the grain temperature) at the time of formation of the molecules. We find ortho/para ratios ranging from 1.0 to 1.3, which indicate that the molecules formed in "high"-temperature (T $\gtrsim$40 K) conditions (Takano et al. 2002), that is, temperatures that are consistent with the inferred temperatures of Galactic center molecular clouds.

Finally, for the majority of sources presented here, we only observed the NH_3 (8,8) and (9,9) lines. As the (8,8) line is a transition of para-NH_3, and the (9,9) a transition of ortho-NH_3, it is necessary to assume an ortho/para ratio in order to determine a temperature using these lines. Adopting an ortho/para ratio of 1.1 (the average value from the fits to M0.25+0.01, M-0.02-0.07, and M-0.13-0.08 reported in Table 4.5), we find rotational temperatures for all but one of these sources (G1.6+0.025, described below) which range from $\sim$200 to 320 K. For comparison, $T_{8,8-9,9}$ for M-0.02-0.07 calculated using the same ortho/para ratio is only $\sim$ 220 K.

For three sources, G1.6+0.025, M0.34+0.06, and G0.18-0.04, if we use the marginal detection or upper limit on the (8,8) line strength, then an assumed ortho/para ratio of 1.1 does not yield a meaningful temperature. For these clouds, it appears that the ortho/para ratio may be slightly anomalous. If we assume a temperature of 200 K (as measured from lines of CH_3OH in G1.6+0.025 by Menten et al. (2009)), then we find ortho/para ratios of 2.6, 2.0, and 2.4 in G1.6+0.025, M0.34+0.06, and G0.18-0.04, respectively. If we assume a temperature of 400 K, then the ortho/para ratios would be correspondingly reduced: 1.7, 1.3, and 1.6. These higher ratios suggest that the NH_3 in these clouds may have formed in relatively low-temperature conditions: $<$ 20 K (Takano et al. 2002),

4.4 Discussion

From the observed sample of 17 pointings toward CMZ molecular clouds, we detect emission from the highly-excited (9,9) inversion transition of NH_3 in thirteen locations. For three of the strongest NH_3 sources, we further observe NH_3 lines up to (15,15) and measure rotational temperatures which, as discussed previously, are lower limits to the actual kinetic temperature of the gas. Below, we compare the temperatures we find to previous NH_3 temperature measurements, and discuss the distribution of these clouds in the CMZ, he nature of this hot gas component, and its potential heating sources. Properties of individual sources in which we detect hot $NH_3$are described in the Appendix

4.4.1 Temperature ranges.

We find that the highest-excitation NH_3 lines we observe have rotational temperatures of 350 - 450 K gas in each of the three clouds for which we were able to determine temperatures. These temperatures are rotational temperatures, and thus a lower limit on the kinetic temperature, which must be greater than or equal to these values. As described in Section 4.3.4.2, these temperatures are derived from both ortho- and para-NH_3 lines with a simultaneous fit for temperature and the ortho/para ratio. The temperatures derived from just the ortho-NH_3 lines appear slightly higher than those derived from just the para-NH_3 lines, however this difference is generally within our measurement uncertainty, so it is not clear that this is a real effect. The observed ortho lines also have higher level energies, so may be more sensitive to presence of hotter gas, yielding rotational temperatures which are closer to the true kinetic temperature of the gas.

Previous temperature measurements in CMZ molecular clouds using metastable

NH_3 inversion lines from (1,1) to (6,6) indicated both a 25-50 K temperature component , and a 200 K temperature component(Güsten et al. 1985; Hüttemeister et al. 1993a). As the lines used in these temperature analyses are lower-excitation lines of NH_3, they are less sensitive to the presence of hot gas, and likely do trace intrinsically cooler gas in the cloud. However, the 200 K temperature component reported by Hüttemeister et al. (1993a) is actually a rotational temperature, and thus a lower limit to the true kinetic temperature of the gas. Using the results of large-velocity-gradient modeling of NH_3 excitation (Ott et al. 2005, 2011) which relate observed rotational temperatures to kinetic temperatures, we find that 2/3 of the Hüttemeister et al. (1993a) rotational temperatures derived from the (4,4)-(5,5) NH_3 lines are consistent with a kinetic temperature of $>$ 300 K. Observations of the (5,5) and (7,7) NH_3 lines by Mauersberger et al. (1986) in the same three clouds for which we measure temperatures also yielded higher rotational temperature estimates of $\sim$300 K. This suggests that the hot gas (T $\geq$ 350-450 K) we detect with highly-excited lines of NH_3 could be the same as the warm gas component previously detected by Hüttemeister et al. (1993a) and Mauersberger et al. (1986), and consistent with a model of just two temperature components in CMZ clouds: a cooler component of 25-50 K, and a hot component of $>$ 300 K. We test this idea in Section 4.4.2.2 using our observations of M-0.02-0.07, which include the (1,1) through (6,6) lines.

4.4.1.1 Caveats.

The temperatures we derive are based on several assumptions. First, we assume that the observed emission is roughly uniform over an area larger than the beam sizes of these observations. If the emission arises from a source that is more compact than the smallest beam (20″), then the observed brightness temperatures

would need to be corrected for the different beam size at each frequency. For M-0.02-0.07, in the extreme case that the NH_3 emission originated in a point source, we would determine a rotational temperature of ∼370 K, instead of ∼450 K. However, we find it extremely unlikely that the highly-excited NH_3 arises in compact sources (like hot cores). As we show below in Section 4.4.2.2, in M-0.02-0.07 we find that the majority of the NH_3 (9,9) flux arises on scales larger than tens of arcseconds. We also assume that the excitation temperature T_{ex} is the same for all of the NH_3 lines measured, which may not be valid over the wide range of level energies these transitions cover. Wilson et al. (2006) estimate for Sgr B2 that the variation in T_{ex} is roughly a factor of two: decreasing from 6 K for NH_3 (1,1) to 3 K for NH_3 (18,18).

The upper level energies of NH_3 assumed for these calculations, from the JPL Submillimeter, Millimeter, and Microwave Spectral Line Catalog (Table 4.2; Pickett et al. 1998), are systematically larger than upper level energies taken from the Spectral Line Atlas of Interstellar Molecules (SLAIM) (Available at http://www.splatalogue.net, F. J. Lovas, private communication; Remijan et al. 2007). The difference in level energies increases from 0.1%, for the (8,8) transition to 1.6%, for the (15,15) transition. Using the lower SLAIM values would result in temperatures 10-20 K lower than we report, a difference which is slightly larger than our estimated uncertainty.

4.4.2 The nature of the 400 K gas component

4.4.2.1 Distribution of NH_3 (9,9) in the CMZ

The positions where we detect NH_3 (9,9) are distributed throughout the central 3 degrees of the Galaxy. We detect this line in G1.6-0.25, which is 240 pc in projection to the east of Sgr A* (assuming $R_0 = 8.4$ kpc; Ghez et al. 2008; Gillessen

et al. 2009a), as well as in Sgr C (R = 80 pc to the west). We also detect the (9,9) line very strongly in M0.25-0.01, which in the infrared continuum appears strongly in absorption against the extended background emission (Longmore et al. 2012), suggesting that it is located at the front edge of the CMZ. The detection of the (9,9) line toward all of these positions implies that hot NH_3 is present in CMZ molecular clouds over a broad range of galactocentric radii. However, there are too few clouds in our sample for which we determine temperatures to be able to identify any correlations in the distribution or temperature of the hot gas with respect to location in the CMZ. We can say however that the presence of hot gas in a cloud does not require the cloud to be actively forming stars, as M0.25+0.01 is apparently almost entirely quiescent, having no embedded warm IR sources or compact HII regions.

Our maps of highly-excited NH_3 in two clouds in the central 10 pc (M-0.13-0.08 and M-0.02-0.07, Figures 4.8, 4.9, and 4.10) further show that the hot NH_3, as traced by the (8,8) and (9,9) lines, is truly concentrated in the dense centers of the CMZ clouds. The distribution of emission from these higher-excitation lines is almost identical to that of the lower-excitation (1,1) through (6,6) lines, which should trace, cool, dense gas. The $1.5' - 2'$ extended sizes of the hot NH_3 clouds, and their morphologies, are additionally very similar to those of the submillimeter and millimeter continuum emission from cool dust in the cores of these clouds. We also find that the hot NH_3 emission is morphologically and kinematically similar to emission from the dense-gas-tracing HC_3N 3-2 line, which we also observe in our GBT data.

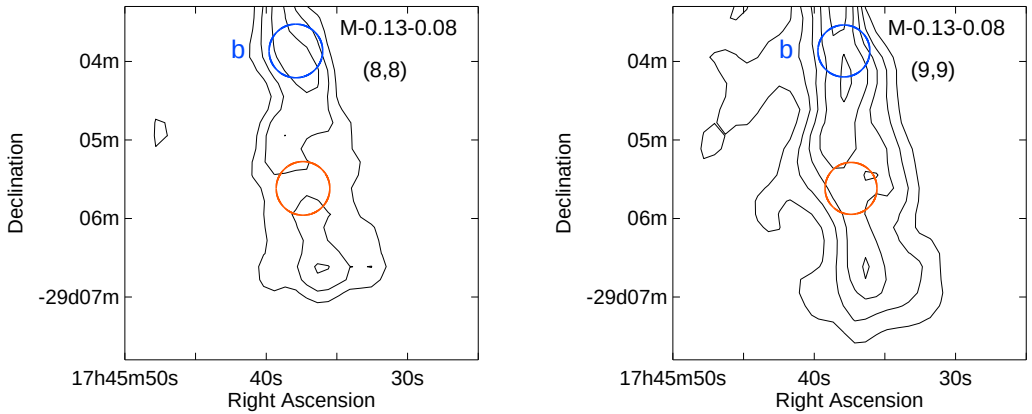

Figure 4.8: Maps of NH_3 (8,8) and (9,9) integrated main-beam brightness temperature in M-0.13-0.08. The contour levels are linearly spaced by 1.5 K km s^{-1}, with the lowest contour being 4.0 K km s^{-1}. The peak integrated brightness temperatures in the (8,8) and (9,9) maps are 7.8 K km s^{-1} and 10.8 K km s^{-1}, respectively.The noise levels in the images are 1.0 K km s^{-1} and 0.7 K km s^{-1}, respectively.

As the hot gas component traced by highly excited lines of NH_3 appears to be associated with the dense cores of molecular clouds, it is qualitatively different than another warm gas component (T= 200-350 K, n = 50-100 cm^{-3}) which has been detected in the CMZ from the absorption of H_3^+ along multiple lines of sight (Oka et al. 2005; Goto et al. 2008, 2011). In addition to being cooler and more tenuous, the gas component traced by H_3^+ is suggested to widespread throughout the entire CMZ (Goto et al. 2008), in contrast to the concentrated distribution of hot NH_3 that we observe toward the cores of CMZ clouds.

4.4.2.2 NH_3 in M-0.02-0.07

We observe the largest number of NH_3 transitions toward M-0.02-0.07, allowing us to probe in greater detail the properties of the hot NH_3 component in this cloud. In particular, we have mapped emission from the (1,1), (2,2), (3,3), (4,4), (6,6), (8,8) and (9,9) lines, allowing us to derive maps of the rotational temperature for selected transitions. We avoid the (1,1) and (2,2) lines, due to their uncertain opacity, and present maps of the rotational temperature between the (3,3) and (6,6) lines, the (4,4) and (8,8) lines, and the (6,6) and (9,9) lines (Figure 4.11). In order to create these maps, the higher-excitation line was convolved to the resolution of the lower-excitation line, and the maps were interpolated to have the same pixelization. Because the highest-excitation line used in these maps is the (9,9) line, the rotational temperatures shown in these maps are lower than the 400 K temperature component we derive for this cloud using transitions above (9,9). However, the average rotational temperatures do rise with the level of excitation of the two lines being used to construct the map.

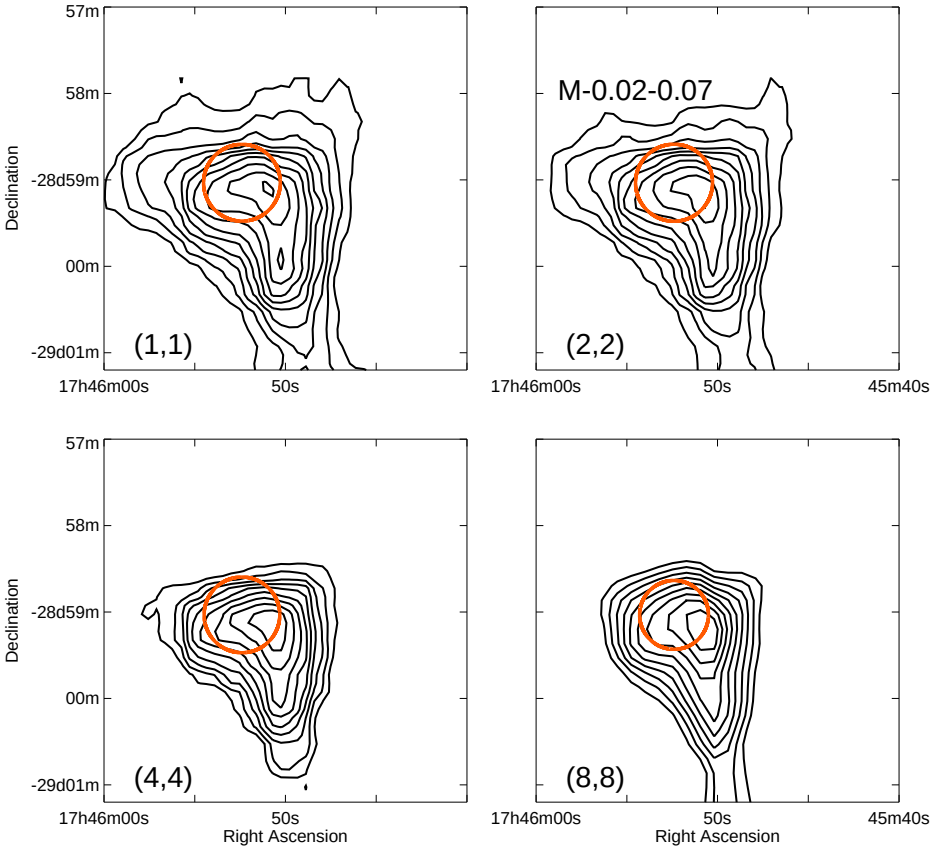

Figure 4.9: Maps of integrated main-beam brightness temperature for the para-NH_3 lines in M-0.02-0.07. The contours are linearly spaced from the peak integrated brightness temperature (290, 236, 106, and 16.4 K km s^{-1}, for the (1,1), (2,2), (4,4) and (8,8) lines, respectively) to 1/10 of this value. The noise levels in each map are 5, 5, 4, and 0.8 K km s^{-1}, respectively.

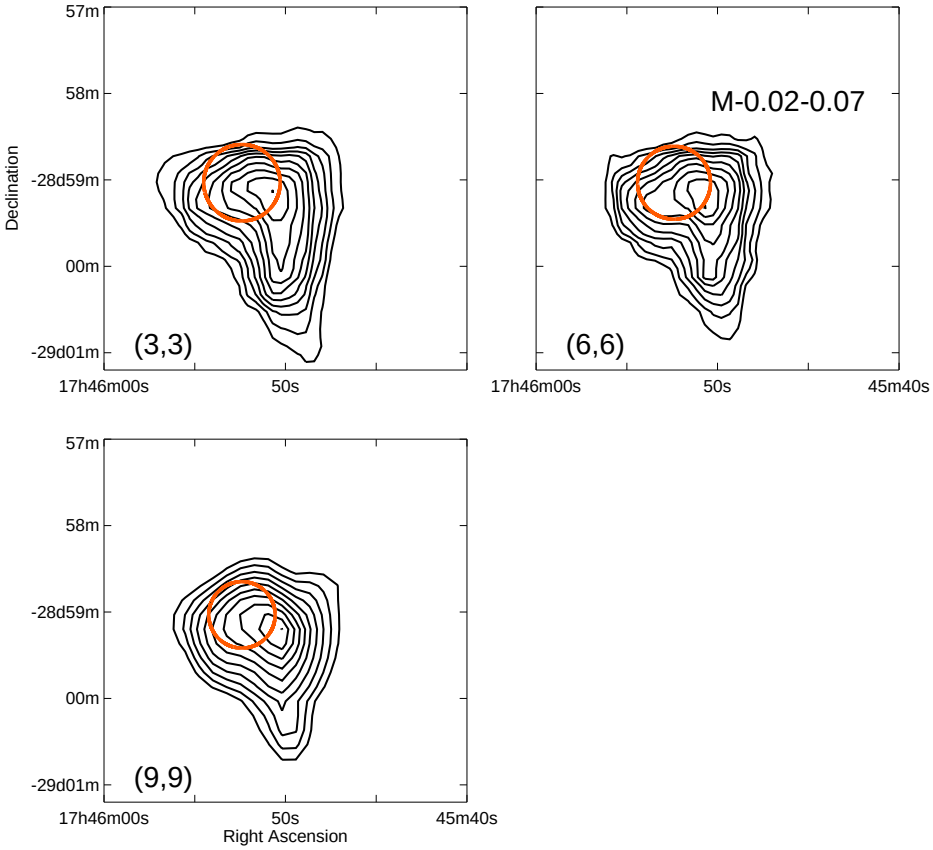

Figure 4.10: Maps of integrated main-beam brightness temperature for the ortho-NH_3 lines in M-0.02-0.07. The contours are linearly spaced from the peak integrated brightness temperature (608, 91, and 25.1 K km s^{-1} for the (3,3),(6,6), and (9,9) lines, respectively) to 1/10 of this value. The noise levels in each map are 6, 3, and 1.0 K km s^{-1}, respectively.

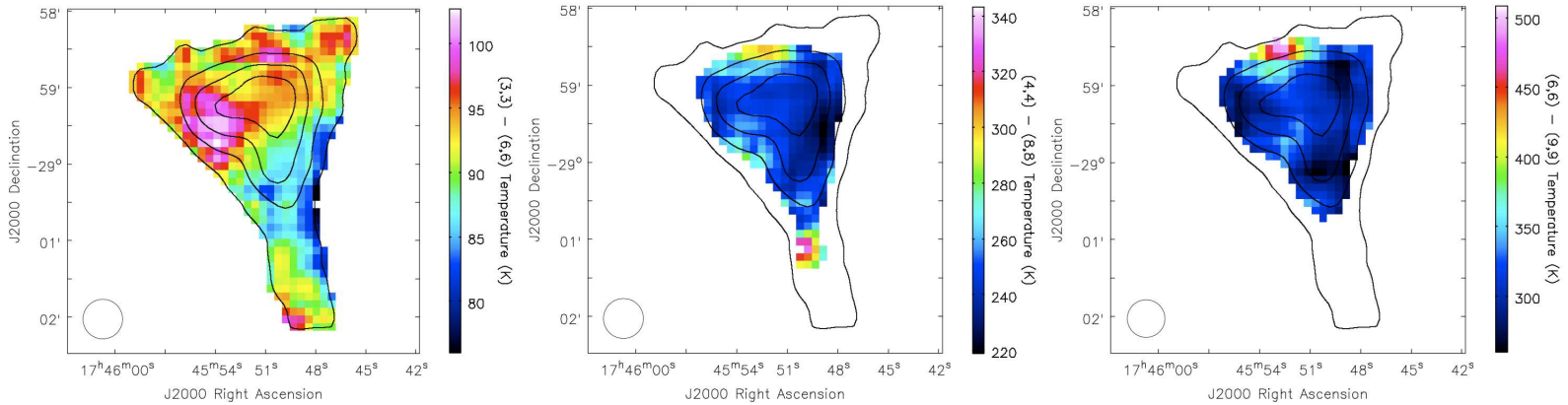

Figure 4.11: Maps of the rotational temperature in M-0.02-0.07 derived from the NH_3 (3,3) and (6,6) lines (Top), the NH_3 (4,4) and (8,8) lines (Middle), and the NH_3 (6,6) and (9,9) lines (Bottom). Contours of emission from the NH_3 (6,6) line are overplotted in black. As the rotational temperature is a lower limit to the kinetic temperature of the cloud, the rotational temperatures measured with these relatively low-excitation lines underestimate the temperature of the hottest gas measured in this cloud using lines above (9,9). The apparent peak in temperature in the (4,4)-(8,8) temperature map at the southern edge of the cloud lies on the edge of the (8,8) map, and so may not be a real feature.

All of the temperature maps show two main features. First, the variation in temperature across the cloud in all of the maps is relatively small: generally less than 50 K over the majority of the cloud. Secondly, as is especially apparent in the (3,3)-(6,6) temperature map, the western edge of the cloud is generally cooler than the eastern extension of the cloud. The western edge is the location of the ridge of compressed gas which is believed to have been swept up by the expansion of the adjoining Sgr A East supernova remnant (Serabyn et al. 1992). All three maps also show some evidence for higher temperatures near the southeast edge of the cloud. One possible source of these higher temperatures could be the four compact HII regions which are embedded in this part of the cloud (Goss et al. 1985; Yusef-Zadeh et al. 2010; Mills et al. 2011). The temperature maps using the (8,8) and (9,9) lines also show an additional, prominent feature: an apparent peak in the temperature on the northern edge of the cloud. This peak is not associated with any previously-identified feature of the cloud or its environment. We discuss potential heating mechanisms for this cloud in more detail in Section 4.4.5

Although we are able to construct temperature maps of M-0.02-0.07, the resolution of our GBT data ($\sim 25''$) is insufficient to check whether the hot NH_3 emission is truly uniform over the $1' - 2'$ dense centers of CMZ clouds, or whether it originates in unresolved compact structures within the clouds. To investigate this, we also made VLA observations of the (9,9) line in M-0.02-0.07 to measure the fraction of emission resolved out on angular scales approaching that defined by the shortest VLA baseline used for these observations ($\sim 60''$). Figure 4.12 shows the resulting VLA image of NH_3 (9,9) in M-0.02-0.07, smoothed to $10''$ resolution. Although the emission appears clumpy, the total integrated flux detected with the VLA is 26 Jy km s^{-1}, compared to a total integrated flux of 660 Jy km s^{-1} derived from our GBT observations. This means that 96% of the

emission is resolved out, originating from structures on tens of arcsecond scales, and so any apparent clumps are likely just minor peaks in this extended emission. We note that a significantly larger fraction of NH_3 (9,9) emission is resolved out by the VLA than was the case with NH_3 (3,3) ($\nu = 23.870$ GHz) in the similar M-0.13-0.08 cloud, 10 pc away in projection from M-0.02-0.07 (Armstrong et al. 1985). In M-0.13-0.08, Armstrong et al. found that 75% of the NH_3 (3,3) emission detected with a single-dish telescope was resolved out by the VLA. The largest recoverable angular scale should be $\sim$ 15% smaller at 27.5 GHz than at 23.9 GHz, and so, were the emission from the (3,3) and (9,9) lines on the same size scale, one would expect only slightly more emission to be resolved out in our higher-frequency observations. The much larger fraction of flux which is resolved out for the (9,9) line suggests that this higher-excitation line originates in a more extended component than the lower-excitation (3,3) line.

Although this would appear to favor an extended envelope as the origin of the highly-excited NH_3 emission, we also consider that our maps of NH_3 (8,8) and (9,9) emission in M-0.02-0.07 and M-0.13-0.08 do show the NH_3 emission to be somewhat concentrated toward the cloud centers. This suggests that most of this hot gas is found in the regions of highest gas column density, and is potentially co-extensive with the highest-density gas and cool dust in these clouds. We suggest that this is more consistent with the highly-excited NH_3 being distributed throughout the cloud, perhaps in a hot inter-clump medium, as opposed to being in a larger-scale envelope around the cloud's exterior. If in fact the hot NH_3 originates in a relatively uniform network of unresolved shocks, this could explain both the large fraction of emission which is resolved out by an interferometer, and the apparent concentration of the hot NH_3 emission toward the column density peaks of these clouds.

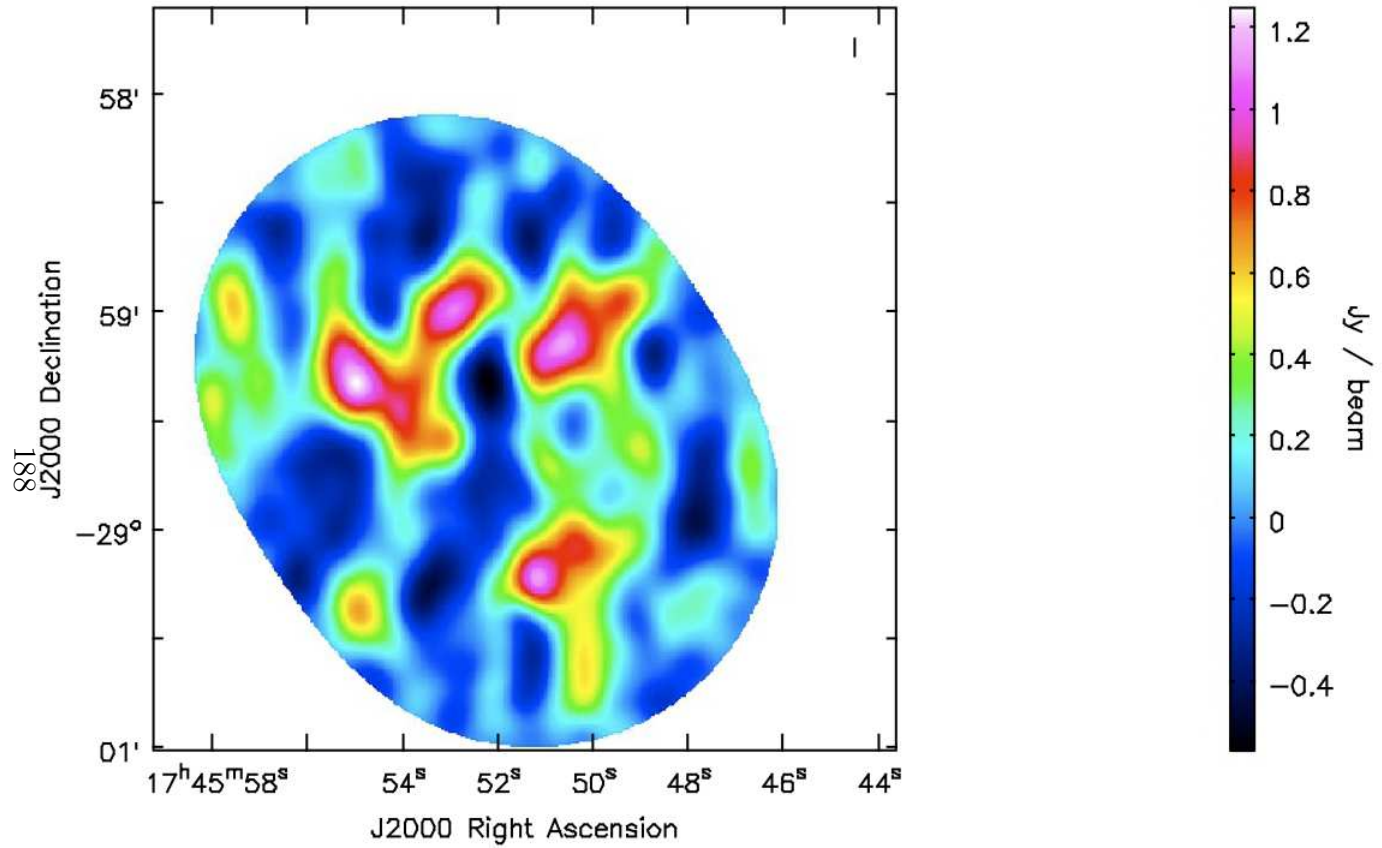

Figure 4.12: Map of resolved NH_3 (9,9) emission in M-0.02-0.07 from the VLA, convolved to a $10'' \times 10''$ resolution. The RMS noise in the image is 0.25 Jy beam^{-1}.

In M-0.02-0.07, for which we detected 14 transitions of NH_3, we can determine the fraction of the measured NH_3 column which arises from the most highly-excited transitions. To determine the total column density, we sum the contributions from all of the metastable levels up to J=15. We interpolate to estimate the column density for the J=5,7 and 14 levels, as we did not observe these lines. We also extrapolate to estimate the column density of the J=0 level using the column density of the J=1 level and the temperature determined from the (1,1), (2,2) and (4,4) lines ($\sim$ 50 K). In this way, we find that the total column density of NH_3 in M-0.02-0.07 is $\sim 2.1 \times 10^{16}$ cm^{-2}. If we assume that all of the column density above J=10 originates in a hot component, which is at a temperature of 400 K, then we can calculate the fraction of the column density in lower lines which is also due to this hot component. In this way, we calculate that 12% of the total measured NH_3 column in M-0.02-0.07 arises in a T$\geq$400 K component (see Figure 4.7).

However, the J=1 and J=2 column densities, which dominate the total column density, are also the most uncertain, due to difficulties in fitting the hyperfine structure of the (1,1) and (2,2) lines (See section 4.3.4.1). We can, however, determine a lower limit on the fraction of the NH_3 column which is hot by using the upper limits on the J=1 and J=2 column densities in the case that they are maximally opaque. Using these higher values (and further using a minimum temperature of 25 K to extrapolate to the column density of the J=0 level) we find an upper limit on the total column density of $\sim 2.9 \times 10^{16}$ cm^{-2}. The minimum fraction of the total NH_3 column density in M-0.02-0.07 which arises from a T $\geq$ 400 K component is then 7% (this fraction could also be higher if the beam filling factor of the (1,1) and (2,2) lines is less than 1, see discussion in Section 4.3.4.1). Note that this is only the fraction of NH_3 which arises from this hot component; for example, if the NH_3 abundance relative to H_2 is enhanced in the

hot component, the fraction of H_2 which is hot could be less than 7%.

Finally, in Figure 4.7 it is clear that there is a significant portion of the observed (6,6) and (8,8) column density (40% and 25%, respectively) which cannot be attributed either to a 50 K or 400 K temperature component. This excess column density indicates that two temperature components provide only an incomplete fit to the full range of temperatures in this cloud, which either requires an intermediate temperature component (like the ∼200-300 K component found by Hüttemeister et al. (1993a) or, more likely, a continuum of temperatures in order to properly fit all of the observed NH_3 line intensities.

4.4.3 Properties of clouds where NH_3 (9,9) is not detected

The three positions for which we do not detect emission from either NH_3 (8,8) or (9,9) – the Polar Arc, M0.16-0.10, and M-0.32-0.19 – are not strong submillimeter or millimeter sources (red circles in Figure 4.1). The latter two of these clouds were studied by (Rodríguez-Fernández et al. 2001, hereafter RF01), who measure strong emission from the S(3), S(4) and S(5) rotational lines of H_2, and derive rotational temperatures of ∼600 K. There are several possible reasons why we might not detect these clouds in highly-excited lines of NH_3, one of which is that these clouds are not sufficiently dense to give rise to strong NH_3 emission lines (to observe NH_3 in emission requires densities of $\gtrsim 10^3$ cm^{-3}). As RF01 find it most likely that these higher H_2 lines arise in very dense gas (n $\sim 10^6$ cm^{-3}), this is unlikely to be the explanation.

Another possibility is then that the column density of NH_3 in these two clouds is too low for highly-excited lines of NH_3 to be detectable. In one of these clouds, M-0.32-0.19, Hüttemeister et al. (1993a) also observe NH_3 lines from (1,1) to (6,6) and find evidence for a warm gas component with a temperature of ∼ 150

K. However, compared to M0.25+0.01, in which we do detect more highly-excited lines of NH_3, the column density of NH_3in M-0.32-0.19 is much lower: only 1/5 of the M0.25+0.01 column in the J=5 level. If the hot NH_3 column in M-0.32-0.19 is also 1/5 that of M0.25+0.01, this is consistent with the upper limits implied by our nondetection.

We also marginally detect NH_3 (8,8) and (9,9) in M0.83-0.10, which favors the idea that the H_2 and NH_3 may trace the same hot gas, but that the column density of NH_3 in many of these clouds is below our detection limit. RF01 find that their hot component makes up $\lesssim$1% of the column density of warm (T$\sim$ 150 K) H_2 in these clouds (which is itself only $\sim$25-30% of the total H_2 column), compared to our finding that the hot NH_3 component in M-0.02-0.07 makes up $\sim$10% of the total NH_3 column density in this cloud. If the hot gas in M0.83-0.10 has the same properties as that we detect in M-0.02-0.07, we can use the comparison of its (8,8) column density to that measured for M-0.02-0.07 and obtain an estimate of the total NH_3 column density in M0.83-0.10. Assuming that 10% of this gas arises in a T$\sim$ 400 K component, then the column density of hot NH_3 in this cloud would be $\sim 5 \times 10^{14}$ cm^{-2}, and compared to the column density of hot gas RF01 detect in this cloud would yield $[NH_3]/[H_2] \sim 2 \times 10^{-6}$. This is consistent with the NH_3 abundance Ceccarelli et al. (2002) find for the hot NH_3 envelope of Sgr B2. It then seems most likely that the clouds we observed which were detected by RF01, while having a relatively high fractional abundance of NH_3, simply have an NH_3 column density which is too low to be detected by our survey.

Finally, there is one cloud in common between our sample and that of RF01(M-0.13-0.08, referred to as M-0.15-0.07 in RF01) for which we do measure a hot gas component of $\sim$400 K, but RF01 do not detect a high-temperature gas compo-

nent. RF01 only detect the two lowest H_2 rotational lines, S(0) and S(1), in this cloud, from which they measure an intermediate-temperature component of $\sim$ 140 K. The fact that hot NH_3 is detected in this cloud, but not hot H_2, could either indicate that this cloud has a higher relative NH_3 abundance, or that the hot NH_3 and hot H_2 arise in different environments, and may be heated by separate mechanisms.

4.4.4 Density

The critical density of the highest-excitation NH_3 inversion lines, assuming a kinetic temperature of 300 K and extrapolating the expected collisional rates from the values calculated for transitions up to (6,6) by Danby et al. (1988), is a few $\times 10^3$ cm^{-3}. Thus, to detect these NH_3 transitions in emission requires gas that is at least this dense. The morphology and kinematics of the hot NH_3 emission mapped in M-0.02-0.07 and M-0.13-0.08 are also similar to those of the HC_3N 3-2 line, observed simultaneously, which has a critical density of n = 10^4 cm^{-3}. However, if the hot NH_3 has a substantially higher density than 10^4 cm^{-3}, there are two issues. First, one might expect this dense gas to arise in more compact sources, which would be inconsistent with our finding that $\sim$ 96% of the hot NH_3 emission is resolved out in our VLA observations. Gas in the cloud interior which is denser than $\sim 10^5$ cm^{-3} should also reach thermal equilibrium with dust in the cloud (Goldsmith 2001; Juvela & Ysard 2011). As no hot dust is detected from these clouds (Molinari et al. 2011; Longmore et al. 2012), this also favors a density lower than $\sim 10^5$ cm^{-3}.

The density of the similarly-hot NH_3 component in Sgr B2 was determined by a large-velocity-gradient model to be $< 10^4$ cm^{-3} (Ceccarelli et al. 2002), which is consistent with the density we infer for the hot gas in our cloud sample. Though

the NH_3 in Sgr B2 is hotter (600-700 K, compared to 400-500 K in the clouds we study), the emitting region appears to have a similar size to those we detect in M-0.02-0.07 and M-0.13-0.08. Mauersberger et al. (1986) mapped the slightly lower-excitation NH_3 (7,7) line in Sgr B2, measuring extended emission over a $\sim$ 1.5 arcminute area. For comparison, our maps of (8,8) and (9,9) toward M-0.02-0.07 and M-0.13-0.08 show that the emitting region has a size of $\sim 1.5' - 2'$. However, we note that the Sgr B2 cloud is a very actively star forming cloud which is an order of magnitude more massive than other CMZ clouds, and its properties are not generally typical of other Galactic center molecular clouds.

There are also three clouds in our sample for which RF01 derive the physical conditions from pure-rotational lines of H_2, finding T $\sim$ 600 K and n $\sim 10^6$ cm^{-3}. We marginally detect emission from the (8,8) and (9,9) lines in one of these clouds (M0.83-0.10), and suggest that for the others, the column density of hot NH_3 is below our detection limits. If the hot NH_3 and hot H_2 arise in the same gas component, this suggests that the hot NH_3 does arise in gas denser than 10^5 cm^{-3}, in which case, it is not clear why this gas is not in thermal equilibrium with the dust in these clouds. However, the RF01-derived temperatures and densities are based on purely collisional excitation of H_2; if there is additional radiative excitation, the actual H_2 densities and temperatures could be lower, possibly avoiding this discrepancy.

We also detect non-metastable lines of NH_3 in both M-0.02-0.07 and M-0.13-0.08, the only clouds in our sample for which we observed these lines (Figure 4.13). The presence of non-metastable NH_3 implies that either the emitting gas is quite dense, or that there is a strong far-infrared radiation field (Zuckerman et al. 1971; Sweitzer et al. 1979). However, the density of this gas may be unrelated to the hot NH_3 component we observe, as Hüttemeister et al. (1993a)

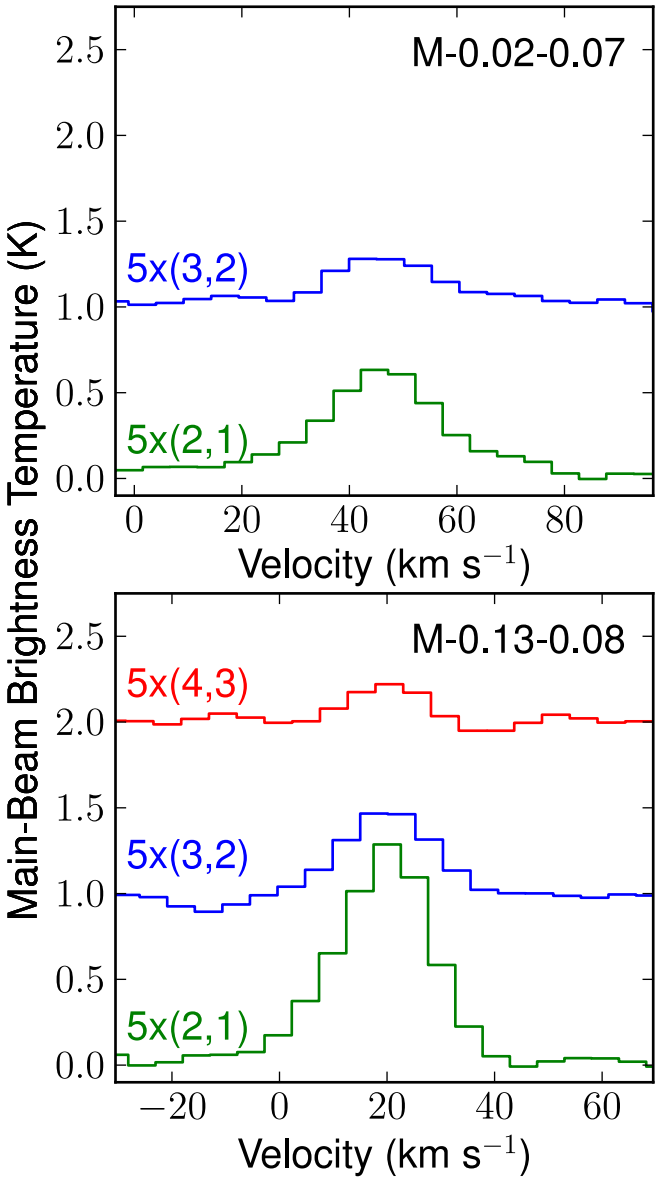

Figure 4.13: Spectra of non-metastable NH_3 lines toward M-0.02-0.07 and M-0.13-0.08.

showed that the lower-excitation NH_3 lines trace a separate, cool gas component of T$\sim$ 25 K. Further, the nonmetastable and metastable emission even from lower-excitation lines can arise from different regions of the cloud. In Sgr B2, maps of both nonmetastable and metastable lines show that the nonmetastable NH_3 emission is clearly spatially distinct from the emitting region of the lower-excitation metastable NH_3 lines (Hüttemeister et al. 1993b).

4.4.5 Heating

We first consider whether the NH_3 emission might be nonthermal: the result of formation in a highly-excited state (a phenomenon known as formation pumping). In this case, the highly-excited NH_3 which we observe would be the result of the incomplete thermalization of these molecules after their formation. Formation at high temperatures implies an ortho/para ratio of 1, largely consistent with our observations (Takano et al. 2002). However, our determination that $\sim$10% of the NH_3 column in M-0.02-0.07 is hot also puts a tight constraint on the NH_3 formation rate. Assuming that it takes $\sim$ 5-10 collisions for an NH_3 molecule to reach thermal equilibrium with the surrounding gas after it has been formed, and given a collision rate coefficient of $\sim 2\times10^{-10}$ cm^3 s^{-1} and a gas density of at least 10^3 cm^{-3}, we find that an NH_3 molecule will come to thermal equilibrium in $\sim$ 1 year. This means that 10% of the NH_3 in these clouds must have formed within a few years. Thus in a steady state (inferred from the fact that hot ammonia is observed to be widespread throughout the CMZ), the typical lifetime of an NH_3 molecule in the gas phase in CMZ clouds would only be $\sim$ 10 years. Looking at this another way, if NH_3 must be destroyed at the same rate at which it is formed, then every hundredth collision an NH_3 molecule experiences is with a molecule (like H_3^+) which destructively reacts with the NH_3, which would indicate a highly

unlikely abundance of reactants. Although the NH_3 could be destroyed on these timescales via photodissociation if it is located in PDRs (Rodríguez-Fernández et al. 2004), the authors find this unlikely, as it would require an unreasonably high inflow rate of NH_3-rich gas into the PDR regions to maintain the observed NH_3 abundance. Another possibility, the continuous formation and destruction of NH_3 in dissociative (J-type) shocks, has also been ruled out by Rodríguez-Fernández et al. (2004), who find that J-type shock models do not reproduce the observed fine-structure line intensities in the CMZ. We thus conclude that the highly-excited NH_3 we observe is likely to be due to a thermal and truly hot component of CMZ clouds.

The widespread distribution of highly-excited NH_3 in cloud throughout the CMZ favors a global heating source, such as shocks, cosmic rays, or possibly X-rays. Cosmic rays (Yusef-Zadeh et al. 2007; Goto et al. 2008), and the dissipation of turbulence (possibly magnetohydrodynamic turbulence) via shocks (Arons & Max 1975; Wilson et al. 1982; Martín-Pintado et al. 1997), have both been suggested to be possible sources of CMZ heating. Both also can result in gas temperatures systematically higher than dust temperatures, an observed property of clouds in the CMZ (Molinari et al. 2011). RF01 also find that their hot (T$\sim$600 K) H_2 component is consistent with either models of dense PDRs or shocks, though the exact relationship between this component and the 400 K NH_3 presented here is unclear.

It is possible that PDRs do play some role in heating these clouds. In our temperature maps of M-0.02-0.07, we noticed consistently higher temperatures on the southeast edge of this cloud, a location which roughly corresponds with a group of 4 compact HII regions embedded in the cloud. However, while the embedded HII regions may make some local contribution to the heating of this

cloud, we note that many of the clouds in which we detect highly-excited NH_3 do not have embedded HII regions or associated star formation (e.g., M0.25+0.01, M0.11-0.08, M0.34+0.06). This suggests that heating due to embedded sources is not the dominant heating mechanism for this hot NH_3 .

The emission from these highly-excited NH_3 lines also appears concentrated toward the cloud centers, and is thereby unlikely to arise in the cloud envelopes (see the discussion in Section 4.4.2.2). This argues against the heating occurring in an irradiated outer layer, though a penetrating heating source, such as cosmic rays, could be plausible. However, recent modeling of a typical CMZ cloud (M0.25+0.01; Clark et al. 2013) suggests that cosmic ray heating, even for relatively high cosmic-ray ionization rates of $\zeta \sim$ a few 10^{-14} s^{-1} (e.g., Yusef-Zadeh et al. 2007, 2013b; Yusef-Zadeh et al. 2013), does not heat even the most tenuous gas (n$\sim$ 10^3 cm^{-3}) above 300 K, which is less than the lower limits on the kinetic temperature we derived from the rotational temperatures of the three clouds studied (M0.25+0.01, M-0.02-0.07, and M-0.13-0.08). Finally, as the emission is also largely resolved out by interferometric observations with the VLA, it must be extended on spatial scales of tens of arcseconds and distributed relatively uniformly throughout the cloud. This could then either occur if the emission originates in structures too narrow to resolve with the VLA (such as shock fronts), or if the emission emanates from a generally smooth component, such as a less-dense inter-clump medium.

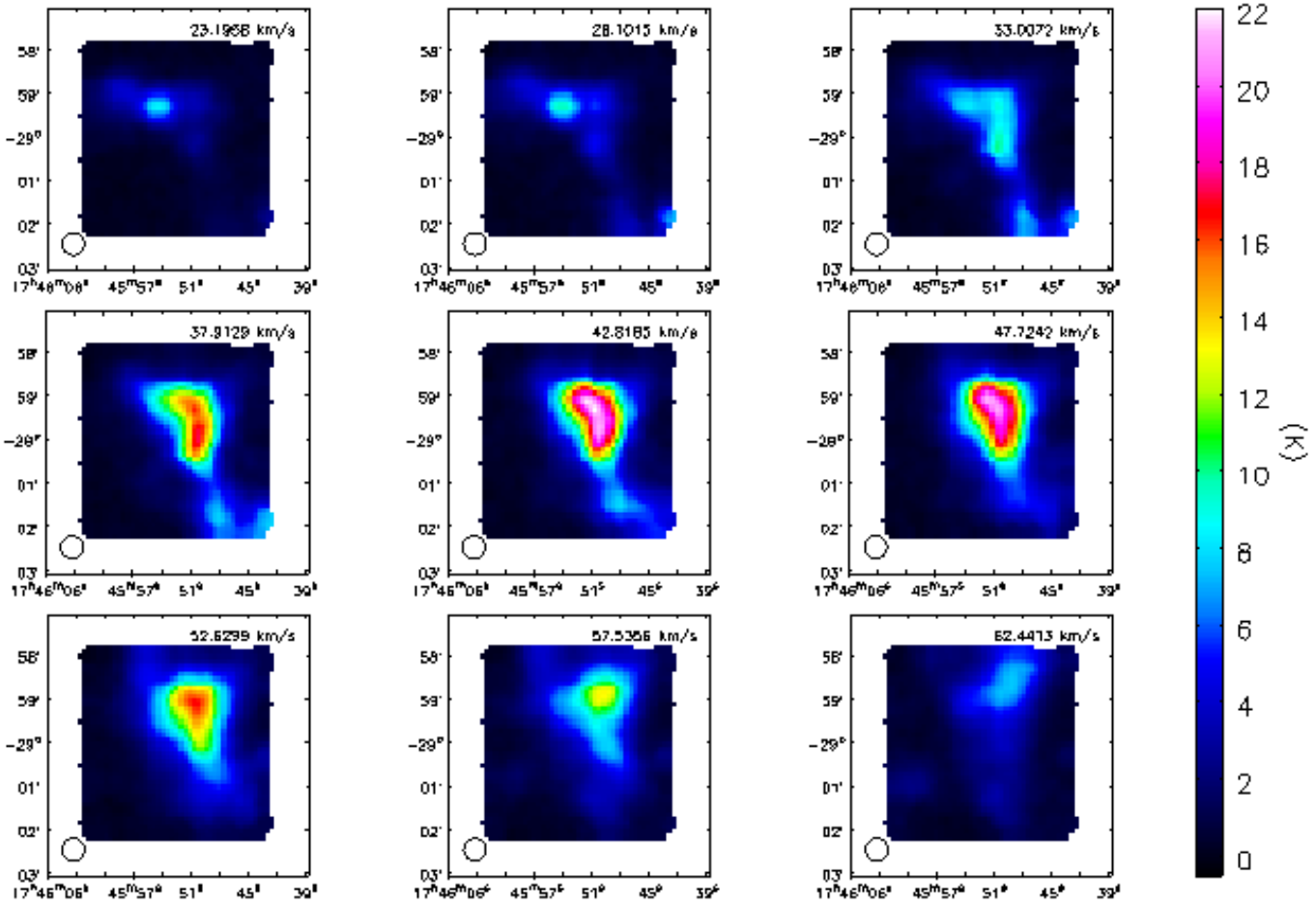

Figure 4.14: Channel maps of NH_3 (3,3) emission in M-0.02-0.07.

We briefly investigate the role of cloud-cloud collisions on heating in M-0.02-0.07 by comparing the temperature maps with the kinematic structure of the cloud. Figure 4.14 shows the channel maps of the ammonia (3,3) line, the strongest line in this cloud, and thus the best tracer of the underlying kinematic structure. This cloud exhibits emission over a relatively wide range of velocities, from 20 to 70 km s^{-1}. In the righthand side of Figure 4.15, we show an intensity-weighted velocity map of the cloud, also using the (3,3) line. Here, one can see two prominent velocity gradients: a north-south gradient from 40 to 65 km s^{-1}on the western edge of the cloud, corresponding to the ridge of material swept up by the supernova shell Sgr A east, and an east-west gradient from 25 to 45 km s^{-1}, where the eastern extension of the cloud appears to join this swept-up shell. The area where these velocity components blend is host to a large number of collisionally-excited (Class I) CH_3OH masers (Sjouwerman et al. 2010; Pihlström et al. 2011), indicative of strong shocks. We hypothesize that the higher temperatures on the southeast edge of M-0.02-0.07 which are seen in all of the maps may actually not be due to the embedded HII regions, but instead to the collision of these two components of the cloud. The strong temperature peak on the northern edge of the cloud seen in the (4,4)-(8,8) and (6,6)-(9,9) temperature maps could also be related to this interaction. If large-scale collisions do contribute to variations in temperature in the hot gas component we observe, then other clouds with strong emission from highly-excited lines of NH_3 such as M0.25+0.01, M-0.13-0.08, and M0.11-0.08, should also show a correlation between their temperature structure and their kinematics, as well as emission from shock-tracers such as Class I CH_3OH masers.

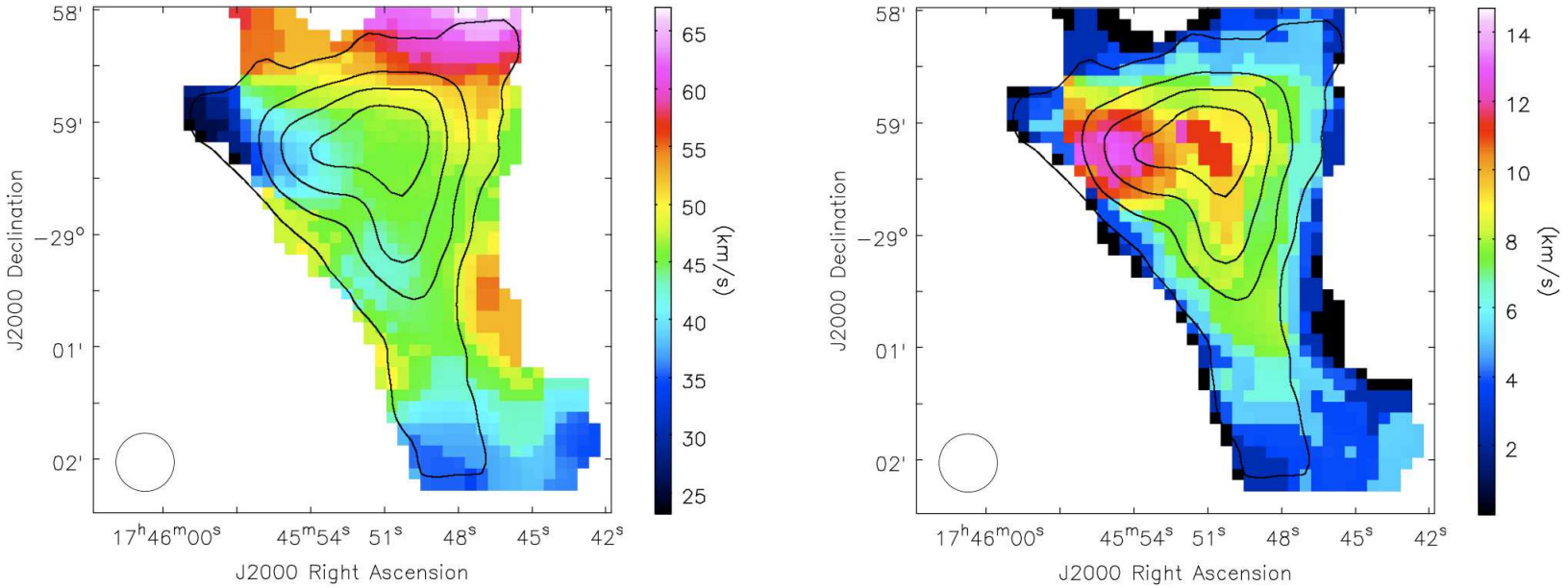

Figure 4.15: **Left:** Intensity-weighted velocity in M-0.02-0.07, from the the NH_3 (3,3) line. **Right:** Intensity-weighted velocity dispersion in M-0.02-0.07, from the the NH_3 (3,3) line. Contours of emission from the NH_3 (6,6) line are overplotted on both maps in black.

Finally, we also compare the velocity dispersion in M-0.02-0.07 with its temperature. The lefthand side of Figure 4.15 shows the velocity dispersion of the (3,3) line. The velocity dispersion is generally higher toward the center of the cloud, and peaks at the eastern edge. It is possible that this region of larger velocity dispersion is related to the slightly enhanced temperatures in this area of the (3,3) to (6,6) rotational temperature map (Figure 4.11). However, the other two temperature maps, which are derived from more highly-excited lines of NH_3, show no correlation of temperature with an increased turbulent line width.

There are several potential methods for further distinguishing between the different mechanisms for heating the hot gas component we detect in CMZ clouds. With higher-resolution interferometric observations of highly-excited NH_3 (for example, in absorption against HII regions) one could test whether the distribution of highly excited NH_3 varies on the small scales which would be consistent with arising in narrow shocks. One could also examine a larger sample of clouds for a correlation between higher temperatures or a larger fraction of hot gas and tracers of enhanced shock activity in these clouds, for example, collisionally-excited CH_3OH masers which have been found to be extremely abundant throughout the CMZ (Yusef-Zadeh et al. 2013a). Ao et al. (2013) also suggest several means to distinguish between cosmic rays and turbulent shocks as the heating source for CMZ clouds. They suggest both searching for an enhanced ionization fraction which would be indicative of a high cosmic ray ionization rate, and looking for hot, low-velocity-dispersion structures within individual clouds, which would indicate that the dissipation of turbulent energy is not the primary source of cloud heating.

4.5 Conclusions

Based on our detections of NH_3 lines with energy levels up to 2200 K above the ground state, this paper presents the following findings:

1. We have detected a hot gas component associated with a large number of Galactic center molecular clouds. Of the 17 positions we surveyed for NH_3 emission, we detect NH_3 (9,9) toward 13 positions, and marginally detect it toward two positions. For those clouds in which we observed only (8,8) and (9,9), we estimate T$> 200 - 300$ K.

2. For three clouds, M0.25+0.01, M-0.02-0.07, and M-0.13-0.08, we have detected emission from lines of NH_3 up to (15,15) and measure temperatures of T $\sim$ 350-450 K. A similar, though hotter, gas component was previously known in Sgr B2 (T=600-700 K; Ceccarelli et al. 2002; Wilson et al. 2006), but the observations presented here indicate that hot gas is widespread in both lower mass and more quiescent CMZ clouds throughout the central 300 parsecs.

3. For M-0.02-0.07, we have also mapped the NH_3 (9,9) emission with VLA, and find that, compared to our GBT observations, $\sim$96% of the flux from this line is resolved out. This indicates that the hot NH_3 emission is uniform on $\sim$ 10 arcsecond scales, either because it arises in a smooth, extended component, or in a network of unresolved structures, such as shocks.

4. We have also measured the NH_3 (1,1) through (6,6) lines in M-0.02-0.07, allowing us to determine that the hot (T $\sim$ 400 K) NH_3 in this cloud contributes 7-12% of the total NH_3 column density. This makes it unlikely that the highly-excited NH_3 lines are a result of formation pumping– a nonthermal population of the NH_3 levels due to formation in a highly-excited state.

4.6 Appendix: Properties of clouds for which we detect NH_3 (9,9)

4.6.0.1 G1.6-0.025

G1.6-0.025 is a cloud at the extreme high-longitude end of the CMZ. This cloud exhibits remarkably strong lines of CH_3OH, indicative of intense shocks (Menten et al. 2009). We detect relatively strong emission from the (9,9) line in this cloud, but do not detect the (8,8) line, which is surprising given the apparent strength of the (9,9) line. Because of the discrepant strength of the (9,9) line, G1.6-0.025 is one of two clouds which we suggest in Section 4.3.4.3 may have an anomalous ortho to para NH_3 ratio (O/P $>$ 1.5). This ratio, which is larger than that measured toward the clouds in Table 4.5, indicates that the NH_3 in this cloud may have formed at cooler temperatures (or if it formed via grain surface reactions, that it reflects cooler grain temperatures in this cloud).

4.6.0.2 M0.83-0.10

M0.83-0.10 lies to the southeast of Sgr B2. The temperature of this cloud has previously been measured by Rodríguez-Fernández et al. (2001) using pure-rotational lines of H_2. They find two temperature components: a warm component, with T $\sim$ 180 K, and a hot component, with T$\sim$ 600 K. The warm component is estimated to make up 25% of the total H_2 column density in this cloud. We marginally detect the NH_3(8,8) and (9,9) lines toward this source.

4.6.0.3 Sgr B2

We detect NH_3 (8,8) and (9,9) in absorption against the continuum from the hot cores Sgr B2-M and Sgr B2-N. Higher lines of NH_3 have previously been studied in Sgr B2 (Hüttemeister et al. 1993b; Flower et al. 1995; Ceccarelli et al. 2002; Wilson et al. 2006), yielding rotational temperatures in excess of 700 K. The Sgr B2 cloud has an extremely high NH_3 column density, leading to suggestions that the NH_3 abundance is enhanced, perhaps by shocks (Ceccarelli et al. 2002). We measure $N/T_{ex} \sim 10^{13}$ cm^{-2}, comparable to that measured by Hüttemeister et al. (1995) and Wilson et al. (2006). Wilson et al. (2006) estimate that the NH_3 excitation temperature varies from 6 K for NH_3 (1,1) to 3 K for NH_3 (18,18), so the total NH_3 column densities in these lines are likely $\lesssim$ a few $\times 10^{13}$.

In our spectra of NH_3 (9,9) toward these sources we also detect the $J_K = 13_2$-13_1 line of CH_3OH, with a rest frequency of 27.47253 GHz. The rest frequency of this line is very similar to that of the (9,9) line at 27.477943, and it appears in emission at a velocity offset of $\sim$120 km s^{-1} in the (9,9) spectra of both Sgr B2-N and Sgr B2-M, in Figure 4.2. That this is not an NH_3 emission feature is apparent both from this velocity offset, which is inconsistent with the radial velocities of many species from these sources, and from the fact that no corresponding emission feature is observed in the (8,8) spectra. Additional $J_K = J_2$-J_1 transitions of CH_3OH have also been previously detected toward both sources (Pei et al. 2000).

4.6.0.4 M0.34+0.06

M0.34+0.06 is one of the clouds in the 'Dust Ridge' that stretches from M0.25+0.01 to Sgr B2 (Lis et al. 1994). More recently, these clouds have been interpreted as representing gas on x2 orbits in the Galactic center potential (Molinari et al.

2011). Although several clouds in the dust ridge have associated 6.7 GHz (Class I or radiatively-excited) CH_3OH masers (Caswell et al. 2010), which imply the presence of embedded star formation, this cloud shows no indication of ongoing star formation. Emission from highly-excited lines of NH_3 in this cloud is relatively faint, with linewidths $\sim$ 20 km s^{-1}.

4.6.0.5 M0.25+0.01

M0.25+0.01 is another apparently quiescent cloud in the Dust Ridge: the only evidence for ongoing star formation in this cloud is a single, weak water maser (Lis et al. 1994). Linewidths in this cloud vary from 15 to 20 km s^{-1}. The cloud is quite massive (M $\sim 10^5 M_\odot$) and has a very high total column density ($N_{H_2} \sim 4 \times 10^{23}$ cm^{-2}). As it appears prominently in absorption in infrared images, it likely lies toward the near edge of the CMZ (Longmore et al. 2012). Although this cloud has previously been measured to be relatively cold (Hüttemeister et al. (1993a) measure NH_3 temperatures of 17 and 80 K in this cloud, and Ao et al. (2013) find a temperature of $\sim$ 70 K using lines of H_2CO), we find that this cloud also has a hot gas component of $\sim$400 K.

4.6.0.6 G0.18-0.04

G0.18-0.04 is an HII region (the Sickle) and an intense photodissociation region (PDR) on the face of a molecular cloud adjacent to the massive Quintuplet star cluster (Yusef-Zadeh & Morris 1987b; Nagata et al. 1990). Although the cloud is detected in relatively highly-excited 3–2 and 5–4 transitions of CS (Serabyn & Güsten 1991), we detect only faint NH_3 emission from the (9,9) line and marginally detect the (8,8) line toward this cloud. Compared to M-0.02-0.07, for which the ratio of CS 5–4 (measured by Serabyn et al. (1992)) to NH_3 (9,9) is $\sim$5,

the ratio in this cloud is 20. This suggests that either this cloud, as a strong PDR, has a smaller fraction of hot molecular gas than other clouds we survey, or that the hot NH_3 is located in a less-shielded region of this cloud than the CS where it is preferentially destroyed, as both molecules have similar photodissociation rates (Martín et al. 2012; Roberge et al. 1981).

4.6.0.7 G0.07+0.04

The G0.07+0.04 cloud is also associated with an intense PDR region, and its ionized surface forms part of the thermal arched filaments complex (Serabyn & Guesten 1987; Lang et al. 2001, 2002), which is ionized by the massive Arches star cluster (Nagata et al. 1995; Cotera et al. 1996). It is prominent in maps of the CII cooling line (Poglitsch et al. 1991). Similar to G0.18-0.04, the NH_3 (9,9) emission we detect from this cloud is very faint, despite both sources being clouds with dense molecular gas immersed in a PDR, an environment in which one might expect to find hot gas. Again, this suggests either that hot NH_3 is not associated with PDRs, and so PDRs are not a strong source of this emission, or that hot NH_3 does exist in PDRs, but is depleted in the most intense such environments.

4.6.0.8 M0.11-0.08

M0.11-0.08 is one of several prominent molecular cloud cores just to the east of Sgr A and is a relatively bright continuum source at millimeter and submillimeter wavelengths (Pierce-Price et al. 2000; Bally et al. 2010) as well as as in several molecular tracers (Güsten et al. 1981; Armstrong & Barrett 1985). It is also part of the larger M0.11-0.11 complex which is notable for having a very high column density of SiO (Tsuboi et al. 1997; Handa et al. 2006). We find that M0.11-0.08

has one of the highest column densities of NH_3 (9,9) in our sample, next to M-0.13-0.08 and M-0.02-0.07 (and Sgr B2, which we observe only in absorption). Ao et al. (2013) also found that this was the second hottest cloud in the central 100 parsecs (T$\sim$125 K) as measured with millimeter transitions of formaldehyde. There are no known signs of star formation associated with this cloud.

4.6.0.9 M-0.02-0.07

M-0.02-0.07 is one of two giant molecular clouds in the Sgr A complex, lying on the eastern edge of the Sgr A East supernova remnant, which is apparently compressing the edge of this cloud (Serabyn et al. 1992). There are also four compact HII regions that appear to be partially embedded within this cloud (Goss et al. 1985; Yusef-Zadeh et al. 2010; Mills et al. 2011) . The NH_3 (9,9) line emission from this cloud is the strongest of all the positions we observed, from which we infer that this cloud has the highest hot NH_3 column density of all clouds in our sample, next to Sgr B2. Ao et al. (2013) found that this was the hottest cloud in the central 100 parsecs (T $\sim$ 190 K) as measured with millimeter transitions of formaldehyde. We discuss this cloud more in Section 4.4.2.2.

4.6.0.10 The Circumnuclear disk / Southern streamer

The Circumnuclear disk (CND) is a ring of gas and dust surrounding the central supermassive black hole at a radius of 1.5 pc (Becklin et al. 1982; Genzel et al. 1985). Lower-excitation lines of NH_3 up to (6,6) have been detected in the CND (McGary et al. 2001; Herrnstein & Ho 2002), and we marginally detect emission from NH_3 (8,8) and (9,9) at $\sim$60 km s^{-1}. This velocity is consistent with the previous NH_3 spectra of the CND toward this position, which is offset from Sgr A* by (R.A, Dec.) = (-6$''$,-39$''$). However, because the broad width of these lines

are comparable to the width of fluctuations in the surrounding baseline of the spectra, their intrinsic shape is uncertain, and we are unable to robustly fit for the properties of these lines.

We also detect both the (8,8) and (9,9) lines in absorption, likely against the 'minispiral' of Sgr A (Ekers et al. 1983; Zhao et al. 2009), at a velocity of 35 km s^{-1}. This gas is likely part of the 'Southern streamer', identified by Coil & Ho (1999) and Coil & Ho (2000) as an extension of M-0.13-0.08 that may interact with the CND.

4.6.0.11 M-0.13-0.08

M-0.13-0.08 is the second giant molecular cloud in the Sgr A complex, lying to the west of Sgr A West and the CND. Like M-0.02-0.07, this cloud shows some evidence for recent star formation, as it has a single embedded HII region (Ho et al. 1985). The cloud also appears to be interacting with a supernova remnant on its periphery (Coil & Ho 2000). After M-0.02-0.07, this cloud has the strongest high-excitation NH_3 emission line strengths in our sample.

4.6.0.12 Sgr C

As the distribution of targets in our sample follows the distribution of dense gas in the CMZ, which is predominantly located to the east of Sgr A* at positive latitudes (Morris & Serabyn 1996), we observed relatively few positions at negative latitudes. Of the four positions we observed that lie to the east of Sgr A*, Sgr C is the only one aside from M-0.13-0.08 in which we detect NH_3 (9,9). The line emission is, however, quite weak.

CHAPTER 5

A VLA Survey of the Central Molecular Zone

All that we currently know about the properties of the molecular gas in the central 600 parsecs has been determined from studies of single molecular clouds, or low-resolution surveys of the entire CMZ, which yield an incomplete picture of conditions in this region. Surveys have determined average CMZ cloud densities to be $\sim 10^4$ cm^{-3} (Bally et al. 1987; Jackson et al. 1993), and studies of individual clouds indicate higher densities of 10^5 to 10^6 cm^{-3} exist in some clouds (Serabyn et al. 1992; Requena-Torres et al. 2012; Longmore et al. 2012, Mills et al., in prep.). Surveys of CMZ clouds measure average temperatures of < 200 K, but do not constrain the temperature structure in cloud interiors (Güsten et al. 1985; Hüttemeister et al. 1993a). Hotter gas, with temperatures > 200 K, is known to exist in a handful of the most massive CMZ clouds (Wilson et al. 1982; Mauersberger et al. 1986; Wilson et al. 2006; Mills & Morris 2013), and may in fact be a common feature of CMZ clouds (Mills & Morris 2013). From these studies, almost all of which have been conducted using single-dish telescopes with resolutions $> 30''$ (~ 1 parsec at the distance of the Galactic center) it is clear that conditions in CMZ clouds are extreme in a Galactic context, but are they only extreme on the large scales which have been previously probed? Are the measured bulk gas properties throughout the CMZ actually characteristic of conditions in the unresolved individual star-forming cores, and will variations in these conditions affect the star formation process in the CMZ?

The low resolution and heterogeneous nature of prior studies are not sufficient to constrain the true variation in physical parameters in the dense gas across the CMZ and interior to individual CMZ clouds. To distinguish between different scenarios for the the heating, injection of turbulence, and lack of star formation in CMZ clouds requires a homogeneous study of the dense gas conditions which is sensitive to the presence of multiple temperature and density components and allows for the physical conditions to be analyzed on both global scales and the small scales most relevant to star formation. The survey which is described in this chapter is a first step toward a uniform survey of Galactic center gas at sub-parsec resolutions. Below, I describe interferometric observations of six typical clouds in the CMZ in multiple transitions of NH_3. These observations will probe the temperature, density, and kinematic structure of these clouds in unprecedented detail. This chapter presents early results and highlights from the ongoing analysis of these survey data.

5.1 Observations and Data Calibration

The observations presented in this chapter were made with the new WIDAR correlator of the Karl G. Jansky Very Large Array (VLA), a facility of the National Radio Astronomy Observatory[1]. The data were taken in two different frequency bands on two separate dates: in Ka-band (27-36 GHz) on January 13th, and in K-band (24-25 GHz) on January 14th 2012. Both observations used the hybrid DnC array, as the Galactic center has a low elevation as viewed from the VLA site.

[1]The National Radio Astronomy Observatory is a facility of the National Science Foundation operated under cooperative agreement by Associated Universities, Inc.

5.1.1 Targets

VLA observations were made toward 18 pointings in 6 clouds (Sgr B2 M&N, M0.25+0.01, M-0.11-0.08, M-0.02-0.07, the CND, and M-0.13-0.08) which are part of 4 large complexes in the CMZ (Sgr B2, the Dust ridge, M0.11+0.11, and the Sgr A clouds; Figure 5.1). These targets were selected in order to probe a wide variety of environments in the CMZ. Clouds in this sample probe galactocentric distances ranging from less than ten to more than a hundred parsecs. The clouds in this sample also show varying levels of star formation, from highly active to apparently absent, which will help to identify conditions which aid or suppress current star formation in the CMZ. These clouds also are suggested to experience different degrees of irradiation from X-rays, cosmic rays, and nearby stellar clusters, which allows for a wide range of potential heating sources for gas in the CMZ to be probed.

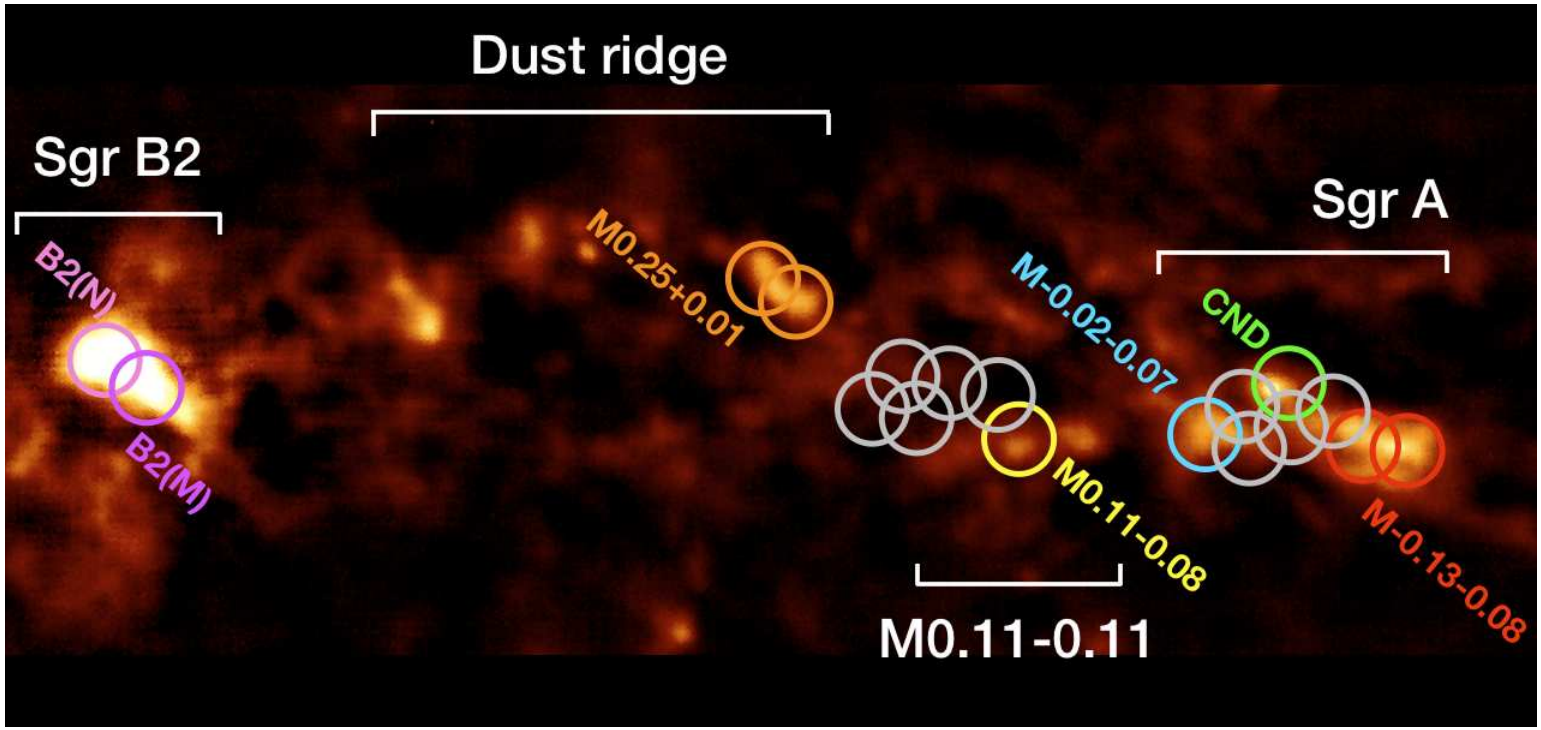

Figure 5.1: The 18 positions observed with the VLA as part of a survey of molecular clouds in the CMZ are shown overlaid on a 1.1 mm map of cool dust emission (Bally et al. 2010). The size of the plotted circles corresponds to the $\sim 2'$ primary beam of the VLA at a frequency of 25 GHz. Pointings corresponding to individual clouds are colorized.

All of these clouds have been previously observed in highly-excited lines of NH_3 using the GBT (Chapter 4). Additionally, the CND was observed in sub-millimeter transitions of HCN and HCO^+ (Chapter 3) and radio continuum and infrared observations of the HII regions in M-0.02-0.07 were previously discussed in Chapter 2.

5.1.2 Spectral Setup

As the primary goals of these observations are to survey the conditions in the dense gas, the observations were designed to cover a large number of NH_3 transitions. As described in Chapter 4, NH_3 is a good tracer of gas with densities greater than a moderate 10^3 cm^{-3}. Observations of multiple inversion transitions of NH_3 can furthermore yield a good approximation of the kinetic temperature of this gas. Seven transitions of NH_3 with energies from 20 to 840 K above the ground state are observed, which are collectively sensitive to a wide range of gas temperatures. In addition to observing these NH_3 transitions, the observations were designed to cover transitions of several additional species, including HC_3N and CH_3OH. By observing all of these lines with relatively low velocity resolution (typically 3 km s^{-1}, sufficient to resolve the wide linewidths of CMZ clouds) these observations also include a total continuum bandwidth of $\sim$ 4 GHz.

The settings of the WIDAR correlator used for these observations, including the lines which are covered, and the channel resolution of the spectral line and continuum data in both frequency and velocity are described in Table 5.1. The observations in each band (K and Ka) are divided into two separate, continuous subbands 0.86 GHz wide which are each comprised of 7 spectral windows. In K band, the subbands are centered on 24.054 GHz and 25.375 GHz, and for Ka-band the subbands are centered on 27.515 GHz and 36.35 GHz. The typical

spectral resolution is 250 kHz, however for three spectral windows, covering (1) the NH_3 (1,1) and (2,2) lines and their hyperfine structure, (2) the 36.1 GHz CH_3OH maser line, and (3) the CH_3CN (2_k-1_k) transitions, the resolution is doubled to better resolve the line structure. The continuum data were obtained with the same setup used to observe the spectral line data: the continuum images were ultimately constructed using the line-free channels. Further details of the full spectral setup are given in Table 5.1.

Table 5.1: Spectral Setup

Molecule	**Transition** (J,K)	**Frequency** (GHz)	**Spectral Resolution** (kHz)	**Velocity Resolution** km s^{-1}
		K band		
Continuum		23.606 - 24.502	125-250	1.58-3.14
NH_3	(1,1)	23.6945	125	1.58
NH_3	(2,2)	23.7226	125	1.58
NH_3	(3,3)	23.8701	250	3.14
HC_5N	(9-8)	23.9639	250	3.13
NH_3	(4,4)	24.1394	250	3.10
OCS	(2-1)	24.3259	250	3.08
NH_3	(5,5)	24.5329	250	3.05
Continuum		24.927 - 25.823	250	2.90-3.01
NH_3	(6,6)	25.0560	250	2.99
NH_3	(7,7)	25.7152	250	2.91
		Ka band		
Continuum		26.939 - 27.835	250	2.69-2.78
HC_3N	(3-2)	27.2943	250	2.75
NH_3	(9,9)	27.4779	250	2.73
Continuum		35.902 - 36.670	125-250	1.02-2.09
CH_3OH		36.1693	125	1.04
HC_3N	(4-3)	36.3923	250	2.06
CH_3CN	(2-1)	36.7956	125	1.02

In neither K band nor Ka band was any significant radio frequency interference (RFI) encountered. However, there was a source of internal RFI which manifested in a single antenna (ea04) of the Ka-band observations. This antenna was thus removed from the data before calibrating and imaging the data.

5.1.3 Calibration and Imaging

All data were calibrated using the CASA reduction package[1]. The phase calibrator was J1744-3116, and was observed approximately every 15 minutes. The bandpass calibrator was J1733-1304. The data were flux calibrated using 3C286, observed at elevations comparable to the Galactic center sources ($\sim 15^\circ - 30^\circ$).

After calibration, the data were imaged using the CLEAN algorithm in CASA and a CLEAN cycle of several thousand iterations, resulting in noise in the final images which was typically $\sim$1 mJy beam^{-1} channel^{-1} for the spectral line images, and $\sim$30 μJy beam^{-1} for the continuum images. The full width at half maximum (FWHM) of the synthesized clean beam ranged from $2''.3 \times 2''.5$ at 25 GHz (including 7/8 of the NH_3 lines) to $1''.9 \times 2''.2$ at 27 GHz and 1.5×1.7 at 36 GHz. The primary beam size (the field of view) of a single pointing varied from $124''$ at 25 GHz to $100''$ at 27 GHz and $76''$ at 36 GHz. As shown in Figure 5.1, pointings were chosen to overlap for clouds which are more extended than the primary beam size.

5.2 Overview of Results

One of the most surprising findings of this survey is the detection of hundreds of 36.1 GHz CH_3OH point sources, which are likely masers. The majority of

[1]http://casa.nrao.edu/

these sources are relatively weak, with intensities of 0.5 - 1 Jy beam^{-1}. Strong (>100 Jy) 36.1 and 44 GHz methanol masers have previously been detected in the Sgr A clouds and Sgr B2 (Mehringer & Menten 1997; Sjouwerman et al. 2010; Pihlström et al. 2011), but these are the first detections of a large population of weaker CH_3OH sources in CMZ clouds. Figure 5.2 shows the distribution of these sources for two typical dense clouds, in which CH_3OH point sources are detected for the first time. These sources are seen in every pointing, even toward relatively low column density and strong photodissociation environment such as G0.18-0.04 (the Sickle, Figure 5.3).

Another unexpected result of this survey is strong NH_3 (3,3) emission in CMZ clouds. Although NH_3 (3,3) is expected to be stronger than the lower-excitation NH_3 (1,1) and (2,2) lines in sufficiently hot gas, this line may be out of thermal equilibrium in CMZ clouds such as M0.25+0.01. Figure 5.4 shows the relationship between the rotational temperatures measured between NH_3 inversion levels and the actual kinetic temperature of the gas. If all of these lines trace gas of the same temperature, then in equilibrium, the rotational temperature derived using the (3,3) and (6,6) lines will always be higher than that derived using the (4,4) and (5,5) lines. However, the (3,3)-(6,6) temperature in M0.25+0.01 is significantly lower than the (4,4) -(5,5) temperature in this cloud. This discrepancy is explained either if the (3,3) line is stronger than expected because it is weakly masing, or if the (3,3) line is tracing a cooler gas component than lines (4,4) and higher. Ammonia (3,3) masers are a relatively rare phenomenon, and have generally been observed to be localized point sources, often coincident with collisionally-excited CH_3OH masers (Mangum & Wootten 1994; Kraemer & Jackson 1995; Zhang & Ho 1995; Martin-Pintado et al. 1999). As discussed in Section 5.3, this masing could have important implications for the gas density in this cloud.

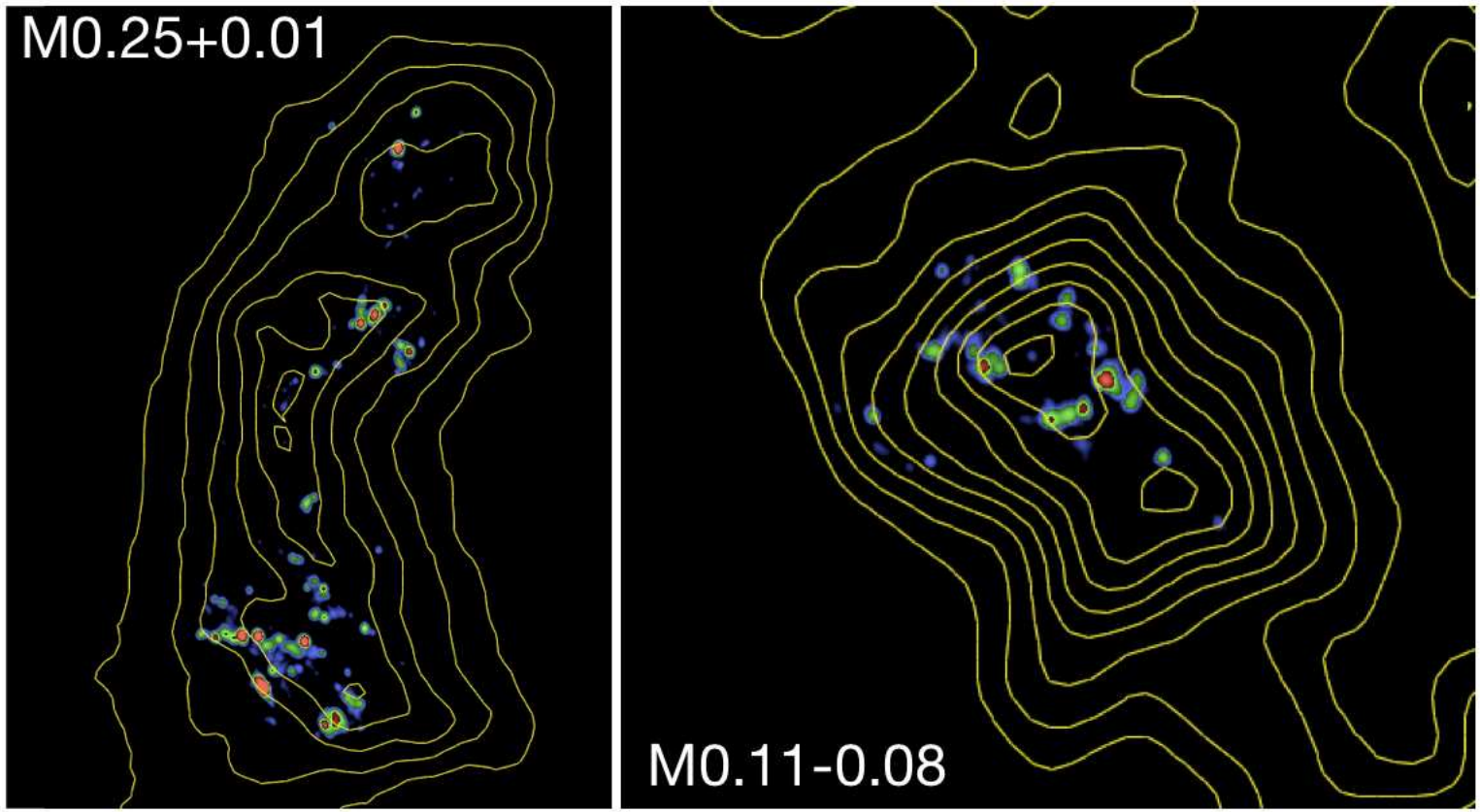

Figure 5.2: A large number of candidate 36.1 GHz CH_3OH masers are found in two quiescent CMZ clouds, M0.25+0.01 and M0.11-0.08. The image shows a map of the maximum emission from the 36.1 CH_3OH GHz line in the two data cubes. The yellow contours correspond to the 850 μm continuum emission from cool dust in these clouds. The candidate masers are seen to be distributed non-uniformly throughout these clouds: CH_3OH sources are clustered in the south part of M0.25+0.01 and in the north part of M0.11-0.08

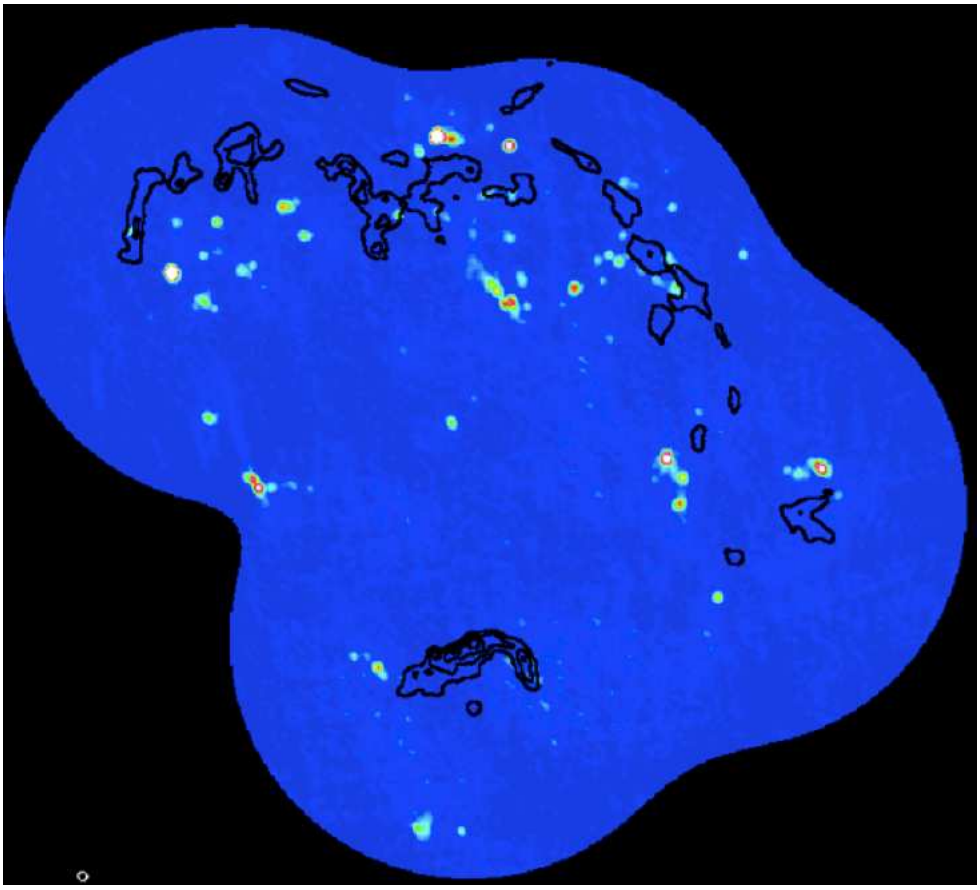

Figure 5.3: A large number of weak 36.1 GHz CH_3OH maser candidates are also found in the vicinity of the Sickle, a giant HII region surrounding the massive Quintuplet star cluster. The image shows a map of the maximum emission from the 36.1 GHz CH_3OH line in the data cube. Radio continuum from the HII region is plotted as black contours on top of the 36.1 GHz image.

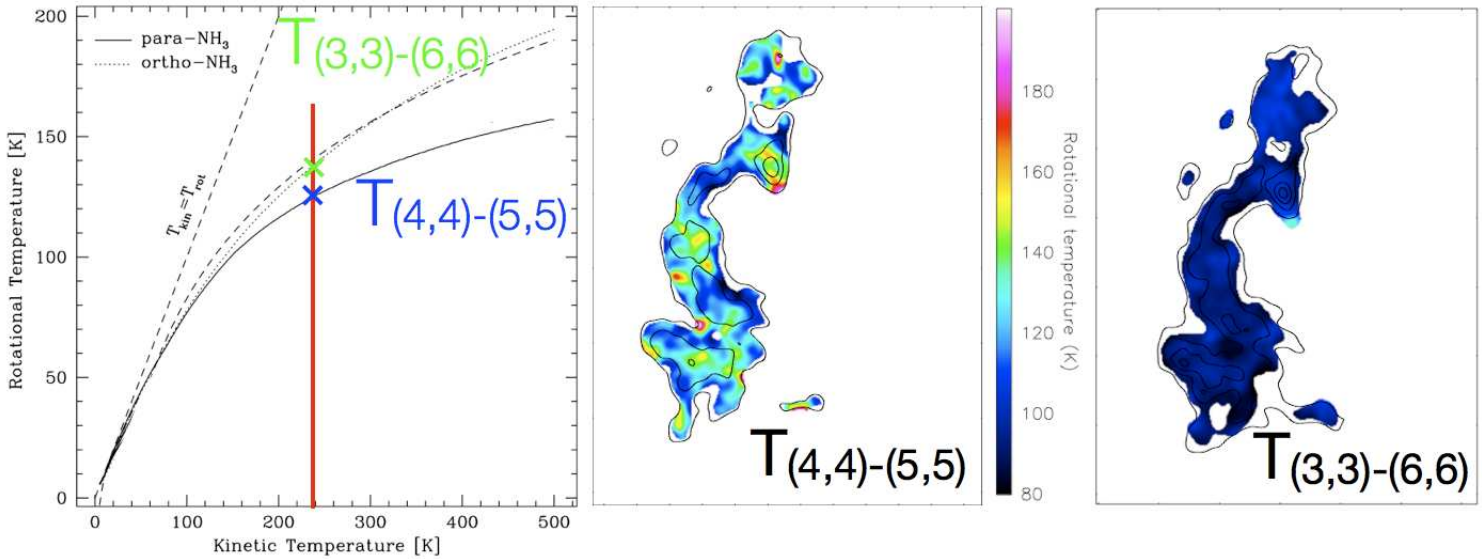

Figure 5.4: **Left:** In gas which is in thermal equilibrium at a single temperature, the rotational temperature derived from the (3,3) and (6,6) NH_3 lines is always higher than that derived using the lower-excitation (4,4) and (5,5) lines. **Middle and Right:** However, in M0.25+0.01, the opposite is seen to be true: the (3,3)-(6,6) temperature is uniformly lower than the (4,4)-(5,5) temperature. This discrepancy is explained either if the NH_3 (3,3) line emission is weakly masing throughout the cloud, or if the (3,3) line is tracing gas cooler than that traced by lines (4,4) and higher.

Below, I discuss additional results related to specific clouds, including M0.25+0.01, the clouds in the Sgr A complex, and Sgr B2.

5.3 M0.25+0.01

M0.25+0.01 (or G0.253+0.016, or G0.25+0.01, as it has also been referred to in the literature) is a molecular cloud which is particularly quiescent for its size, unique not just in the CMZ, but in the entire Galaxy. This 'Bean' or 'Brick'-shaped cloud has an extremely high column density ($\sim 4 \times 10^{23}$ cm^{-2}; Etxaluze et al. 2011; Longmore et al. 2012), an estimated density of $\sim 10^5$ cm^{-3} (Lis et al. 2001; Longmore et al. 2012; Kauffmann et al. 2013), and is a strong source of gas and dust emission in surveys of the CMZ (Güsten & Henkel 1983; Pierce-Price et al. 2000; Molinari et al. 2011). However, its appearance as a prominent infrared dark cloud (IRDC) suggests that it lies on the near side of the CMZ, occulting most of the infrared emission from the nuclear bulge (Lis & Menten 1998). In total, M0.25+0.01 is suggested to have a mass of $1 - 2 \times 10^5$ M$_\odot$, making it one of the most massive clouds in the Galactic center (Lis et al. 1994; Longmore et al. 2012). However, unlike other massive CMZ clouds such as the two clouds near Sgr A (M-0.02-0.07 and M-0.13-0.08) and the Sgr B2 complex, there is no evidence in this cloud for ongoing star formation apart from a single water maser (Lis et al. 1994; Longmore et al. 2012; Kauffmann et al. 2013).

The mass and relatively high average density of this cloud ($n \lesssim 1 \times 10^5$ cm^{-3}; Longmore et al. 2012; Kauffmann et al. 2013) suggest that it is capable of massive star formation, though none appears yet to have occurred. The apparently quiescent state of this cloud makes it a unique environment for investigating the initial conditions of such star formation, before embedded star formation begins to affect the environment of the surrounding cloud. Below, new constraints on

the temperature, density, and turbulent structure of this cloud are presented.

5.3.1 Physical conditions

As previously discussed in Chapter 4, there is a hot (T $\sim 350-400$ K) component of gas in M.25+0.01, measured with highly-excited lines of NH_3. Using lower-excitation lines of NH_3 observed with the VLA, it is possible to additionally constrain the temperature of cooler gas in this cloud. I find gas of T $\sim$ 100-200 K traced by the (4,4) and (5,5) lines (Figure 5.4). However, single-dish observations by Hüttemeister et al. (1993a) of NH_3 (4,4) and (5,5) lines indicate a warm gas component of only 80 K, suggesting that the clumps observed with the VLA may actual be hotter than gas in an extended emission component. Hüttemeister et al. (1993a) also find that the NH_3 (1,1) and (2,2) lines indicate gas as cold as 17$\pm$1 K in this cloud, which would be near thermal equilibrium with the dust (T $\sim$ 19-25 K, Lis et al. 1994; Longmore et al. 2012). If, as Hüttemeister et al. (1993a) suggest, 75% of the gas is in a cold component with T $<$ 20 K, this would be an argument either against heating from a high local cosmic ray ionization rate, or for the existence of extremely dense gas in this cloud (n $> 10^7$ cm^{-3}, Clark et al. 2013).

Although one of the primary goals of these observations was to use NH_3 to measure the gas temperatures, a surprising finding was that one of the NH_3 lines may be out of thermal equilibrium in this cloud. As discussed in Section 5.2, the NH_3 (3,3) inversion line is much stronger than expected compared to the other lines of NH_3 which were observed – (1,1) through (7,7) and (9,9) – and may be weakly masing. This maser was predicted by Walmsley & Ungerechts (1983), who showed that that the conditions for weak masing depend sensitively on the density (Figure 5.5). This implies that the density of the gas which is strongly

emitting in NH_3 (3,3), if it has temperatures < 50 K, is between 10^4 and a few 10^5 cm^{-3}. However, the (3,3) line is not seen to be anomalously strong in single-dish observations of this or other CMZ clouds (Hüttemeister et al. 1993a), which suggests that the bulk of the gas may not be masing, and that maser conditions may be restricted to the brightest (3,3) point sources. Modeling the excitation of both the NH_3 (3,3) and (6,6) inversion doublets with the radiative transfer code RADEX (van der Tak et al. 2007) over a larger parameter space shows that density limits are relaxed for temperatures above 50 K, for which the density of masing gas can exceed 10^6 cm^{-3} (Figure 5.6). These models also illustrate that there is a substantial range of temperatures and densities for which the (6,6) line will also be weakly masing. This is not observed in M0.25+0.01, although this phenomenon is observed in several extragalactic sources (private communication, Jeff Mangum). The fact that NH_3 (6,6) is not observed to be masing in M0.25+0.01 can be used to further constrain the conditions in gas which is masing in this cloud: either the temperature is less than ~ 75 K, or the density must be in either of the ranges $10^{3.5-4.5}$ cm^{-3} or $10^{5.5-6.5}$ cm^{-3}.

Compared to the distribution of NH_3 in M0.25+0.01, which is strongest in the southern part of the cloud, millimeter emission from cool dust and emission from the dense-gas-tracing molecule HC_3N are more uniformly distributed throughout the cloud (Figures 5.2, 5.7). In fact, both of these tracers peak at the center of the cloud, where there is little NH_3 emission. This suggests that the NH_3 emission does not follow the densest gas in this cloud. In fact, there is no NH_3 (or N_2H^+ Kauffmann et al. 2013) emission observed at the location of the submillimeter dust clump coincident with the detected water maser in this cloud (Lis et al. 1994). Water masers are believed to trace very dense shocked gas, with pre-shock densities of $\sim 10^7$ cm^{-3} and relatively high temperatures (Elitzur et al. 1989). It is not clear why NH_3 or N_2H^+ would be depleted or underabundant in

this environment.

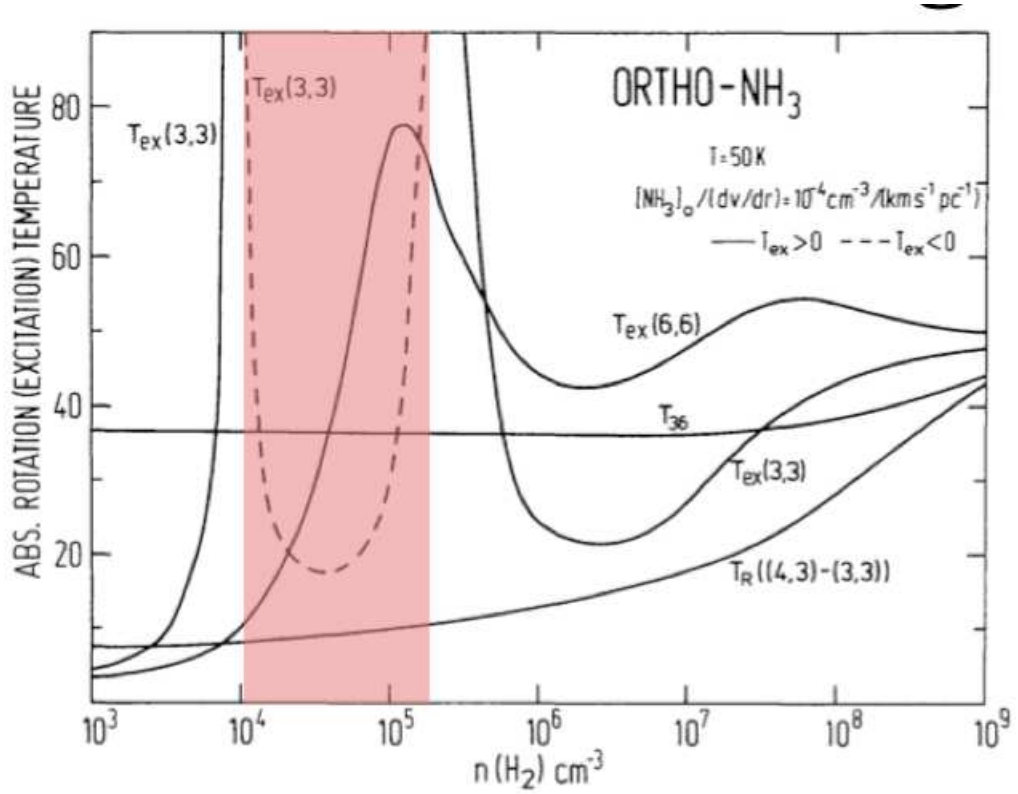

Figure 5.5: An illustration of the density range (shaded in red) for which the excitation temperature of the NH_3 (3,3) line is calculated to be negative, and in which it will be weakly masing. Figure from (Walmsley & Ungerechts 1983).

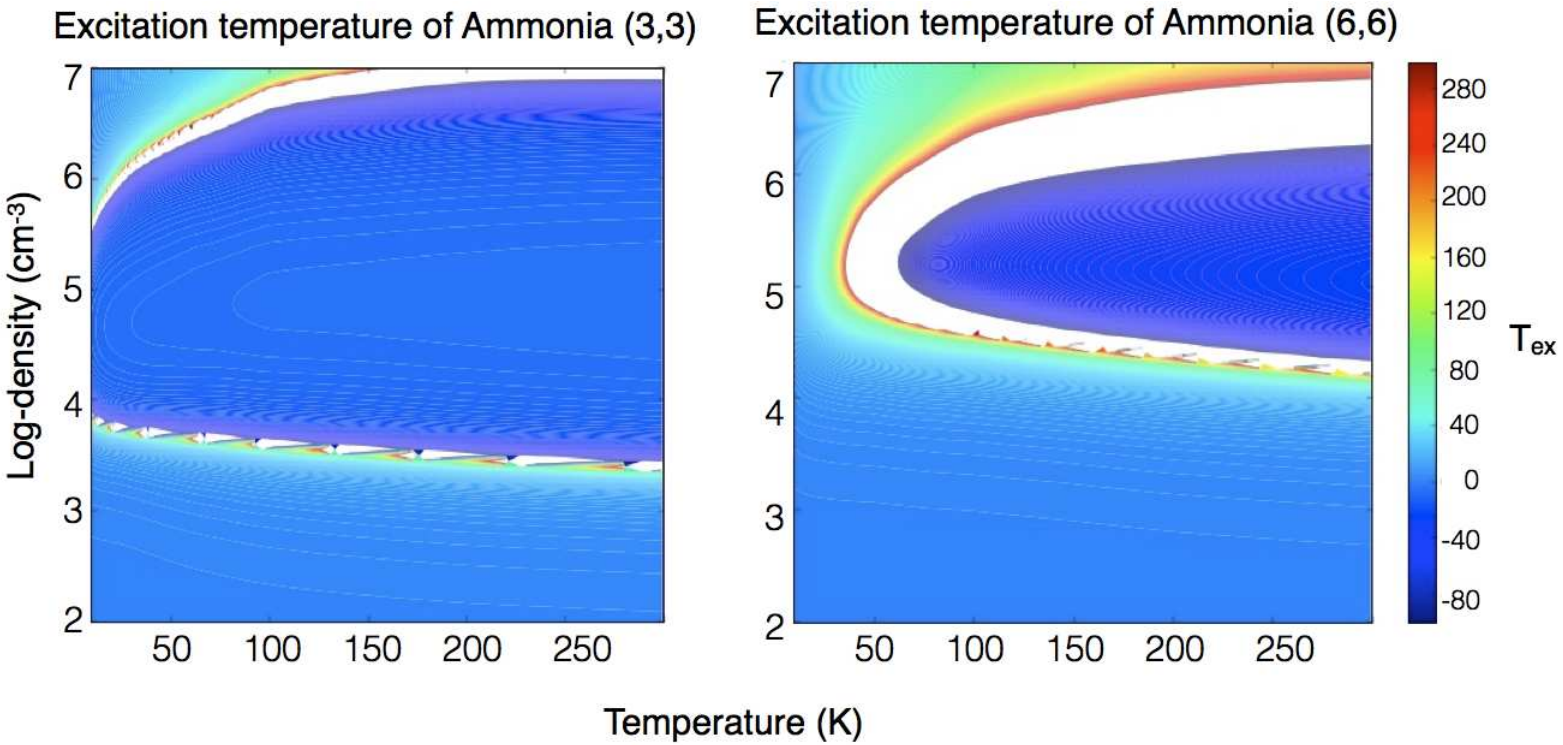

Figure 5.6: Radiative transfer modeling of NH_3 (3,3) and (6,6) with RADEX illustrates the larger parameter space over which both transitions will be weakly masing ($T_{ex} < 0$, dark blue-shaded region), for a typical NH_3 column density of 10^{15} cm^{-2}. In the observations of M0.25+0.01, only the (3,3) line is possibly masing. White regions are excitation temperatures in excess of the displayed scale, where the excitation temperature increases exponentially before inverting.

5.3.2 Kinematics: Shocks and Large velocity gradients

M0.25+0.01, like all clouds detected in this survey, has an extremely large population of 36.1 GHz CH_3OH-emitting point sources which are candidate masers (Figure 5.8, Left). Although widespread emission in the CMZ from this line has been previously noted by Yusef-Zadeh et al. (2013a), their paper identifies only eight candidate sources in M0.25+0.01. From the VLA data, an initial catalog of 36.1 GHz candidate maser sources in M0.25+0.01 is made. A conservative selection criterion (compact sources $> 10\sigma$ above the noise in each channel) yields 75 sources, almost an order of magnitude more candidate masers. Of these sources, 63 are almost certainly masers, having brightness temperatures greater than the hottest gas identified in this cloud (400K, Figure 5.9). However, some of these sources are spatially resolved, which suggests that there is either confusion with multiple masers at that position, or as often happens, the maser emission is superposed with thermal CH_3OH emission from the surrounding gas (Mehringer & Menten 1997). Those sources which have brightness temperatures less than 400 K may still be masers, but the spatial and spectral resolution of these data are insufficient to ascertain that these sources are nonthermal. Strangely, none of the maser candidate positions match the positions for the eight candidate masers presented in Yusef-Zadeh et al. (2013a). It is not clear what the cause of this discrepancy is. As discussed below, the positions of masers detected in this VLA survey are a good match to the gas traced by NH_3.

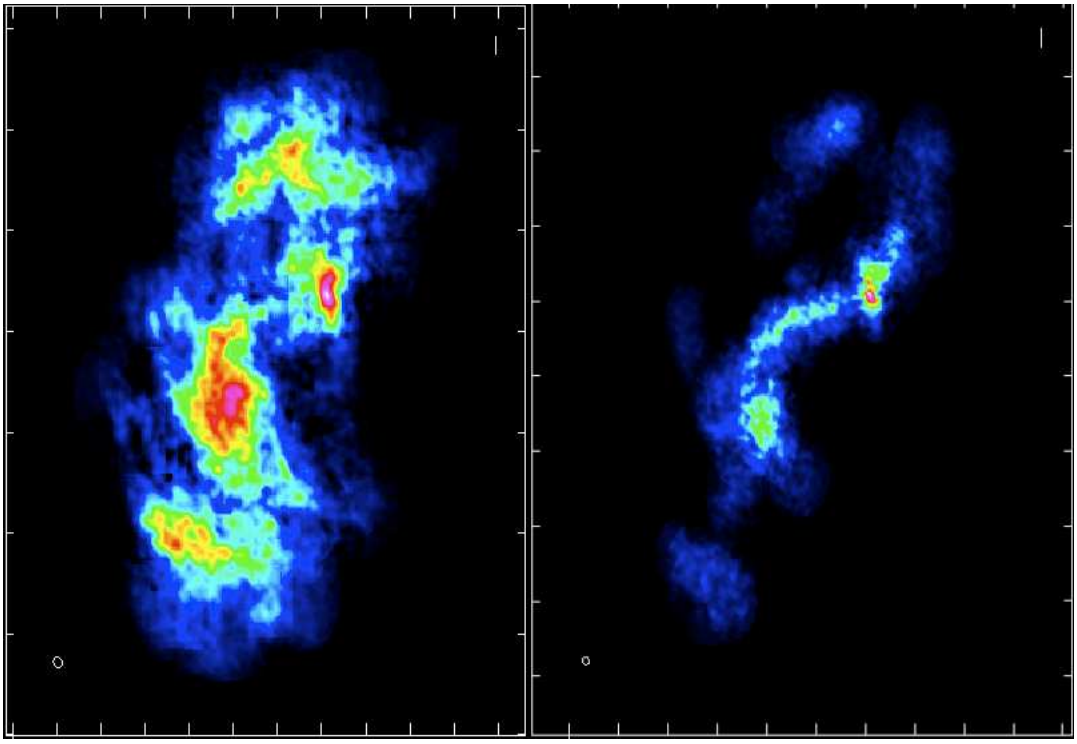

Figure 5.7: Integrated intensity images of HC_3N 3–2 (left) and 4–3 (right) in M0.25+0.01, using the same intensity scale. The distribution of HC_3N, which is a good tracer of dense gas, is more concentrated toward the center of the cloud than either CH_3OH or NH_3.

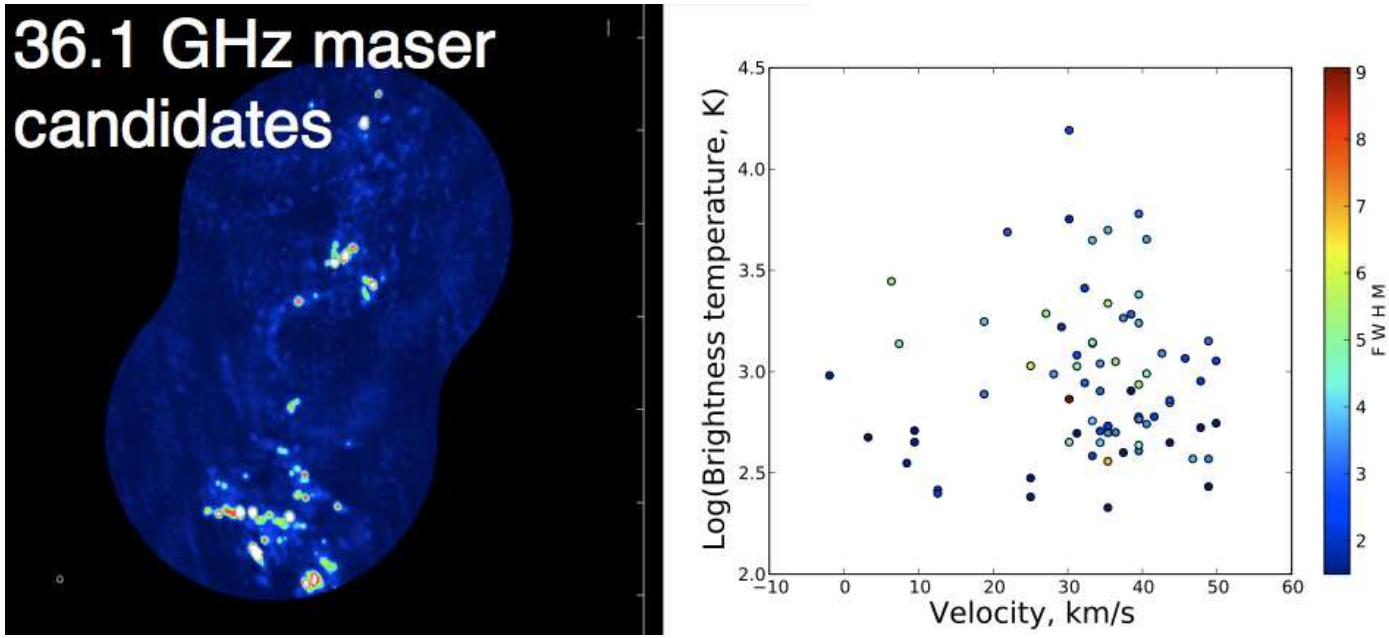

Figure 5.8: **Left:** a peak intensity image of the CH_3OH masers in M0.25+0.01. **Right:** The velocity of the 75 selected sources ($> 10\sigma$ above the noise in each channel) is plotted against their brightness temperatures. The points are additionally colorized by the FWHM of the line profile for each source.

The 36.1 GHz $4_{-1} \rightarrow 3_0 E$ CH_3OH maser is the most common and easiest to excite of the collisionally-excited CH_3OH masers (Cragg et al. 1992; Menten 1991a). Unlike the 6.7 $5_1 \rightarrow 6_0 A^+$ and 12 GHz $2_0 \rightarrow 3_{-1} E$ CH_3OH masers which are radiatively-excited (Menten 1991a,b), 36.1 GHz masers are believed to be excited in shocks. In star-forming regions, these collisionally-excited masers are considered to be signposts of early stages of massive stellar evolution, tracing the shocks from outflows which form before the central object is sufficiently luminous to excite the radiatively-excited CH_3OH masers. However, in the CMZ, where shocks are common (as traced by elevated abundances of SiO, e.g., Martin-Pintado et al. 1997) and physical and chemical conditions in the entire region are typical of those found in high-mass protostars (Requena-Torres et al. 2006), this is not a safe assumption. I also conducted follow-up VLA observations of the 6.7 GHz CH_3OH maser, which would unambiguously trace (later stages of) star formation, toward M0.25+0.01. Two masers were detected in the field of view, however neither were associated with the cloud, consistent with previous, lower resolution observations (Caswell 1996; Caswell et al. 2010). This is in line with a picture of the M0.25+0.01 cloud in which very little star formation is occurring.

Compared to the distribution of dust and dense gas in this cloud (Figures 5.2, 5.7), which are distributed relatively uniformly over the cloud, and concentrated in the center, the distribution of likely masers is quite inhomogeneous. In general, the 36.1 GHz CH_3OH emission, like the bulk of the NH_3 emission, arises predominately in the southern half of the M0.25+0.01 cloud. Figure 5.10 compares the velocities of the 36.1 GHz sources to the velocity field of the NH_3 gas, showing that the majority of the 36.1 GHz sources are associated with a high-velocity region (orange and pink in the figure) where two opposing east-west flows appear to converge. This suggests that the bulk of the masers may arise in a region where a large-scale shock between two components of the cloud is occurring. An

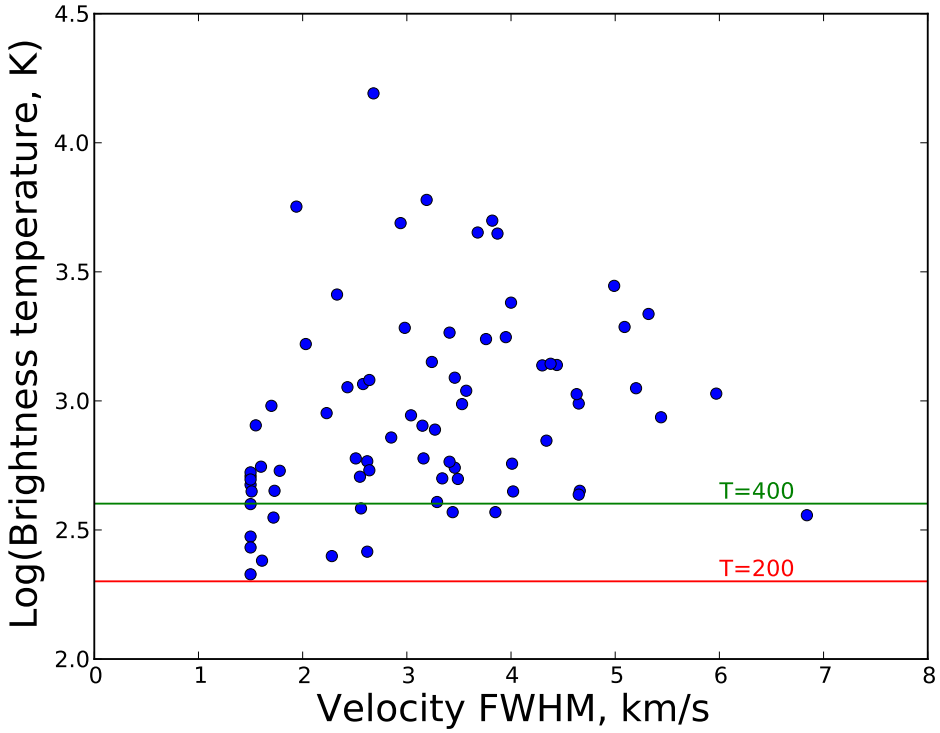

Figure 5.9: The logarithm of the brightness temperatures of maser candidates (in K) are plotted on the y-axis, against their measured FWHM in km s^{-1}, plotted on the x-axis. The red and green lines indicate temperatures which have been measured for gas in this cloud (200 and 400 K, respectively). Sources which have brightness temperatures in excess of the highest gas temperatures measured for this cloud (400 K) are likely nonthermal (maser) emission sources.

alternative hypothesis is that abundant methanol point sources in the CMZ are due to an enhanced methanol abundance from a high cosmic ray flux (Yusef-Zadeh et al. 2013a). While it is possible that cosmic rays do play a role in the high overall abundance of CH_3OH in the CMZ, the anisotropic distribution of CH_3OH masers in the clouds surveyed, as well as the kinematic association of the masers with regions having strong velocity gradients, suggests that shocks are the source of these masers.

The two separate components of M0.25+0.01, which appear to converge on the location of the maser overdensity, are better shown in channel maps of the emission in the the NH_3 (3,3) line (Figure 5.11) and a position-velocity diagram of this emission (Figure 5.12). The (3,3) line is used for this kinematic analysis as it is the strongest line observed in this cloud (apart from the CH_3OH masers). In the channel maps, two continuous velocity structures both begin at the northern tip of the cloud, one at 0 km s^{-1}, the other at 20 km s^{-1}, and converge at the bottom of the cloud at velocities between 30 and 40 km s^{-1}. This is best seen in the declination-velocity plot, where these 'streams' are seen to be separated by more than 20 km s^{-1} at declinations north of $-28°41'00''$, but south of declinations of $-28°43'00''$ they are no longer distinct, and have blended together.

The position-velocity plots show several other important features. First, there is a clear north-south velocity gradient in the cloud, spanning more than 80 km s^{-1}. Secondly, individual clumps in the cloud have FWHM ranging from 5-10 km s^{-1}, significantly less than the typical single-dish line widths of 15 to 20 km s^{-1} for this cloud (see, e.g., Chapter 4). This implies that much of the 'turbulence' inferred from large linewidths in this cloud is due to bulk motions and large-scale velocity gradients. Millimeter interferometric observations of N_2H^+ cores in this cloud have recently indicated even narrower linewidths, on the order of 1-2 km

s^{-1} (Kauffmann et al. 2013). Kauffmann et al. (2013) also suggest that, given the large velocities within this cloud, and the apparent lack of high-density (> a few 10^6 cm^{-3}) gas, the cloud may also be gravitationally unbound.

5.3.3 Where is the star formation?

Although it appears that, like the Sgr B2 cloud, M0.25+0.01 could be undergoing a large-scale collision, there still does not appear to be evidence for star formation, aside from a single water maser in the northeast of the cloud (Lis et al. 1994). In addition to the molecular line studies of this cloud, sensitive maps of its continuum emission were also made, in order to search for deeply embedded compact HII regions that would signify the presence of more active star formation in this cloud. An unexpected finding of these observations was low-level ($\sim$ 0.5 mJy $beam^{-1}$), extended continuum emission distributed throughout cloud. Contours of the 25 GHz continuum emission are shown overlaid on the NH_3 image in Figure 5.13. Spectral indices of emission associated with the cloud are flat (indicating the emission is thermal in nature) or positive (indicating that the emission could be due to dust emission, which has a spectral index of 4, or it could be optically-thick free-free emission). There are also two point sources located outside of the cloud that have non-thermal (negative) spectral indices. The distribution of emission, which is largely exterior to the molecular gas traced by NH_3, suggests that this emission is predominantly due to external ionization of the cloud by the ambient radiation field. There is also some good correspondence between the 25 GHz continuum emission and the structure of this cloud seen at 90 GHz with ALMA (J. Rathborne, private communication 2013). Although the majority of this correspondence is likely due to the detection of free-free emission at both frequencies, there is at least one point source in the northern part of the

cloud which has a significantly positive spectral index of ~ 2, which could be consistent with a mix of cool dust and ionized gas, as it this spectral index is less than expected for pure dust, however the source is still prominent at 1 mm (K. Johnston, private communication 2013), a wavelength at which the emission should be solely due to dust. The detected free-free emission does not appear to be consistent with embedded HII regions, though this claim has recently been made on the basis of higher resolution VLA observations, which resolve out much of the extended emission (Rodríguez & Zapata 2013).

In summary, M0.25+0.01 still appears to lack indicators of ongoing star formation, though with the evidence for widespread shocks, high temperatures, and large velocity gradients, it can hardly be called quiescent.

5.4 Sgr A Molecular Clouds

The Sagittarius A complex of molecular clouds (the Sgr A clouds, not to be confused with the associated complex of radio continuum sources of the same name) consists of three main clouds: M-0.02-0.07 (the 50 km s^{-1} cloud), M-0.13-0.08 (the 20 km s^{-1} cloud), and the circumnuclear disk (CND, described in Chapter 3). These clouds are projected to lie within the central 10 pc of the Galaxy, and are believed to be physically close as well, based upon their interactions with each other and with the gravitational potential of the central supermassive black hole (Coil & Ho 2000; Herrnstein & Ho 2005; Ferrière 2012).

In particular, as is illustrated in Figure 5.14, M-0.02-0.07 is interacting with the supernova remnant Sgr A East, which is compressing a dense ridge in this cloud (the molecular ridge, Serabyn et al. 1992), which extends to the south, connecting this cloud to M-0.13-0.08 (Herrnstein & Ho 2005). The continuation

of this ridge on the back side of the supernova remnant is identified as the 'western ridge' (McGary et al. 2001). A 'northern ridge' of gas (McGary et al. 2001) also connects this ridge and gas in M-0.02-0.07 to the CND, a ring of gas surrounding the central supermassive black hole at a radius of $\sim$ 1.5 pc (Güsten et al. 1987; Jackson et al. 1993). M-0.13-0.08 also appears to be interacting with the CND, via the 'southern streamer' (Coil & Ho 1999, 2000). It is suggested that these structures are feeding the CND (Coil & Ho 2000; Liu et al. 2013), which may itself be slowly feeding the central parsec as gas from the CND extends inward toward the orbiting ionized 'minispiral' of gas (Zhao et al. 2009; Kunneriath et al. 2012; Martín et al. 2012; Liu et al. 2012, 2013).

The two largest clouds, M-0.02-0.07 and M-0.13-0.08, both have embedded HII regions: Three compact and one ultracompact HII regions are associated with in M-0.02-0.07 (Goss et al. 1985; Ho et al. 1985; Yusef-Zadeh et al. 2010; Mills et al. 2011, Chapter 2) and one compact HII region is found in M-0.13-0.08 (Ho et al. 1985). Each of these HII regions is consistent with ionization from a single early B or late-type O star, indicating that there is a small amount of recent massive star formation in these clouds. There have also been suggestions that there is ongoing massive star formation in the CND, however these claims are mostly based on the detection of shock-tracing molecules (e.g. SiO and collisionally-excited CH_3OH masers; Yusef-Zadeh et al. 2008, 2013c) which are also likely to be present due to collisions, infall, and the general turbulence of gas in this environment, making this an ambiguous tracer of star formation, at best.

VLA observations of NH_3 in the Sgr A clouds breaks the clouds into a multitude of compact cores and filaments (Figures 5.15, 5.16). Overall, there is a strong velocity gradient across the field from -10 km s^{-1} at the tip of M-0.13-0.08, to 50 km s^{-1} in M-0.02-0.07 and the gas surrounding the Sgr A East supernova rem-

nant. There are also several velocity components which deviate from this overall velocity structure; the eastern part of M-0.02-0.07 has radial velocities from 10 to 30 km s^{-1}, and radial velocities in the gas detected in the CND, surrounding the black hole, range from -100 km s^{-1} to 50 km s^{-1}.

The strongest sources of NH_3 emission are M-0.02-0.07, and the southern peak of M-0.13-0.08. However, comparing the maps of NH_3 (3,3) emission to that from the dense gas tracing line HC_3N (3-2), the southern peak of M-0.13-0.08 is entirely absent in this line (Figure 5.16). There is also no HC_3N emission seen from the CND, which is either an indication that gas in this region is less dense, or that HC_3N is under-abundant or destroyed in this environment (Martín et al. 2012). Several strong, compact sources of NH_3 (3,3) emission, which are likely masers, are also found in the CND, coincident with observed 44 GHz CH_3OH masers (Yusef-Zadeh et al. 2008). Overall however, NH_3 emission from the CND is relatively weak in comparison to emission from M-0.02-0.07 and M-0.13-0.08.

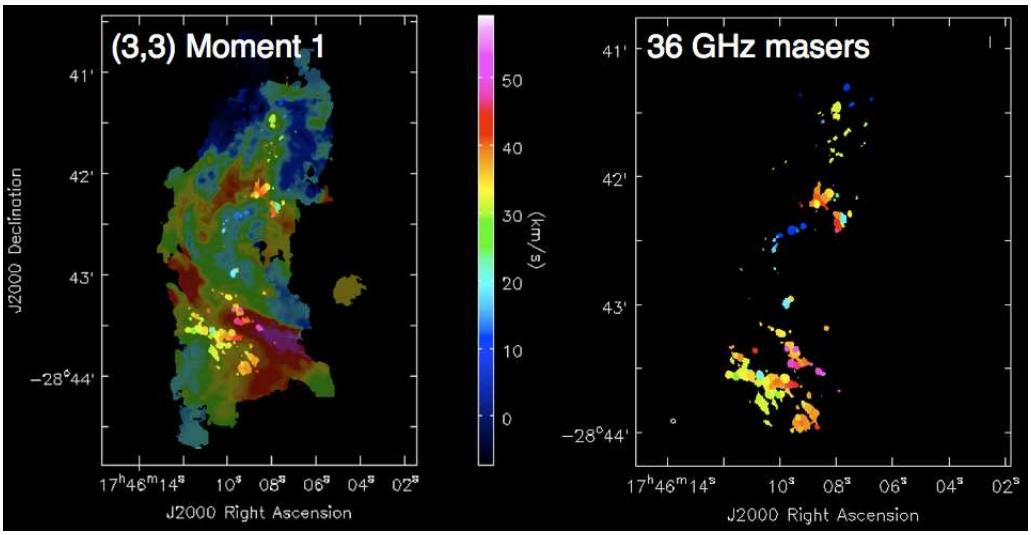

Figure 5.10: **Left:** A moment 1 (intensity-weighted velocity) map of M0.25+0.01 from NH_3 (3,3) emission. The velocities of the 36.1 GHz CH_3OH maser candidates are shown both as a semitransparent overlay on this map, and in a separate map (**Right**).

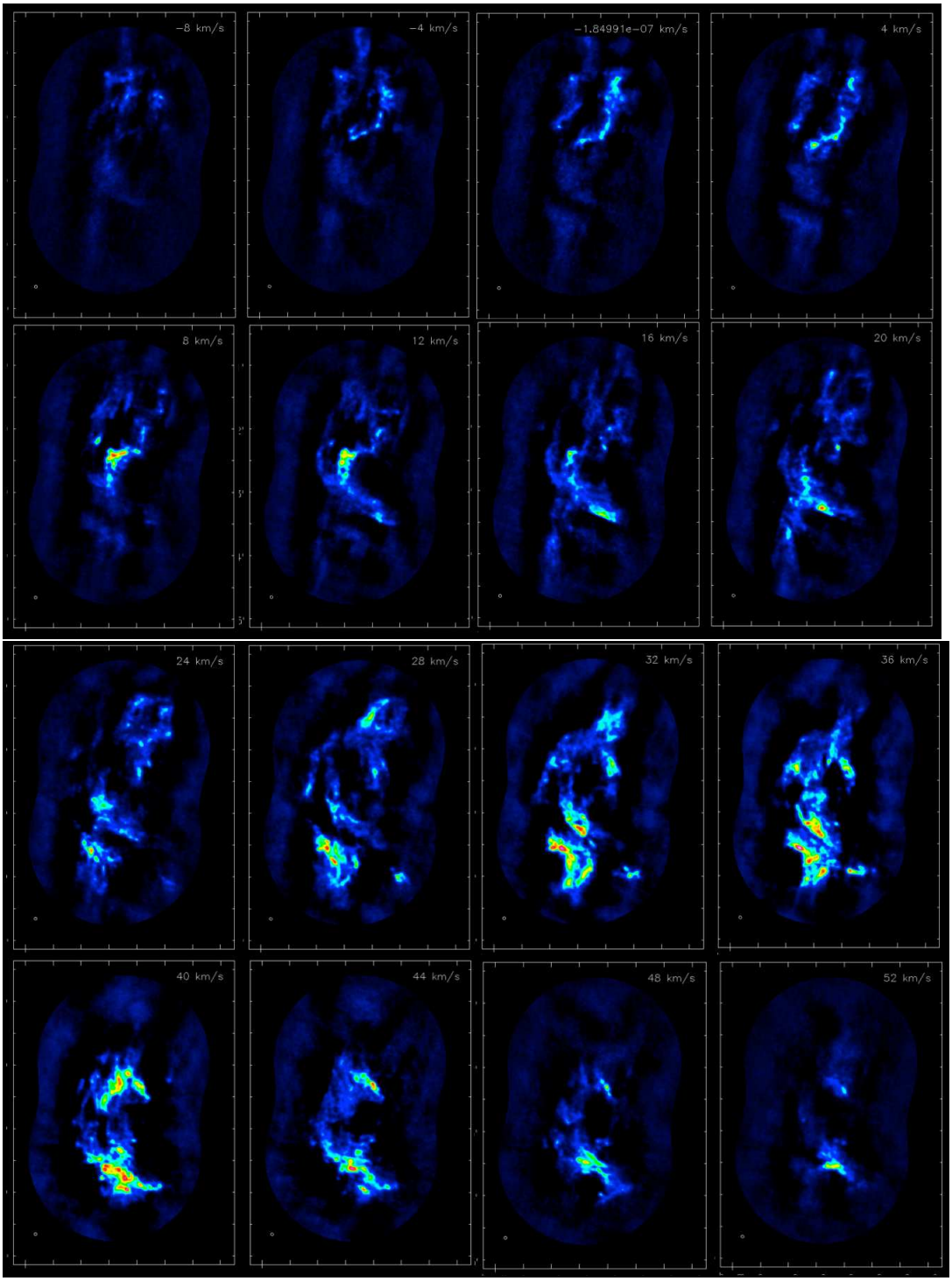

Figure 5.11: Channel maps of NH_3 (3,3), the brightest line detected in M0.25+0.01. Emission is shown for a subset of velocities from -8 to 52 km s^{-1}, with channel widths of 4 km s^{-1}.

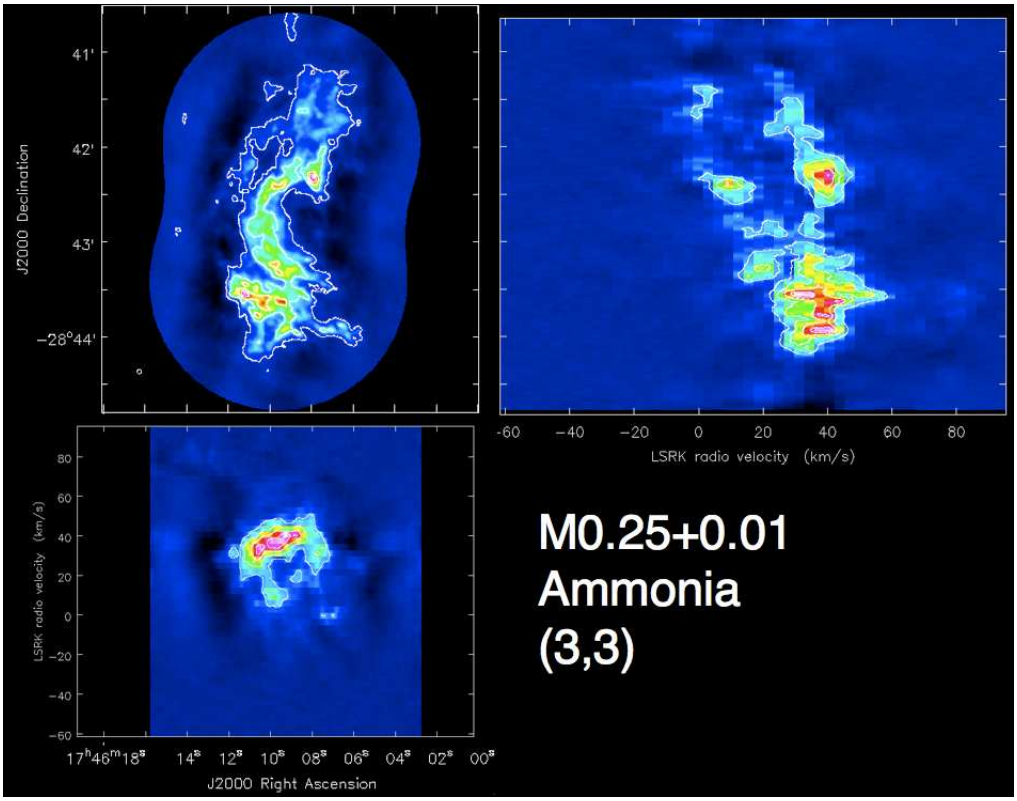

Figure 5.12: Position velocity maps of NH_3 (3,3), the brightest line detected in M0.25+0.01. **Top Left:** a map of NH_3 (3,3) emission in M0.25+0.01 integrated over all velocities. **Top Right:** A map of NH_3 (3,3) emission as a function of declination and velocity, integrated over the right ascension coordinate. In this map, two distinct velocity components, one at 10 km s^{-1} and one at 40 km s^{-1}, are seen in the northern region of the cloud, and appear to merge at the southern tip of the cloud. **Bottom Left:** A map of NH_3 (3,3) emission as a function of right ascension and velocity, integrated over the declination coordinate.

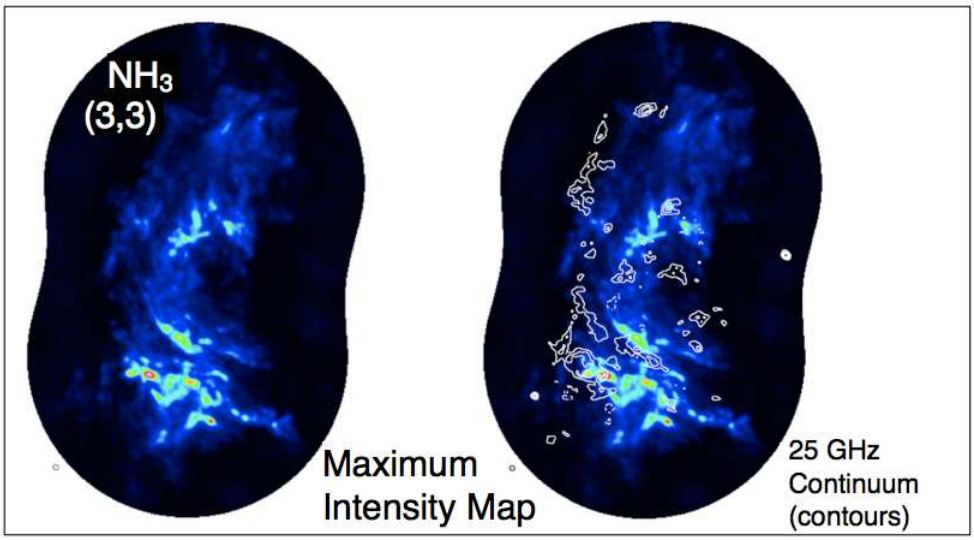

Figure 5.13: Comparison of the continuum (contours) and the molecular gas, traced by NH_3 (3,3) in M0.25+0.01. The bulk of the continuum emission is seen to arise outside of the NH_3 emission, suggesting that the cloud is being externally ionized.

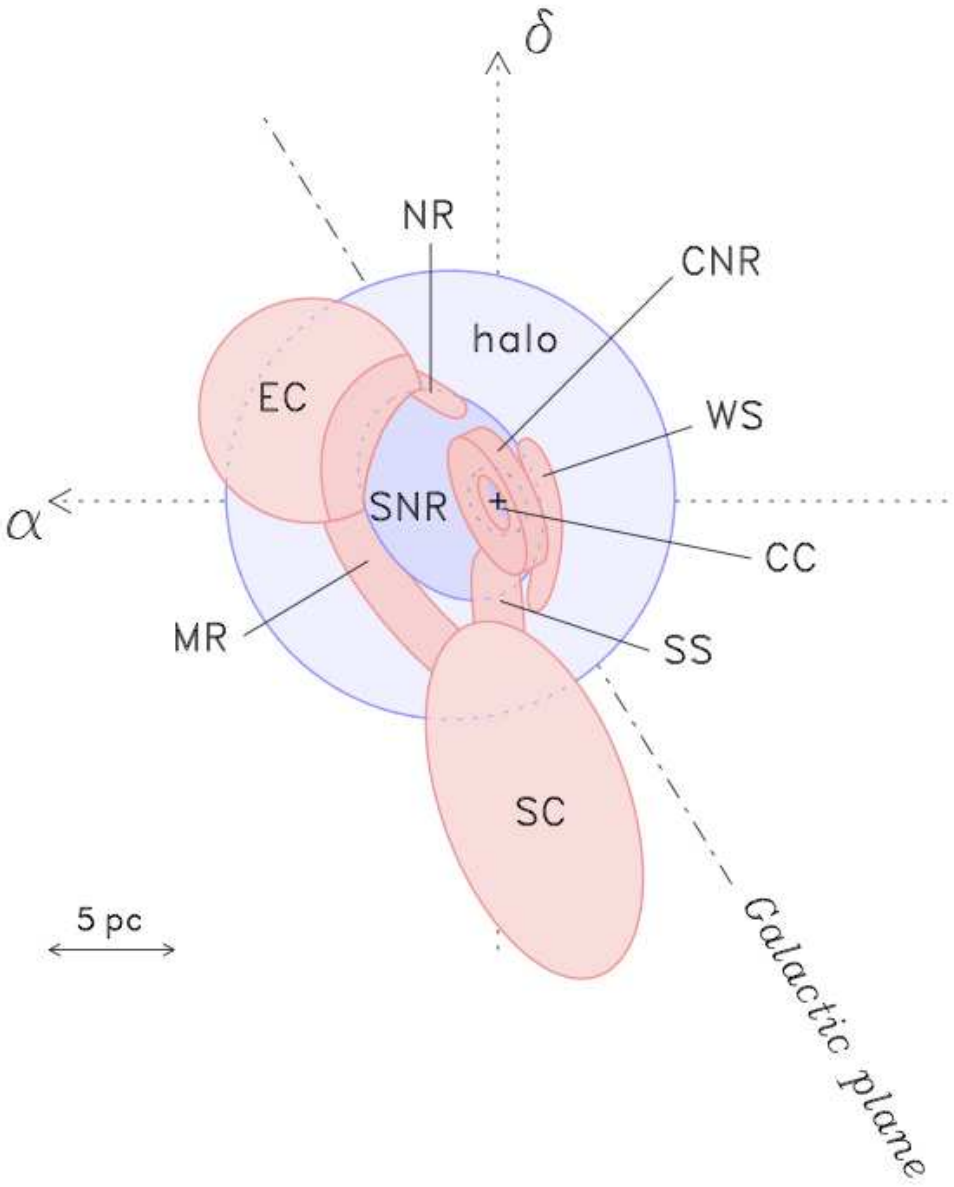

Figure 5.14: A schematic representation of the components of Sgr A, in the plane of the sky. Diffuse and primarily ionized components are colored light blue, including the central cavity (CC), the Sgr A East supernova remnant, and the radio halo. Dense, largely molecular components are represented in red. These include the Circumnuclear ring or disk (CNR), the southern cloud M-0.13-0.08 (SC), the eastern cloud M-0.02-0.07 (EC), the molecular ridge (MR), the southern streamer (SS), the western streamer (WS) and the northern ridge (NR). Figure reproduced from Ferrière (2012)

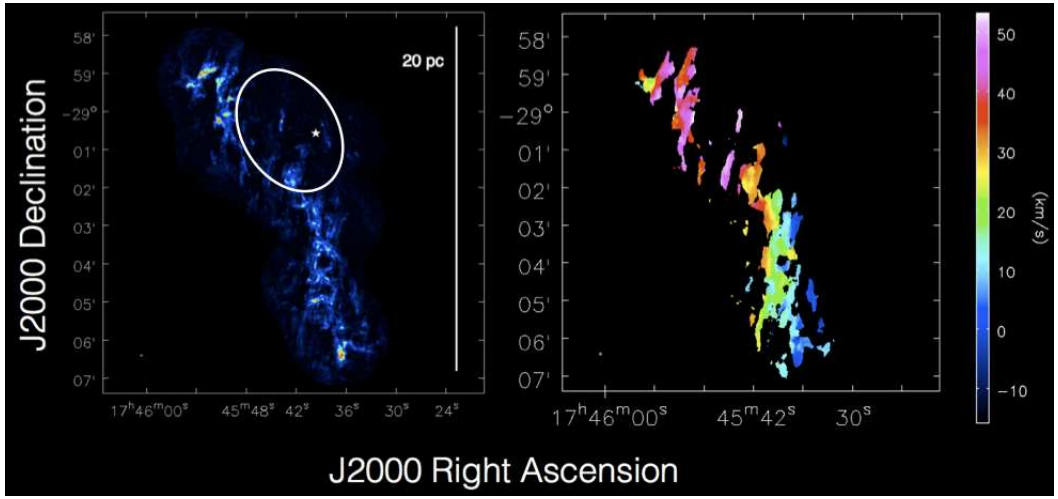

Figure 5.15: **Left:** A map of the peak intensity in the NH_3 (3,3) cube of the Sgr A clouds. **Right:** The intensity-weighted velocity (Moment 1) map derived from the NH_3 (3,3) cube. A strong north-south velocity gradient runs through both clouds, from 50 to -10 km s^{-1}. The white star represents the location of Sgr A*, and the white ellipse represents the position of Sgr A East from Figure 5.14

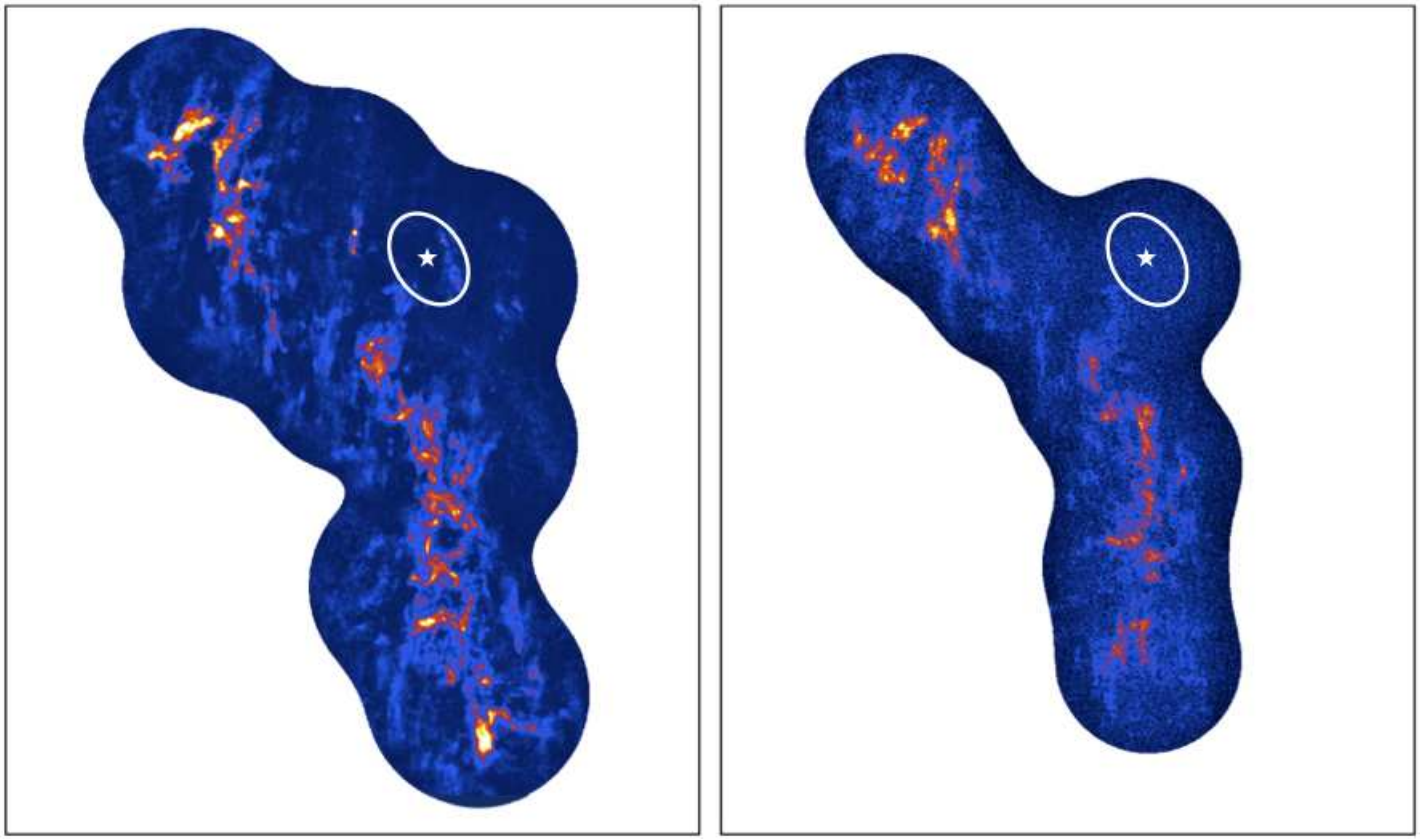

Figure 5.16: **Left:** a map of the peak intensity in the NH_3 (3,3) cube of the Sgr A clouds. **Right:** a map of the peak emission in the HC_3N (3-2) cube of the Sgr A clouds. The distribution of NH_3 and HC_3N is similar in M-0.02-0.07, at the top of the image, however there are several differences elsewhere in the Sgr A clouds. First, faint NH_3 emission is observed toward the CND in the top right corner of the image, but HC_3N emission is entirely lacking from this region. HC_3N emission is also absent toward the southernmost NH_3 peak in M-0.13-0.08 at the bottom of the map. In each map, the white star represents the location of Sgr A*, and the white ellipse represents the position of the CND from Figure 5.14

5.4.1 The CND

NH_3 (3,3) emission in the CND is shown in greater detail in Figure 5.17. Four main features are detected in this map: emission from clumps S, SW, and W (identified previously in Chapter 3) and emission to the west of the CND from the Western ridge (McGary et al. 2001). Clump W is one of the sources which appears to be a (3,3) NH_3 maser; it is positionally coincident with a 44 GHz CH_3OH maser (Yusef-Zadeh et al. 2008), and has a linewidth of $\sim$ 8 km s^{-1}, which, although it is not so narrow as to be nonthermal, is relatively narrow for the CND. In contrast, the similarly compact clump S has a linewidth of 30 km s^{-1}. Clump S has also recently been found to be the strongest submillimeter source in the CND (and in the central 5 pc, Figure 5.17; Liu et al. 2013). Although Liu et al. (2013) did not estimate the density of this clump, the strong, compact dust emission from this source indicates it is substantially more dense than other gas in the CND, consistent with my analysis using APEX data in Chapter 3.

In addition to emission from the (3,3) line, emission from the (6,6) line is also detected toward the CND (Figure 5.18). As both of these lines belong to the ortho species of NH_3 the ratio of their intensities can be used to estimate the kinetic temperature of gas in the CND. The resulting temperature map for the SW clump is shown in Figure 5.18. The derived rotational temperatures for clump SW range from 90 to 140 K, and from 80 to 120 for clump S. Using the relation of (Ott et al. 2011) to estimate the gas kinetic temperatures from these rotational temperatures yields kinetic temperatures of 120-240 K for clump SW and 100-140 for clump S. However, if the (3,3) line is weakly masing, as may be the case for the CMZ cloud M0.25+0.01 (Section 5.3), then this temperature could be an underestimate of the actual CND gas temperature. Whether or not the (3,3) line is masing, these temperatures are a strong lower limit for the gas temperature in

the CND. In particular, for clump S, for which the HCN excitation analysis of Chapter 3 indicated densities between $10^{6.5}$ and $10^{7.6}$ cm^{-3}, a kinetic temperature greater than 100 K constrains the gas density to be less than $10^{6.8}$ cm^{-3}, and thus implies that this clump, the densest detected in the CND, is also neither tidally stable nor in virial equilibrium (though as the HCN density analysis is based on single-dish data, it is possible that contributions from surrounding gas to the intensities measured for this clump may lead to an underestimate of its density).

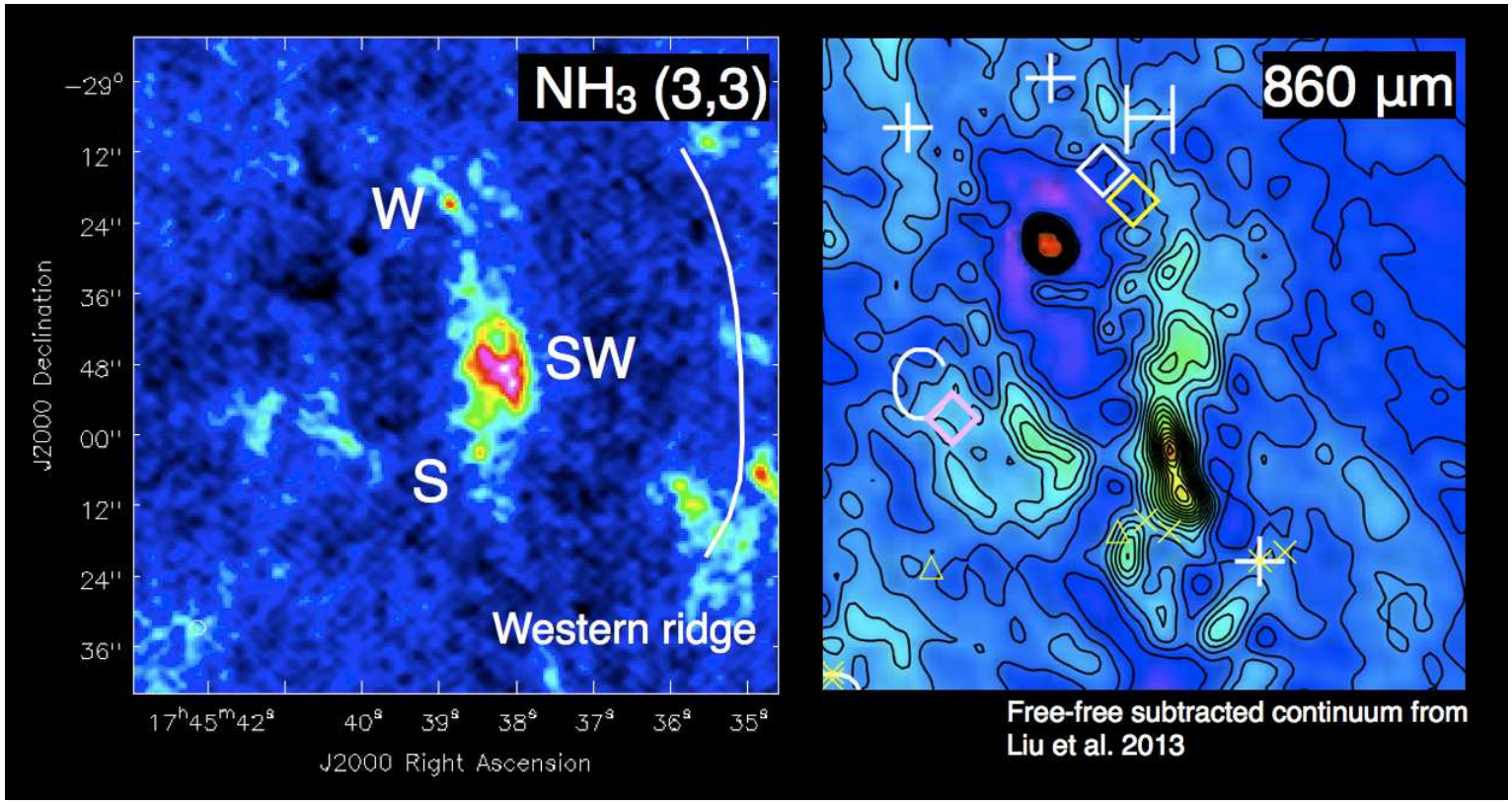

Figure 5.17: **Left:** A map of NH_3 (3,3) emission in the CND. The synthesized beam width of these observations is $2''.4 \times 2''.5$ (corresponding to a spatial resolution of ~ 0.1 pc at a distance of 8.4 kpc), making this the highest resolution image of gas in the CND to date. Four structures are identified: clumps W, SW and S, and the Western Ridge, indicated with a line. **Right:** a map of the 860 μm dust continuum in the CND on the same scale, with the free-free emission subtracted, from Liu et al. (2013). The strongest peak in this map corresponds to clump S. The synthesized beam width of these observations is $5''.1 \times 4''.2$

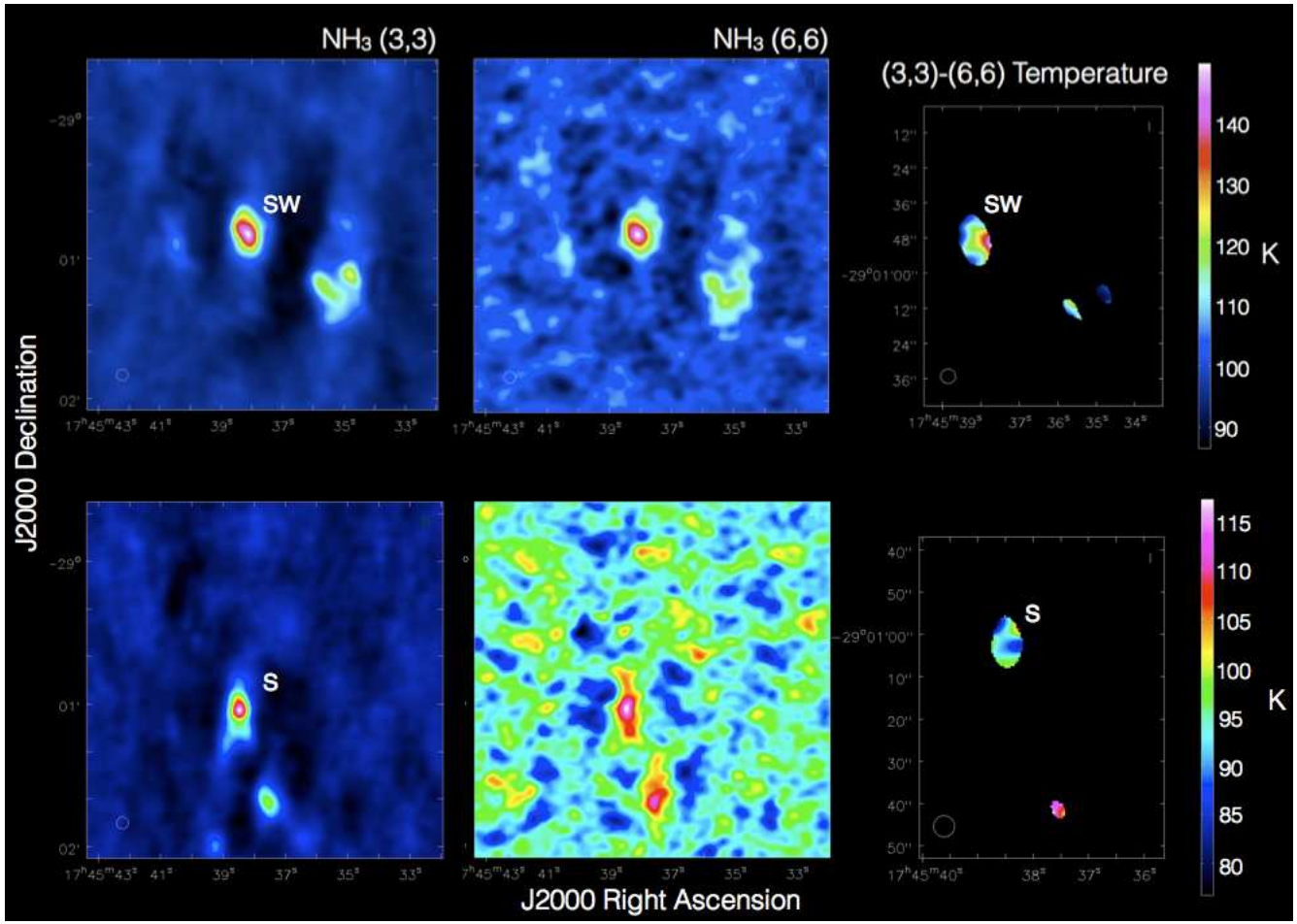

Figure 5.18: **Left, Middle Columns:** Smoothed images of NH_3 (3,3) and (6,6) emission at the velocity of the Southwest emission peak (Top: clump SW, -20 km s^{-1}) and the Southern emission peak (Bottom: clump S, -100 km s^{-1}) in the CND, observed with the VLA. **Right:** The resulting temperature maps show NH_3 rotational temperatures which vary from 90 to 140 K for the Southwest emission peak, and from 80 to 120 K for the Southern emission peak. These temperatures correspond to kinetic temperatures of 100-250 K, though this may be an underestimate if the NH_3 (3,3) line is weakly masing.

5.4.2 A peculiar CH_3OH source

In addition to the previously-identified strong 36.1 CH_3OH masers in M-0.02-0.07 (Sjouwerman et al. 2010), the VLA observations reveal an unusual, spatially-extended source of CH_3OH emission in this cloud. This source is located in the dense ridge of gas which is apparently compressed by Sgr A East (Serabyn et al. 1992), close to the ultracompact HII region Sgr D (Figure 5.19). This source is either thermal, or consists of several relatively weak masers on top of thermal CH_3OH emission, with a velocity gradient of 10 km s^{-1} across the source (Figure 5.20). The bipolar appearance of this source, with blue- and red-shifted emission lobes, suggests that the CH_3OH could be tracing a low-velocity outflow. If so, this would be evidence for ongoing star formation in M-0.02-0.07 in the gas which is being compressed by the Sgr A East supernova remnant (see Chapter 2). Higher resolution follow-up observations of this source in additional molecular tracers are needed to determine whether there is truly an energetic source powering this outflow, whether the CH_3OH emission traces a shock structure unrelated to ongoing star formation, or whether this represents a remarkably fortuitous superposition of two (possibly maser) sources at different velocities.

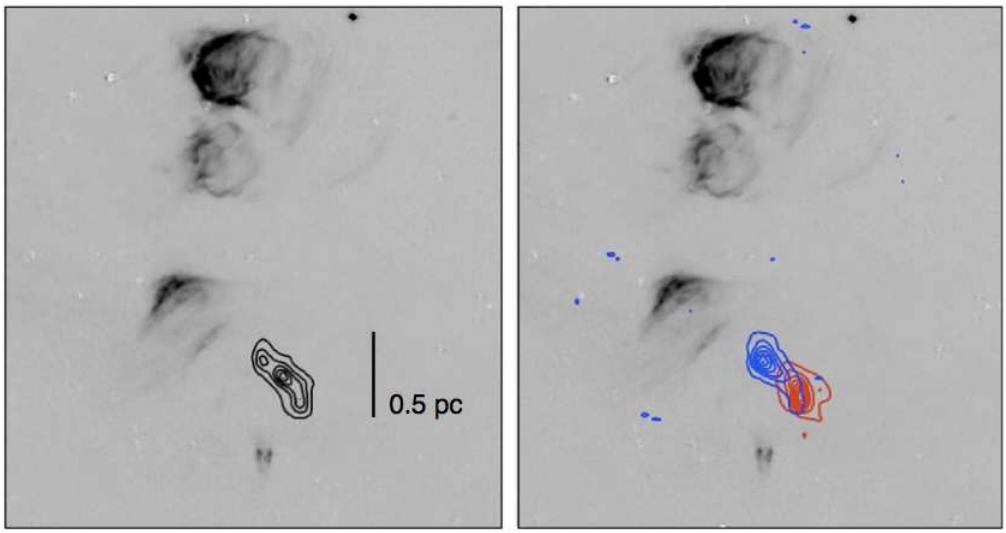

Figure 5.19: Contours of emission from a candidate CH_3OH outflow source in M-0.02-0.07 are shown superposed upon a Paschen α image of the compact HII regions in this cloud. **Left:** contours of integrated CH_3OH emission. **Right:** separate contours for the blueshifted and redshifted lobes are shown. This candidate outflow source lies just above the most compact and likely youngest of the HII regions, source D.

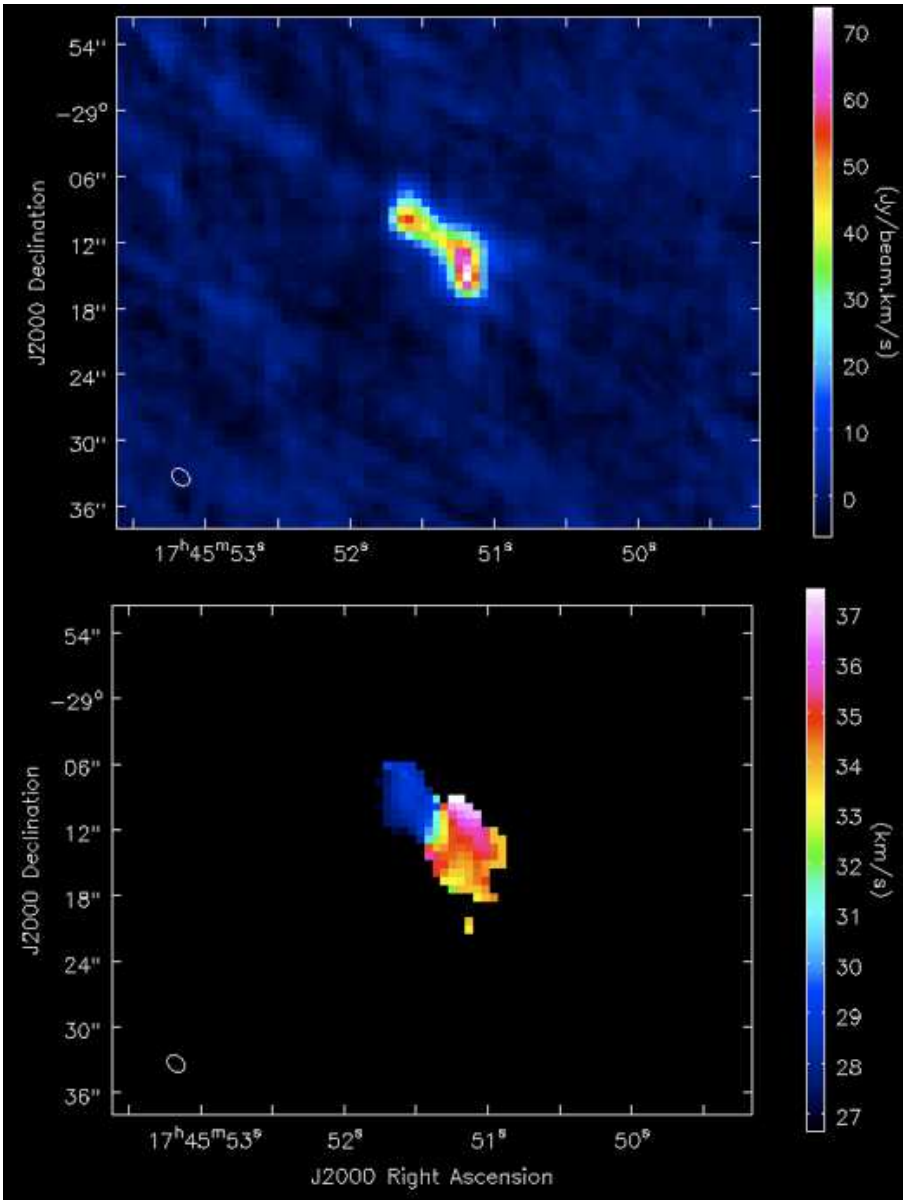

Figure 5.20: Moment 0 (integrated emission, Top) and Moment 1 (intensity-weighted velocity field, Bottom) from the peculiar 36.1 GHz CH_3OH source in M-0.02-0.07

CHAPTER 6

Conclusions

The work presented in this thesis has covered a diverse range of sources in the CMZ, elucidating the properties of the molecular gas and its environment in the central 600 parsecs.

In Chapter 2, I presented a study of the HII regions in the M-0.02-0.07 cloud in the CMZ, adjacent to the Sgr A East supernova remnant. To better depict the physical relationship between these sources, I used archival VLA observations and Paschen α images from the Hubble Space telescope to determine the extinction toward the HII regions (Mills et al. 2011). From the measured extinctions and source morphologies, I determined that three of the HII regions lie on the front side of the cloud and formed in the eastern part of the cloud which is still unaffected by the expansion of the supernova remnant. The higher extinction of the fourth HII region indicates that it is embedded in the supernova-compressed ridge, and though younger than the other HII regions, is still older than the supernova. This work is an important determination of the line-of-sight placement of these sources which helps to define their interaction and strengthens the case that the supernova did not trigger the formation of the HII regions.

Chapter 3 presents results from a project I led to survey a sample of CMZ clouds for hot gas using the Green Bank Telescope (Mills & Morris 2013). I observed multiple highly-excited lines of NH_3 and detected emission from the (9,9) line of NH_3 (excitation energy = 840 K) in 13 of 17 clouds, many of which

have no associated star formation. For the three strongest sources, I derived rotation temperatures of 350-450 K, substantially higher than the temperatures of 200-300 K previously measured for these clouds (Mauersberger et al. 1986). The widespread detections of gas hotter than 400 K indicates for the first time that this hot gas must be heated by global processes in the CMZ. These extremely high temperatures, present in about 10% of the NH_3-emitting molecular gas in the CMZ where highly-excited ammonia emission is present, also suggest that cosmic rays are not responsible for the heating of this gas.

In Chapter 4, I presented a determination of the density of the CND using multiple transitions of HCN and $HCO^+$with the APEX telescope, a 12m ALMA propotype dish. These molecules have critical densities $> 10^7$ cm^{-3} and directly constrain the existence of high-density gas. The excitation analysis of HCN and HCO^+ yields new limits on the typical densities in this gas ($n = 10^{5.0} - 10^{7.0}$ cm^{-3}), however even with these limits, I cannot rule out the possibility that a small number of individual gas clumps are tidally stable or in virial equilibrium (Mills et al., in prep.). The detection of the $v_2 = 1$ vibrationally-excited J=4-3 HCN line also indicates that infrared radiation may play a role in the excitation of HCN in this source, but it is not clear whether radiative excitation in the CND is a localized or global phenomenon.

In Chapter 5, I presented a summary of early results from a survey of four molecular cloud complexes in the CMZ (Mills et al. in prep.), which I led using the new capabilities of the VLA. The goal of this work is to determine the variation in temperature in these clouds on 0.1 pc scales to ultimately identify their heating sources. An unanticipated discovery of this study has been hundreds of weak, collisionally-excited CH_3OH masers which are detected in all of the clouds surveyed. The masers are distributed non-uniformly in the clouds, with concen-

trations indicating regions of shock activity which may be driving the evolution of physical conditions in these clouds. I also find that the NH_3 (3,3) line may be weakly masing in several sources, which can be used to put constraints on the density of the gas clumps in these clouds (Walmsley & Ungerechts 1983).

As part of this work, I also observed the CND in multiple lines of NH_3. The temperature measurements I derive in this study can be used to refine the densities I derived from my excitation analyses of HCN and HCO^+. I find preliminary CND gas temperatures of 100-200 K, which further limits the gas density in the densest clumps in the CND to be $< 10^{6.8}$ cm^{-3}, indicating that even the densest gas clumps may not be virialized or tidally stable.

Overall, I have used a diverse set of observations to set new constraints on the extreme gas conditions which exist in the CMZ. However, the work presented in this thesis is only the beginning of projects which the capabilities of the new VLA and ALMA will make possible. Much work remains to be done to understand the variation of physical conditions throughout the CMZ, and how these conditions locally affect the star formation process. Future projects with these existing data will involve constructing detailed temperature maps of the molecular clouds to determine the temperature distribution in the densest gas, and whether it is sufficiently warm to be consistent with cosmic ray heating.

Future projects will examine the distribution of gas denser than 10^6 cm^{-3}, like that found in the CND, using VLA observations of non-metastable NH_3 in this sample of CMZ clouds, in order to determine how the distribution of the densest gas and shocked gas is related to the star formation content of individual clouds. ALMA observations of the CND are also planned to investigate the dense gas in individual cores, and to better assess the importance of correcting for the radiative excitation in the determination of densities in this environment.

The Galactic center, after all, offers one of the nearest extreme environments for molecular gas and star formation which can be observed; it is important to be able to put limits on the physical and chemical properties of this environment, and to determine just how extreme conditions in this gas may be found to be.

Bibliography

Abadi, M. G., Navarro, J. F., Steinmetz, M., & Eke, V. R. 2003, ApJ, 597, 21

Alves, J. F., Lombardi, M., & Lada, C. J. 2007, Astronomy and Astrophysics, 462, L17

Amo-Baladrón, M. A., Martín-Pintado, J., & Martín, S. 2011, A&A, 526, A54+

An, D., Ramirez, S. V., & Sellgren, K. 2013, arXiv.org, astro-ph.GA

An, D., Ramírez, S. V., Sellgren, K., Arendt, R. G., Adwin Boogert, A. C., Robitaille, T. P., Schultheis, M., Cotera, A. S., Smith, H. A., & Stolovy, S. R. 2011, ApJ, 736, 133

Ao, Y., Henkel, C., Menten, K. M., Requena-Torres, M. A., Stanke, T., Mauersberger, R., Aalto, S., Mühle, S., & Mangum, J. 2013, A&A, 550, A135

Armstrong, J. T. & Barrett, A. H. 1985, ApJS, 57, 535

Armstrong, J. T., Ho, P. T. P., & Barrett, A. H. 1985, ApJ, 288, 159

Arons, J. & Max, C. E. 1975, ApJL, 196, L77

Arthur, S. J. & Hoare, M. G. 2006, ApJS, 165, 283

Baganoff, F. K., Bautz, M. W., Brandt, W. N., Chartas, G., Feigelson, E. D., Garmire, G. P., Maeda, Y., Morris, M., Ricker, G. R., Townsley, L. K., & Walter, F. 2001, Nature, 413, 45

Balick, B. & Brown, R. L. 1974, ApJ, 194, 265

Bally, J., Aguirre, J., Battersby, C., Bradley, E. T., Cyganowski, C., Dowell, D., Drosback, M., Dunham, M. K., Evans II, N. J., Ginsburg, A., Glenn, J.,

Harvey, P., Mills, E., Merello, M., Rosolowsky, E., Schlingman, W., Shirley, Y. L., Stringfellow, G. S., Walawender, J., & Williams, J. 2010, ApJ, 721, 137

Bally, J., Stark, A. A., Wilson, R. W., & Henkel, C. 1987, ApJS, 65, 13

—. 1988, ApJ, 324, 223

Bania, T. M. 1977, ApJ, 216, 381

Becklin, E. E., Gatley, I., & Werner, M. W. 1982, ApJ, 258, 135

Becklin, E. E., Matthews, K., Neugebauer, G., & Willner, S. P. 1978, ApJ, 219, 121

Becklin, E. E. & Neugebauer, G. 1968, ApJ, 151, 145

—. 1975, ApJL, 200, L71

Belloche, A., Menten, K. M., Comito, C., Müller, H. S. P., Schilke, P., Ott, J., Thorwirth, S., & Hieret, C. 2008, A&A, 482, 179

Beuther, H., Tackenberg, J., Linz, H., Henning, T., Schuller, F., Wyrowski, F., Schilke, P., Menten, K., Robitaille, T. P., Walmsley, C. M., Bronfman, L., Motte, F., Nguyen-Luong, Q., & Bontemps, S. 2012, ApJ, 747, 43

Binney, J., Gerhard, O. E., Stark, A. A., Bally, J., & Uchida, K. I. 1991, MNRAS, 252, 210

Bland-Hawthorn, J. & Cohen, M. 2003, ApJ, 582, 246

Blitz, L. & Spergel, D. N. 1991, ApJ, 379, 631

Bovy, J., Allende Prieto, C., Beers, T. C., Bizyaev, D., da Costa, L. N., Cunha, K., Ebelke, G. L., Eisenstein, D. J., Frinchaboy, P. M., García Pérez, A. E.,

Girardi, L., Hearty, F. R., Hogg, D. W., Holtzman, J., Maia, M. A. G., Majewski, S. R., Malanushenko, E., Malanushenko, V., Mészáros, S., Nidever, D. L., O'Connell, R. W., O'Donnell, C., Oravetz, A., Pan, K., Rocha-Pinto, H. J., Schiavon, R. P., Schneider, D. P., Schultheis, M., Skrutskie, M., Smith, V. V., Weinberg, D. H., Wilson, J. C., & Zasowski, G. 2012, ApJ, 759, 131

Bower, G., Falcke, H., Gillessen, S., Marrone, D., Narayan, R., Nowak, M., Ott, J., Ozel, F., Reid, M. J., & Yusef-Zadeh, F. 2012

Bradford, C. M., Stacey, G. J., Nikola, T., Bolatto, A. D., Jackson, J. M., Savage, M. L., & Davidson, J. A. 2005, ApJ, 623, 866

Burton, W. B. & Liszt, H. S. 1978, Astrophysical Journal, 225, 815

Capelli, R., Warwick, R. S., Porquet, D., Gillessen, S., & Predehl, P. 2012, A&A, 545, A35

Carretti, E., Crocker, R. M., Staveley-Smith, L., Haverkorn, M., Purcell, C., Gaensler, B. M., Bernardi, G., Kesteven, M. J., & Poppi, S. 2013, Nature, 493, 66

Carroll, T. J. & Goldsmith, P. F. 1981, ApJ, 245, 891

Caselli, P., Walmsley, C. M., Terzieva, R., & Herbst, E. 1998, ApJ, 499, 234

Caswell, J. L. 1996, Mon. Not. R. Astron. Soc., 283, 606

Caswell, J. L., Fuller, G. A., Green, J. A., Avison, A., Breen, S. L., Brooks, K. J., Burton, M. G., Chrysostomou, A., Cox, J., Diamond, P. J., Ellingsen, S. P., Gray, M. D., Hoare, M. G., Masheder, M. R. W., McClure-Griffiths, N. M., Pestalozzi, M. R., Phillips, C. J., Quinn, L., Thompson, M. A., Voronkov,

M. A., Walsh, A. J., Ward-Thompson, D., Wong-McSweeney, D., Yates, J. A., & Cohen, R. J. 2010, MNRAS, 404, 1029

Ceccarelli, C., Baluteau, J.-P., Walmsley, M., Swinyard, B. M., Caux, E., Sidher, S. D., Cox, P., Gry, C., Kessler, M., & Prusti, T. 2002, Astronomy and Astrophysics, 383, 603

Cheung, A. C., Rank, D. M., Townes, C. H., Knowles, S. H., & Sullivan, III, W. T. 1969, ApJL, 157, L13

Chomiuk, L. & Povich, M. S. 2011, AJ, 142, 197

Christopher, M. H., Scoville, N. Z., Stolovy, S. R., & Yun, M. S. 2005, ApJ, 622, 346

Churchwell, E. 2002, ARAA, 40, 27

Churchwell, E. & Walmsley, C. M. 1975, A&A, 38, 451

Clark, P. C., Glover, S. C. O., Ragan, S. E., Shetty, R., & Klessen, R. S. 2013, ApJL, 768, L34

Clarkson, W. I., Ghez, A. M., Morris, M. R., Lu, J. R., Stolte, A., McCrady, N., Do, T., & Yelda, S. 2012, The Astrophysical Journal, 751, 132

Coil, A. L. & Ho, P. T. P. 1999, ApJ, 513, 752

—. 2000, ApJ, 533, 245

Cotera, A., Morris, M., Ghez, A. M., Becklin, E. E., Tanner, A. M., Werner, M. W., & Stolovy, S. R. 1999a, in Astronomical Society of the Pacific Conference Series, Vol. 186, The Central Parsecs of the Galaxy, ed. H. Falcke, A. Cotera, W. J. Duschl, F. Melia, & M. J. Rieke, 240

Cotera, A. S., Erickson, E. F., Colgan, S. W. J., Simpson, J. P., Allen, D. A., & Burton, M. G. 1996, ApJ, 461, 750

Cotera, A. S., Simpson, J. P., Erickson, E. F., Colgan, S. W. J., Burton, M. G., & Allen, D. A. 1999b, ApJ, 510, 747

—. 2000, ApJS, 129, 123

Cragg, D. M., Johns, K. P., Godfrey, P. D., & Brown, R. D. 1992, MNRAS, 259, 203

Crocker, R. M. 2012a, MNRAS, 423, 3512

Crocker, R. M. 2012b, in IAU Symposium, Vol. 284, IAU Symposium, ed. R. J. Tuffs & C. C. Popescu, 371–378

Crocker, R. M., Jones, D. I., Melia, F., Ott, J., & Protheroe, R. J. 2010, Nature, 463, 65

Dahmen, G., Huttemeister, S., Wilson, T. L., & Mauersberger, R. 1998, A&A, 331, 959

Dalgarno, A. 2006, Proceedings of the National Academy of Science, 103, 12269

Danby, G., Flower, D. R., Valiron, P., Schilke, P., & Walmsley, C. M. 1988, MNRAS, 235, 229

Davidson, J. A., Werner, M. W., Wu, X., Lester, D. F., Harvey, P. M., Joy, M., & Morris, M. 1992, ApJ, 387, 189

de Pree, C. G., Gaume, R. A., Goss, W. M., & Claussen, M. J. 1996, Astrophysical Journal v.464, 464, 788

de Pree, C. G., Goss, W. M., & Gaume, R. A. 1998, Astrophysical Journal v.500, 500, 847

de Vaucouleurs, G. 1964, in IAU Symposium, Vol. 20, The Galaxy and the Magellanic Clouds, ed. F. J. Kerr, 195

de Vaucouleurs, G. 1970, in IAU Symposium, Vol. 38, The Spiral Structure of our Galaxy, ed. W. Becker & G. I. Kontopoulos, 18

Dgani, R. & Soker, N. 1998, ApJ, 495, 337

Dong, H., Wang, Q. D., & Morris, M. R. 2012, MNRAS, 425, 884

Dumouchel, F., Faure, A., & Lique, F. 2010, MNRAS, 406, 2488

Eckart, A. & Genzel, R. 1996, Nature, 383, 415

—. 1997, MNRAS, 284, 576

Ekers, R. D., van Gorkom, J. H., Schwarz, U. J., & Goss, W. M. 1983, A&A, 122, 143

Elitzur, M., Hollenbach, D. J., & McKee, C. F. 1989, Astrophysical Journal, 346, 983

Enoch, M. L., Evans, II, N. J., Sargent, A. I., Glenn, J., Rosolowsky, E., & Myers, P. 2008, ApJ, 684, 1240

Espinoza, P., Selman, F. J., & Melnick, J. 2009, A&A, 501, 563

Etxaluze, M., Smith, H. A., Tolls, V., Stark, A. A., & Gonzalez-Alfonso, E. 2011, arXiv, astro-ph.GA

Falcke, H. & Markoff, S. 2000, A&A, 362, 113

Farrah, D., Lonsdale, C. J., Weedman, D. W., Spoon, H. W. W., Rowan-Robinson, M., Polletta, M., Oliver, S., Houck, J. R., & Smith, H. E. 2008, ApJ, 677, 957

Ferrière, K. 2012, A&A, 540, A50

Figer, D. F., McLean, I. S., & Morris, M. R. 1999, The Astrophysical Journal, 514, 202

Figer, D. F., Rich, R. M., Kim, S. S., Morris, M., & Serabyn, E. 2004, ApJ, 601, 319

Figer, D. F. et al. 2002, ApJ, 581, 258

Fleck, Jr., R. C. 1980, ApJ, 242, 1019

Flower, D. R. 1999, MNRAS, 305, 651

Flower, D. R., des Forets, G. P., & Walmsley, C. M. 1995, Astronomy and Astrophysics (ISSN 0004-6361), 294, 815

Font, A. S., Johnston, K. V., Bullock, J. S., & Robertson, B. E. 2006, ApJ, 646, 886

Freedman, W. L. & Madore, B. F. 1990, ApJ, 365, 186

Fryer, C. L., Rockefeller, G., Hungerford, A., & Melia, F. 2006, ApJ, 638, 786

Gando Ryu, S., Nobukawa, M., Nakashima, S., Tsuru, T. G., Koyama, K., & Uchiyama, H. 2012, ArXiv e-prints

Gaume, R. A. & Claussen, M. J. 1990, Astrophysical Journal, 351, 538

Gaume, R. A., Claussen, M. J., de Pree, C. G., Goss, W. M., & Mehringer, D. M. 1995, Astrophysical Journal v.449, 449, 663

Geballe, T. R. & Oka, T. 2010, ApJL, 709, L70

Genzel, R., Crawford, M. K., Townes, C. H., & Watson, D. M. 1985, ApJ, 297, 766

Genzel, R., Eckart, A., Ott, T., & Eisenhauer, F. 1997, MNRAS, 291, 219

Genzel, R., Eisenhauer, F., & Gillessen, S. 2010, Reviews of Modern Physics, 82, 3121

Genzel, R., Thatte, N., Krabbe, A., Kroker, H., & Tacconi-Garman, L. E. 1996, ApJ, 472, 153

Ghez, A. M., Klein, B. L., Morris, M., & Becklin, E. E. 1998, ApJ, 509, 678

Ghez, A. M. et al. 2008, ApJ, 689, 1044

Gillessen, S., Eisenhauer, F., Fritz, T. K., Bartko, H., Dodds-Eden, K., Pfuhl, O., Ott, T., & Genzel, R. 2009a, ApJL, 707, L114

Gillessen, S., Eisenhauer, F., Trippe, S., Alexander, T., Genzel, R., Martins, F., & Ott, T. 2009b, ApJ, 692, 1075

Glassgold, A. E., Galli, D., & Padovani, M. 2012, ApJ, 756, 157

Goicoechea, J. R., Etxaluze, M., Cernicharo, J., Gerin, M., Neufeld, D. A., Contursi, A., Bell, T. A., De Luca, M., Encrenaz, P., Indriolo, N., Lis, D. C., Polehampton, E. T., & Sonnentrucker, P. 2013, ApJL, 769, L13

Goicoechea, J. R., Rodríguez-Fernández, N. J., & Cernicharo, J. 2004, ApJ, 600, 214

Goldreich, P. & Kwan, J. 1974, ApJ, 189, 441

Goldsmith, P. F. 2001, ApJ, 557, 736

Gordon, M. A., Berkermann, U., Mezger, P. G., Zylka, R., Haslam, C. G. T., Kreysa, E., Sievers, A., & Lemke, R. 1993, A&A, 280, 208

Goss, W. M., Schwarz, U. J., van Gorkom, J. H., & Ekers, R. D. 1985, MNRAS, 215, 69P

Goto, M., Indriolo, N., Geballe, T. R., & Usuda, T. 2013, ArXiv e-prints

Goto, M., Usuda, T., Geballe, T. R., Indriolo, N., McCall, B. J., Henning, T., & Oka, T. 2011, PASJ, 63, L13

Goto, M., Usuda, T., Nagata, T., Geballe, T. R., McCall, B. J., Indriolo, N., Suto, H., Henning, T., Morong, C. P., & Oka, T. 2008, arXiv, astro-ph

Guo, F. & Mathews, W. G. 2012, ApJ, 756, 181

Güsten, R. 1989, in IAU Symposium, Vol. 136, The Center of the Galaxy, ed. M. Morris, 89–+

Güsten, R., Baryshev, A., Bell, A., Belloche, A., Graf, U., Hafok, H., Heyminck, S., Hochgürtel, S., Honingh, C. E., Jacobs, K., Kasemann, C., Klein, B., Klein, T., Korn, A., Krämer, I., Leinz, C., Lundgren, A., Menten, K. M., Meyer, K., Muders, D., Pacek, F., Rabanus, D., Schäfer, F., Schilke, P., Schneider, G., Stutzki, J., Wieching, G., Wunsch, A., & Wyrowski, F. 2008, in Society of Photo-Optical Instrumentation Engineers (SPIE) Conference Series, Vol. 7020, Society of Photo-Optical Instrumentation Engineers (SPIE) Conference Series

Güsten, R., Genzel, R., Wright, M. C. H., Jaffe, D. T., Stutzki, J., & Harris, A. I. 1987, ApJ, 318, 124

Güsten, R. & Henkel, C. 1983, A&A, 125, 136

Güsten, R., Nyman, L. Å., Schilke, P., Menten, K., Cesarsky, C., & Booth, R. 2006, A&A, 454, L13

Güsten, R., Walmsley, C. M., & Pauls, T. 1981, A&A, 103, 197

Güsten, R., Walmsley, C. M., Ungerechts, H., & Churchwell, E. 1985, A&A, 142, 381

Habibi, M., Stolte, A., Brandner, W., Hußmann, B., & Motohara, K. 2012, ArXiv e-prints

Hammer, F., Puech, M., Chemin, L., Flores, H., & Lehnert, M. D. 2007, ApJ, 662, 322

Handa, T., Sakano, M., Naito, S., Hiramatsu, M., & Tsuboi, M. 2006, The Astrophysical Journal, 636, 261

Harris, A. I., Jaffe, D. T., Silber, M., & Genzel, R. 1985, ApJL, 294, L93

Harris, G. J., Tennyson, J., Kaminsky, B. M., Pavlenko, Y. V., & Jones, H. R. A. 2006, MNRAS, 367, 400

Hauschildt, H., Güsten, R., & Schilke, P. 1995, in Lecture Notes in Physics, Berlin Springer Verlag, Vol. 459, The Physics and Chemistry of Interstellar Molecular Clouds, ed. G. Winnewisser & G. C. Pelz, 52–53

Hayward, C. C. 2013, MNRAS

Herrnstein, R. M. & Ho, P. T. P. 2002, The Astrophysical Journal, 579, L83

Herrnstein, R. M. & Ho, P. T. P. 2005, ApJ, 620, 287

Heyminck, S., Kasemann, C., Güsten, R., de Lange, G., & Graf, U. U. 2006, A&A, 454, L21

Ho, P. T. P., Jackson, J. M., Barrett, A. H., & Armstrong, J. T. 1985, ApJ, 288, 575

Hogerheijde, M. R. & Tak, F. F. S. v. d. 2000, Astronomy and Astrophysics, 362, 697

Hollenbach, D. J., Takahashi, T., & Tielens, A. G. G. M. 1991, ApJ, 377, 192

Hopkins, A. M. & Beacom, J. F. 2006, ApJ, 651, 142

Hußmann, B., Stolte, A., Brandner, W., Gennaro, M., & Liermann, A. 2012, Astronomy and Astrophysics, 540, A57

Hüttemeister, S., Wilson, T. L., Bania, T. M., & Martin-Pintado, J. 1993a, Astronomy and Astrophysics (ISSN 0004-6361), 280, 255

Hüttemeister, S., Wilson, T. L., Henkel, C., & Mauersberger, R. 1993b, A&A, 276, 445

Hüttemeister, S., Wilson, T. L., Mauersberger, R., Lemme, C., Dahmen, G., & Henkel, C. 1995, Astronomy and Astrophysics (ISSN 0004-6361), 294, 667

Indriolo, N. & McCall, B. J. 2012, ApJ, 745, 91

Inui, T., Koyama, K., Matsumoto, H., & Tsuru, T. G. 2009, PASJ, 61, 241

Jackson, J. M., Geis, N., Genzel, R., Harris, A. I., Madden, S., Poglitsch, A., Stacey, G. J., & Townes, C. H. 1993, ApJ, 402, 173

Jensen, J. B., Tonry, J. L., Barris, B. J., Thompson, R. I., Liu, M. C., Rieke, M. J., Ajhar, E. A., & Blakeslee, J. P. 2003, ApJ, 583, 712

Jogee, S., Scoville, N., & Kenney, J. D. P. 2005, ApJ, 630, 837

Johnson, S. P., Dong, H., & Wang, Q. D. 2009, MNRAS, 399, 1429

Jones, P. A., Burton, M. G., Cunningham, M. R., Requena-Torres, M. A., Menten, K. M., Schilke, P., Belloche, A., Leurini, S., Martín-Pintado, J., Ott, J., & Walsh, A. J. 2012, MNRAS, 419, 2961

Jones, P. A., Burton, M. G., Cunningham, M. R., Tothill, N. F. H., & Walsh, A. J. 2013, ArXiv e-prints

Juvela, M. & Ysard, N. 2011, ApJ, 739, 63

Karlsson, R., Sjouwerman, L. O., Sandqvist, A., & Whiteoak, J. B. 2003, A&A, 403, 1011

Kasemann, C., Güsten, R., Heyminck, S., Klein, B., Klein, T., Philipp, S. D., Korn, A., Schneider, G., Henseler, A., Baryshev, A., & Klapwijk, T. M. 2006, in Society of Photo-Optical Instrumentation Engineers (SPIE) Conference Series, Vol. 6275, Society of Photo-Optical Instrumentation Engineers (SPIE) Conference Series

Kauffmann, J., Pillai, T., & Zhang, Q. 2013, ApJL, 765, L35

Kennicutt, R. C. & Evans, N. J. 2012, ARAA, 50, 531

Klypin, A., Zhao, H., & Somerville, R. S. 2002, ApJ, 573, 597

Kormendy, J. 2004, Coevolution of Black Holes and Galaxies, 1

Kormendy, J., Bender, R., & Cornell, M. E. 2011, Nature, 469, 374

Kormendy, J., Drory, N., Bender, R., & Cornell, M. E. 2010, ApJ, 723, 54

Kormendy, J. & Gebhardt, K. 2001, in American Institute of Physics Conference Series, Vol. 586, 20th Texas Symposium on relativistic astrophysics, ed. J. C. Wheeler & H. Martel, 363–381

Koyama, K., Awaki, H., Kunieda, H., Takano, S., & Tawara, Y. 1989, Nature, 339, 603

Koyama, K., Maeda, Y., Sonobe, T., Takeshima, T., Tanaka, Y., & Yamauchi, S. 1996, PASJ, 48, 249

Kraemer, K. E. & Jackson, J. M. 1995, Astrophysical Journal, 439, L9

Kruijssen, J. M. D., Longmore, S. N., Elmegreen, B. G., Murray, N., Bally, J., Testi, L., & Kennicutt, Jr., R. C. 2013, ArXiv e-prints

Kuan, Y.-J. & Snyder, L. E. 1996, ApJ, 470, 981

Kunneriath, D., Eckart, A., Vogel, S. N., Teuben, P., Muzic, K., Schödel, R., Garcia-Marin, M., Moultaka, J., Staguhn, J., Straubmeier, C., Zensus, J. A., Valencia-S, M., & Karas, V. 2012, Astronomy and Astrophysics, 538, A127

Lada, C. J., Muench, A. A., Rathborne, J., Alves, J. F., & Lombardi, M. 2008, ApJ, 672, 410

Lang, C. C., Goss, W. M., & Morris, M. 2001, AJ, 121, 2681

—. 2002, AJ, 124, 2677

Lang, C. C., Goss, W. M., & Wood, D. O. S. 1997, Astrophysical Journal v.474, 474, 275

Lang, C. C., Miller Goss, W., Cyganowski, C., & Clubb, K. I. 2010, ArXiv e-prints

Lau, R. M., Herter, T. L., Morris, M. R., Becklin, E. E., & Adams, J. D. 2013, ArXiv e-prints

Launhardt, R., Zylka, R., & Mezger, P. G. 2002a, A&A, 384, 112

—. 2002b, A&A, 384, 112

Law, C. 2008, Massive Stars as Cosmic Engines, 250, 407

Law, C. J. 2010, ApJ, 708, 474

Le Floc'h, E., Papovich, C., Dole, H., Bell, E. F., Lagache, G., Rieke, G. H., Egami, E., Pérez-González, P. G., Alonso-Herrero, A., Rieke, M. J., Blaylock, M., Engelbracht, C. W., Gordon, K. D., Hines, D. C., Misselt, K. A., Morrison, J. E., & Mould, J. 2005, ApJ, 632, 169

Lis, D. C., Goldsmith, P. F., Carlstrom, J. E., & Scoville, N. Z. 1993, ApJ, 402, 238

Lis, D. C. & Menten, K. M. 1998, ApJ, 507, 794

Lis, D. C., Menten, K. M., Serabyn, E., & Zylka, R. 1994, ApJL, 423, L39

Lis, D. C., Pearson, J. C., Neufeld, D. A., Schilke, P., Müller, H. S. P., Gupta, H., Bell, T. A., Comito, C., Phillips, T. G., Bergin, E. A., Ceccarelli, C., Goldsmith, P. F., Blake, G. A., Bacmann, A., Baudry, A., Benedettini, M., Benz, A., Black, J., Boogert, A., Bottinelli, S., Cabrit, S., Caselli, P., Castets, A., Caux, E., Cernicharo, J., Codella, C., Coutens, A., Crimier, N., Crockett, N. R., Daniel, F., Demyk, K., Dominic, C., Dubernet, M.-L., Emprechtinger, M., Encrenaz, P., Falgarone, E., Fuente, A., Gerin, M., Giesen, T. F., Goicoechea, J. R., Helmich, F., Hennebelle, P., Henning, T., Herbst, E., Hily-Blant, P., Hjalmarson, Å., Hollenbach, D., Jack, T., Joblin, C., Johnstone, D., Kahane,

C., Kama, M., Kaufman, M., Klotz, A., Langer, W. D., Larsson, B., Le Bourlot, J., Lefloch, B., Le Petit, F., Li, D., Liseau, R., Lord, S. D., Lorenzani, A., Maret, S., Martin, P. G., Melnick, G. J., Menten, K. M., Morris, P., Murphy, J. A., Nagy, Z., Nisini, B., Ossenkopf, V., Pacheco, S., Pagani, L., Parise, B., Pérault, M., Plume, R., Qin, S.-L., Roueff, E., Salez, M., Sandqvist, A., Saraceno, P., Schlemmer, S., Schuster, K., Snell, R., Stutzki, J., Tielens, A., Trappe, N., van der Tak, F. F. S., van der Wiel, M. H. D., van Dishoeck, E., Vastel, C., Viti, S., Wakelam, V., Walters, A., Wang, S., Wyrowski, F., Yorke, H. W., Yu, S., Zmuidzinas, J., Delorme, Y., Desbat, J.-P., Güsten, R., Krieg, J.-M., & Delforge, B. 2010a, A&A, 521, L9

Lis, D. C., Phillips, T. G., Goldsmith, P. F., Neufeld, D. A., Herbst, E., Comito, C., Schilke, P., Müller, H. S. P., Bergin, E. A., Gerin, M., Bell, T. A., Emprechtinger, M., Black, J. H., Blake, G. A., Boulanger, F., Caux, E., Ceccarelli, C., Cernicharo, J., Coutens, A., Crockett, N. R., Daniel, F., Dartois, E., de Luca, M., Dubernet, M.-L., Encrenaz, P., Falgarone, E., Geballe, T. R., Godard, B., Giesen, T. F., Goicoechea, J. R., Gry, C., Gupta, H., Hennebelle, P., Hily-Blant, P., Kołos, R., Krełowski, J., Joblin, C., Johnstone, D., Kaźmierczak, M., Lord, S. D., Maret, S., Martin, P. G., Martín-Pintado, J., Melnick, G. J., Menten, K. M., Monje, R., Mookerjea, B., Morris, P., Murphy, J. A., Ossenkopf, V., Pearson, J. C., Pérault, M., Persson, C., Plume, R., Qin, S.-L., Salez, M., Schlemmer, S., Schmidt, M., Sonnentrucker, P., Stutzki, J., Teyssier, D., Trappe, N., van der Tak, F. F. S., Vastel, C., Wang, S., Yorke, H. W., Yu, S., Zmuidzinas, J., Boogert, A., Erickson, N., Karpov, A., Kooi, J., Maiwald, F. W., Schieder, R., & Zaal, P. 2010b, A&A, 521, L26

Lis, D. C., Schilke, P., Bergin, E. A., Emprechtinger, M., & the HEXOS Team. 2012, Phil. Trans. R. Soc. A, 370, 5162

Lis, D. C., Serabyn, E., Zylka, R., & Li, Y. 2001, ApJ, 550, 761

Liszt, H. S. & Burton, W. B. 1978, ApJ, 226, 790

—. 1980, ApJ, 236, 779

Liszt, H. S., Burton, W. B., Sanders, R. H., & Scoville, N. Z. 1977, ApJ, 213, 38

Liu, H. B., Ho, P. T.-P., Wright, M. C. H., Su, Y.-N., Hsieh, P.-Y., Sun, A.-L., Kim, S. S., & Minh, Y. C. 2013, ArXiv e-prints

Liu, H. B., Hsieh, P.-Y., Ho, P. T. P., Su, Y.-N., Wright, M., Sun, A.-L., & Minh, Y. C. 2012, ApJ, 756, 195

Liu, S.-Y. & Snyder, L. E. 1999, ApJ, 523, 683

Longmore, S. N. 2012, ArXiv e-prints

Longmore, S. N., Bally, J., Testi, L., Purcell, C. R., Walsh, A. J., Bressert, E., Pestalozzi, M., Molinari, S., Ott, J., Cortese, L., Battersby, C., Murray, N., Lee, E., Kruijssen, J. M. D., Schisano, E., & Elia, D. 2013, MNRAS, 429, 987

Longmore, S. N., Rathborne, J., Bastian, N., Alves, J., Ascenso, J., Bally, J., Testi, L., Longmore, A., Battersby, C., Bressert, E., Purcell, C., Walsh, A., Jackson, J., Foster, J., Molinari, S., Meingast, S., Amorim, A., Lima, J., Marques, R., Moitinho, A., Pinhao, J., Rebordao, J., & Santos, F. D. 2012, ApJ, 746, 117

Lu, J. R., Do, T., Ghez, A. M., Morris, M. R., Yelda, S., & Matthews, K. 2013, The Astrophysical Journal, 764, 155

Lugten, J. B., Stacey, G. J., Harris, A. I., Genzel, R., & Townes, C. H. 1987, in American Institute of Physics Conference Series, Vol. 155, The Galactic Center, ed. D. C. Backer, 118–122

Lutz, D., Feuchtgruber, H., Genzel, R., Kunze, D., Rigopoulou, D., Spoon, H. W. W., Wright, C. M., Egami, E., Katterloher, R., Sturm, E., Wieprecht, E., Sternberg, A., Moorwood, A. F. M., & de Graauw, T. 1996, Astronomy and Astrophysics, 315, L269

Magnelli, B., Lutz, D., Santini, P., Saintonge, A., Berta, S., Albrecht, M., Altieri, B., Andreani, P., Aussel, H., Bertoldi, F., Béthermin, M., Bongiovanni, A., Capak, P., Chapman, S., Cepa, J., Cimatti, A., Cooray, A., Daddi, E., Danielson, A. L. R., Dannerbauer, H., Dunlop, J. S., Elbaz, D., Farrah, D., Förster Schreiber, N. M., Genzel, R., Hwang, H. S., Ibar, E., Ivison, R. J., Le Floc'h, E., Magdis, G., Maiolino, R., Nordon, R., Oliver, S. J., Pérez García, A., Poglitsch, A., Popesso, P., Pozzi, F., Riguccini, L., Rodighiero, G., Rosario, D., Roseboom, I., Salvato, M., Sanchez-Portal, M., Scott, D., Smail, I., Sturm, E., Swinbank, A. M., Tacconi, L. J., Valtchanov, I., Wang, L., & Wuyts, S. 2012, A&A, 539, A155

Majewski, S. R., Skrutskie, M. F., Weinberg, M. D., & Ostheimer, J. C. 2003, ApJ, 599, 1082

Maness, H., Martins, F., Trippe, S., Genzel, R., Graham, J. R., Sheehy, C., Salaris, M., Gillessen, S., Alexander, T., Paumard, T., Ott, T., Abuter, R., & Eisenhauer, F. 2007, The Astrophysical Journal, 669, 1024

Mangum, J. G. & Wootten, A. 1994, The Astrophysical Journal, 428, L33

Markoff, S., Bower, G. C., & Falcke, H. 2007, MNRAS, 379, 1519

Marr, J. M., Wright, M. C. H., & Backer, D. C. 1993, ApJ, 411, 667

Marshall, J., Lasenby, A. N., & Harris, A. I. 1995, MNRAS, 277, 594

Martin, C. L., Walsh, W. M., Xiao, K., Lane, A. P., Walker, C. K., & Stark, A. A. 2004, ApJS, 150, 239

Martín, S., Martín-Pintado, J., Montero-Castaño, M., Ho, P. T. P., & Blundell, R. 2012, A&A, 539, A29

Martín-Pintado, J., de Vicente, P., Fuente, A., & Planesas, P. 1997, ApJ, 482, L45

Martin-Pintado, J., de Vicente, P., Fuente, A., & Planesas, P. 1997, ApJL, 482, L45+

Martin-Pintado, J., Gaume, R. A., Rodríguez-Fernández, N., de Vicente, P., & Wilson, T. L. 1999, The Astrophysical Journal, 519, 667

Martins, F., Schaerer, D., & Hillier, D. J. 2005, Astronomy and Astrophysics, 436, 1049

Mauerhan, J. C., Cotera, A., Dong, H., Morris, M. R., Wang, Q. D., Stolovy, S. R., & Lang, C. 2010a, ApJ, 725, 188

Mauerhan, J. C., Morris, M. R., Cotera, A., Dong, H., Wang, Q. D., Stolovy, S. R., Lang, C., & Glass, I. S. 2010b, ApJL, 713, L33

Mauerhan, J. C., Muno, M. P., & Morris, M. 2007, ApJ, 662, 574

Mauerhan, J. C., Muno, M. P., Morris, M. R., Stolovy, S. R., & Cotera, A. 2010c, ApJ, 710, 706

Mauersberger, R., Henkel, C., Weiß, A., Peck, A. B., & Hagiwara, Y. 2003, A&A, 403, 561

Mauersberger, R., Henkel, C., Wilson, T. L., & Walmsley, C. M. 1986, A&A, 162, 199

McClure-Griffiths, N. M., Dickey, J. M., Gaensler, B. M., Green, A. J., Green, J. A., & Haverkorn, M. 2012, ApJS, 199, 12

McClure-Griffiths, N. M., Green, J. A., Hill, A. S., Lockman, F. J., Dickey, J. M., Gaensler, B. M., & Green, A. J. 2013, arXiv.org, astro-ph.GA

McConnachie, A. W. 2012, AJ, 144, 4

McGary, R. S., Coil, A. L., & Ho, P. T. P. 2001, ApJ, 559, 326

Mehringer, D. M. & Menten, K. M. 1997, ApJ, 474, 346

Mehringer, D. M., Palmer, P., Goss, W. M., & Yusef-Zadeh, F. 1993, Astrophysical Journal, 412, 684

Meidt, S. E., Schinnerer, E., Garcia-Burillo, S., Hughes, A., Colombo, D., Pety, J., Dobbs, C. L., Schuster, K. F., Kramer, C., Leroy, A. K., Dumas, G., & Thompson, T. A. 2013, ArXiv e-prints

Meier, D. S. & Turner, J. L. 2001, ApJ, 551, 687

Meier, D. S. & Turner, J. L. 2004, The Astronomical Journal, 127, 2069

Meier, D. S. & Turner, J. L. 2005, ApJ, 618, 259

Meier, D. S., Turner, J. L., & Hurt, R. L. 2008, The Astrophysical Journal, 675, 281

Meijerink, R., Spaans, M., & Israel, F. P. 2006, The Astrophysical Journal, 650, L103

—. 2007, Astronomy and Astrophysics, 461, 793

Menten, K. 1991a, in Astronomical Society of the Pacific Conference Series, Vol. 16, Atoms, Ions and Molecules: New Results in Spectral Line Astrophysics, ed. A. D. Haschick & P. T. P. Ho, 119

Menten, K. M. 1991b, ApJL, 380, L75

Menten, K. M., Wilson, R. W., Leurini, S., & Schilke, P. 2009, ApJ, 692, 47

Menten, K. M., Wyrowski, F., Belloche, A., Güsten, R., Dedes, L., & Müller, H. S. P. 2011, A&A, 525, A77

Mezger, P. G., Chini, R., Kreysa, E., & Gemuend, H.-P. 1986, Astronomy and Astrophysics (ISSN 0004-6361), 160, 324

Mezger, P. G. & Henderson, A. P. 1967, ApJ, 147, 471

Mezger, P. G., Zylka, R., Salter, C. J., Wink, J. E., Chini, R., Kreysa, E., & Tuffs, R. 1989, A&A, 209, 337

Miao, Y., Mehringer, D. M., Kuan, Y.-J., & Snyder, L. E. 1995, ApJL, 445, L59

Mills, E., Morris, M. R., Lang, C. C., Dong, H., Wang, Q. D., Cotera, A., & Stolovy, S. R. 2011, ApJ, 735, 84

Mills, E. A. C. & Morris, M. R. 2013, ApJ, 772, 105

Mizuno, A. & Fukui, Y. 2004, in Astronomical Society of the Pacific Conference Series, Vol. 317, Milky Way Surveys: The Structure and Evolution of our Galaxy, ed. D. Clemens, R. Shah, & T. Brainerd, 59

Molinari, S., Bally, J., Noriega-Crespo, A., Compiègne, M., Bernard, J. P., Paradis, D., Martin, P., Testi, L., Barlow, M., Moore, T., Plume, R., Swinyard,

B., Zavagno, A., Calzoletti, L., Di Giorgio, A. M., Elia, D., Faustini, F., Natoli, P., Pestalozzi, M., Pezzuto, S., Piacentini, F., Polenta, G., Polychroni, D., Schisano, E., Traficante, A., Veneziani, M., Battersby, C., Burton, M., Carey, S., Fukui, Y., Li, J. Z., Lord, S. D., Morgan, L., Motte, F., Schuller, F., Stringfellow, G. S., Tan, J. C., Thompson, M. A., Ward-Thompson, D., White, G., & Umana, G. 2011, ApJL, 735, L33

Monje, R. R., Emprechtinger, M., Phillips, T. G., Lis, D. C., Goldsmith, P. F., Bergin, E. A., Bell, T. A., Neufeld, D. A., & Sonnentrucker, P. 2011, ApJL, 734, L23

Montero-Castaño, M., Herrnstein, R. M., & Ho, P. T. P. 2009, ApJ, 695, 1477

Morris, M. 1975, ApJ, 197, 603

Morris, M. 1989, in IAU Symposium, Vol. 136, The Center of the Galaxy, ed. M. Morris, 171

—. 1993, ApJ, 408, 496

Morris, M., Polish, N., Zuckerman, B., & Kaifu, N. 1983, AJ, 88, 1228

Morris, M. & Serabyn, E. 1996, ARAA, 34, 645

Morris, M., Zuckerman, B., Palmer, P., & Turner, B. E. 1973, ApJ, 186, 501

Muno, M. P., Baganoff, F. K., Bautz, M. W., Brandt, W. N., Broos, P. S., Feigelson, E. D., Garmire, G. P., Morris, M. R., Ricker, G. R., & Townsley, L. K. 2003, ApJ, 589, 225

Muno, M. P., Bauer, F. E., Baganoff, F. K., Bandyopadhyay, R. M., Bower, G. C., Brandt, W. N., Broos, P. S., Cotera, A., Eikenberry, S. S., Garmire, G. P., Hyman, S. D., Kassim, N. E., Lang, C. C., Lazio, T. J. W., Law, C.,

Mauerhan, J. C., Morris, M. R., Nagata, T., Nishiyama, S., Park, S., Ramìrez, S. V., Stolovy, S. R., Wijnands, R., Wang, Q. D., Wang, Z., & Yusef-Zadeh, F. 2009, ApJS, 181, 110

Murakami, H., Koyama, K., Sakano, M., Tsujimoto, M., & Maeda, Y. 2000, ApJ, 534, 283

Nagai, M., Tanaka, K., Kamegai, K., & Oka, T. 2007, Publications of the Astronomical Society of Japan, 59, 25

Nagata, T., Woodward, C. E., Shure, M., & Kobayashi, N. 1995, AJ, 109, 1676

Nagata, T., Woodward, C. E., Shure, M., Pipher, J. L., & Okuda, H. 1990, ApJ, 351, 83

Nakanishi, H. & Sofue, Y. 2006, PASJ, 58, 847

Nayakshin, S., Cuadra, J., & Springel, V. 2007, MNRAS, 379, 21

Nayakshin, S. & Sunyaev, R. 2005, MNRAS, 364, L23

Nishiyama, S., Nagata, T., Tamura, M., Kandori, R., Hatano, H., Sato, S., & Sugitani, K. 2008, ApJ, 680, 1174

Nishiyama, S., Tamura, M., Hatano, H., Kato, D., Tanabé, T., Sugitani, K., & Nagata, T. 2009, ApJ, 696, 1407

O'Connell, R. W. & Mangano, J. J. 1978, ApJ, 221, 62

Oka, T., Geballe, T. R., Goto, M., Usuda, T., & McCall, B. J. 2005, ApJ, 632, 882

Oka, T., Hasegawa, T., Handa, T., Hayashi, M., & Sakamoto, S. 1996, Astrophysical Journal v.460, 460, 334

Oka, T., Hasegawa, T., Hayashi, M., Handa, T., & Sakamoto, S. 1998a, Astrophysical Journal v.493, 493, 730

Oka, T., Hasegawa, T., Sato, F., Tsuboi, M., & Miyazaki, A. 1998b, The Astrophysical Journal Supplement Series, 118, 455

Oka, T., Hasegawa, T., Sato, F., Tsuboi, M., Miyazaki, A., & Sugimoto, M. 2001, The Astrophysical Journal, 562, 348

Oka, T., Nagai, M., Kamegai, K., & Tanaka, K. 2011, ApJ, 732, 120

Oka, T., Onodera, Y., Nagai, M., Tanaka, K., Matsumura, S., & Kamegai, K. 2012, ApJS, 201, 14

Oka, T., Shimizu, F. O., Shimizu, T., & Watson, J. K. G. 1971, AJ, 165, L15

Ossenkopf, V. & Henning, T. 1994, A&A, 291, 943

Osterbrock, D. E. 1989, Astrophysics of gaseous nebulae and active galactic nuclei (Mill Valley, CA: University Science Books)

Ott, J., Henkel, C., Braatz, J. A., & Weiß, A. 2011, ApJ, 742, 95

Ott, J., Weiss, A., Henkel, C., & Walter, F. 2005, ApJ, 629, 767

Ott, J., Weiss, A., Staveley-Smith, L., & Henkel, C. 2006, in Bulletin of the American Astronomical Society, Vol. 38, American Astronomical Society Meeting Abstracts, 920–+

Ott, M., Witzel, A., Quirrenbach, A., Krichbaum, T. P., Standke, K. J., Schalinski, C. J., & Hummel, C. A. 1994, A&A, 284, 331

Padoan, P. & Scalo, J. 2005, ApJL, 624, L97

Pan, L. & Padoan, P. 2009, ApJ, 692, 594

Papadopoulos, P. P. 2010, ApJ, 720, 226

Paumard, T., Genzel, R., Martins, F., Nayakshin, S., Beloborodov, A. M., Levin, Y., Trippe, S., Eisenhauer, F., Ott, T., Gillessen, S., Abuter, R., Cuadra, J., Alexander, T., & Sternberg, A. 2006, ApJ, 643, 1011

Pei, C. C., Liu, S.-Y., & Snyder, L. E. 2000, The Astrophysical Journal, 530, 800

Perets, H. B., Gualandris, A., Kupi, G., Merritt, D., & Alexander, T. 2009, ApJ, 702, 884

Pérez-González, P. G., Rieke, G. H., Egami, E., Alonso-Herrero, A., Dole, H., Papovich, C., Blaylock, M., Jones, J., Rieke, M., Rigby, J., Barmby, P., Fazio, G. G., Huang, J., & Martin, C. 2005, ApJ, 630, 82

Pickett, H., Poynter, R., Cohen, E., Delitsky, M., Pearson, J., & Muller, H. 1998, J. Quant. Spectrosc. & Rad. Transfer, 60, 883

Pierce-Price, D. et al. 2000, The Astrophysical Journal, 545, L121

Pihlström, Y. M., Sjouwerman, L. O., & Fish, V. L. 2011, The Astrophysical Journal, 739, L21

Poglitsch, A., Stacey, G. J., Geis, N., Haggerty, M., Jackson, J., Rumitz, M., Genzel, R., & Townes, C. H. 1991, ApJL, 374, L33

Ponti, G., Terrier, R., Goldwurm, A., Belanger, G., & Trap, G. 2010, ApJ, 714, 732

Pritchet, C. J. & van den Bergh, S. 1999, AJ, 118, 883

Purcell, C. R., Longmore, S. N., Walsh, A. J., Whiting, M. T., Breen, S. L., Britton, T., Brooks, K. J., Burton, M. G., Cunningham, M. R., Green, J. A., Harvey-Smith, L., Hindson, L., Hoare, M. G., Indermuehle, B., Jones, P. A., Lo, N., Lowe, V., Phillips, C. J., Thompson, M. A., Urquhart, J. S., Voronkov, M. A., & White, G. L. 2012, MNRAS, 426, 1972

Qin, S.-L., Zhao, J.-H., Moran, J. M., Marrone, D. P., Patel, N. A., Wang, J.-J., Liu, S.-Y., & Kuan, Y.-J. 2008, The Astrophysical Journal, 677, 353

Quireza, C., Rood, R. T., Bania, T. M., Balser, D. S., & Maciel, W. J. 2006, ApJ, 653, 1226

Reid, M. J., Menten, K. M., Trippe, S., Ott, T., & Genzel, R. 2007, ApJ, 659, 378

Reid, M. J. et al. 2009, ApJ, 700, 137

Remijan, A. J., Markwick-Kemper, A., & ALMA Working Group on Spectral Line Frequencies. 2007, in Bulletin of the American Astronomical Society, Vol. 39, American Astronomical Society Meeting Abstracts, 132.11

Requena-Torres, M. A., Güsten, R., Weiß, A., Harris, A. I., Martín-Pintado, J., Stutzki, J., Klein, B., Heyminck, S., & Risacher, C. 2012, A&A, 542, L21

Requena-Torres, M. A., Martin-Pintado, J., Rodríguez-Franco, A., Martín, S., Rodríguez-Fernández, N. J., & de Vicente, P. 2006, Astronomy and Astrophysics, 455, 971

Rieke, G. H. & Lebofsky, M. J. 1985, ApJ, 288, 618

Riquelme, D., Amo-Baladron, M. A., Martin-Pintado, J., Mauersberger, R., Martin, S., & Bronfman, L. 2010, ArXiv e-prints

Riquelme, D., Amo-Baladrón, M. A., Martín-Pintado, J., Mauersberger, R., Martín, S., & Bronfman, L. 2013, A&A, 549, A36

Roberge, W. G., Dalgarno, A., & Flannery, B. P. 1981, ApJ, 243, 817

Rodríguez, L. F. & Zapata, L. A. 2013, ApJL, 767, L13

Rodríguez-Fernández, N. & Martin-Pintado, J. 2005, Astronomy and Astrophysics, 429, 923

Rodríguez-Fernández, N. J., Martín-Pintado, J., Fuente, A., de Vicente, P., Wilson, T. L., & Hüttemeister, S. 2001, A&A, 365, 174

Rodríguez-Fernández, N. J., Martín-Pintado, J., Fuente, A., & Wilson, T. L. 2004, A&A, 427, 217

Rolffs, R., Schilke, P., Comito, C., Bergin, E. A., Tak, F. F. S. v. d., Lis, D. C., Qin, S.-L., Menten, K. M., Güsten, R., Bell, T. A., Blake, G. A., Caux, E., Ceccarelli, C., Cernicharo, J., Crockett, N. R., Daniel, F., Dubernet, M.-L., Emprechtinger, M., Encrenaz, P., Gerin, M., Giesen, T. F., Goicoechea, J. R., Goldsmith, P. F., Gupta, H., Herbst, E., Joblin, C., Johnstone, D., Langer, W. D., Latter, W. D., Lord, S. D., Maret, S., Martin, P. G., Melnick, G. J., Morris, P., Müller, H. S. P., Murphy, J. A., Ossenkopf, V., Pearson, J. C., Pérault, M., Phillips, T. G., Plume, R., Schlemmer, S., Stutzki, J., Trappe, N., Vastel, C., Wang, S., Yorke, H. W., Yu, S., Zmuidzinas, J., Diez-Gonzalez, M. C., Bachiller, R., Martin-Pintado, J., Baechtold, W., Olberg, M., Nordh, L. H., Gill, J. J., & Chattopadhyay, G. 2010, Astronomy and Astrophysics, 521, L46

Rubin, R. H. 1968, ApJ, 154, 391

Sakamoto, K., Aalto, S., Evans, A. S., Wiedner, M. C., & Wilner, D. J. 2010, The Astrophysical Journal, 725, L228

Schilke, P., Comito, C., Müller, H. S. P., Bergin, E. A., Herbst, E., Lis, D. C., Neufeld, D. A., Phillips, T. G., Bell, T. A., Blake, G. A., Cabrit, S., Caux, E., Ceccarelli, C., Cernicharo, J., Crockett, N. R., Daniel, F., Dubernet, M.-L., Emprechtinger, M., Encrenaz, P., Falgarone, E., Gerin, M., Giesen, T. F., Goicoechea, J. R., Goldsmith, P. F., Gupta, H., Joblin, C., Johnstone, D., Langer, W. D., Latter, W. B., Lord, S. D., Maret, S., Martin, P. G., Melnick, G. J., Menten, K. M., Morris, P., Murphy, J. A., Ossenkopf, V., Pagani, L., Pearson, J. C., Pérault, M., Plume, R., Qin, S.-L., Salez, M., Schlemmer, S., Stutzki, J., Trappe, N., van der Tak, F. F. S., Vastel, C., Wang, S., Yorke, H. W., Yu, S., Erickson, N., Maiwald, F. W., Kooi, J., Karpov, A., Zmuidzinas, J., Boogert, A., Schieder, R., & Zaal, P. 2010, A&A, 521, L11

Schödel, R., Merritt, D., & Eckart, A. 2009, Astronomy and Astrophysics, 502, 91

Schöier, F. L., van der Tak, F. F. S., van Dishoeck, E. F., & Black, J. H. 2005, A&A, 432, 369

Schuller, F., Omont, A., Felli, M., Testi, L., Bertoldi, F., & Menten, K. M. 2005, in ESA Special Publication, Vol. 577, ESA Special Publication, ed. A. Wilson, 235–238

Schultheis, M., Sellgren, K., Ramírez, S., Stolovy, S., Ganesh, S., Glass, I. S., & Girardi, L. 2009, A&A, 495, 157

Scoville, N. Z., Stolovy, S. R., Rieke, M., Christopher, M., & Yusef-Zadeh, F. 2003, ApJ, 594, 294

Serabyn, E. & Guesten, R. 1987, A&A, 184, 133

Serabyn, E. & Güsten, R. 1991, A&A, 242, 376

Serabyn, E., Güsten, R., & Evans, II, N. J. 1989, in IAU Symposium, Vol. 136, The Center of the Galaxy, ed. M. Morris, 417–+

Serabyn, E., Lacy, J. H., & Achtermann, J. M. 1992, ApJ, 395, 166

Shaver, P. A., McGee, R. X., Newton, L. M., Danks, A. C., & Pottasch, S. R. 1983, MNRAS, 204, 53

Shukla, H., Yun, M. S., & Scoville, N. Z. 2004, ApJ, 616, 231

Simon, J. D. & Geha, M. 2007, ApJ, 670, 313

Simpson, J. P., Colgan, S. W. J., Cotera, A. S., Erickson, E. F., Hollenbach, D. J., Kaufman, M. J., & Rubin, R. H. 2007, ApJ, 670, 1115

Sjouwerman, L. O. & Pihlström, Y. M. 2008, ApJ, 681, 1287

Sjouwerman, L. O., Pihlstrom, Y. M., & Fish, V. L. 2010, The Astrophysical Journal, 710, L111

Sjouwerman, L. O., Pihlström, Y. M., & Fish, V. L. 2010, ApJL, 710, L111

Snyder, L. E., Kuan, Y.-J., & Miao, Y. 1994, in Lecture Notes in Physics, Berlin Springer Verlag, Vol. 439, The Structure and Content of Molecular Clouds, ed. T. L. Wilson & K. J. Johnston, 187

Sofue, Y. & Handa, T. 1984, Nature, 310, 568

Soker, N. & Dgani, R. 1997, ApJ, 484, 277

Sonnentrucker, P., Neufeld, D. A., Gerin, M., De Luca, M., Indriolo, N., Lis, D. C., & Goicoechea, J. R. 2013, The Astrophysical Journal, 763, L19

Stolovy, S., Ramirez, S., Arendt, R. G., Cotera, A., Yusef-Zadeh, F., Law, C., Gezari, D., Sellgren, K., Karr, J., Moseley, H., & Smith, H. A. 2006, Journal of Physics Conference Series, 54, 176

Su, M. & Finkbeiner, D. P. 2012, ApJ, 753, 61

Su, M., Slatyer, T. R., & Finkbeiner, D. P. 2010, ApJ, 724, 1044

Sutton, E. C., Danchi, W. C., Jaminet, P. A., & Masson, C. R. 1990, ApJ, 348, 503

Sweitzer, J. S., Palmer, P., Morris, M., Turner, B. E., & Zuckerman, B. 1979, ApJ, 227, 415

Tacconi, L. J., Genzel, R., Smail, I., Neri, R., Chapman, S. C., Ivison, R. J., Blain, A., Cox, P., Omont, A., Bertoldi, F., Greve, T., Förster Schreiber, N. M., Genel, S., Lutz, D., Swinbank, A. M., Shapley, A. E., Erb, D. K., Cimatti, A., Daddi, E., & Baker, A. J. 2008, ApJ, 680, 246

Takano, S., Nakai, N., & Kawaguchi, K. 2002, PASJ, 54, 195

Telesco, C. M., Davidson, J. A., & Werner, M. W. 1996, Astrophysical Journal v.456, 456, 541

Tielens, A. G. G. M. & Hollenbach, D. 1985, ApJ, 291, 722

Tsuboi, M., Handa, T., & Ukita, N. 1999, ApJS, 120, 1

Tsuboi, M. & Miyazaki, A. 2012, Publications of the Astronomical Society of Japan, 64, 111

Tsuboi, M., Ukita, N., & Handa, T. 1997, Astrophysical Journal v.481, 481, 263

van den Bergh, S. 1988, Comments on Astrophysics, 12, 131

van der Tak, F. F. S., Belloche, A., Schilke, P., Güsten, R., Philipp, S., Comito, C., Bergman, P., & Nyman, L.-Å. 2006, A&A, 454, L99

van der Tak, F. F. S., Black, J. H., Schöier, F. L., Jansen, D. J., & van Dishoeck, E. F. 2007, A&A, 468, 627

Vogel, S. N., Genzel, R., & Palmer, P. 1987, ApJ, 316, 243

Walmsley, C. M. & Ungerechts, H. 1983, A&A, 122, 164

Walsh, A. J., Breen, S. L., Britton, T., Brooks, K. J., Burton, M. G., Cunningham, M. R., Green, J. A., Harvey-Smith, L., Hindson, L., Hoare, M. G., Indermuehle, B., Jones, P. A., Lo, N., Longmore, S. N., Lowe, V., Phillips, C. J., Purcell, C. R., Thompson, M. A., Urquhart, J. S., Voronkov, M. A., White, G. L., & Whiting, M. T. 2011, MNRAS, 416, 1764

Wang, Q. D., Gotthelf, E. V., & Lang, C. C. 2002, Nature, 415, 148

Wang, Q. D. et al. 2010, MNRAS, 402, 895

Watkins, L. L., Evans, N. W., & An, J. H. 2010, MNRAS, 406, 264

Weaver, H. 1970, in IAU Symposium, Vol. 38, The Spiral Structure of our Galaxy, ed. W. Becker & G. I. Kontopoulos, 126

Wilson, T. L. 1999, Reports on Progress in Physics, 62, 143

Wilson, T. L., Henkel, C., & Hüttemeister, S. 2006, A&A, 460, 533

Wilson, T. L. & Rood, R. 1994, ARAA, 32, 191

Wilson, T. L., Ruf, K., Walmsley, C. M., Martin, R. N., Batrla, W., & Pauls, T. A. 1982, A&A, 115, 185

Wood, D. O. S. & Churchwell, E. 1989, ApJS, 69, 831

Yang, H.-Y. K., Ruszkowski, M., Ricker, P. M., Zweibel, E., & Lee, D. 2012, ApJ, 761, 185

Yusef-Zadeh, F., Arendt, R., Bushouse, H., Cotton, W., Haggard, D., Pound, M. W., Roberts, D. A., Royster, M., & Wardle, M. 2012, ApJL, 758, L11

Yusef-Zadeh, F., Braatz, J., Wardle, M., & Roberts, D. 2008, ApJL, 683, L147

Yusef-Zadeh, F., Cotton, W., Viti, S., Wardle, M., & Royster, M. 2013a, ApJL, 764, L19

Yusef-Zadeh, F., Hewitt, J. W., Wardle, M., Tatischeff, V., Roberts, D. A., Cotton, W., Uchiyama, H., Nobukawa, M., Tsuru, T. G., Heinke, C., & Royster, M. 2013b, ApJ, 762, 33

Yusef-Zadeh, F., Lacy, J. H., Wardle, M., Whitney, B., Bushouse, H., Roberts, D. A., & Arendt, R. G. 2010, ApJ, 725, 1429

Yusef-Zadeh, F. & Morris, M. 1987a, AJ, 94, 1178

—. 1987b, AJ, 94, 1178

Yusef-Zadeh, F., Morris, M., & Chance, D. 1984, Nature, 310, 557

Yusef-Zadeh, F., Muno, M., Wardle, M., & Lis, D. C. 2007, ApJ, 656, 847

Yusef-Zadeh, F., Roberts, D. A., Goss, W. M., Frail, D. A., & Green, A. J. 1996, ApJL, 466, L25+

Yusef-Zadeh, F., Royster, M., Wardle, M., Arendt, R., Bushouse, H., Lis, D. C., Pound, M. W., Roberts, D. A., Whitney, B., & Wootten, A. 2013c, ApJL, 767, L32

Yusef-Zadeh, F., Stolovy, S. R., Burton, M., Wardle, M., & Ashley, M. C. B. 2001, ApJ, 560, 749

Yusef-Zadeh, F., Wardle, M., Lis, D., Viti, S., Brogan, C., Chambers, E., Pound, M., & Rickert, M. 2013, arXiv.org, astro-ph.GA

Yusef-Zadeh, F., Wardle, M., & Roy, S. 2007, ApJ, 665, L123

Yusef-Zadeh, F. et al. 2009, ApJ, 702, 178

Zhang, Q. & Ho, P. T. P. 1995, Astrophysical Journal Letters v.450, 450, L63

Zhao, J.-H., Desai, K., Goss, W. M., & Yusef-Zadeh, F. 1993, Astrophysical Journal v.418, 418, 235

Zhao, J.-H., Morris, M. R., Goss, W. M., & An, T. 2009, ApJ, 699, 186

Zhao, J.-H. & Wright, M. C. H. 2011, The Astrophysical Journal, 742, 50

Zhu, Q., Lacy, J. H., Jaffe, D. T., Richter, M. J., & Greathouse, T. K. 2005, ApJ, 631, 381

Ziurys, L. M. & Turner, B. E. 1986, ApJL, 300, L19

Zubovas, K. & Nayakshin, S. 2012, MNRAS, 424, 666

Zuckerman, B., Morris, M., Turner, B. E., & Palmer, P. 1971, ApJ, 169, L105

Zylka, R., Guesten, R., Henkel, C., & Batrla, W. 1992, A&AS, 96, 525